UNIVERSITETET
I OSLO

Master's Thesis

Synthesis and structural characterization of heteroleptic dipyridophenazine–based $[Cu(N^N)(P^P)]^+$ complexes.

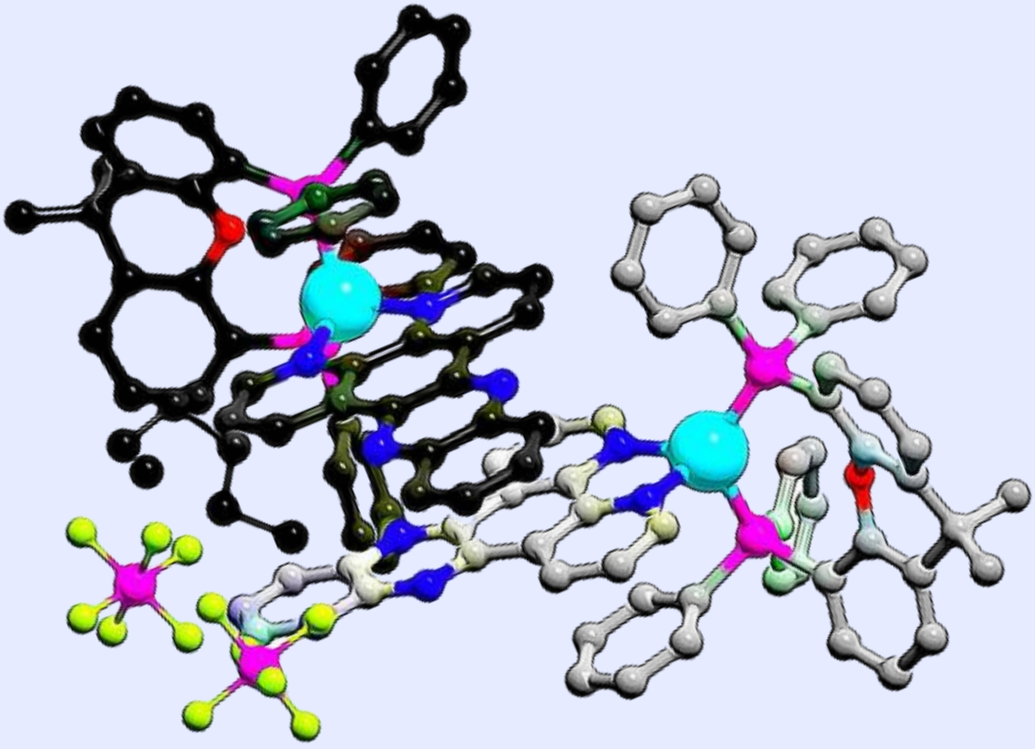

Melchizedek Amoakwah

A thesis submitted for a Master's degree in Organic Chemistry
[60 credits], **Spring 2023**

Department of Chemistry
Faculty of mathematics and natural sciences

Synthesis and structural characterization of heteroleptic dipyridophenazine–based $[Cu(N^N)(P^P)]^+$ complexes.

http://www.duo.uio.no/

Printing: Reprosentralen, Universitetet i Oslo.

Acknowledgements

Thanksgiving is accorded to the following persons for their invaluable assistance amongst other reasons leading to the successful completion of the assigned project; Supervisor Assoc. Prof. Mamou Amedjkouh, for this project, the many varied discussions concerning organic synthesis and experimental results, and guidance over the years. Raquel Jiménez Rama for the taught lessons on Schlenk-line, solvent-degassing and inert reaction techniques. Professor Mats Tilset, for the fruitful NMR discussions on specialised multiplets with unusual split patterns. Rafael C. S. Pupo and Inga L. Schmidtke for the help with the SC–XRD measurement and data refinement. Snr. Engr. Dirk Peterson for the taught lessons on *ledbpgp* DOSY pulse program and subsequent NMR request services. Erlend Steinvik, for the ESI– and APCI–MS measurements. Bjørn Gading Solemsli, for the introductory sessions on FT-IR instrument operation. Bjørn Terjei Austenaa, for providing the literature reference[48] on sulfo-nitric synthesis of phendione, and Professor Ola Nilsen for the introductory session on UV–Vis DRS measurements.

Abstract

For the purposes of solar–induced multi–electron storage and charge transfer reactions, heteroleptic $[Cu(N^N)(P^P)]^+$–type copper(I) complexes where (N^N)= diimine ligand and (P^P)= bulky diphosphine ligand, have become promising and viable alternatives to noble metal photosensitizers. In this thesis, the synthesis, structural and geometrical configurations of a series of electron–withdrawing *para*–substituted dipyrido–[3, 2–a: 2', 3'–c]phenazine(dppz) copper complexes (inclusive of the non-substituted) are studied. With bromo, cyano and 4–methoxycarbonyl nitrophenyl as the substituents and (9,9-Dimethyl-9*H*-xanthene-4,5-diyl)bis(diphenylphosphane) (xantphos), 1,1'-Bis (diphenylphosphino)ferrocene (dppf) and ([1,1'-Binaphthalene]-2,2'-diyl)bis(diphenylphosphane) (binap) as the (P^P) ligands, the corresponding complexes were synthesized via a one–pot two–step method and characterized using multinuclear NMR, DOSY, FTIR and UV–Vis DR spectroscopy. The dppz ligands were obtained in quantitative yields via bromination, cyanation and Suzuki–type coupling reactions conducted on an intermediate benzothiadiazole scaffold. The cyano and alkyl benzoate derivatives were chosen for the prospective aim of incorporating the complexes into Zr–based MOFs UiO–66 and UiO–68 respectively. The free bromo– and cyano–dppz ligands exhibited severe solubility issues, with NMR characterization being possible upon strong acid addition. The complexes showed satisfying stability upon exposure to air and water with DOSY studies in *N*–donor solvents showing the fortunate absence of dissociative speciation and ligand exchange reactions leading to the formation of homoleptic species. Through–space correlations and solid–state structures defined by NOESY/ROESY NMR and SC–XRD indicated π–stacking properties among the complexes caused by a distorted tetrahedral coordination sphere around the Cu^I metal. From the UV-Vis DRS studies, it was inferred that the presence of *para*-substituted EWGs on the distal benzenoid ring promoted red-shifting of the absorption properties for both the ligands and complexes within the visible region.

Table of Contents

Abbreviations

Note: *For convenience reasons, this section only comprises abbreviations whose meanings have not been fully written in the actual text. Hence, abbreviations like MLCT or PS are not included.*

AcOH	Acetic acid	**LUMO**	Lowest unoccupied molecular orbital
Al	Aluminium	**MeOH**	Methanol
APCI	Atmospheric pressure chemical ionization	**MHz**	Megahertz
aq	aqueous	**MO**	Molecular Orbital
BTD	Benzothiadiazole	**m.p.**	melting point
ca.	circa	***m/z***	mass–to–charge ratio
$CDCl_3$	Deuterated chloroform	**NBS**	N-Bromosuccinimide
CD_3CN	Deuterated acetonitrile	**NH_4PF_6**	Ammonium hexafluorophosphate
Co	Cobalt	***O_h***	full Octahedral symmetry
conc.	concentrated	**o.n.**	overnight
CNST13	Constant 13 (NMR parameter)	**ORTEP**	Oak Ridge Thermal Ellipsoid
COSY	Correlation spectroscopy	**Pd**	Palladium
CPK	Corey–Pauling–Koltun	**ppm**	Parts per million
Da	Dalton	**PS**	Photosensitizer
DEPT	Distortionless Enhancement by Polarization Transfer	**Pt**	Platinum
DFT	Density-functional theory	**ref**	Reference (literature)
DNA	Deoxyribonucleic acid	**Rh**	Rhodium
equiv.	equivalents	**RVB**	Rosenmund–von Braun
ESI	Electrospray ionization	**r.t.**	room temperature
et. al.	*et alia*	**SelTOCSY**	Selective Total Correlation Spectroscopy
EXSY	Exchange Spectroscopy	**Sn**	Stannum (Tin)

HMBC	Heteronuclear Multiple Bond Correlation	**TEOA**	Triethanolamine
HOMO	Highest occupied molecular orbital	**THF**	Tetrahydrofuran
HR/LR MS	High-resolution/ Low-resolution mass spectrometry	**UiO**	Universitetet i Oslo (MOF)
HSQC	Heteronuclear single quantum coherence spectroscopy	**Zn**	Zinc
ILCT	Inter-ligand charge transfer	δ	Chemical shift
J	Coupling constant	υ	vibrational stretch (FTIR)

1. Introduction

1.1. Photosensitizer–based Artificial Photosynthetic Systems

For a world that demands renewable and green energy sources to power modern society, the search for a practical artificial photosynthetic (AP) system for solar energy conversion to chemical fuel has become of growing interest.[1–2] The ideal photocatalytic system (consisting of metal-free or organometallic-based chromophores) should be capable of (i)efficiently absorbing light for transformation to an excited state (ii) charge generation facilitating an electron transfer between the excited state and an electron donor or acceptor, (iii) storing multiple photoexcited electrons and (iv) possessing the redox potentials necessary to drive target reactions including photoelectrochemical water-splitting, solar H_2 generation or CO_2 reduction.[1, 3]

In photosensitizer(*PS*)–involved photocatalysis, light absorption by the ground state metal–complex chromophore promotes metal-centered (MC) or ligand-centered (LC) electron transition and metal–to–ligand charge transfer (MLCT). In an octahedral d^6 metal polypyridine complex for instance, the MLCT corresponds to the electron transition between the metal–localized t_{2g} orbitals (HOMO) to the ligand–localized antibonding π^* orbitals (LUMO) to form the excited state PS* (**Figure 1.1. a**).[3, 4] An electron transfer thenceforth from an external sacrificial reagent (*D* in **Figure 1.1. b**) to *PS** to generate PS^- before subsequent oxidation to ground state *PS* by a water–oxidation catalyst (WOC) is termed reductive quenching. In oxidative quenching on the other hand, *PS** is oxidized back to PS^+ by a CO_2–reduction catalyst (CO2RC) before reduction to ground state *PS* by the sacrificial reagent (**Figure 1.1. b**).[2, 4]

There are several issues that can affect the photocatalytic output of the chromophores. These include transient excited state lifetime or side reactions such as the back electron transfer between the sacrificial reagent and *PS*, and non–radiative decay (k_{nr}) of *PS** to *PS*. To facilitate an effective catalytic cycle as shown in **Figure 1.1. b**, the *PS* should thence have a high molar extinction coefficient (ε) in the visible region, adequate chemical or photostability within aqueous or organic solvents, a sufficient excited state lifetime (ns → μs) for the charge transfer process and to overcome such side reactions.[5]

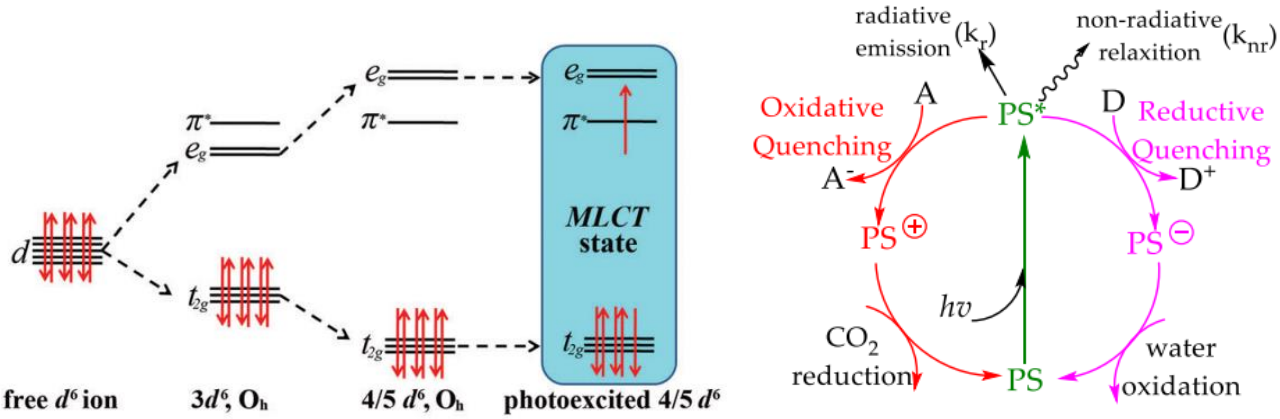

Figure 1.1 a (left): Schematic MO diagram for O_h d^6 metal polypyridine complexes. **b (right):** Quenching pathways in PS–involved photocatalysis with A= sacrificial acceptor, D = sacrificial donor, PS = photosensitizer, ***** = excited state. Excerpted from ref.[2, 4]

1.2. Noble vs. Non–noble metal–complex photosensitizers

The study of metal–complex chromophores for AP systems has been primarily focused on noble transition metals which include ruthenium[6], platinum[7], iridium[8], osmium[9], etc., with Ru^{II} polypyridine and cyclometallated Ir^{III} complexes being the most extensively investigated. However, the search for alternate non–precious transition metals with favourably matching photophysical properties for H_2 production or CO_2 reduction, higher earth abundancy, low cost and low toxicity has been gaining traction.[10] Studies over the past decades has led to the development of noble–metal–free photosensitizers which include iron–, copper–, manganese–based photosensitizers etc.[11] Discussions hereinafter are limited to ruthenium and copper complex PSs.

1.2.1. Ruthenium complex photosensitizers

One of the earliest *PS*–based AP systems practically developed, employed $[Ru(bpy)_3]^{2+}$ as the metal–complex chromophore due to the demonstration of intense absorption properties in the visible light range (λ_{max} = 452 nm in aqueous solutions), sufficient lifetime τ = 1.1 μs for its photoexcited state $[Ru(bpy)_3]^{2+*}$ and the property of being more reducing and oxidizing than its ground state species $[Ru(bpy)_3]^{2+}$, i.e., the excited state can transfer electron to an external acceptor.[12 – 14] The Ru–*PS* was coupled into a $[Ru(bpy)_3]^{2+}$–$[Rh(bpy)_3]^{3+}$–Pt–TEOA system (**Figure 1.2**) with $[Rh(bpy)_3]^{3+}$ as the oxidative quenching catalyst and TEOA as the sacrificial agent.[15] The Rh^{III} bis–pyridyl species undergoes two electron reduction before relaying the electrons to platinum for catalytic H_2 production. However, ligand dissociation of the Rh–species eventually caused decomposition of the AP system.

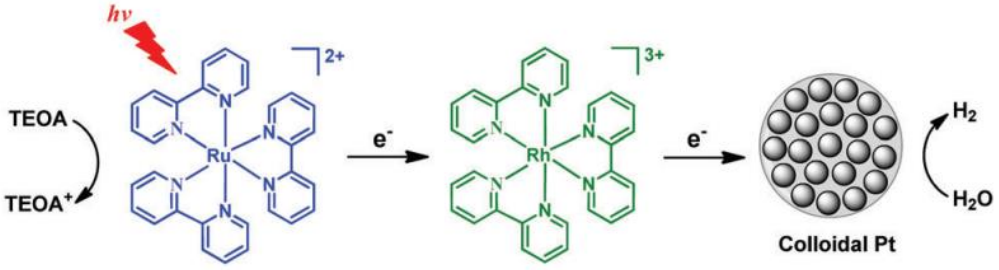

Figure 1.2. $[Ru(bpy)_3]^{2+}$–$[Rh(bpy)_3]^{3+}$–Pt–TEOA AP system for photocatalytic H_2 production. Excerpted from ref[3]

Substituting the Rh^{III}–species with metal-free methylviologen (MV^{2+}) to create a $[Ru(bpy)_3]^{2+}$–MV^{2+}–Pt–TEOA system resulted in better turnover numbers (TON). However, the AP system suffered low catalytic performance in a long run.[16] Further improvements considered, involved linking the *PS* to the MV^{2+} acceptor to promote intramolecular electron transfer. Although monoviologen–linked Ru^{II} complexes (**2** and **3** in **Figure 1. 3**) did show evidence of H_2 production, rapid back electron transfer from the MV^{2+} to the Ru-complex moiety reduces the lifetime of the charge–separated state.[17–18] Turnover frequency (TOF) and luminescence lifetime measurements of multi-viologen–linked Ru(II) complexes (**4 – 11** in **Figure 1.3.**) indicated not only the essence of rapid multi-electron transfer and transient storage in suppressing the back electron transfer but photocatalytic H_2 generation was heavily dependent on the concentration of the acceptor site.[19–21]

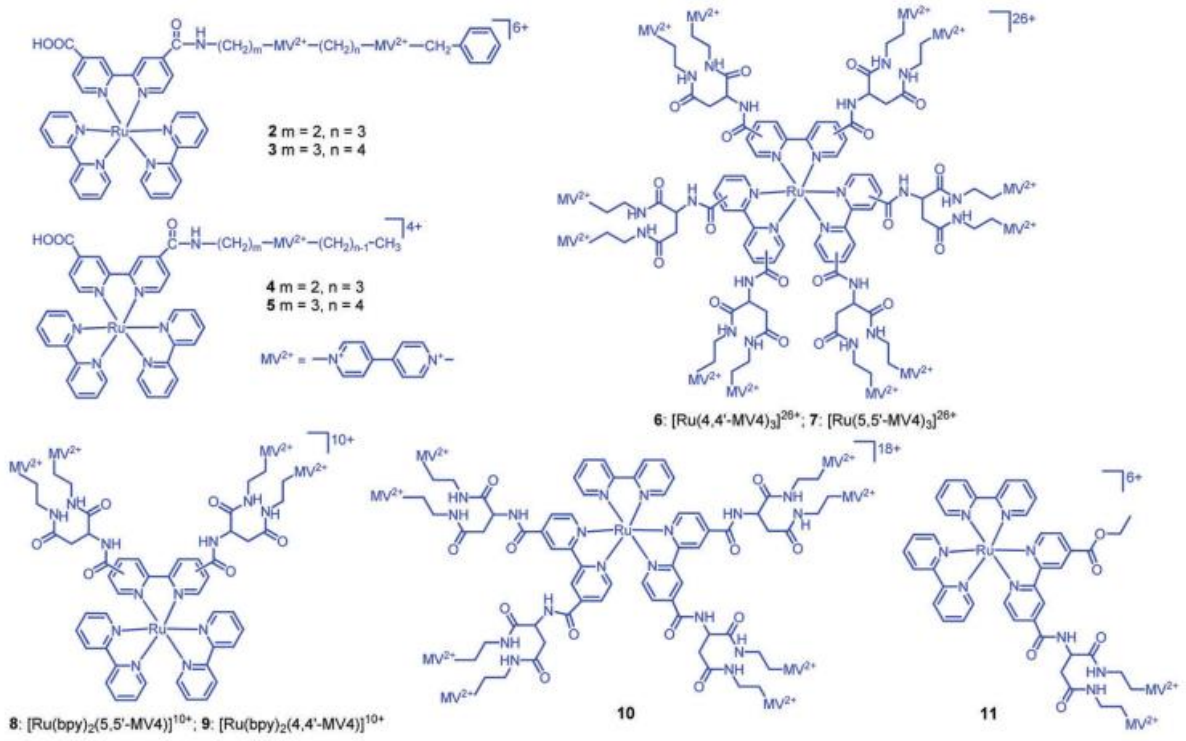

Figure 1.3. Examples of $[Ru(bpy)_3^{2+} – MV^{2+}]$ built for photocatalytic H_2 production. Excerpted from ref.[3]

Recent attempts at improving the multi-electron accumulation and storage for better photocatalytic performance have required ingenuity in ligand design. Findings have indicated dipyrido–[3, 2–a: 2', 3'–c]phenazine amongst other ligands in their metalated–*PS* state to be efficient for the above–explained light driven processes.[22]

1.2.2. Why dipyrido–[3, 2–a: 2', 3'–c]phenazine as the Ligand of Interest?

Dipyrido–[3, 2–a: 2', 3'–c]phenazine (dppz) was primarily popular based on its fluorescence properties in the presence of DNA in aprotic solvents. Due to its planarity and extended aromaticity, it is capable of establishing aromatic π–π intercalations to unwind the double helix, making it applicable in anti-cancer agents or photoluminescent DNA sensors. The emission properties are largely red–shifted from absorption wavelength and due to that, complexes of dppz-derivatives have also become useful components in organic light–emitting–diodes (OLEDs) and dye–sensitized solar cells (DSSCs).[23]

As the nomenclature depicts, the ligand framework consists of two structural features; the phenanthroline (phen: A, B and C) and the phenazine (phz: B, D and E) rings for which the low–energy unoccupied molecular orbitals are spatially distributed (**Figure 1. 4**).[24]

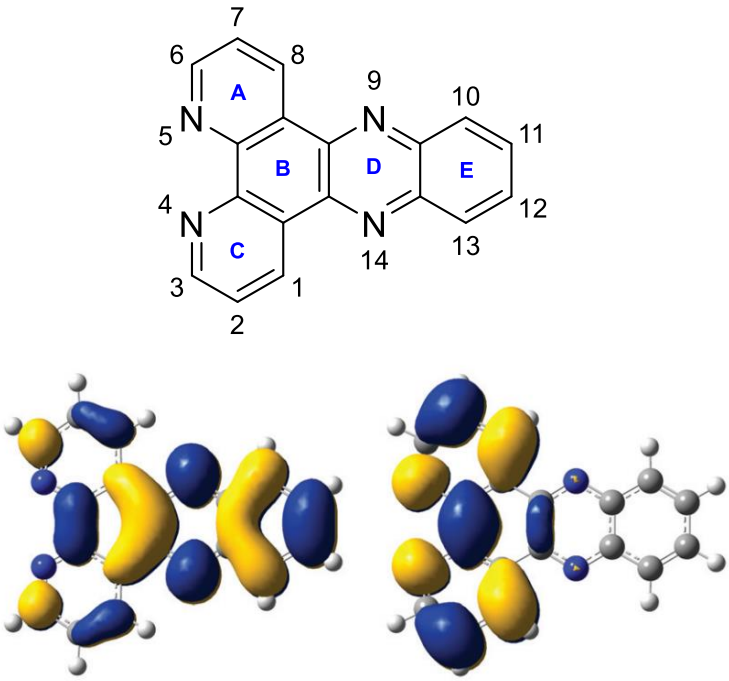

Figure 1.4. a (top): IUPAC numbering and ring labelling for dppz. b (bottom): Low – energy MOs spatially localised on the phenazine moiety (left) and phenanthroline moiety (right). **Figure 1.4** b excerpted from ref.[24]

From an electronic perspective where the ligand is metalated, an MLCT d – π* process leads to electron occupation in the entropically favoured $^3MLCT_{phen}$ excited state and the enthalpically favoured $^3MLCT_{phz}$ excited state. Depending on the temperature, solvent environment or metal ion employed, the charge transfer can occur directly into the two segregated excited states or by gradual depopulation from the emissive $^3MLCT_{phen}$ to the non-emissive $^3MLCT_{phz}$ state (**Figure 1. 5**).[25]

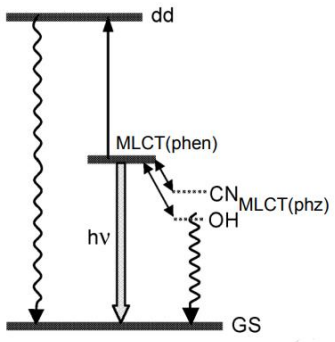

Figure 1.5. Energy level diagram depicting electron transitions between excited states of $[Ru(bpy)_2(dppz)]^{2+}$, where CN and OH refer to nitrile and alcohol local solvent environments. Figure excerpted from ref. [25]

The phz MOs are lower in energy (**Figure 1.5.**) and have lower wavefunction and amplitude at the solvent–chelating nitrogens than phen MOs highlighting their electron–withdrawing property. Hence, the diaza N-9 and N-14 serve as appropriate sites for multi-electron storage via formation of radical anions upon reduction with charges further stabilized for solvent interaction (**Figure 1.6**).

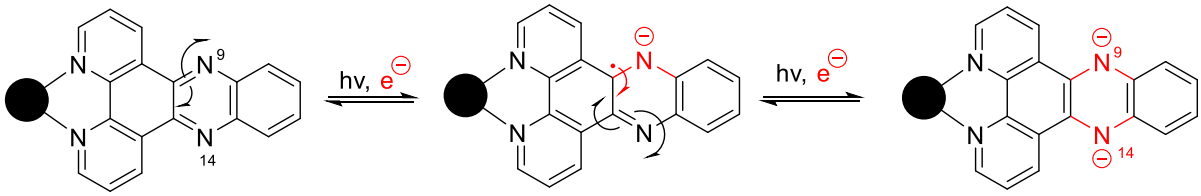

Figure 1. 6. Stepwise reduction of phenazine component of dppz under light irradiation conditions demonstrating their electron-storage ability. ● represents $[(L)_n(\text{Metal ion})]$.

The use of different substituents (electron–withdrawing or donating) is known to imbue different changes to the MO energies, electrochemical properties of the entire PS and the MLCT intensity which usually tends to be of lower oscillator strength than LC transitions. DFT calculations have proven that the more electron–withdrawing the 10→13 substituents, the higher the % phz contribution to the LUMO.[26] Moreover, electron–withdrawing substituents result in less negative reduction potential E_{red}, red–shifting effect in the absorption bands and lowering of the MLCT energy, and vice versa for the electron–donating group. Findings also show that these effects are more pronounced with the disubstituted than the monosubstituted dppzs.[27–29] This dissertation deals with the synthesis of dppz–analogues with electron–withdrawing substituents in the 10, 13– E ring positions (**Figure 1.7.**).

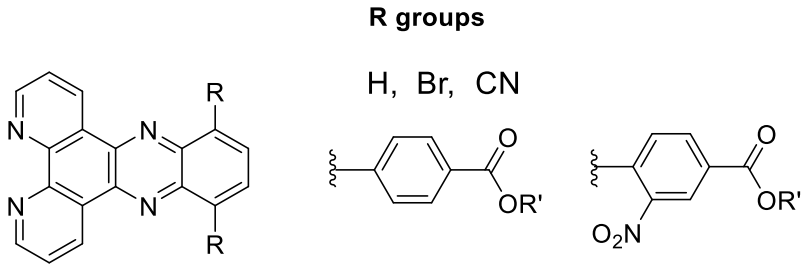

Figure 1.7. 10, 13–disubstituted dppz analogues of interest in this thesis.

1.2.3. "If it ain't broke with Ruthenium, why fix with Copper?"

Even though Ru–based PSs have demonstrated strong absorption properties in the visible region with applicable potentials for photocatalytic systems, they still suffer poor durability due to eventual chromophore degradation. This photo–instability is as a result of electron occupancy of a low–lying antibonding triplet metal–centered (^{3}MC) excited state, which weakens the metal–ligand bond causing ligand dissociation.[30]

Not only are environmental impact, low cost and the necessity to bring such AP assemblies to work on larger scale, the obvious reasons for considering complexes of copper as viable alternative, but the interesting photophysical and electrochemical properties they possess.[11] Cu(I) complexes have a closed shell d^{10} electron configuration in the ground state and in solid states, prefer a pseudotetrahedral D_{2d} geometry. However, due to aromatic π–stacking effect, steric and torsional motion, the D_{2d} geometry is distorted to a D_2 geometry with the dihedral angle (< 90°) between the two ligand planes being influenced by the counteranion. Light absorption promotes intense UV ligand–centered (LC) transitions followed by moderate visible MLCT transition which generates an oxidized metal centre $\left([Cu^{I}(L)(L')]^{+} \overset{h\nu}{\rightarrow} [Cu^{II}(L^{-})(L')]^{+*}\right)$. Due to the asymmetric d^9 electron configuration, the transiently formed Cu(II) complex undergoes a pseudo–Jahn–Teller (PJT) distortion towards a Franck–Condon (FC) ^{1}MLCT$_{\text{flattened}}$ state with a square planar geometry (**Figure 1.8.**).[31]

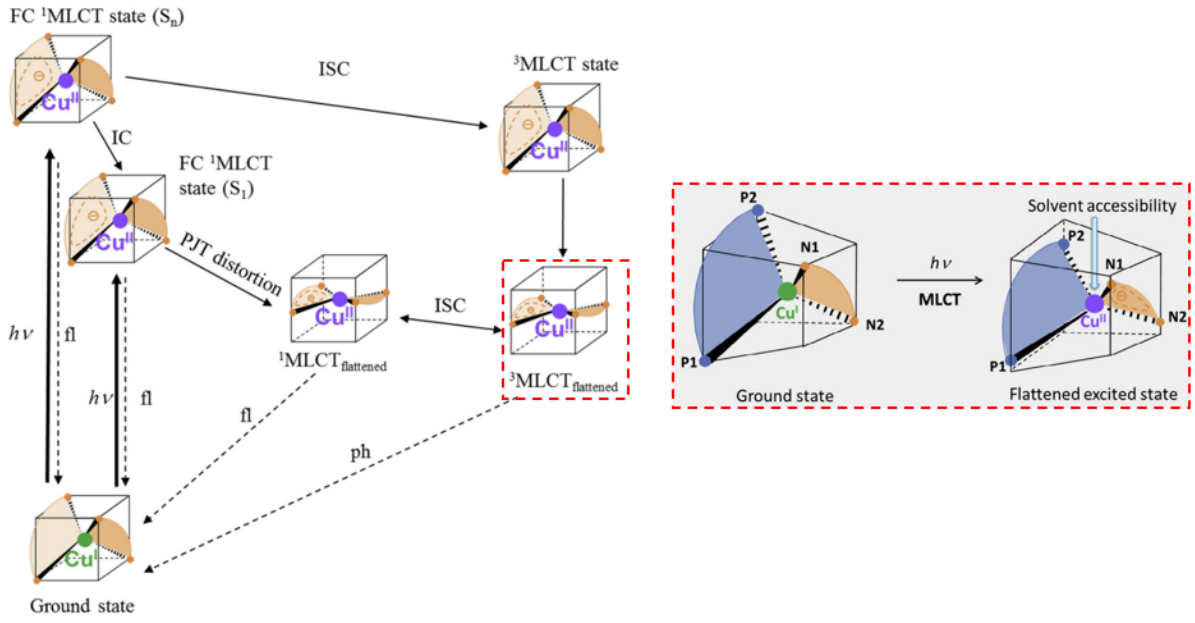

Figure 1.8. a (left). Geometrical changes associated with Cu(I) complexes upon MLCT excitations. b (right) Ground state → ^{3}MLCT$_{\text{flattened state}}$ → exciplex intermediate formation as a result of solvent interactions with Cu(I) centre. Figure excerpted from ref. [31]

In addition, excitation to a higher energy FC ^{1}MLCT state also generates minor ^{3}MLCT state via a fast intersystem crossing (ISC) which bypasses the flattening distortion. This usually occurs when bulky substituents such as *tert*-butyl are placed in 2, 9 positions of the diamine ligand (3, 6 positions of dppz rings A and C in **Figure 1.4. a**). Both ^{1}MLCT$_{flattened}$ and ^{3}MLCT states resolve into an unstable ^{3}MLCT$_{flattened}$ which opens up accessibility of the Cu(I) centre to surrounding Lewis base, counteranions (e.g. PF_6^-, BF_4^-, ClO_4^-, NO_3^-, etc), or donor solvent molecules (e.g. MeCN, H_2O, MeOH etc.) to form a stabilized excited pentacoordinated complex (exciplex) intermediate (**Figure 1.8. b**). As a consequence, the energy gap between the ^{3}MLCT$_{flattened}$ and the ground state is lowered causing the excited state lifetime of the Cu(I) complex is diminished.[32] All these MLCT states return back to the ground states via favoured radiative transitions (e.g. phosphorescence or fluorescence). Fortunately, the extent of this flattening distortion can be suppressed to increase the luminescence lifetime based on how the chosen ligands are sterically tuned or designed.[33 – 34] Hence, it is the study of the interplay between the various MLCT state structures and their luminescence lifetimes or energetics that enables further exploration into the potential applications of Cu(I) complexes in PS–based AP systems.

2. Experimental Methods

2.1. Synthetic perspectives towards [Cu^{I}(N^N)(P^P)]-type complexes

2.1.1. Rationale behind the choice of Diphosphine co-ligands

The use of phosphine ligands in homogeneous catalysis and transition metal complexes stem from their steric (natural bite angle, accessible surface area, etc.) and electronic properties (σ–donating or π–accepting).[35–36] The phosphorus atoms of diphosphines can act as σ–Lewis bases by donation of their lone pair to the copper centre, and as π–acceptors via π–backbonding. The π–acidity which is dependent on the P–bound substituents tend to be stronger with aryl groups.[37] The selection of commercially available (9,9-Dimethyl-9*H*-xanthene-4,5-diyl)bis(diphenylphosphane) (Xantphos), 1,1'-Bis(diphenylphosphino)ferrocene (dppf) and ([1,1'-Binaphthalene]-2,2'-diyl)bis(diphenylphosphane) (BINAP) (**Figure 2.1.**) for this thesis is primarily based on how their varying bite angles will influence their three–dimensionality in ground state and stability in donor solvents.

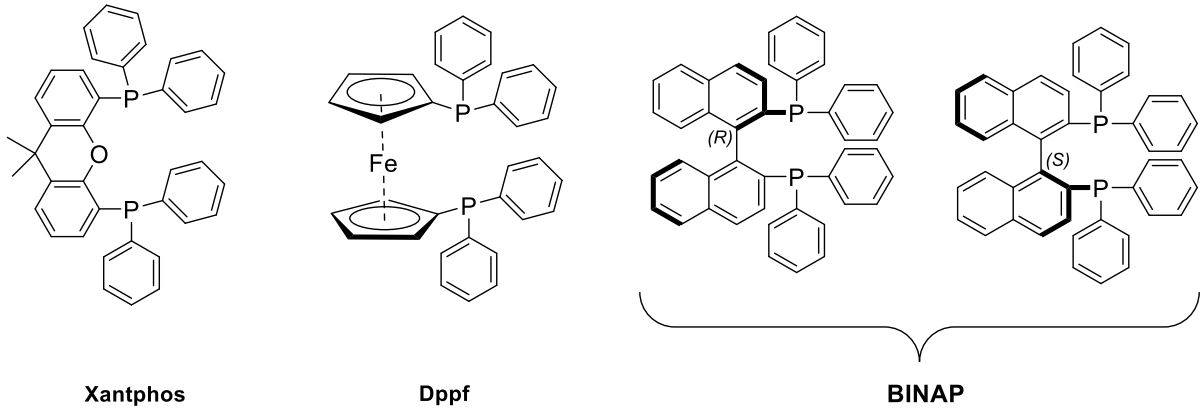

Figure 2.1. Structure of selected diphosphine ligands incorporated into the Cu(I) complexes

Together with the lone pair, the three phosphorus–bound aryl substituents form a distorted tetrahedron. The N–donor atoms of the counterpart diimine ligand on the other hand, exhibit a flat trigonal planar environment with three dimensionality only imposed by the presence of substituents.[38] It has been reported that diphosphines with wider steric bite angles tend to confer more stabilization to the tetrahedral coordination environment and destabilize the square planar geometry.[39] In addition, when the aryl substituents on the phosphorus were replaced by

tert–butyl groups, the photoluminescence of the corresponding $[Cu^{I}(N^{\wedge}N)(P^{\wedge}P)]^{+}$ complexes attributed to vibrational quenching effects were reduced significantly.[40] Hence, it was very essential to retain the aryl substituents on phosphorus with (P^P) ligands related to xantphos.

2.1.2. 1º aim of the project: Rationale behind dppz ligand design

Besides tuning the redox potential and absorption properties of dppz for multielectron storage, the motivation behind the synthesis of the 10, 13–disubstituted analogues were their potential to serve as precursor linkers for Zirconium (Zr)–based metal organic frameworks (MOFs). Cyano groups of the phenazine moiety could for instance be transformed into carboxylates for anchoring the [Cu(N^N)(P^P)] species onto the internal surface of UiO–66 (–CO_2H) for photocatalytic reactions (**Figure 2.2**).

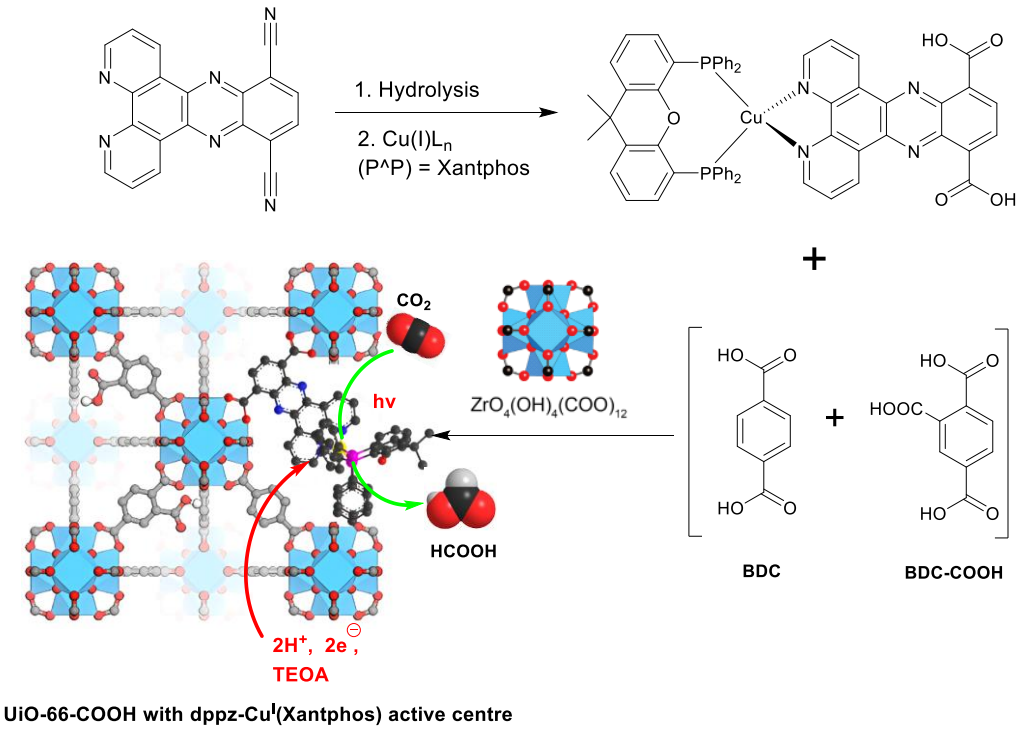

Figure 2.2. Transformation of dppz–*p*–CN to dppz–*p*–COOH, Premade Linker synthesis (PMLS) of UiO-66 with benzene dicarboxylic acid (BDC) and BDC-COOH, and subsequent photocatalytic CO_2 reduction to formic acid via Dppz-Cu^{I}(xantphos) active center. Hydrogens are omitted from model for clarity. Pink = Phosphorus, yellow = Copper, blue =nitrogen.

For precursor linkers with alkyl benzoate or alkyl nitrobenzoate substituents, transformation of the ester groups to carboxylate will enable functionalization of UiO–68 MOF. Dppz analogues without direct entry points into the Zr–based MOFs, can be used to post–synthetically functionalize Cu–loaded BINAP– or Bipyridine(bpy)–based UiO–67 MOFs (**Figure 2.3**).

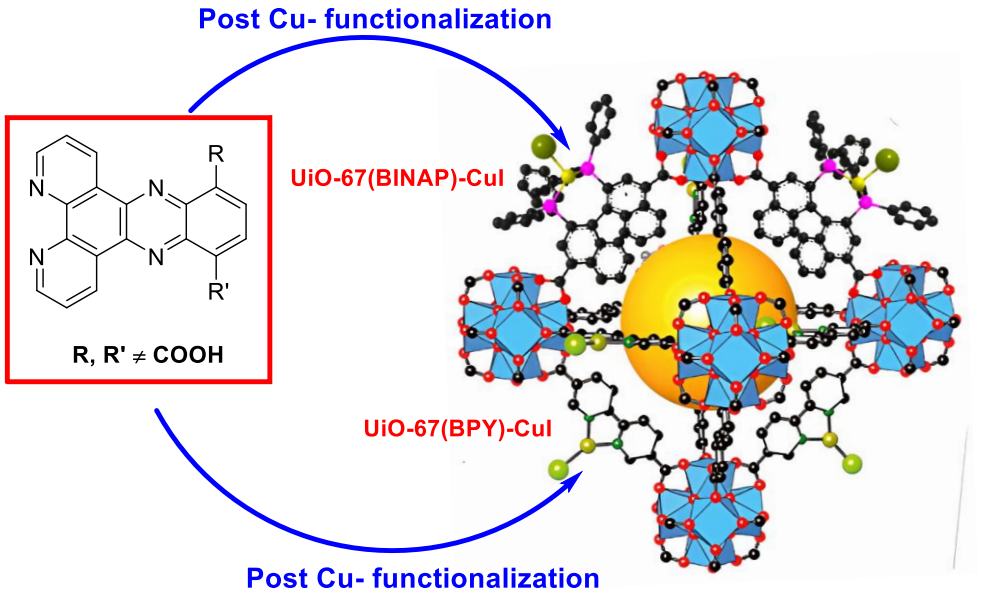

Figure 2.3. Post Dppz-funtionalization of Cu–loaded BINAP– or Bipyridine(bpy)–based UiO–67 MOF with **iodide** as the counteranion. Hydrogens are omitted for clarity. Pink ball = Phosphorus, light green = Copper, deep green =iodide, or bpy nitrogen.

The rationale behind the employment of Zr-based MOFs specifically had been demonstrated in UiO-67-incorporated cyclometallated Ruthenium complexes by the Amedjkouh group to amplify the bathochromic shift and prevent rapid decomposition of the metal-complex chromophore.[41–42] However, it should be noted that the specific methods of heterogenization of the complexes, and the corresponding MOF-based photocatalysis **is beyond the scope of this thesis.** Hence, the theoretical background behind MOFs, their synthesis, decoration with the $[Cu^{I}(N\hat{}N)(P\hat{}P)]^{+}$ complexes as shown above in **Figure 2.2** and **Figure 2.3**, and use as *PS*-based AP system is **not considered.**

2.1.3. Strategies towards 10, 13–disubstituted dppz analogues

Inspiration behind the synthetic pathways toward **L1** – **L5** (**Scheme 2.1**) is drawn from Aslan *et al.* [22] with published schemes of **L2**, **L3**, and 11, 12–disubstituted analogues with corresponding ruthenium complexes. On the other hand, the synthesis of the di-(alkyl benzoate) and di-(alkyl nitrobenzoate) derivatives via Suzuki cross-coupling routes with subsequent complexation with Cu^{I} ion, are new. **L1** to **L5** were to be synthesized by condensation between 1,10–phenanthroline–5, 6–dione ($phenO_2$) and corresponding *o*–phenylenediamines.

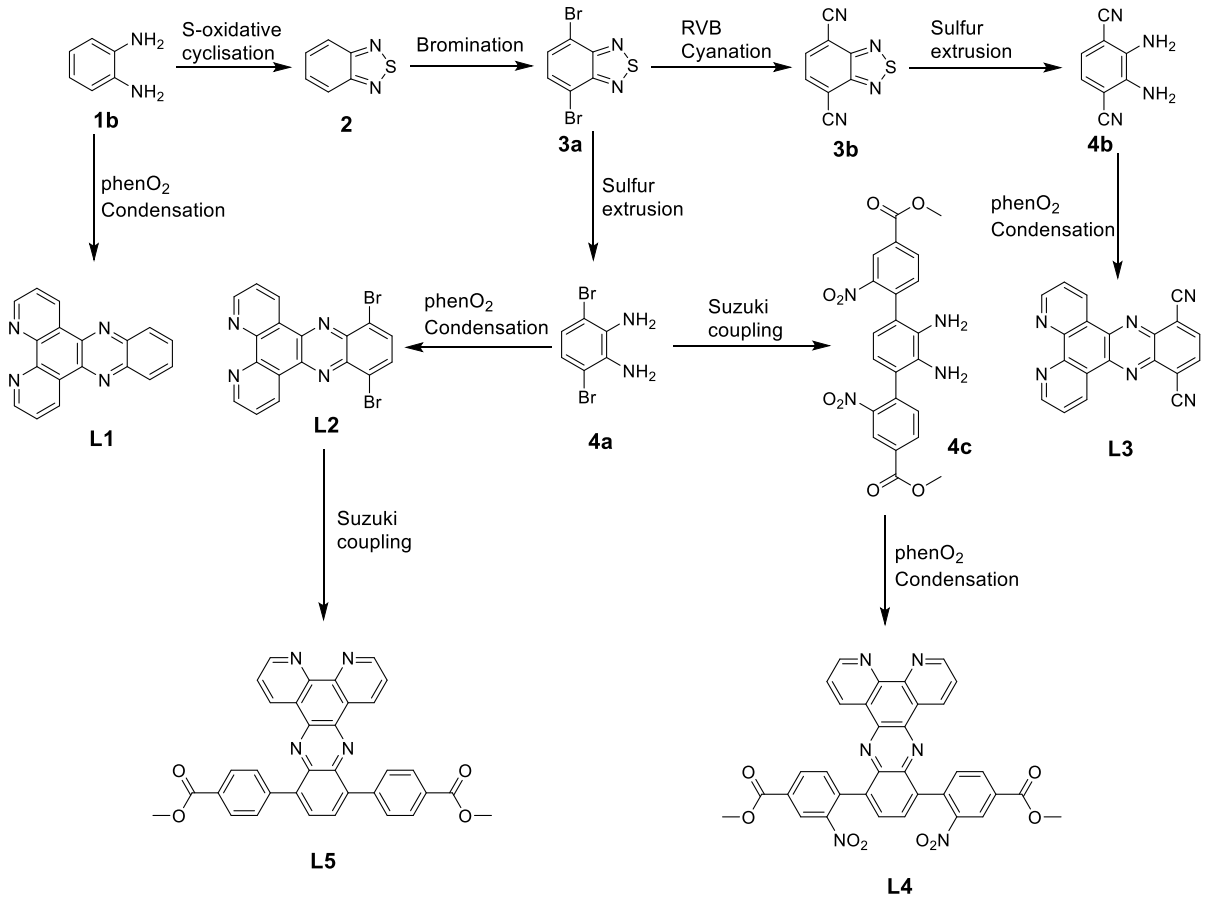

Scheme 2.1 Overall scheme showing the different routes towards 10, 13–disubstituted dppz analogues **L1** to **L5.**

2.1.3.1. Suzuki–Miyaura Cross–Coupling

Using the commercially available boronic acids in **Figure 2.4**, the Suzuki reaction conditions were to be based on protocols designed by Hylland *et al.* [47] with the expectation of producing the corresponding disubstituted benzothiadiazoles and *o*–phenylenediamines in significant yields despite the presence of Pd–chelating amino groups.

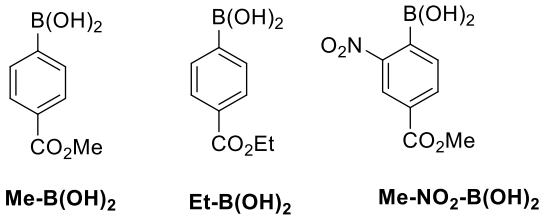

Figure 2.4. Aryl boronic acids to be used for the Suzuki-Miyaura cross coupling.

The rationale behind the use of excess amounts (> 4.0 equiv.) of $KF•2H_2O$ was to serve as a source of water implying the reaction system does not require air or moisture sensitive reagents. Generally, electron–withdrawing substituents such as nitro groups on arylboronic acids are very notorious for causing low reactivity in Suzuki–Miyaura reactions. However, reports have indicated that the use of air stable $HBF_4•P(t\text{–}Bu)_3$ (chelating phosphine source) in conjunction with Pd_2dba_3 (Pd source) proves to be an efficient method in producing quantitative yields despite the EWG-substituted boronic acid.[47, 88]

2.1.3.2. Sulfur extrusion reactions

Scheme 2.1 also involves an amino protection reaction with sulphur forming benzothiadiazoles. The cross-coupling substitution process is followed by a sulphur extrusion reaction. Methodologies developed for the sulfur extrusion process have included an $LiAlH_4$ method [70], Zn–AcOH [71], Al–Hg [72], Sn–HCl [73–75], and a Mg–MeOH method [76]. $LiAlH_4$ had the disadvantage of being too strong as a reducing agent for halo-, cyano- and ester groups under the reaction conditions used. The other methods have required drastic acidic conditions, toxic reagents not suitable for scale–up, led to the reduction of non-targeted functional groups, or were not applicable to a wide variety of substituted benzothiadiazoles.

Attempts to develop a substrate–independent reaction with milder conditions led to a Co^{II}–$NaBH_4$ system designed by Neto *et. al.*[45] which involves the use of sodium borohydride with catalytic amounts of $CoCl_2•6H_2O$. The reaction was reported to be successful with BTD

derivatives with substituents such as bromo, phenyl, phenyl methyl ether, 1–naphthyl, phenyl nitriles and alkyl benzoates. In the case of nitriles and ester groups however, the partial reduction of these groups to amino and alcohol derivatives was observed in low yield. The success of the reaction was attributed to the *in–situ* formation of a cobalt boride Co_2B species which acts as a support surface for the attack of the borohydride counterpart on the attached BTDs (**Figure 2.5**). H_2S is subsequently released as a by–product of the reaction.

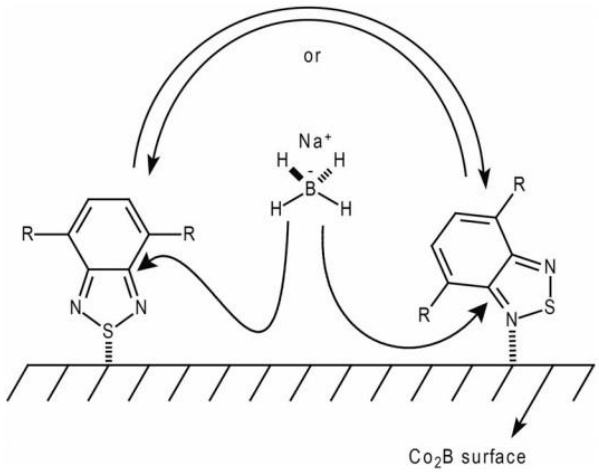

Figure 2.5. Proposed first step in the mechanism for sulfur extrusion of BTD derivatives with Co^{II}–$NaBH_4$. Figure excerpted from ref.[45]

2.1.4. 2º aim of project: A HETPHEN variant for stable $[Cu^{I}(N\hat{}N)(P\hat{}P)]^{+}$ complexes

The synthesis of $[Cu^{I}(N\hat{}N)(P\hat{}P)]^{+}$–type complexes involves a one–pot–two–step method similar to the HETPHEN (HETeroleptic PHENanthroline) strategy developed by Schmittel et al.[43, 44]. Cu(I) complexes are notorious for their lability property which leads to fast ligand scrambling in solution. For instance, an equimolar mixture of Cu^{+} reagent, the (N^N) ligand (**1**) and the (P^P) ligand (**2**) leads to the formation of homoleptic $[Cu(\mathbf{2})_2]^{+}$ and heteroleptic $[Cu(\mathbf{1})(\mathbf{2})]^{+}$ in a statistical ratio of 2 : 1 respectively, without the formation of the homoleptic $[Cu(\mathbf{1})_2]^{+}$.[44] This is attributed to the 4 intra–ligand π–π interactions of $[Cu(\mathbf{2})_2]^{+}$ is thermodynamically favoured over the 2 π–π stacking interactions of $[Cu(\mathbf{1})(\mathbf{2})]^{+}$ **(Scheme 2.2).** In addition, dissociation–association dynamics prevents the formation of $[Cu(\mathbf{1})_2]^{+}$.

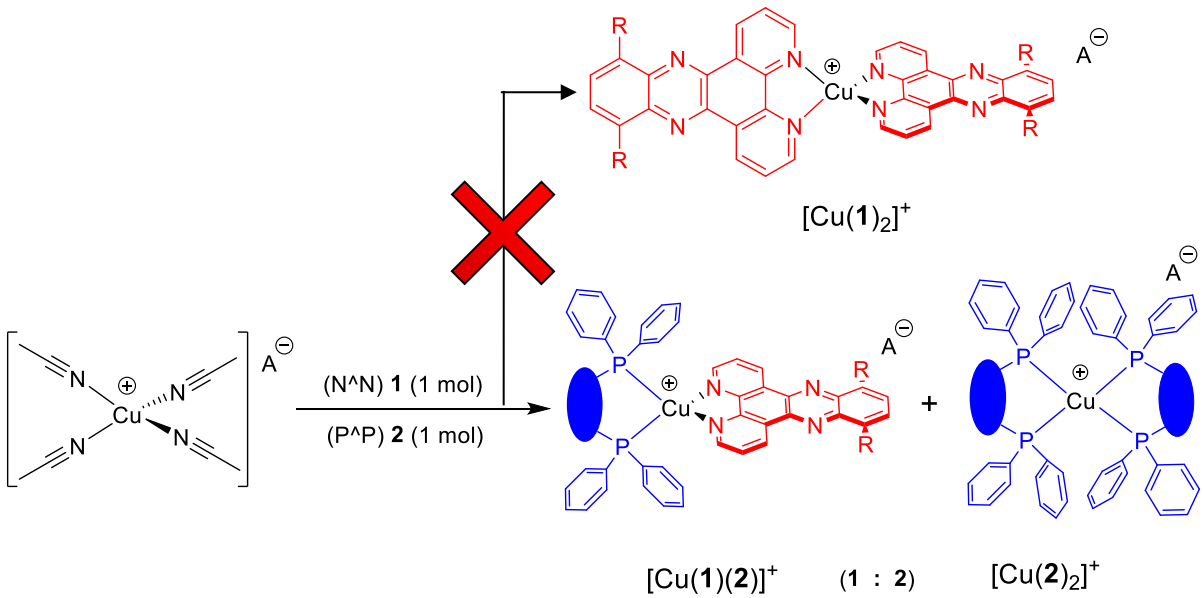

Scheme 2.2. Thermodynamically unbiased system which leads to the formation of the desired [Cu(**1**)(**2**)]$^+$ and undesired [Cu(**2**)$_2$]$^+$ with the homoleptic species being formed significantly over the desired heteroleptic complex. A$^-$ represents the counter anion.

Increasing the energy barrier for [Cu(1)(2)]$^+$ → [Cu(2)$_2$ process to enable the exclusive formation of the desired heteroleptic copper complex will require a first step producing a 1:1 complex with the bulkier ligand (the diphosphine ligand in this case). This prevents the formation of the 2:1 adduct due to the steric hinderance around the copper site.[44] The subsequent step involving the addition of the less–hindered diamine is to provide the desired heteroleptic complex in good yield (**Scheme 2.3**).

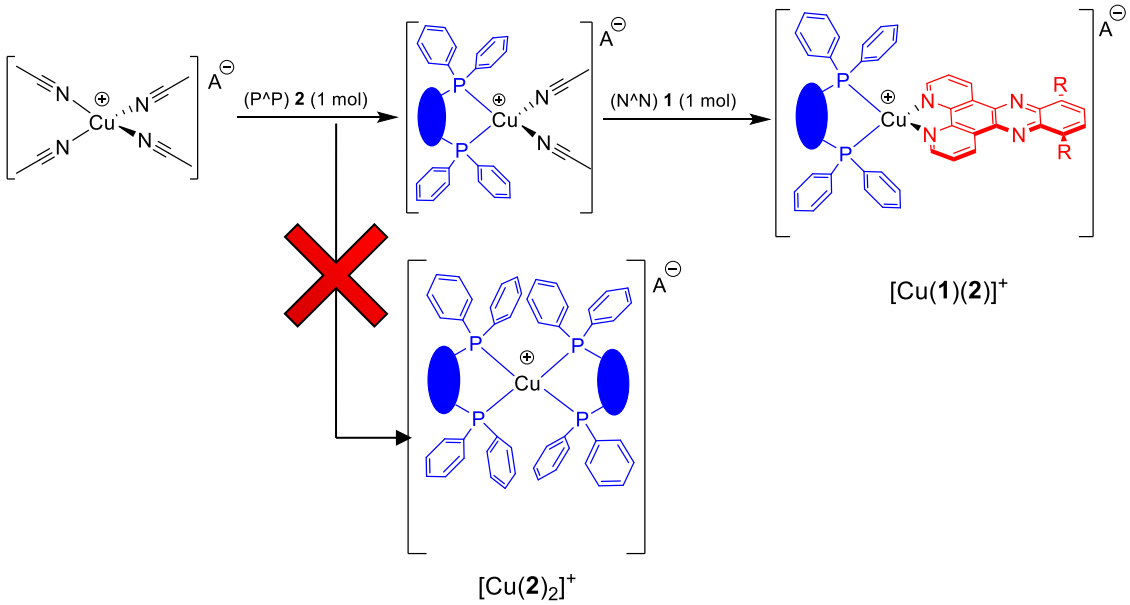

Scheme 2.3. Thermodynamic biased system which leads to the formation of the desired [Cu(**1**)(**2**)]$^+$ without the by-product homoleptic species being formed.

2.2. Spectroscopic Techniques

2.2.1. Nuclear Magnetic Resonance (NMR) Spectroscopy

Structural characterization of organometallic Cu^{I} complexes possessing a variety of spherically asymmetric two–, three–, or four–coordination environment with nitrogen or phosphorus ligands demand a number of spectroscopic tools. Under the condition that the oxidation of $Cu^{I} \rightarrow Cu^{II}$ does not occur, $[Cu(N\hat{}N)(P\hat{}P)]^{+}$ species can be studied by solution NMR techniques, unlike Cu^{II} complexes whose paramagnetic nature presents a real challenge due to long relaxation times and the NMR signals of Cu^{II}-nuclei being broadened beyond detection.

The subsequent sections limit discussions to the theory behind general NMR spectra preacquisition, uncommon techniques such as ^{31}P NMR, Diffusion–ordered spectroscopy (DOSY) and tools used for analysing the conformational changes around the Cu^{I} coordination environment and the ligands. Common and familiar techniques such as ^{1}H, ^{13}C NMR, COSY/TOCSY, DEPT, HSQC, and HMBC NMR acquisitions though were employed to deduce the skeletal framework of the target compounds, will not be discussed. For thorough discussion on those techniques, the reader is referred to texts describing the pulse sequences and acquisition methods[83, 84].

2.2.1.1. Theoretical Background

The principle of NMR spectroscopy involves observing the local magnetic fields around atomic nuclei. These nuclei have a spin angular momentum *P* and an associated quantized spin quantum number *I* related by the equation:

$$P = h\left(\frac{I(I+1)}{2\pi}\right) \quad (1)$$

where h= Planck's constant. If the nuclei are placed in an external magnetic field B_0, only specific P values along the z field axis are observed:

$$P_z = \frac{hm_I}{2\pi} \quad (2)$$

where m_I is a total of $2I + 1$ possible values. Due to quantization, the spin quantum numbers can either be 0, half-integral (1/2, 3/2, etc) or an integral (1, 2, etc). Classifying atomic nuclei according to their spin quantum numbers can be predicted from their mass and atomic numbers. Atomic nuclei such as $^{12}C_6$ and $^{16}O_8$ have even mass and atomic numbers with $I = 0$ and

therefore do not show any NMR signals. Nuclei with odd atomic and mass numbers give $I = n/2$ and hence show sharp NMR signals. ^{63}Cu and ^{65}Cu for instance, both I = 3/2 (quadrupolar) with natural abundances of 69.1% and 30.9%. ^{31}P on the other hand is dipolar with I= ½. Nuclei as such also have a quantized magnetic moment $\boldsymbol{\mu}$ proportional to $\mathbf{P}$ by the relation:

$$\boldsymbol{\mu} = \gamma \cdot \mathbf{P} \;\Rightarrow\; \mu_z = \gamma h m_I / 2\pi \tag{3}$$

where γ is the gyromagnetic ratio and its sign indicates whether $\boldsymbol{\mu}$ is parallel (positive) or antiparallel (negative) to $\mathbf{P}$. ^{63}Cu and ^{65}Cu as examples have gyromagnetic ratios (γ) of 7.1088×10^7 and 7.6104×10^7 rad T^{-1} s^{-1} respectively.

The energy of interaction between the magnetic field and the magnetic moment is described by:

$$E = -\boldsymbol{\mu} \cdot B_0 = -\mu_z \cdot B_0 = -\frac{\gamma h m_I B_0}{2\pi} \tag{4}$$

For a spin ½ nucleus in a magnetic field, i.e., $\mathrm{M}_I = +1/2$ and $-1/2$, there are two energy levels:

$$E_{+\frac{1}{2}} = -\frac{\gamma h m_I B_0}{4\pi} \quad ; \quad E_{-\frac{1}{2}} = +\frac{\gamma h m_I B_0}{4\pi} \tag{5}$$

The +½ state is considered to be the lower spin state in the magnetic field because the magnetic moments align with the field whiles the – ½ state is considered as the higher state because more energy is needed to align the moments against the field than with it. Hence in ^{1}H and ^{13}C, the + ½ state has a higher nuclei population. The signal intensity of the NMR experiment is determined by this population difference. The energy difference between the two states will result as:

$$\Delta E = \frac{\gamma h B_0}{2\pi} \tag{6}$$

With $\Delta E = h\upsilon$ from Planck's relationship, υ which is known as the operating or Larmor frequency will be given as:

$$\upsilon = \frac{\Delta E}{h} = \frac{\gamma h B_0}{2\pi h} = \frac{\gamma B_0}{2\pi}\ \mathrm{s}^{-1} \tag{7}$$

After magnetic equilibrium is achieved by application of B_0, excess spin population between the +½ (α) and – ½ state (β) is treated as an ensemble of spins giving a net bulk magnetization vector along the *z* axis. A second *rf* pulse B_1 (90º or 180º) generated by an oscillator coil and rotating along the *x-y* plane with the same frequency as the Larmor frequency defined by (7) will induce transitions between the spin states which manifest as nuclear precession of the bulk vector toward the *x-y* plane. Once the bulk vector begins its nutation toward the equilibrium *z* axis (spin relaxation), an *rf* signal is emitted as a time-dependent oscillating voltage which is collected by a detector at +*y* and interpreted as a steadily decaying oscillating time-domain

waveform. This time-domain is transformed into a frequency domain consisting of bands of frequencies covering a full range of chemical shifts for ^{1}H, ^{13}C, ^{15}N or ^{31}P. The signal produced from each nucleus coming into resonance is called FID (free induction decay) whose intensity decays as the nuclei lose energy gained from the *rf* pulse. Fourier transformation of the FID data produces the desired NMR spectrum providing information on the molecular structure of the sample.

2.2.1.2. NMR techniques for conformational analysis and DOSY NMR

(i) ^{31}P NMR

^{31}P with a natural abundance of 100% has a magnetogyric ratio (γ) of 10.841×10^{7} rad T^{-1} s^{-1}. As a half–integer spin, ^{31}P has a special characteristic of coupling to any other nuclei with $I > 0$ which includes with itself (P–P coupling) ^{1}H, ^{13}C, ^{19}F, ^{10}B or ^{11}B and a variety of transition metals. Hence, carbon coupling to phosphorus with split patterns can be observed in the ^{13}C NMR spectrum. In the case of metals such as $^{63/65}Cu$, phosphorus as a dipolar nuclei when bonded to such quadrupolar metal nuclei, the NMR signal from the vicinity of their P nuclei can experience severe line broadening with a relatively diminished intensity.[85] Fortunately, this is one way of determining the presence of a Cu^{I}-center within the target complexes. The reference standard used for the ^{31}P–NMR acquisition was 85% H_3PO_4 within a sealed capillary tube because ^{31}P NMR does not require deuterated solvents. Deuterated solvents are only used for purposefully signal locking. Coupling constants in ^{31}P NMR are on a general basis, larger than those of ^{1}H and ^{13}C NMR with magnitudes as large as 1000Hz being observable. As with ^{1}H and ^{13}C, coupling constants decrease with the increase in bonds between the two coupling nuclei. However, there exists no general rule for the magnitude of the coupling constants as there have been observations of $^{3}J_{P-X}$ constants being larger than $^{2}J_{P-X}$ constants.

(ii) NOESY and ROESY NMR

Both the Nuclear Overhauser Effect Spectroscopy (NOESY) and the Rotational Frame Nuclear Overhauser Effect Spectroscopy (ROESY) reveal spectra similar to the COSY spectrum. However, what is revealed is the couplings between protons separated in space by distance <5 Å (even if they are several bonds apart). Both spectra are obtained in phase sensitive mode, with the off-diagonal nOe signals always opposite in phase to diagonal signals for ROESY and usually for NOESY. NOESY uses a mixing time to build up the nOe while ROESY uses a series of pulses to spin-lock the magnetization and preventing it from going to zero and to build up ROE. Both spectra are used for clarifying positions of some substituents if HMBC and COSY data do not allow to do that. They are not useful for elucidating the skeletal structure or framework of the molecule. NOESY is usually recommended to compounds up to *ca.* 600 molecular weight but ROESY for compounds above that molecular weight. NOESY's similarity to COSY is highlighted not only in the resultant spectrum but in the sequence also, shown in **Figure 2.6.** where τ_m is the mixing time for NOE buildup.

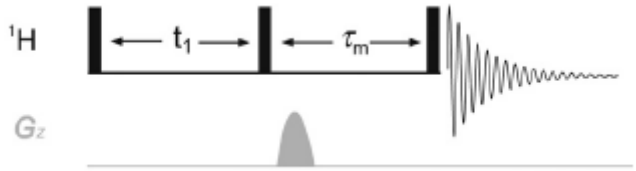

Figure 2.6. Generalized NOESY pulse sequence. The use of pulsed field gradient is optional.

A first 90º pulse nutates the magnetisation vector to the transverse plane. A second pulse then nutates a component of the transverse vector towards the $-z$ axis, to allow transient NOE to build up during τ_m. After τ_m, a final 90º pulse is used for spin population sampling prior to FID collection. τ_m can be optimized by replacing the experimental default d8 value with values from proton T_1-relaxation measuring experiments. This allows the population to recover between transients of at least $5T_1$s in order to obtain a better spectrum.

The pulse sequence for ROESY shown in **Figure 2.7** on the other hand, shows similarity to TOCSY pulse sequence in terms of the magnetization behaviour during the spin-lock period.

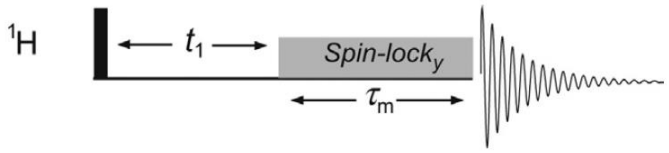

Figure 2.7. Generalized ROESY pulse sequence. Excerpted from [83].

Due to this, certain complications that might arise in the resultant spectrum may include the presence of TOCSY anti-phased artefacts and possibly the presence of COSY-type cross-signals which are in-phase with the diagonal.

(iii) DOSY NMR

The importance of Diffusion-Ordered Spectroscopy (DOSY) is highlighted in its ability to easily assess the purity of a compound (similar to a chromatography technique but with a conventional high-res. NMR spectrometer). The technique involves diffusion measurement of compounds present in a sample along the direction of an applied field gradient ($+z$ axis of gradient probehead) **(Figure 2.8).**

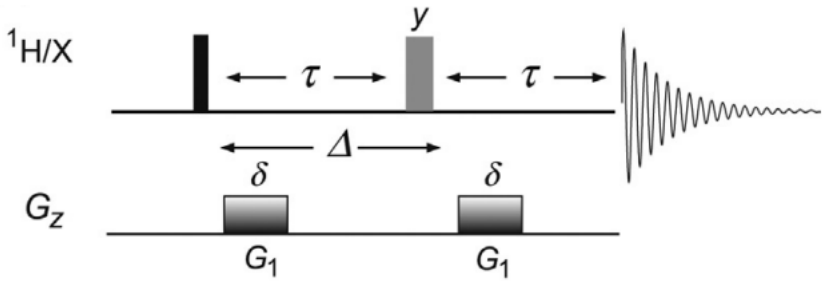

Figure 2.8. The basic Pulse field gradient (PFG) spin–echo commonly used for measuring molecular diffusion. The diffusion during the period Δ is characterised by a series of measurements with increasing gradient pulse strengths (G_1) of fixed duration δ, represented by fading gradients (rectangles). Excerpted from [83]

The root-mean-squared displacement (z_{rms}) travelled by molecules during a time average t is given by:

$$z_{rms} = (2Dt)^{\frac{1}{2}} \tag{8}$$

Where D= diffusion coefficient is the physical parameter that is measured when DOSY is performed with units m^2/s. The resultant spectrum is therefore a pseudo-2D NMR with one axis

being the diffusion coefficients whereas the other axis represents the chemical shifts. Both direct regression analysis to provide the diffusion coefficients and experimentation to produce the pseudo-2D NMR are conducted.

In the case of $[Cu(N^N)(P^P)]^+$–type complexes, the factor to be inspected is either the presence or absence of a dissociative speciation reaction in solution which leads to the formation of homoleptic species (**Scheme 2.4**). With the equilibrium from Scheme X favouring the products, more than one set of species are to be identified with significantly different diffusion coefficient values on the $\mathbf{F_1}$ axis of the obtained NMR spectrum. For the equilibrium favouring the desired heteroleptic species however, only one set of diffusion coefficient range values should be obtained.

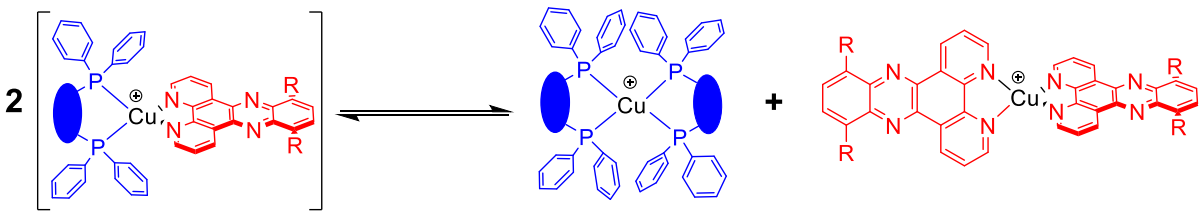

Scheme 2.4. A speciation equilibrium leading to ligand dissociation and subsequent formation of undesired homoleptic species.

An example of a DOSY spectrum with different sets of diffusion coefficients measured on a sample with different species is shown in **Figure 2.9. a**[83]**.** Estimating the molecular weight of the target complex from its diffusion coefficient can be achieved by using the Stokes–Einstein–Geirer–Wirtz Estimation (SEGWE) method[83] (**Figure 2.9. b**). However, the calculation has the requirement of befitting small molecules with $\mathbf{M_w} < 1000$ gmol^{-1} and composed of light atoms (sulfur as the maximum limit). For reasons of the presence of copper alone violating such rule, interpretation of the spectrum will be limited to the assessment of the speciation reaction in **Scheme 2.4** and not pertain heavily on the calculation results.

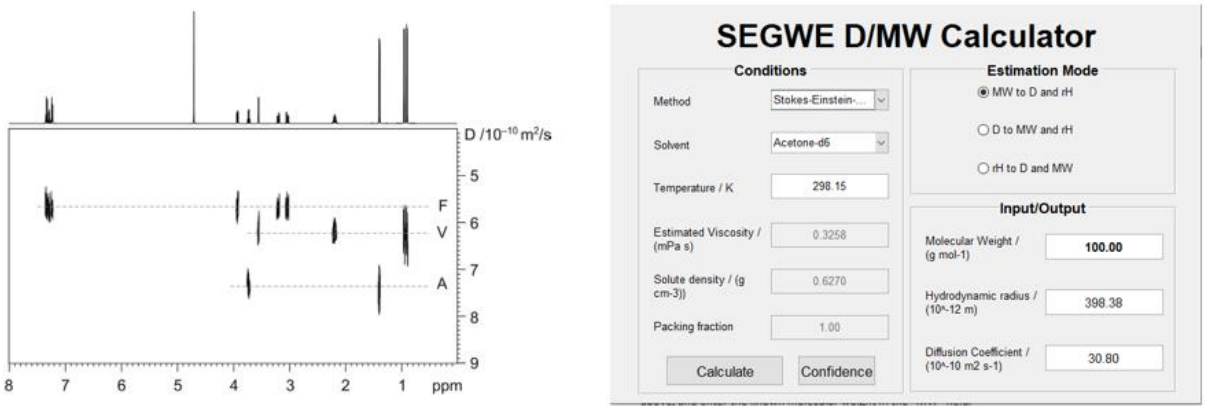

Figure 2.9. (a) left: pseudo 2D-DOSY spectrum showing the different F_1 resonances for an equimolar mixture of *L*-amino acids; alanine (A), valine (V) and phenylalanine (F) in aqueous solution at 298 K. Excerpted from [83] **(b) right:** SEGWE calculator used to determine the estimated molecular weight from the measured diffusion coefficient

2.3. Single Crystal X-ray Diffraction (SC–XRD)

SC–XRD is an experimental method for determining structures of crystals which essentially comprise an ordered array of electron densities. A beam of incident X–rays is scattered in many directions upon striking the crystal structure. Constructive interference of the diffracted X–rays are observed at an angle determined by Braggs law:

$$n\lambda = 2d \sin\theta \tag{9}$$

Where n is an integer multiple of λ, the wavelength of the X–ray beam. θ is the angle at which the incident rays meet the lattice plane and d is the lattice inter–planar distance. A number of corrections and subsequent Fourier transformation of an obtained three–dimensional diffraction pattern with different scattering intensities, provides a three–dimensional electron density image of the unit cell. From this can the mean positions of the atoms within the crystals be determined.

In this thesis, SC–XRD was conducted to investigate the geometry around the Cu^{I} coordination environment and the preferred conformations of the associated ligands. Methods employed for growing crystals suitable for SC–XRD included solvent/anti–solvent layer diffusion and vapour diffusion crystallization.

2.4. Ultraviolet–Visible Diffuse Reflectance Spectroscopy (UV–Vis DRS)

UV–Vis diffuse reflectance spectroscopy is a technique for analysing surface–dispersed electromagnetic radiation of tightly packed powders to evaluate their light absorption abilities. Diffuse reflectance unlike regular (or specular) reflectance, is independent of the angle of the incident radiation. Hence it is a combination of refraction, non–specular reflections and scattering, and is dependent on the colour and physico–chemical properties of the sample. This technique has the advantage of being non–destructive and requiring negligible sample preparation. The experimental setup involves the sample being placed at 0º to the incident beam and usually surrounded by an integration sphere for redirecting the reflected radiation unto a detector (**Figure 2.10**).[86, 87]

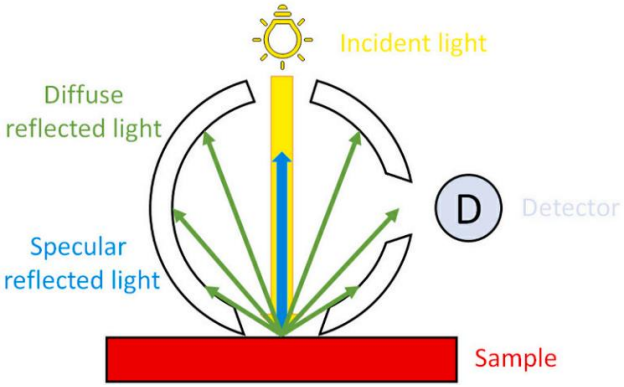

Figure 2.10. Setup for UV – Vis DRS equipped with an integration sphere for redirecting only diffuse reflections (green arrows) onto detector and cancelling out specular reflectance (blue arrow). Excerpted from ref[86]

In the measurements conducted for the free ligand and copper complexes, no integration sphere was used, the sides of the glass vials containing the sample powders were measured as they were, and the angle of the detector was oriented in a position where majority of the diffuse reflectance met. Powder $BaSO_4$ was used as reference standard for performing the instrumental autozero calibration. The spectra obtained after 100 scans consist of the % reflectance (y-axis) against the wavelengths λ of the UV–Vis radiation (380 – 850 nm). The diffuse reflectance *R* of the various measured samples can be analyzed using the Kubelka–Munk equation:

$$(R_\infty) = \frac{(1 - R_\infty)^2}{2R_\infty} = \frac{K}{S} = \frac{2.303\varepsilon C}{S} \qquad (10)$$

Where K= absorption coefficient, C= sample concentration, R_∞= absolute remittance and ε =absorptivity. $BaSO_4$ as the reference for instance, will have R_∞=100%. It should be noted that since the sample measurements in this thesis did not take into consideration the concentration of the packed material, the lack of integration sphere and the thickness of the bottom of the sample glass vials. Hence, assessment of the spectra will be limited to the variations in the absorption bands along the wavelength axis, and not focus on the specific values of the reflectance intensities among the measured materials.

3. Results and Discussion

3.1. Oxidation of aromatic hydrocarbons to quinones

3.1.1. Attempted synthesis of $phenO_2$ (1a) via a $Br^-/HNO_3/H_2SO_4$ method

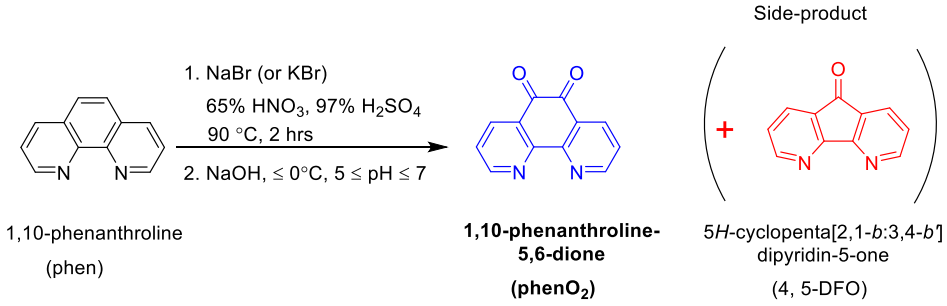

Scheme 3.1. Method 1: Attempted synthesis of **1a** using sulfo-nitric mixture with excess bromide.

The synthesis of **1a** was attempted following a standard (almost the only) protocol by Yamada *et al.* [48] involving the oxidation of 1,10–phenanthroline (phen) in the presence of excess bromide ion and a mixture of sulfo–nitric acids (**Scheme 3.1.**, method 1). Basic pH neutralization during workup inevitably led to the mono–decarbonylation of **1a** to 4, 5–diazafluorene–9–one (4, 5–DFO), a phenomenon already reported by Inglett *et al.* [49] and Ferretti *et al.* [50]. Fortunately, the rate of the 4, 5–DFO side-product formation was reduced by performing the neutralization slowly at low temperature with the final pH not exceeding 7. ^{1}H NMR characterization of the crude showed incomplete conversion of phen to **1a** and the side product; 28% (trial 1) and 0% (trial 2 and 3) (**Figure 3.1**).

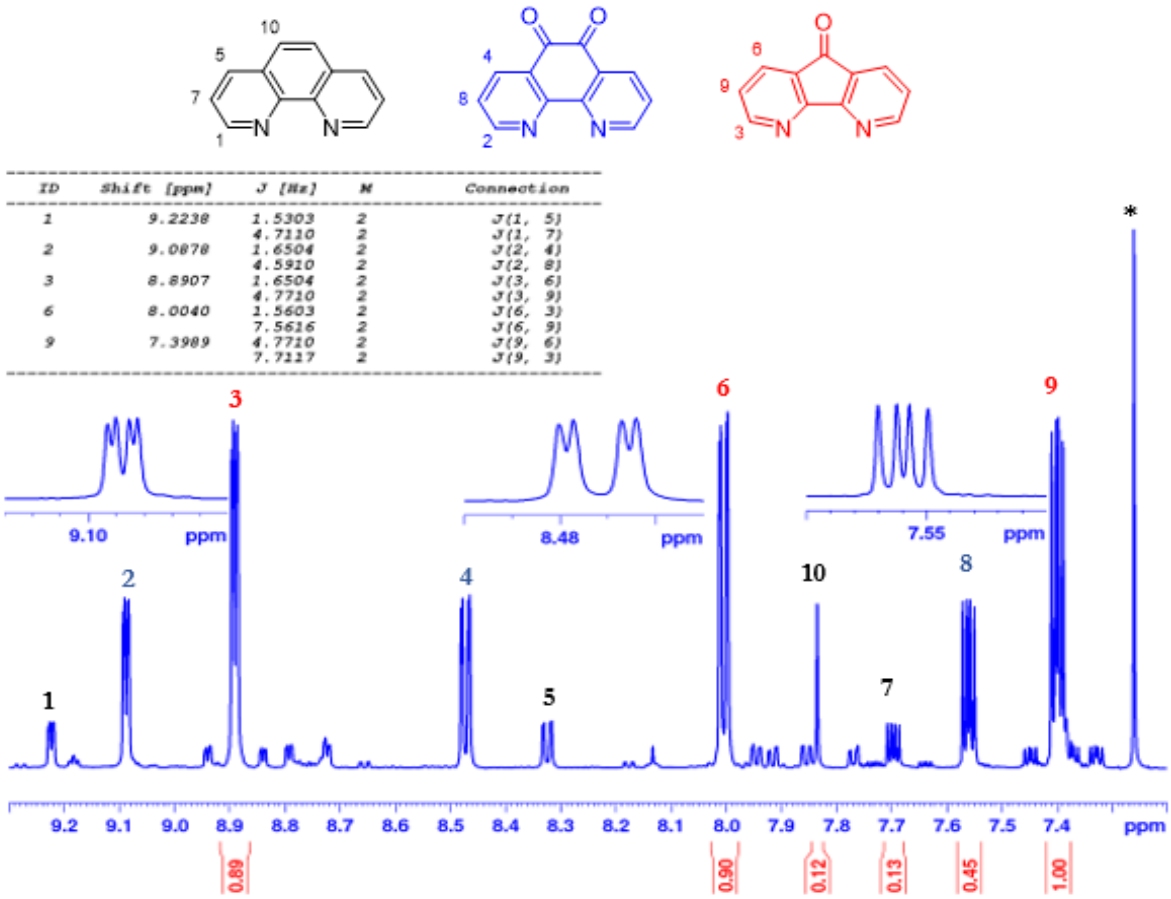

Figure 3.1. ^{1}H NMR (600 MHz, $CDCl_3$) showing aromatic region of Trial 1 crude with 28% NMR conversion by $Br^{-}/HNO_3/H_2SO_4$. ***** $CDCl_3$ peak.

Multiplet analysis of all the aromatic peaks (**1 – 9**) showed doublet of doublet split pattern with peaks **1, 2** and **3** having similar $^{3}J_{HH}$ and $^{4}J_{HH}$ coupling of 4.7 and 1.6 Hz respectively, as are peaks [**4, 5, 6**] with $^{3}J_{HH}$ = 7. 6 Hz and $^{4}J_{HH}$ = 1.6 Hz, and peaks [**7, 8, 9**] with $^{3}J_{HH}$ = 7. 6 Hz and $^{4}J_{HH}$ = 1.6 Hz. Identified coupling partners ("Connections" in **Figure 3.1.**) and integrals indicated peaks [**1, 2, 3**] to be analogous protons in similar chemical environment but in three different compounds, as are peaks [**4, 5, 6**] and [**7, 8, 9**]. The presence of singlet peak **10** with identical integral ratio to peaks [**1, 5, 7**] implies origination from the starting material phen. SelTOCSY only reconfirmed the multiplet analysis and integral results without distinguishing if peaks [**3, 6, 9**] or [**2, 4, 8**] belong to protons from **1a** or 4, 5–DFO**.** Stacked ^{1}H NMR analysis between the crude of trial 2 and a reference **1a** ‡ isolated and recrystallized using a slightly modified protocol, indicated peaks [**2, 4, 8**] to originate from **1a** (**Figure 3.2**).

‡ Reference **1a** was synthesized by colleague Austenaa B.T. in Amedjkouh group working with 11,12–disubstituted dppz analogues.

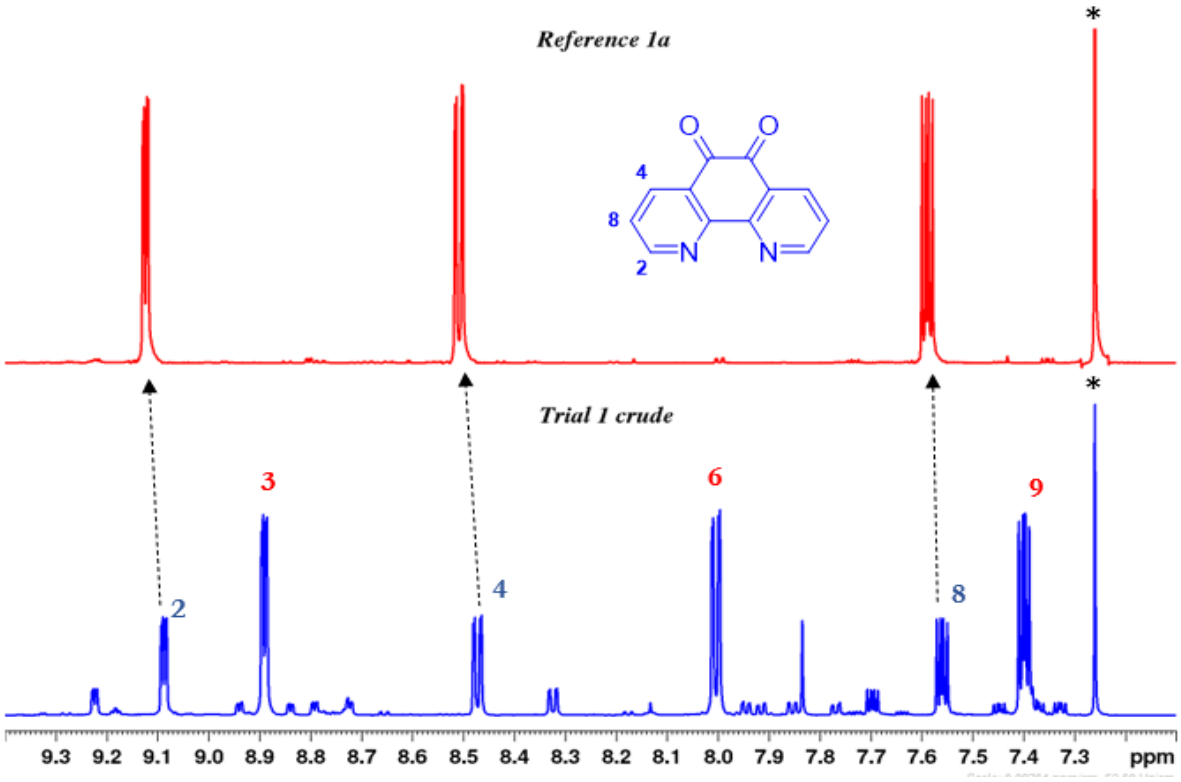

Figure 3.2. Stacked ^{1}H NMR (600 MHz, $CDCl_3$) of Reference **1a** (top) and Trial 1 crude (bottom). ***** $CDCl_3$ peak.

Imperfect matching of the stacking peaks might probably be due π – π stacking interactions between phen, product **1a** and 4, 5–DFO causing slight changes in the chemical shift values. Hence, the [**2, 4, 8**] → $phenO_2$ (**1a**) was based on which peak amongst each set is in close proximity to the reference, and the reasoning that the presence of two electron-withdrawing carbonyl groups justifies [**2, 4, 8**] being more downfield than [**3, 6, 9**].

In addition, high–resolution ESI–MS analysis of the crude in **Figure 3.3** below further indicated the presence of the **phen** as $[M + H]^+$ (181.076 Da), **4, 5–DFO** as $[M+H]^+$ (183.0553 Da) and the desired **1a** as $[M+H]^+$ (211.0501 Da). Hence, it can be inferred that peaks [**3, 6, 9**] in **Figure 3.1** originate from protons of the side–product **4, 5–DFO**.

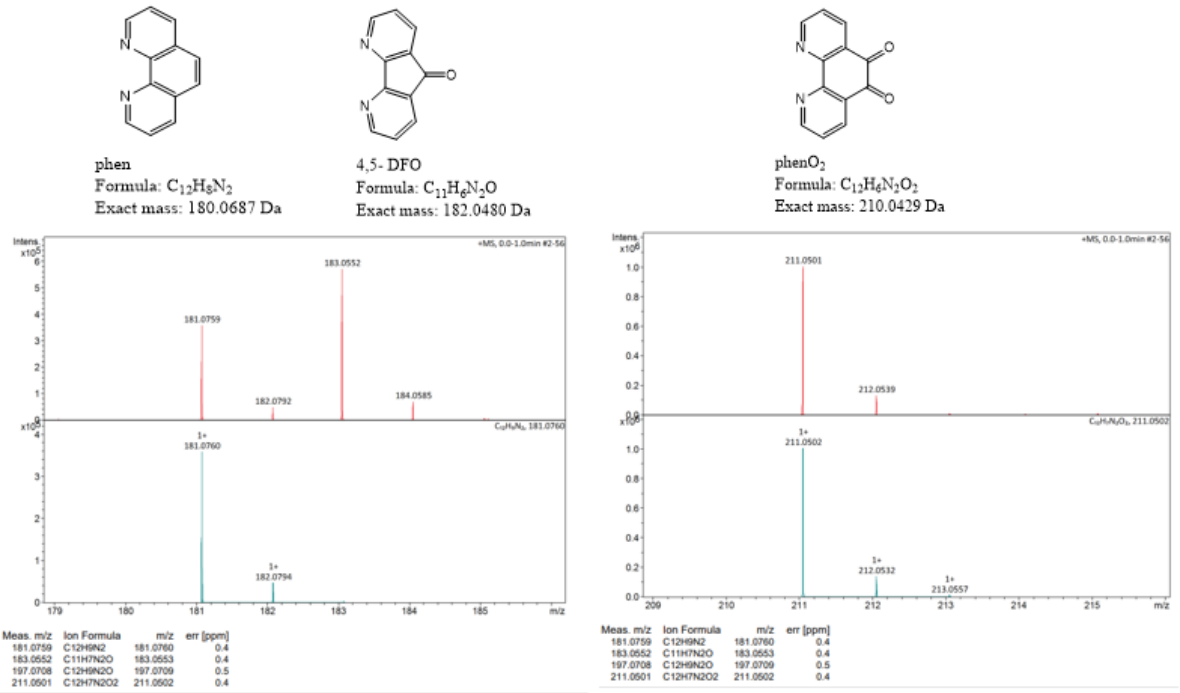

Figure 3.3. ESI – HRMS analysis showing the presence of starting material **phen**, product **1a** and side product **4, 5 DFO**.

The $Br^-/HNO_3/H_2SO_4$ procedure designed by Yamada *et al.* [48] (with a claim of 86% isolated yield) has been applied in numerous published reports. Despite the similarity in the applied procedures, the yield has ranged from 21 – 99% (example yields: 21% at 0 °C [51], 30% at -30 °C [51], 51% at -50 °C [51], 25% [52], 30% [53], 35% [54], 86% [48], 87% [50], 96% [55], 99% [56], 99% [57]). The authors have remarked that the acid mixture should be added to the phen/KBr mixture "through the ice–cooled flask", otherwise the target yield drops to zero.[48] However, the reaction being performed at temperatures as low as -50 °C by Militov *et al.* [51] did not produce a good yield. Even though the mechanism behind the oxidation has not been elucidated, it is evident that the nitric acid acts as an oxidant with the bromide ion being the catalyst. This is justified from the observation that a faster evolution of Br_2 gas due to high temperatures, facilitated the failure of the reaction as a result of side reactions occurring.

3.1.2. Efficient synthesis of phenO_2 (1a) via a BrO_3^-/H_2SO_4 method

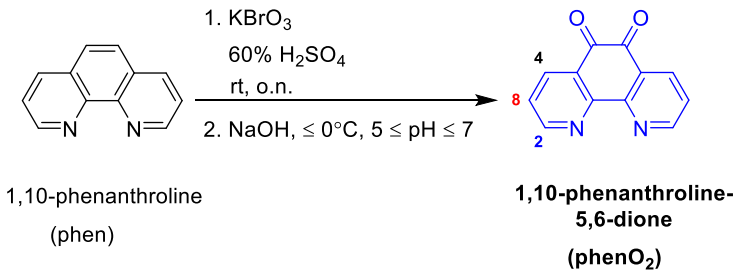

Scheme 3.2. Method 2: Synthesis of **1a** using diluted sulfo-bromate mixture.

A more efficient alternative method prescribed by Zheng *et al.*[58] involves milder conditions and suitable for macroscale output (**Scheme 3.2**). ^{1}H NMR analysis of the crude product showing a full conversion with successful MeOH recrystallization to afford **1a** as bright yellow powdery crystals, enabled the reaction to be successfully carried out on a 20 g scale. Further confirmation of the proton assignments is revealed in a ^{1}H–^{15}N HMBC spectrum where proton **4** (δ 8.51 ppm) expectedly shows no correlation (**Figure 3.4**). With CNST13 = 10 Hz indicating optimization for $^2J \rightarrow {}^3J$ coupling, ^2J coupling was expected to show a denser cross-peak than ^3J. Hence, proton **2** (δ 9.12 ppm) becomes the most downfield and proton **8** (δ 7.59 ppm) becomes the most upfield.

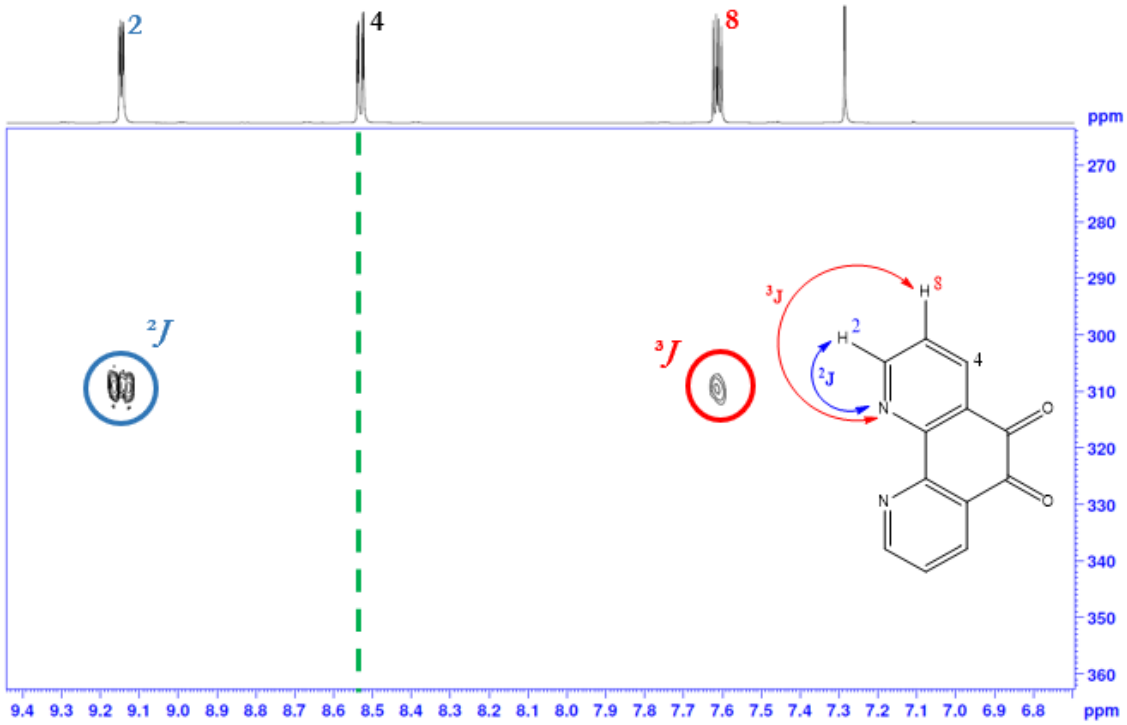

Figure 3.4. Unreferenced ^{1}H–^{15}N HMBC (600 – 61 MHz, $CDCl_3$) of pure **1a.**

3.2. *S*–oxidative cyclisation of *o*–phenylenediamine (OPD)

3.2.1. Synthesis of benzo[c][1,2,5]thiadiazole (2)

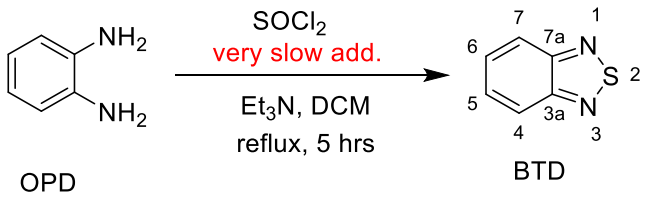

Scheme 3.3. Synthesis of BTD (**2**) with OPD as starting material.

With the well–known instability of substituted *o*–aromatic diamines[59, 60] and necessity to protect the amino groups, the cyclisation process confers stability on the compound and directs subsequent substitution to the 4 and 7 positions (**Scheme 3.3**). BTD (**2**) was synthesized in high yields (93% crude) according to the published procedure[46] by treating freshly grounded OPD with thionyl chloride in the presence of a base. The reaction without the base produced only 4% yield. Besides flash chromatography[61], the most recommended purification technique was steam distillation which had the advantage of yielding exceptionally pure **2** as an orange-yellow solid. Proving the N(1)–S(2)–N(3) connectivity in the product was based on obtained APCI–HRMS spectrum indicating the desired **2** as a radical cation $[M]^+$=136.0064 Da (calculated mass =136.0095 Da) as shown in **Figure 3.5** below.

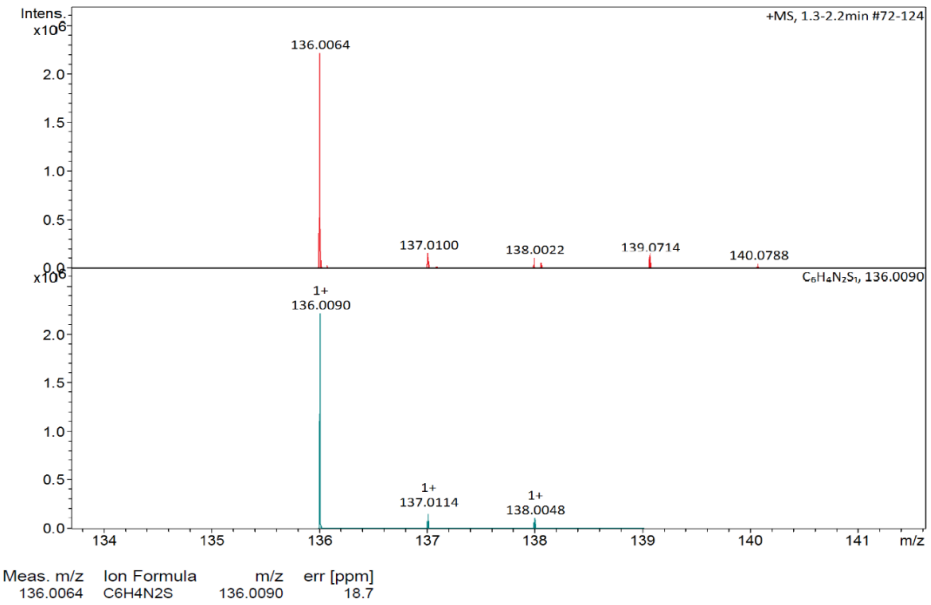

Figure 3.5. APCI–HRMS spectrum indicating the presence of **2**.

^{1}H NMR analysis showed only two aromatic peaks (δ 7.49 (**B**) and 7.90 (**A**) ppm) with split patterns similar to a simple doublet of doublet with an obvious roofing effect and integral values of 2H each. This accounts for the two sets of protons [**4, 7**] and [**5, 6**], considering the C_{2v} symmetry of BTD (**Figure 3.6**).

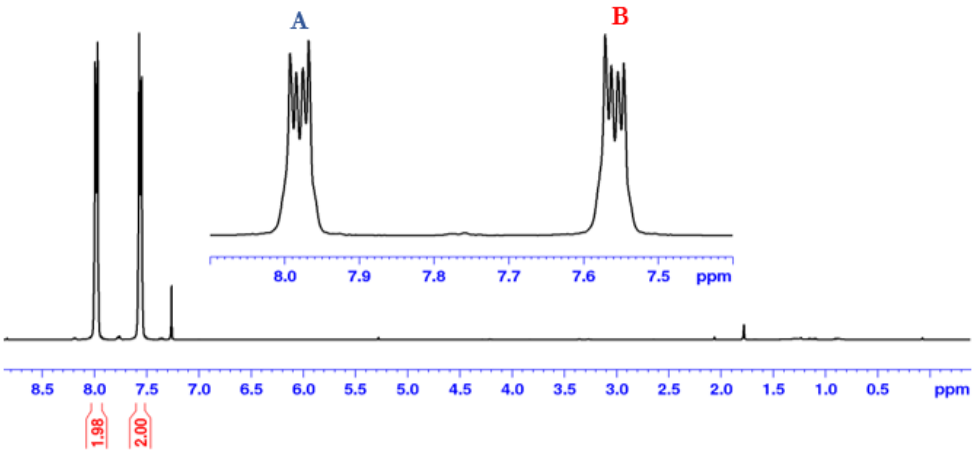

Figure 3.6. ^{1}H NMR (400 MHz, $CDCl_3$) of steam distilled **2.**

Distinguishing between which proton set belongs to **A** or **B** was based on arbitrarily varying the CNST13 [§] values of acquired ^{1}H–^{15}N HMBCs (**Figure 3.7**). Peak **A** showed a less dense cross–peak at a value of 2Hz (**Figure 3.7. a**) and denser cross–peak at a value of 6Hz implying peak **A** to arise from the proton set [**4, 7**] and peak **B** from proton set [**5, 6**] (**Figure 3.7. b**)

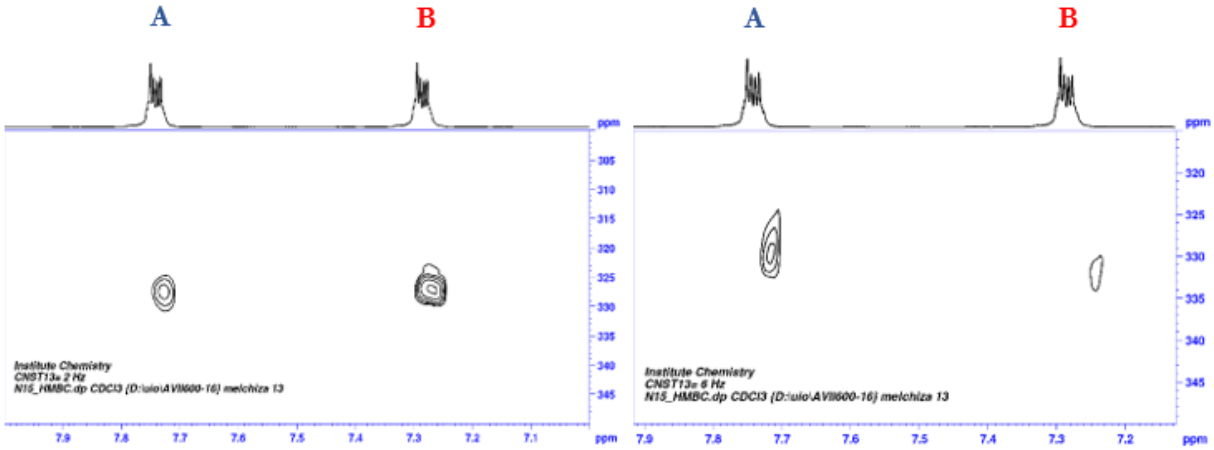

Figure 3.7. a (left): ^{1}H–^{15}N HMBC (600–61 MHz, $CDCl_3$) spectra of product **2** with **CNST13 = 2 Hz**. **b (right):** ^{1}H–^{15}N HMBC (600–61 MHz, $CDCl_3$) spectra of product **2** with **CNST13 = 6 Hz.**

[§] A higher value for this spectra acquisition parameter implies optimization for ^{n}J coupling with lower *n*.

A more thorough examination of peaks **A**/**B** revealed an AA'BB'/AA'XX' unique multiplet splitting pattern arising from a second–order combination of quartets and doublets with each consisting of two coupling constant operation (**Figure 3.8**). For instance, the two mid peaks with the highest peaks is designated as **|N|** doublet with constant $|^3J_{AB} + {}^4J_{AB'}|$ and containing 50% of the area under the entire peak.[62] In the case of BTD, **|N|** was found to be 10.087 Hz.

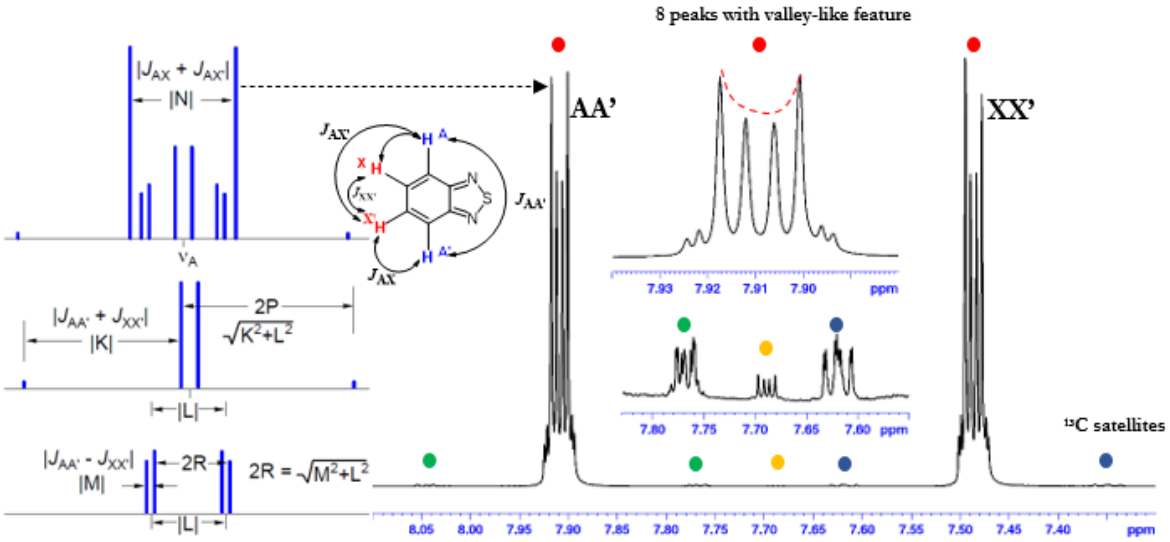

Figure 3.8. A comparison of a generalized AA'XX'(/AA'BB') spectrum with ^{1}H NMR (600 MHz, $CDCl_3$) of steam–distilled **2**. **|K|** $= |^5J_{AA'} + {}^3J_{BB'}|$ ("*J*" of one ab quartet), **|L|** $= |^3J_{AB} - {}^4J_{AB'}|$ ("δ" of both ab quartets), **|M|** $= |^5J_{AA'} - {}^3J_{BB'}|$ ("*J*" of other ab quartet), **|N|** $= |^3J_{AB} + {}^4J_{AB'}|$ ("doublet").[62] Blue and green indicators represent ^{13}C satellites.

The total individual peaks (i.e. 8 peaks) differs from that of the generalized AA'XX' spectrum (i.e. 10 peaks) based on the reasoning that the $^3J_{XX'}$ and small values of $^5J_{AA'}$ causes the central peaks of **|K|** and **|M|** ab quartets to be superimposed leading to less number of resolvable peaks. The **A**/**B** peaks were also supplemented with equidistant ^{13}C satellite peaks on each side (**Figure 3.8**).

3.3. Bromination of Benzothiadiazoles.

3.3.1. Synthesis of 4,7-dibromobenzo[c][1,2,5]thiadiazole 3a

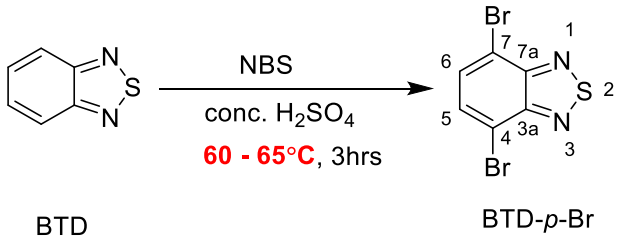

Scheme 3.4. Dibromination of BTD (**2**) to afford BTD–*p*–Br (3a)

The standard and most popular protocol for **Scheme 3.4** involves the dropwise addition of Br_2/HBr to dissolved BTD in HBr solution.[22, 45, 63 – 66] However, for reasons of safety, easy handling and avoiding a time-consuming procedure and workup, **Scheme 3.4** was conducted following an alternative protocol by Sarjadi *et. al.*[67, 68] and Heiskanen *et. al.* [69] which involved the use sulfuric acid to generate Br^+ from NBS, followed by substitution on the more nucleophilic 4 and 7 sites of BTD. An increase in temperature beyond 65 ºC promoted low yield. Subsequent recrystallization of crude with chloroform: hexane (1:2) afforded pure **2a** as off–white needle–like crystals. ^{1}H NMR analysis showed the transformation of the AA'BB' system into a singlet (δ 7.72 ppm) arising from proton set [**5, 6**] in **Scheme 3.4** (**Figure 3.9**).

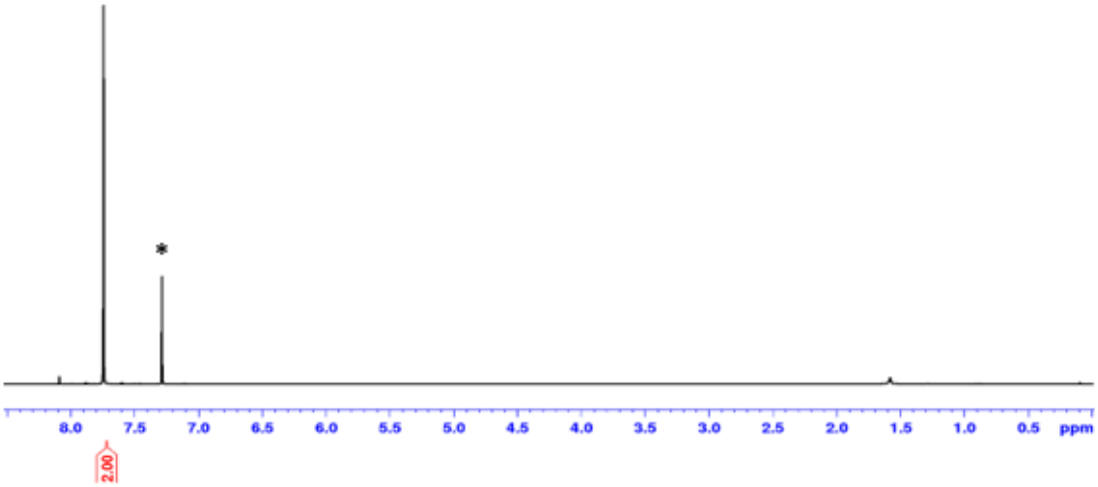

Figure 3.9. ^{1}H NMR (600 MHz, $CDCl_3$) acquired on pure **3a.** * $CDCl_3$ peak.

Confirmation of the presence of Br in the product was by APCI – HRMS indicating 4, 7–BTD–p–Br as a radical cation $[M+H]^{\bullet+}$= 292.8366 Da (calculated mass= 292.8383 Da) (**Figure 3.10**).

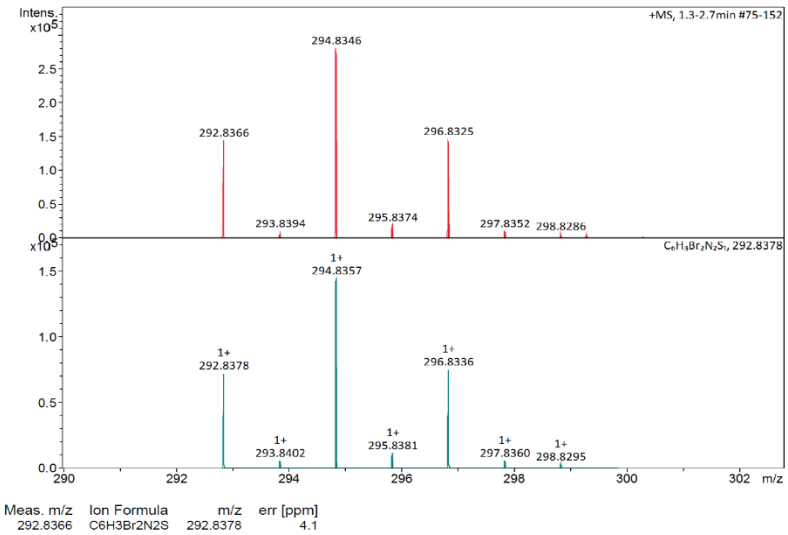

Figure 3.10. APCI–HRMS spectrum indicating the presence of **3a**.

3.4. RVB cyanation of BTD-*p*-Br

3.4.1. Synthesis of benzo[c][1,2,5]thiadiazole-4,7-dicarbonitrile (3b)

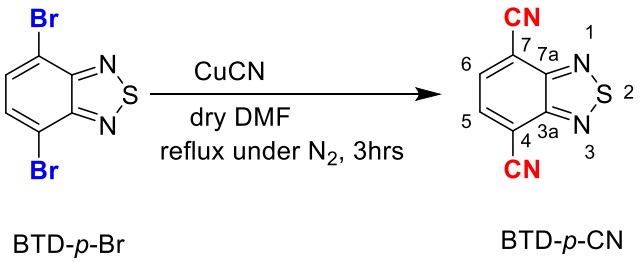

Scheme 3.5. RVB cyanation of BTD-p-Br to afford BTD-p-CN (**3b**)

Scheme 3.5 was conducted following the protocol by Aslan *et al.*[22] Post–reaction workup involved additional stirring of the reaction mixture with an acidic solution of $FeCl_3 \bullet 6H_2O$ to rid off CuBr and $CuBr_2$ by-products. Though **3b** was afforded in good yields on a large scale, the workup was laborious and required large amounts of extraction solvent (DCM) and water to rid the crude off residual DMF. Nevertheless, the afforded crude showed satisfactory purity by NMR for subsequent sulfur extrusion reactions.

^{1}H NMR analysis and comparison with that of BTD-*p*-Br (**3a**) showed the singlet peak arising from proton set [**5, 6**] (**Scheme 3.5.**) to have shifted downfield (δ 7.72 ppm → 8.07 ppm) (**Figure 3.11**) indicating a slight change in the chemical environment.

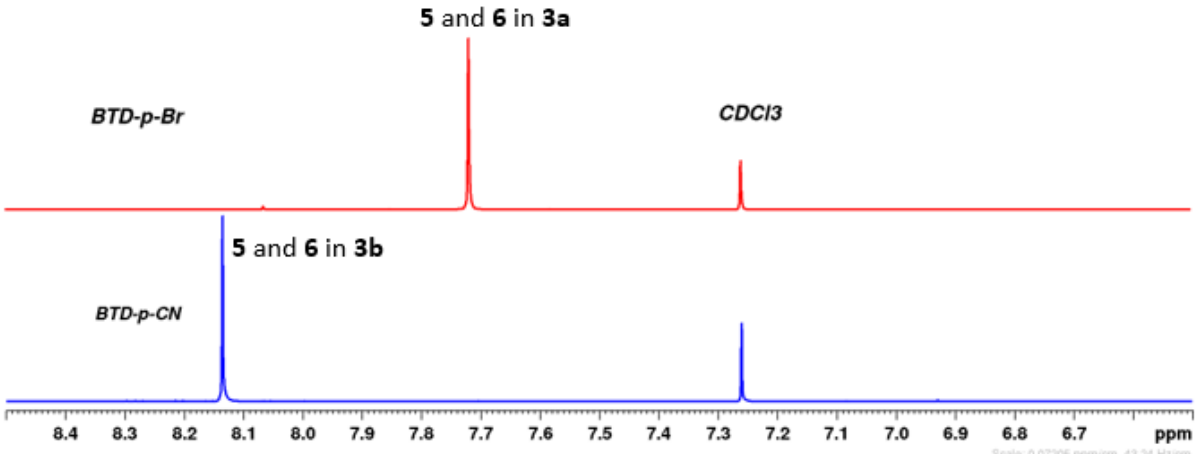

Figure 3.11. Stacked ^{1}H NMR (600 MHz, $CDCl_3$) of BTD-*p*-Br (top) and BTD-*p*-CN (bottom).

In addition, ^{13}C NMR analysis indicated the appearance of an upfield peak (δ 110.7 ppm) absent in ^{13}C NMR of **3a**, which corresponds to the carbon of the cyano groups. (**Figure 3.12**).

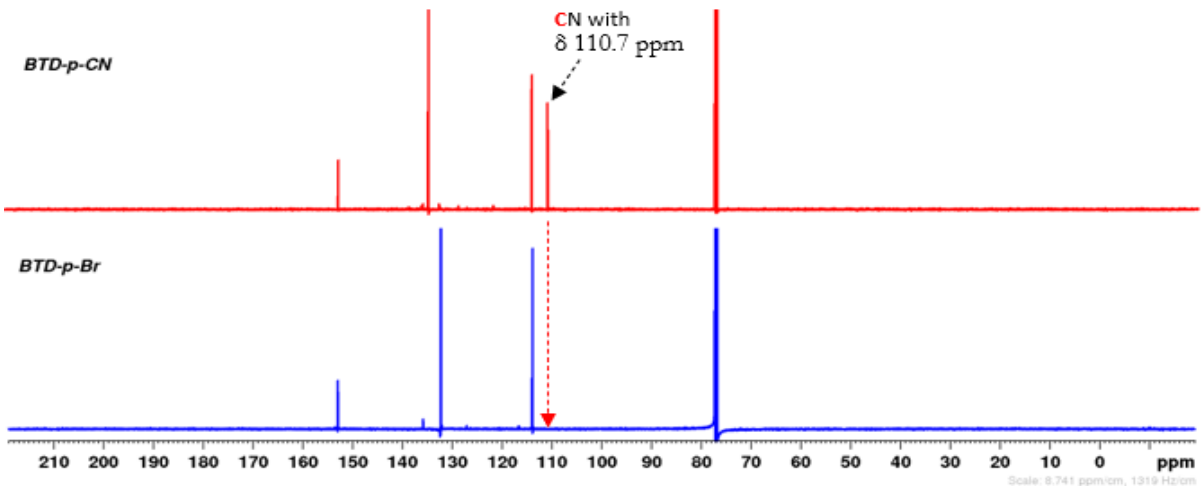

Figure 3.12. Stacked ^{13}C NMR (150 MHz, $CDCl_3$) of BTD-*p*-Br (top) and BTD-*p*-CN (bottom).

Cyano vibrational stretch of **3b** in the approximate range 2213 – 2232 cm^{-1} were expectedly absent in the IR spectra of BTD-p-Br (**3a**) and BTD (**2**) (**Figure 3.13**). C–Br stretches in the range 486 – 671 cm^{-1} also showed significant difference compared with **2** and **3b**. Similar FTIR bands amongst the three compounds include C=C stretching located in the range of 1600 – 1400 cm^{-1} and aromatic C–N stretching corresponding to weak bands of 1152 – 1309 cm^{-1}.

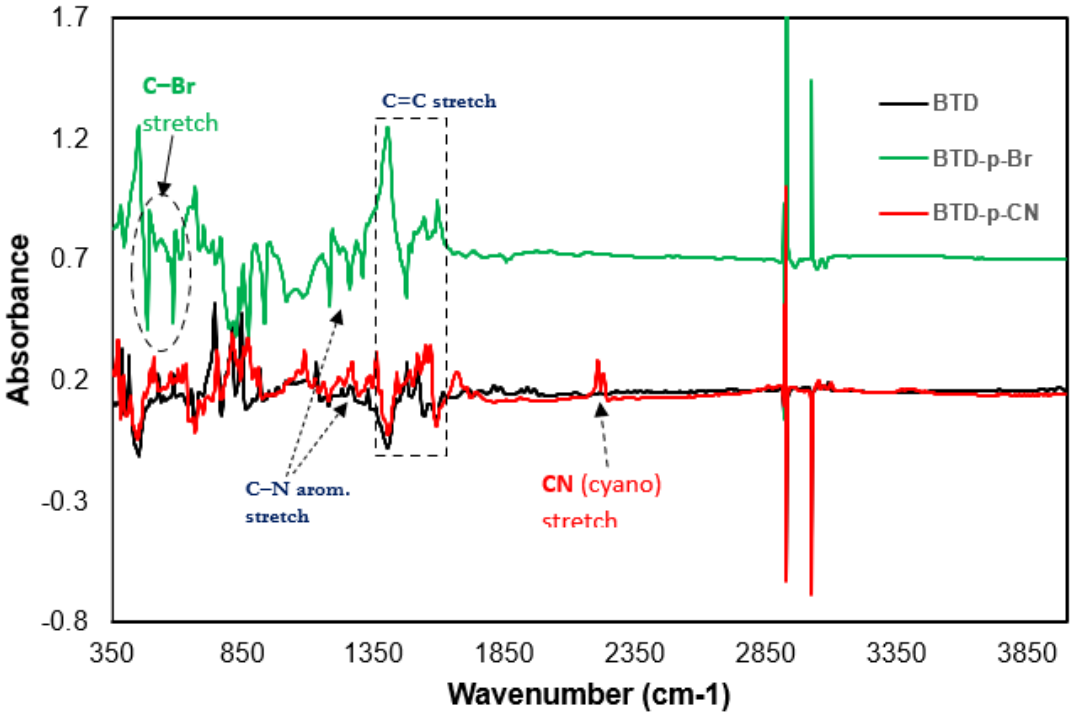

Figure 3.13. FTIR spectra acquired on product **2**, **3a** and **3b**.

3.5. Suzuki–Miyaura cross-coupling

3.5.1. Synthesis of terphenyls (3c – 3e, 4c)

Scheme 3.6 below had the advantage of being scaled up to (> 1) g synthesis scale. **3a** was allowed to react at room temperature overnight to yield **3c** and **3e.** For **3d** and **4c** however, the reaction was conducted under reflux (considering the expected low reactivity) for one hour. In the case of product **4c**, sulfur extrusion process using Co^{II}–$NaBH_4$ system was conducted prior to the coupling reaction. Despite the presence of palladium-chelating amino groups, the reaction followed by chromatographic separation afforded the product with 69% yield as an orange-brown solid.

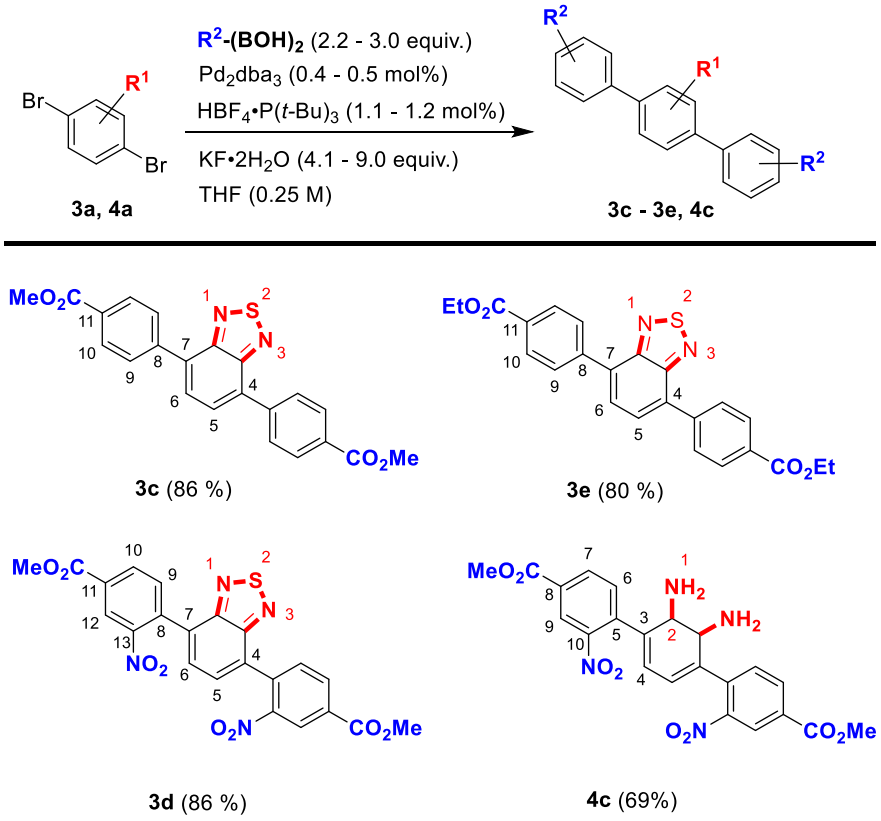

Scheme 3.6. Synthesis of **3c – 3e** and **4c** with yields in parenthesis.

Stacked ^{1}H NMR analysis showed both products **3c** and **3e** to having similar aromatic *para*–substituted *AA'BB'* splitting pattern from proton set [**9, 10**] (*ca.* δ 8.1 ppm, 8.2 ppm seemingly appearing as large doublets) with $|N|$ doublets = 8.5 Hz and $|K|$ ab quartet = 3.8 Hz (**Figure 3.14**). The difference was found in the aliphatic region where the ethoxy group of **3e** was identified as the triplet (δ 1.44 ppm) and quartet (δ 4.44 ppm) whiles that of the **3c**

indicated the presence of the expected singlet (δ 3.97 ppm). Due to the C_{2v} symmetry of **3c** and **3e**, protons in positions 5 and 6 (**Scheme 3.6**.) of the benzothiadiazole moiety appear as a singlet (δ 7.87 ppm) (**Figure 3.14**).

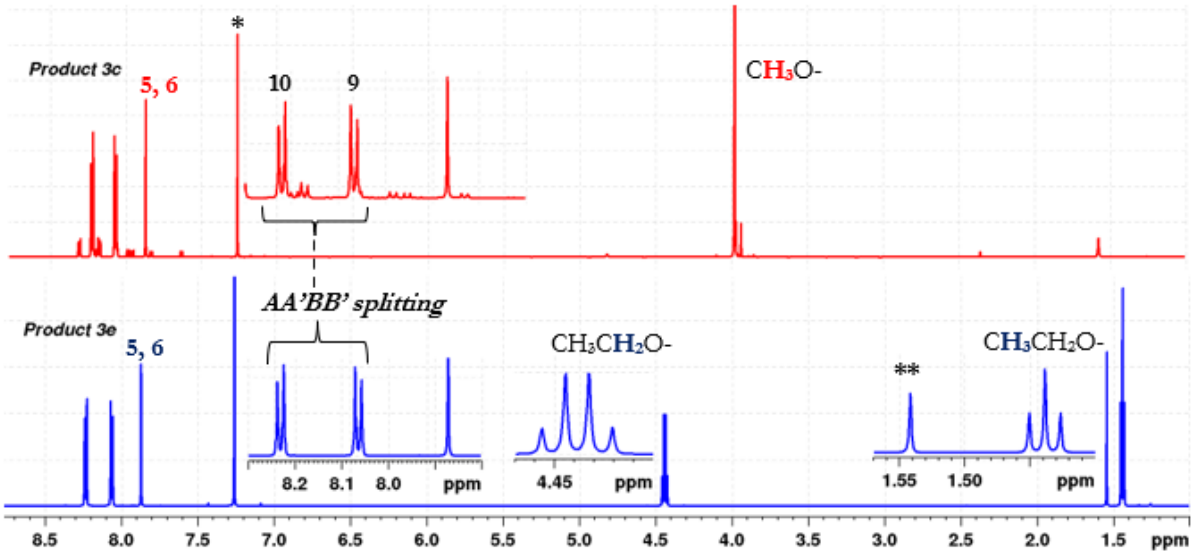

Figure 3.14. Stacked ^{1}H NMR (600 MHz, $CDCl_3$) acquired on products **3c** and **3e**. * $CDCl_3$ peak, **residual MeCN from recrystallization. Numbering corresponds to protons of **3c** and **3e** in **Scheme 3.6**.

In the case of **3d** and **4c**, the appearance of a singlet at δ 3.36 ppm indicating the presence of amino groups in **4c**, differentiates from product **3d**. Protons [**5, 6**] of **3d** appear as a singlet δ 7.76 ppm sandwiched between the doublet of proton 9 (δ 7.75 ppm) (**Figure 3.15**). However, the corresponding proton in product **4c** (identified as proton 4) shifts to an upfield position due to electron-donating amino groups, and splits into a major peak (δ 6.59 ppm) and minor peak (δ 6.61 ppm). With the exception of the amino peak (δ 3.36 ppm) and methoxy singlet (δ 4.01 ppm), this phenomenon occurs with other aromatic peaks where the minor peaks are the exact duplicate of the major with similar coupling constants. The minor peaks do not stem from impurities since the integral values of the amino and methoxy peaks only match if the major and minor peaks are integrated together. Hence, the compound is pure by NMR and the splitting could not be unfortunately explained.

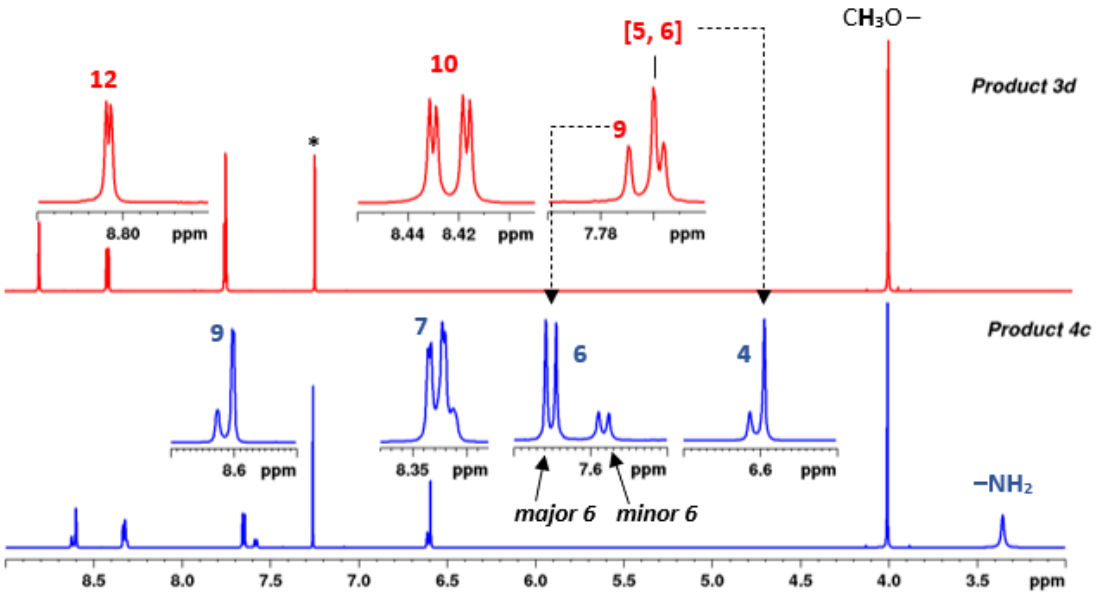

Figure 3.15. Stacked ^{1}H NMR (600 MHz, $CDCl_3$) acquired on products **3d** and **4c**. * $CDCl_3$ peak. Numbering corresponds to protons of **3d** and **4c** in **Scheme 3.6**.

Replicating the reaction which afforded product **3e** with a $Pd(OAc)_2$–PPh_3 system gave a full conversion of the starting material. However, formation of an undesired tricoupled side product (3h) was observed and fortunately separated by TLC analyses and chromatography (**Scheme 3.7**).

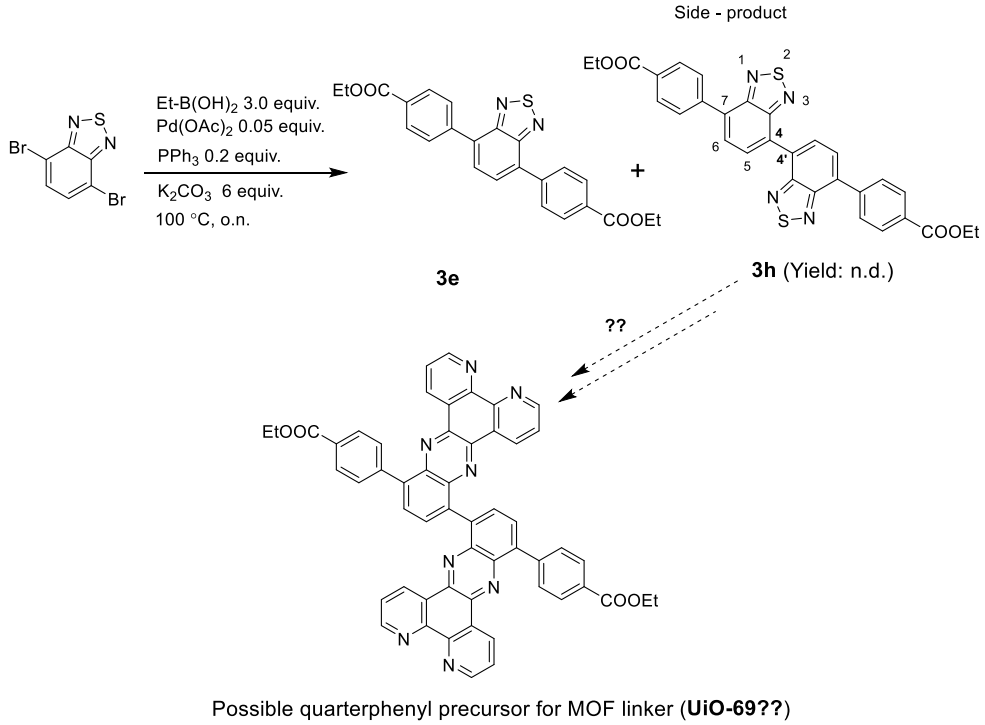

Scheme 3.7. Synthesis of **3e** using a $Pd(OAc)_2$–PPh_3 system with isolation of side product **3h**.

The C_2 axis going through the 4 – 4' bond made all acquired 1D and 2D NMR spectra acquired seem similar to those of a monocoupled bromo biphenyl product (**3g**) with small differences arising from subtle chemical shifts (**Figure 3.16**).

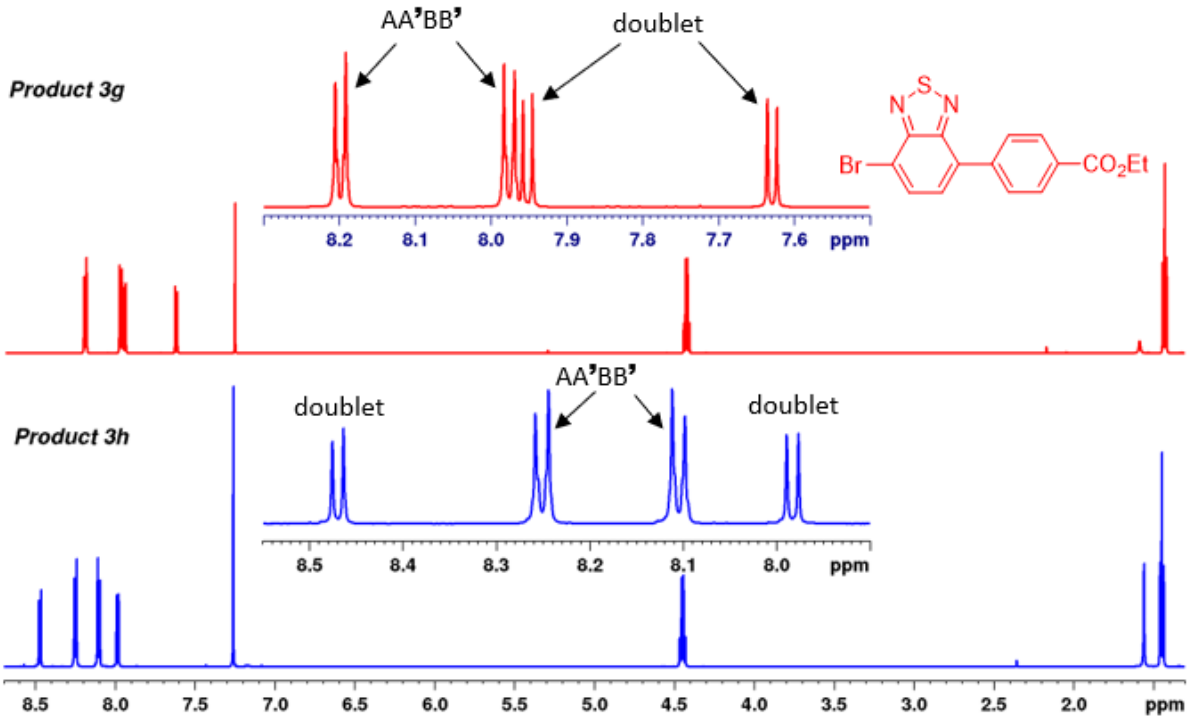

Figure 3.16. Stacked ^{1}H NMR (600 MHz, $CDCl_3$) acquired on products **3g** and **3h**.

Hence, the structure of **3h** was only confirmed by ESI – MS analysis indentifying the product as $[M+Na]^+$ = 589.09 Da and doubly charged dimer $[2M + Na]^+$ = 1155.71 Da, including fragments such as $[M – PhCOOEt + Na + H]^+$= 441.29 Da and $[M+ ½ M + Na]^+$ = 872.65 Da (**Figure 3.17**).

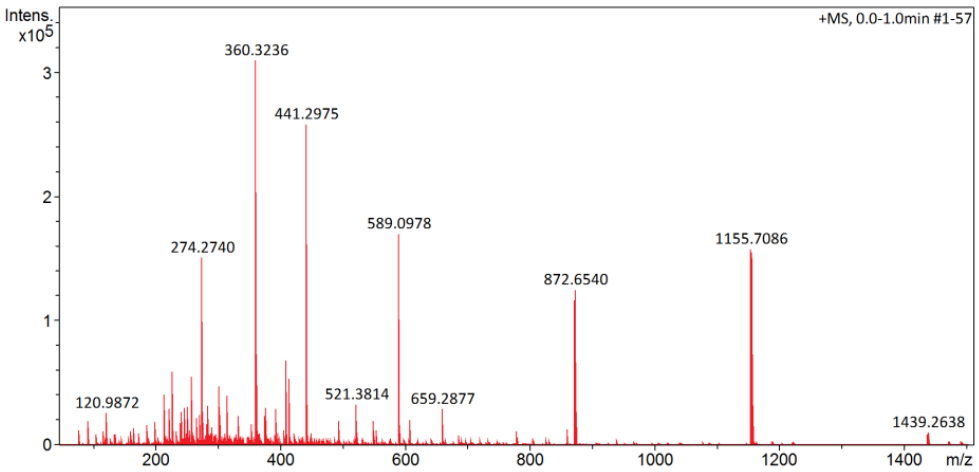

Figure 3.17. ESI–MS spectrum acquired on side product **3h**.

3.5.2. Synthesis of biphenyls (3f, 3g)

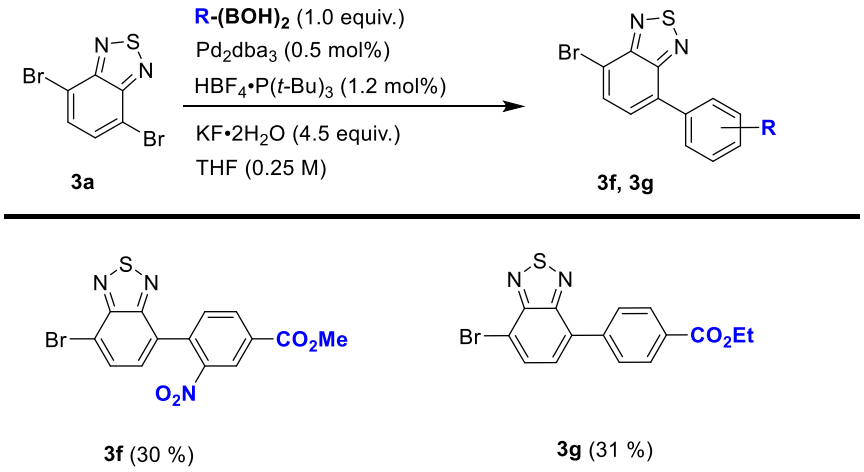

Scheme 3.8. Synthesis of **3f** and **3g** with yields in parenthesis.

The monocoupling products **3f** and **3g** were synthesized using one equivalent of the boronic acid with the same reflux conditions as the terphenyls. The products were isolated via chromatographic separation in poor yields of 30% and 31% as white fluffy solid and yellow powder respectively (**Scheme 3.8**). In addition, the formation of the undesired dicoupled products (**3e** and **3d**) was observed including the unreacted starting material **3a,** which is one explanation for the low yields. ^{1}H NMR of the isolated **3f** is shown below in **Figure 3.18**.

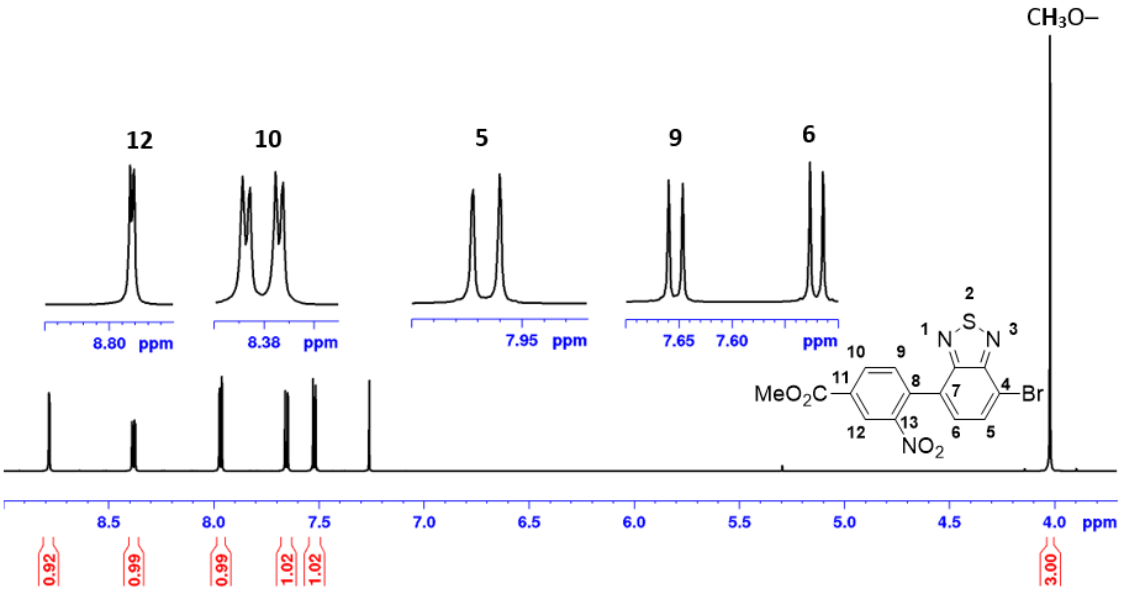

Figure 3.18. ^{1}H NMR (600 MHz, $CDCl_3$) acquired on compound **3f**.

3.6. Sulfur extrusion of disubstituted Benzothiadiazoles

3.6.1. Synthesis of dibromo– and dicyano–*o*–phenylenediamines (4a, 4b)

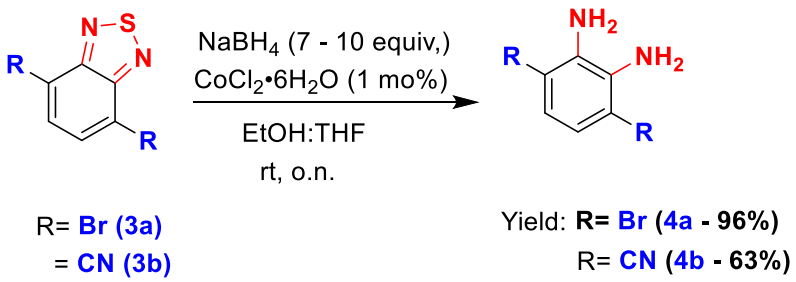

Scheme 3.9. Synthesis of **4a** and **4b** with yields in parenthesis.

Scheme 3.9 was performed with large excess of sodium borohydride to promote full conversion since a trial reaction with four molar equivalents of the borohydride for **3a** led to incomplete conversion. The original protocol involved conducting the reaction in solely ethanol under reflux for 3 hours. THF was used in addition to ethanol to promote dissolution of the inorganic components. Despite the modification in terms of reaction duration and solvent for **Scheme 3.9,** the products **4a** and **4b** were obtained with yields 96% and 63% respectively. H_2S effervescence was observed upon Co^{II} catalyst addition followed by the formation of a black saturating precipitate (Co_2B). Cyano substituted BTDs have been reported to strongly adsorb to the Co_2B surface, which explains the low yield[77, 78]. Increasing the mol% concentration of the Co catalyst according to the protocol, only resulted in lower yields. Hence, 1 mol% was used in both **4a** and **4b** cases. Further purification of the afforded crude was not attempted prior to phenO_2 condensation due to the known instability of *o*–phenylenediamines[59, 60].

Stacked ^{1}H NMR analysis between starting material **3a** and product **4a** showed a shift from δ 7.72 ppm to 6.84 ppm due to the presence of electron-donating amino groups appearing with δ 3.90 ppm (**Figure 3.19**). A similar upfield shift effect occurred with product **4b.** In addition, the partial reduction of the cyano groups to amino groups were not observed (**Figure 3.20**). Product **4a** was isolated as malodorous purple-violet flakes whiles **4b** as yellow solid. All other 1D and 2D NMR data acquired were in accordance with literature.

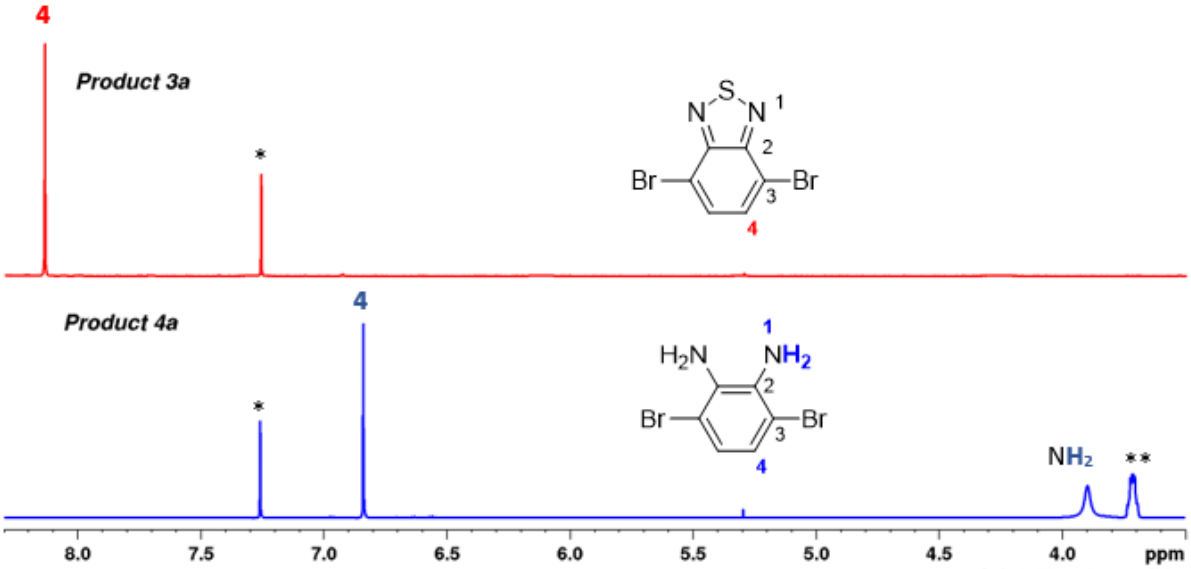

Figure 3.19. Stacked ^{1}H NMR (600 MHz, $CDCl_3$) of **3a** and **4a.** * $CDCl_3$ and **residual ethanol ($CH_3C\mathbf{H_2}$(**)OH)

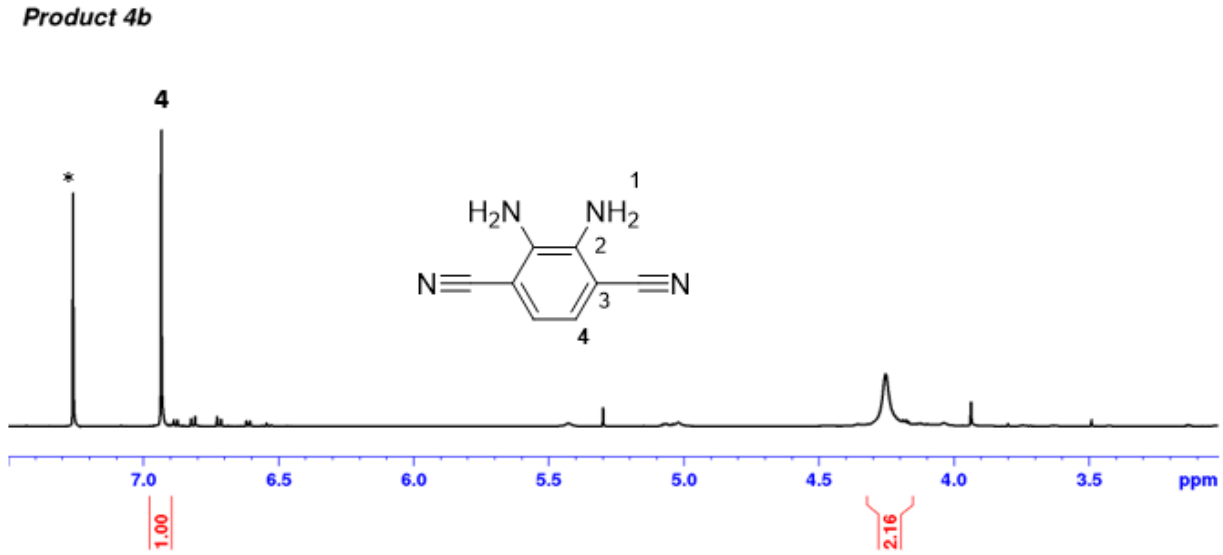

Figure 3.20. Stacked ^{1}H NMR (600 MHz, $CDCl_3$) of **4b**. ***** $CDCl_3$ peak.

3.6.2. Attempted synthesis of *o*-diaminoterphenyls (4d, 4e)

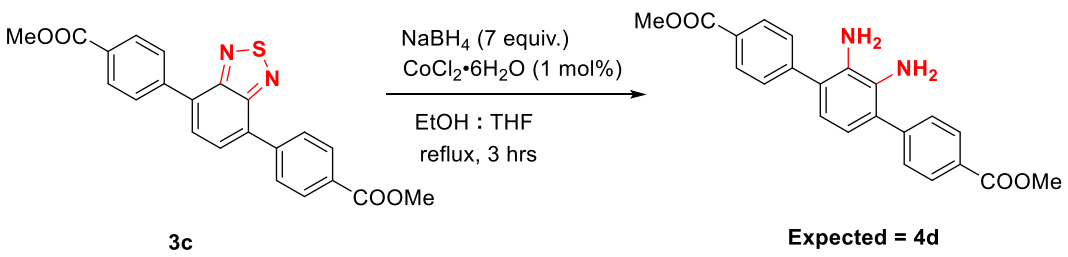

Scheme 3.10. Sulfur extrusion of **3c** to afford **4d**.

The same procedure as the previous section was applied in trials to methyl benzoate substituted BTDs under reflux conditions as shown in **Scheme 3.10**. ^{1}H NMR analysis of two selected crude trials showed dissimilar spectra where the methoxy groups could not be accounted for (**Figure 3.21**). In addition, none of the aromatic peaks showed splitting patterns or integrals values corresponding to the phenyl protons or aromatic proton of the diamino-phenylene ring. The only identifiable peaks were from residual reaction solvent. All other peaks stem from unknown origin.

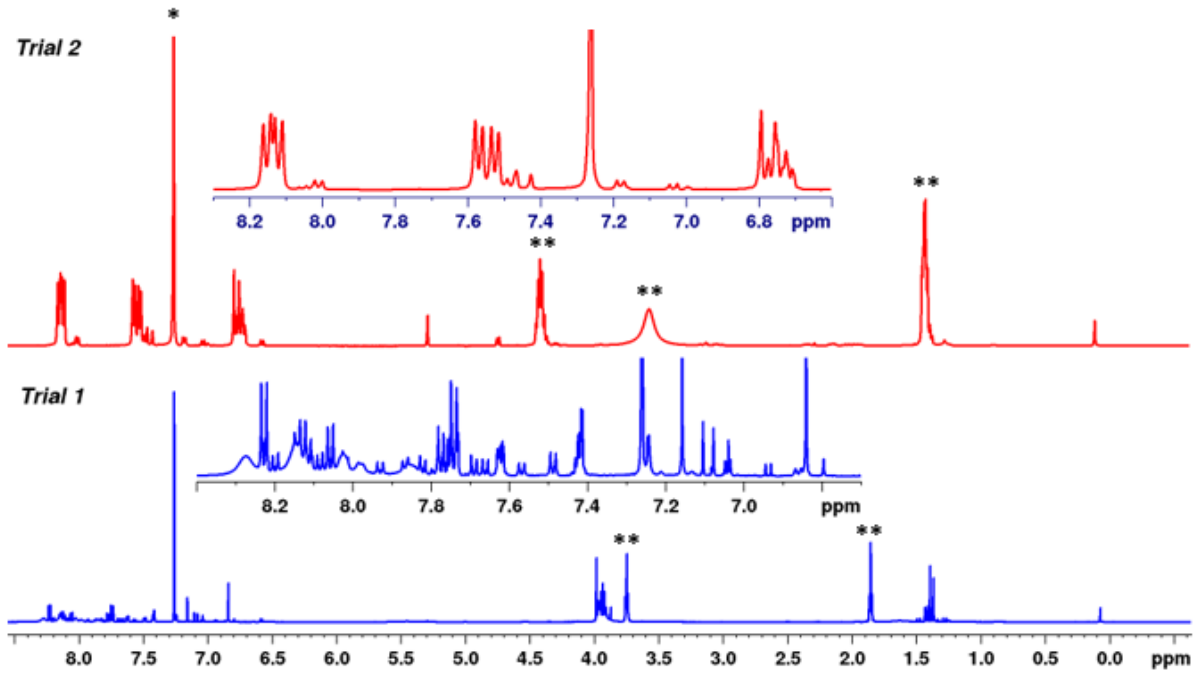

Figure 3.21. ^{1}H NMR (400 MHz, $CDCl_3$) of crude trials from synthesis of **4d** under reflux condition. * $CDCl_3$ peak, ** Residual ethanol solvent.

The reaction was reconducted at room temperature with an overnight duration. DCM extraction during workup led to a surprisingly low crude yield of 33% as black liquid. Crude analysis by ^{1}H NMR showed the presence of phenyl protons with the expected AA'BB' splitting pattern. However, the peak for the methoxy group could still not be accounted since the peak *ca.* δ 5.3 ppm integrating to 3H stems from residual DCM extraction solvent. It was also not certain as to whether the broad singlet δ 3.64 ppm was a combination of the –N**H**$_2$ from the desired product and –O**H** from the reaction solvent (**Figure 3.22**). In addition, matching integral values of extra aromatic peaks indicated the <u>probable</u> presence of a side product as a result partial reduction of the esters to alcohol groups (**Scheme 3.11**).

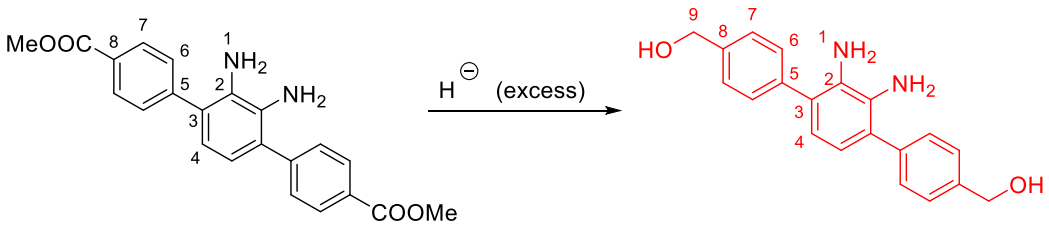

Scheme 3.11. Possible partial reduction of ester groups of 4d to alcohol groups.

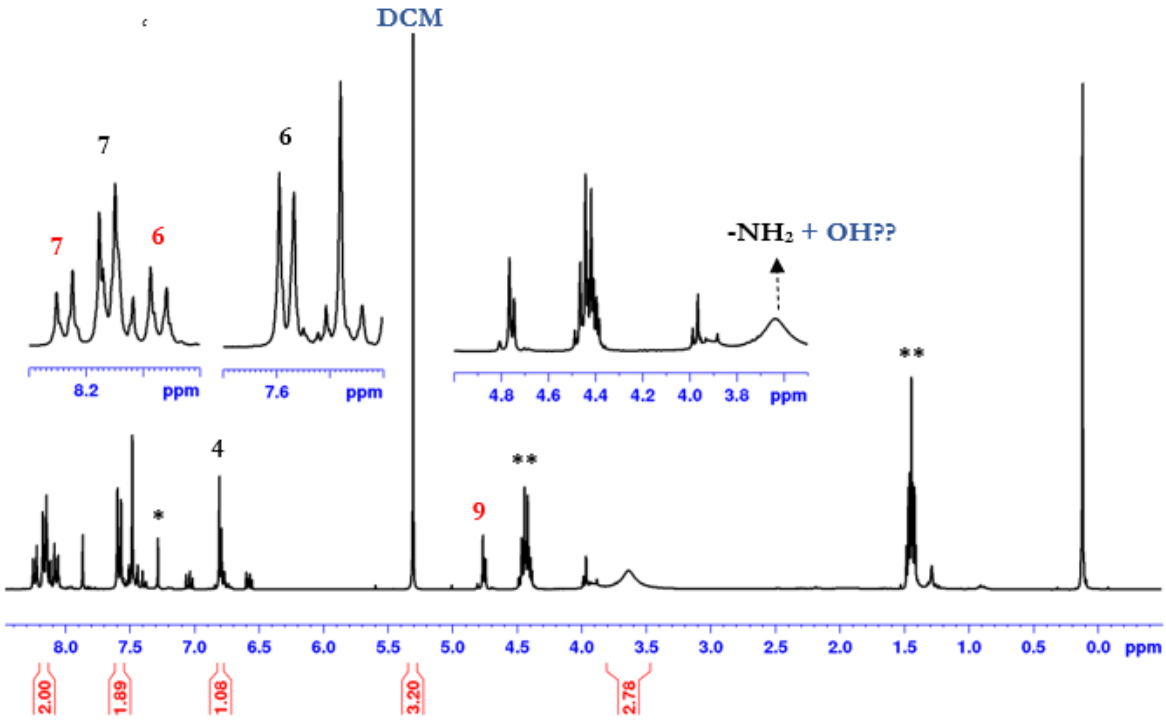

Figure 3.22. ^{1}H NMR (300 MHz, $CDCl_3$) of crude from synthesis of 4d at room temperature. Numbering is in accordance with structures in **Scheme 3.11**. Assignments were based on matching integral values and split patterns.

An alternate efficient sulfur extrusion process which does not target the ester groups was sought for. The zinc dust in acetic acid method published by Naef *et al.*[71] was adopted for ethyl benzoate groups. This involved refluxing the BTD derivative together with 16.0 equiv. of zinc powder in a 1: 1 mixture of *p*–dioxane and acetic acid (**Scheme 3.12**).

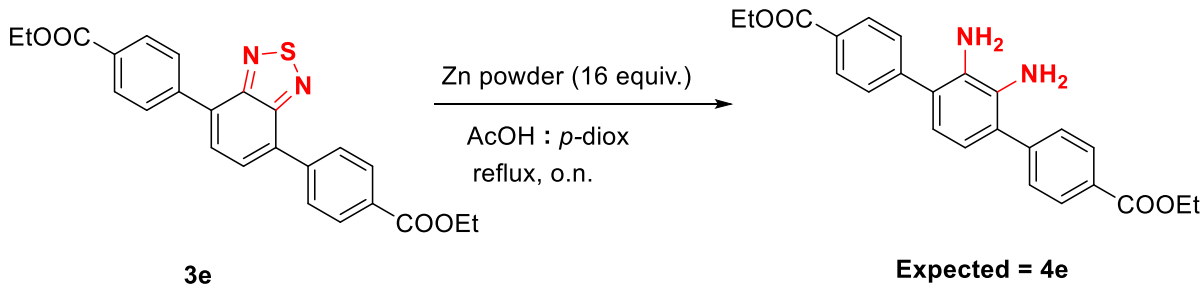

3e **Expected = 4e**

Scheme 3.12. Attempted synthesis of **4e** using Zn–AcOH method.

The solid crude analysed by ^{1}H NMR indicated the ester groups to be fortunately untargeted (**Figure 3.23**). However, the aromatic peaks corresponding to the phenyl groups showed unexpected multiplet patterns. In addition, the amino groups could not be accounted for. Hence, it cannot be inferred that the reaction was successful. Purification and further analysis by NMR was not attempted due to time constraint.

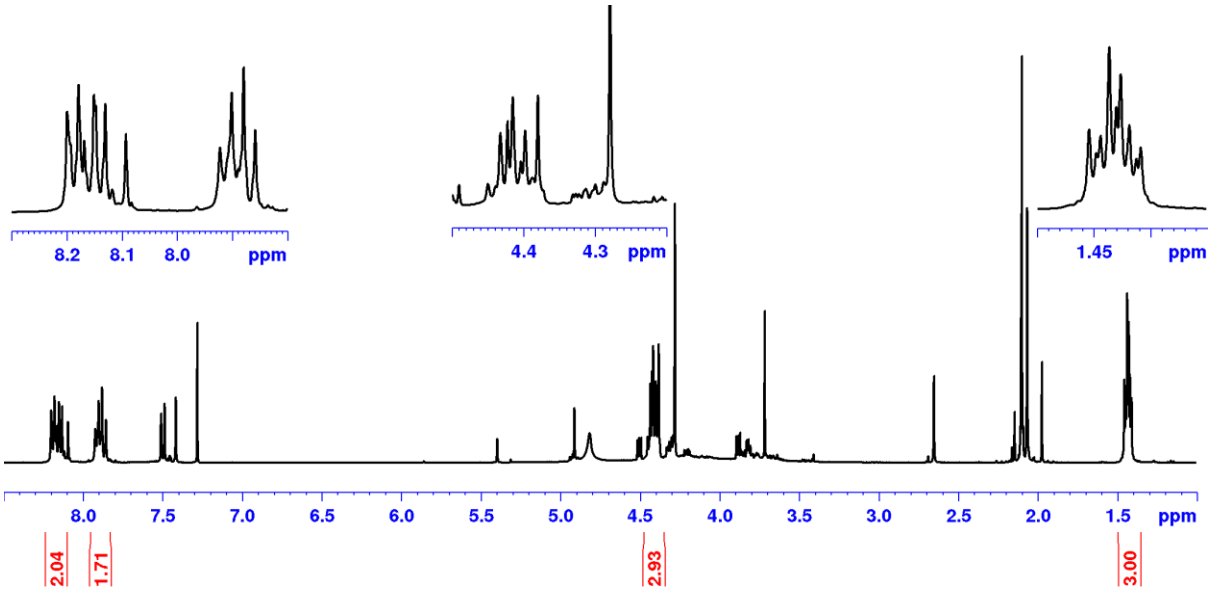

Figure 3.23. ^{1}H NMR (400 MHz, $CDCl_3$) of crude 4e synthesized according to **Scheme 3.12**.

3.7. Condensation of *o*–phenylenediamines with phenO_2(1a).

3.7.1. Synthesis, NMR studies and IR characterisation of L1 – L4.

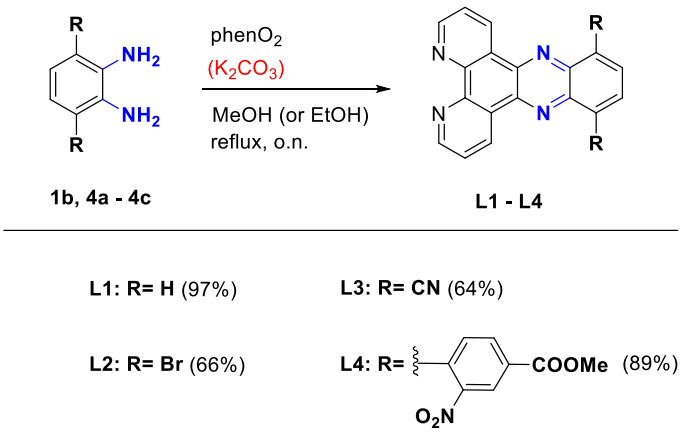

Scheme 3.13. Synthesis of **L1 – L4**.

The synthesis of **L1** to **L4** involved refluxing phenO_2 (**1a**) with the corresponding diamines in methanol (for **L1** and **L4**) and ethanol (with K_2CO_3 for **L2** and **L3**) under inert conditions (**Scheme 3.13**).[22] Synthesis of **L5** on the other hand, was attempted via Suzuki coupling on **L2** (**Scheme 3.14**).

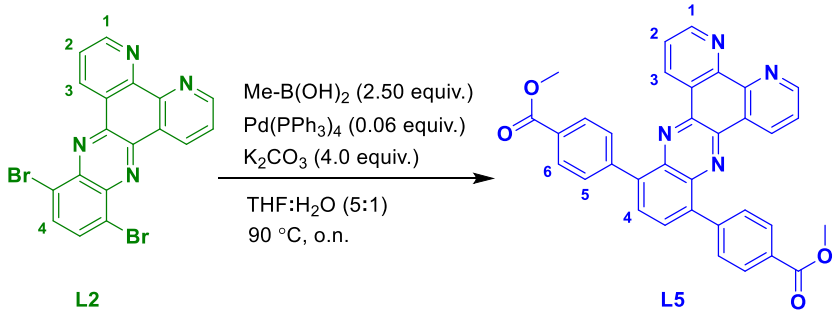

Scheme 3.14. Attempted synthesis of **L5** via Suzuki coupling on **L2**.

Although incomplete conversion (69 %) was observed from the crude, **L5** was characterized by NMR analysis on an isolated emulsion as a result of solubility issues suffered during extraction (**Figure 3.24**). As regards **L1** to **L4**, ^{1}H NMR confirmed the molecular structures with **L2** and **L3** requiring the use of strong acids (deuterated trifluoroacetic acid) to circumvent very severe solubility issues in NMR solvents. **L1** for instance, was isolated as hard off-white crystals, **L2** as a stubborn non-solvating yellow powder and **L3** as stony charcoal–like solids. The unique features present in the acquired 1D and 2D NMR spectra of phenO_2 and the diamines were similar to the corresponding dppz analogues with most peaks falling within the same range of chemical shifts.

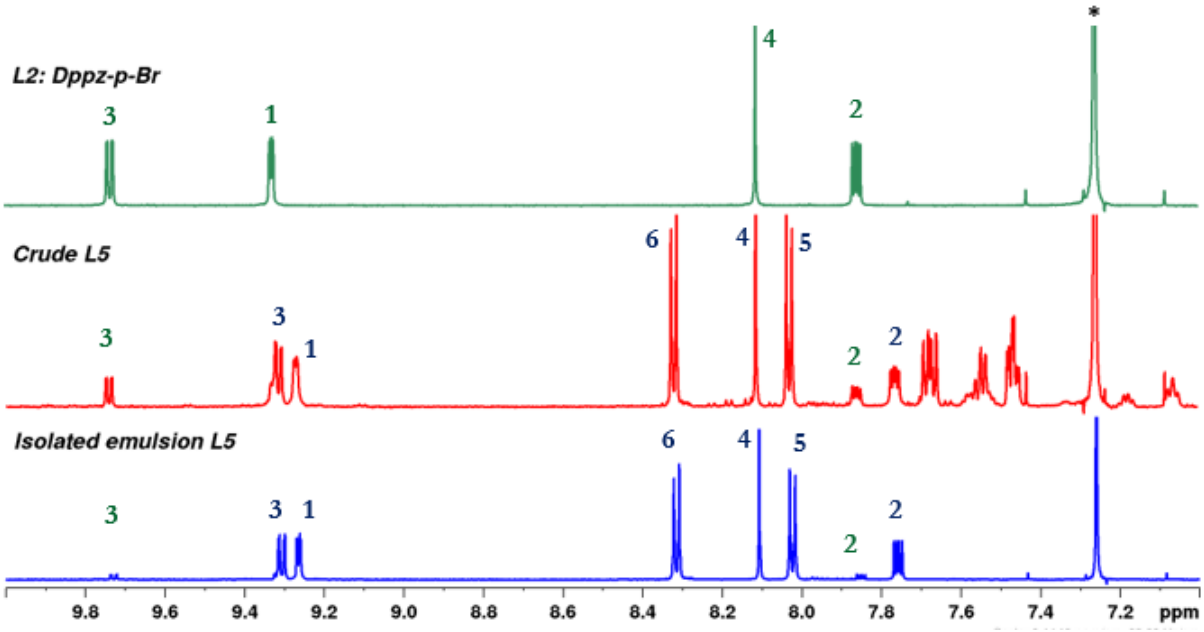

Figure 3.24. Stacked ^{1}H NMR (600 MHz, $CDCl_3$) of starting material **L2** (green), Crude results from **Scheme 3.14** (red) and desired product **L5** (blue). Numbering and colour code is in accordance with Scheme **3.14.** * $CDCl_3$ peak

Subtle differences were as a result of the slight change in chemical environments that comes with the dppz analogue formation. An example is shown in **Figure 3.25** where the distinction between protons **1** and **3** of **L1** was determined from an HSQC–HMBC overlay. Besides characterizing the various **L1** quartenary carbons, the spectrum also indicated the order of the chemical shifts for protons **1** and **3** to be contrary to the corresponding protons in $phenO_2$ (**1a**).

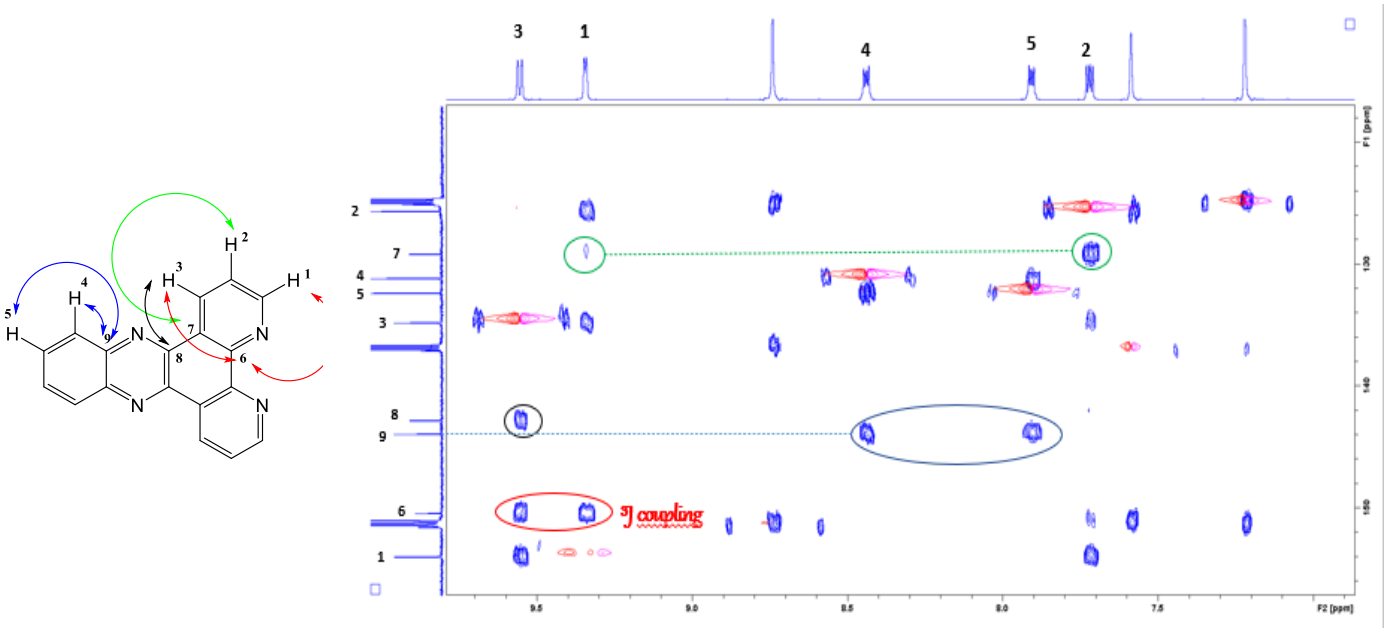

Figure 3.25. ^{1}H – ^{13}C HSQC–HMBC (600 MHz, **Py-*d*$_5$**) overlay for **L1** with the corresponding structural correlations. Colour of spectrum markers correspond with the colour of the correlation arrows.

Determination of NMR inactive nuclei within functional groups present in **L1** to **L4** was conducted by IR as done for the BTD derivatives in **Figure 3.13**. It is worth noticing the strong vibrational bands *ca.* 1722 cm^{-1} and 1525 cm^{-1} corresponding to the respective *C=O* stretching of the ester and the *N–O* stretching of nitro groups of **L4** (Dppz-p-$BzNO_2Me$ in **Figure 3.26**) which are expectedly absent in the IR spectra of **L1** (Dppz), **L2** (Dppz-p-Br) and **L3** (Dppz-p-CN in **Figure 3.26**). Cyano vibrational stretch of **L3** in the approximate range 2210 – 2252 cm^{-1} were very weak but noticeable. C–Br of **L2** stretches indicated as 545 cm^{-1}, 595 cm^{-1} and 661 cm^{-1} also showed significant difference compared with **L1, L3** and **L4**. Significant C=C stretching located in the range of 1500 – 1400 cm^{-1} and aromatic C–N stretching corresponding to strong bands of 1080 – 1150 cm^{-1} in **L1** were also present in **L2** – **L4**. In addition, broad C-H stretching *ca* 3000 cm^{-1} was also present in all four cases.

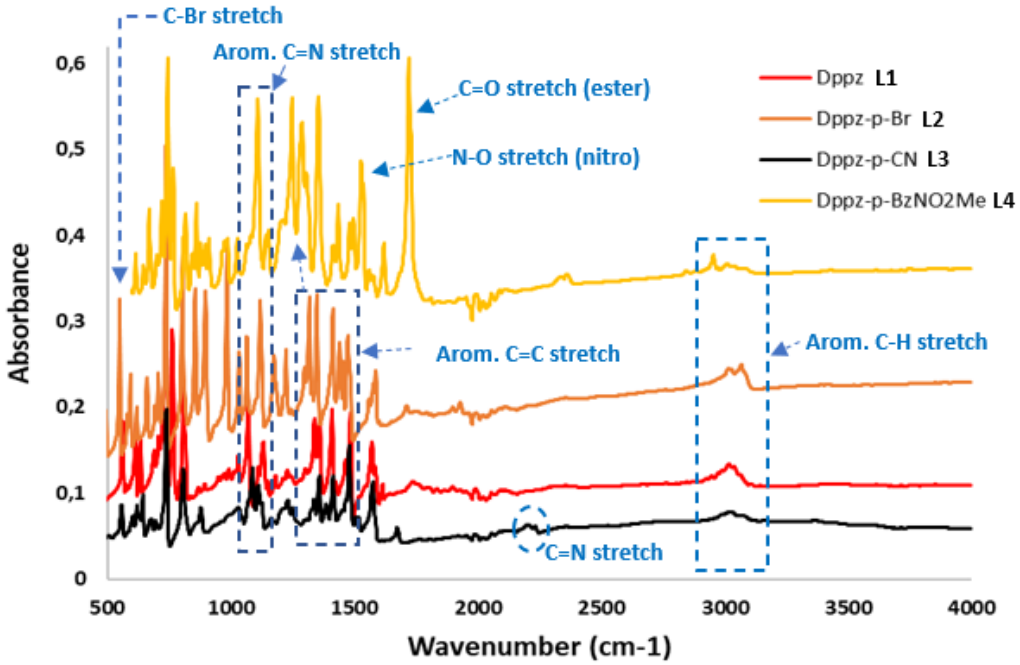

Figure 3.26. Stacked FTIR spectra of **L1** – **L4** showing the various vibrational stretches present within the synthesized ligands.

3.8. Heteroleptic [Cu^{I}(N^N)(P^P)] complexes.

3.8.1. L1 – L4 complexation with Cu^{I}, characterization and solution NMR studies

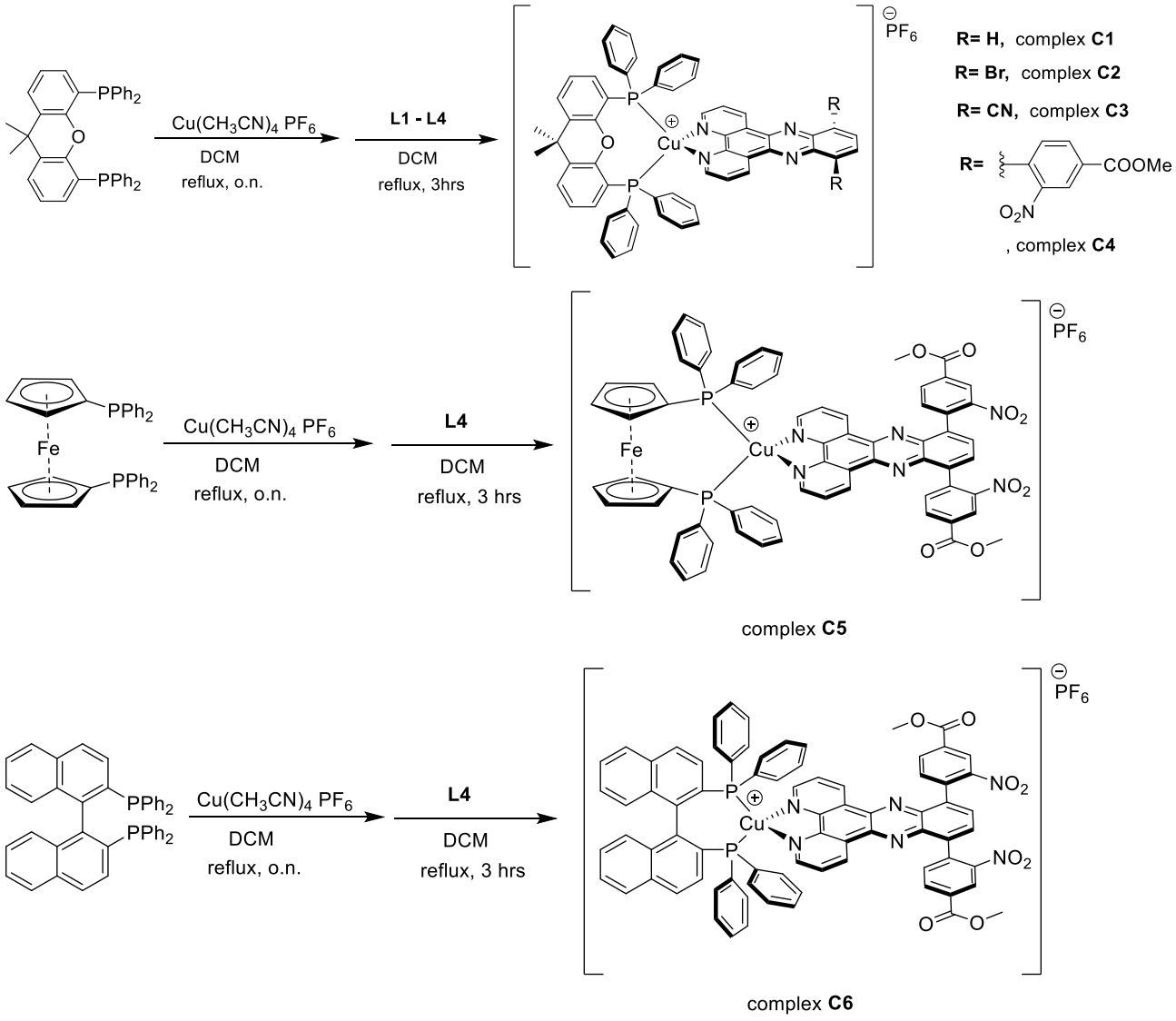

Scheme **3.15.** One-pot two-step synthesis of Copper(I) complexes **C1** – **C5**.

C1 to **C6** as can be seen from Scheme **3.15** were synthesized via a one-pot two-step procedure in distilled, argon–purged dichloromethane following the variant HETPHEN concept and using standard Schlenk–line techniques.[79] (P^P) ligands were used without prior precursor modification or purification. The bulky diphosphine in conjunction with the Cu^{I} source (tetrakis(acetonitrile)copper(I) hexafluorophosphate) were refluxed overnight. In all but one, the

solution remained colourless upon the formation of the non-isolated solvato complex $[Cu^{I}(P^{\wedge}P)(MeCN)_2]^+$ (the exception was $[Cu^{I}(dppf)(MeCN)_2]^+$ which turned red immediately upon heating). Upon addition of the complementary dppz ligand, the solution changed colour evidencing the formation of a copper complex bearing a dppz and a diphosphine ligand. The complexes showed gratifying stability upon exposure to air and water during *n*–hexane–NH_4PF_6 precipitation and workup with quantitative yields; 48% (**C1**), 90% (**C2**), 42 % (**C3**), 84% (**C4**), 85% (**C5**), 83% (**C6**).

ESI–HRMS with matching isotopic patterns confirmed the composition of the complexes. For each compound, the base peak in the positive ESI–LRMS corresponded to the $[M - PF_6]^+$ ion with **C1** m/z= 923 Da, **C2** m/z = 1079 Da, **C3** m/z= 973 Da, **C4** m/z = 1281 Da, **C5** m/z= 1257 Da and **C6** m/z= 1325 Da. Amongst the xantphos-based complexes (C1 – C4), the other significant peak arose from $[Cu(P^{\wedge}P)]^+$ ion with observed m/z = 641 Da (**Figure 3.27**).

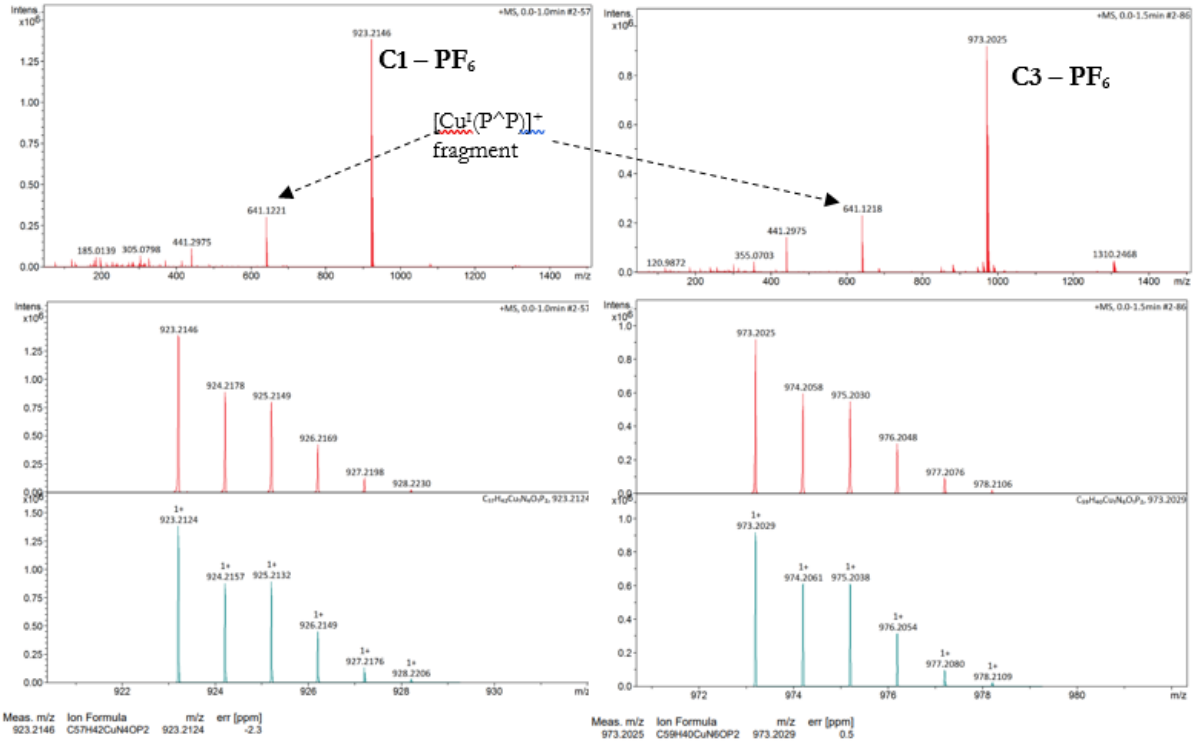

Figure 3.27. Positive mode LR-ESI MS (top) of complex **C1** (left) and complex **C3** (right) with the corresponding HR-ESI MS (bottom) of complex **C1** (left) and complex **C3** (right). The presence of $[Cu^{I}(P^{\wedge}P)]^+$ fragment is highlighted in both **C1** and **C3**. This extends to all xantphos-based complexes (**C1** to **C4**).

The $[PF_6]^-$ counteranions of **C1** to **C6** were confirmed by a similar characteristic septet in an H_3PO_4 referenced (δ 0.00 ppm) $^{31}P\{^1H\}$ NMR spectrum with δ -145.5 ppm and a large $^1J_{PF}$ coupling of 706 Hz. Interestingly, the weak broad singlet at *ca.* δ -13.53 ppm in the $^{31}P\{^1H\}$

NMR spectrum of **C1** in CD_3CN assigned to the phosphorus atoms of the xantphos ligand does not change significantly in comparison to **C2** (δ -13.14 ppm), **C3** (δ -13.33 ppm), and **C4 (**δ -13.27 ppm) (**Figure 3.28**). This implies that the structure around the Cu^I centre and the coordination of the xantphos ligand is unaffected by the variation of the 10, 13– substituents on the dppz ligand. The quadrupolar(Cu)-dipolar(P) bond explains the broadening of the singlet

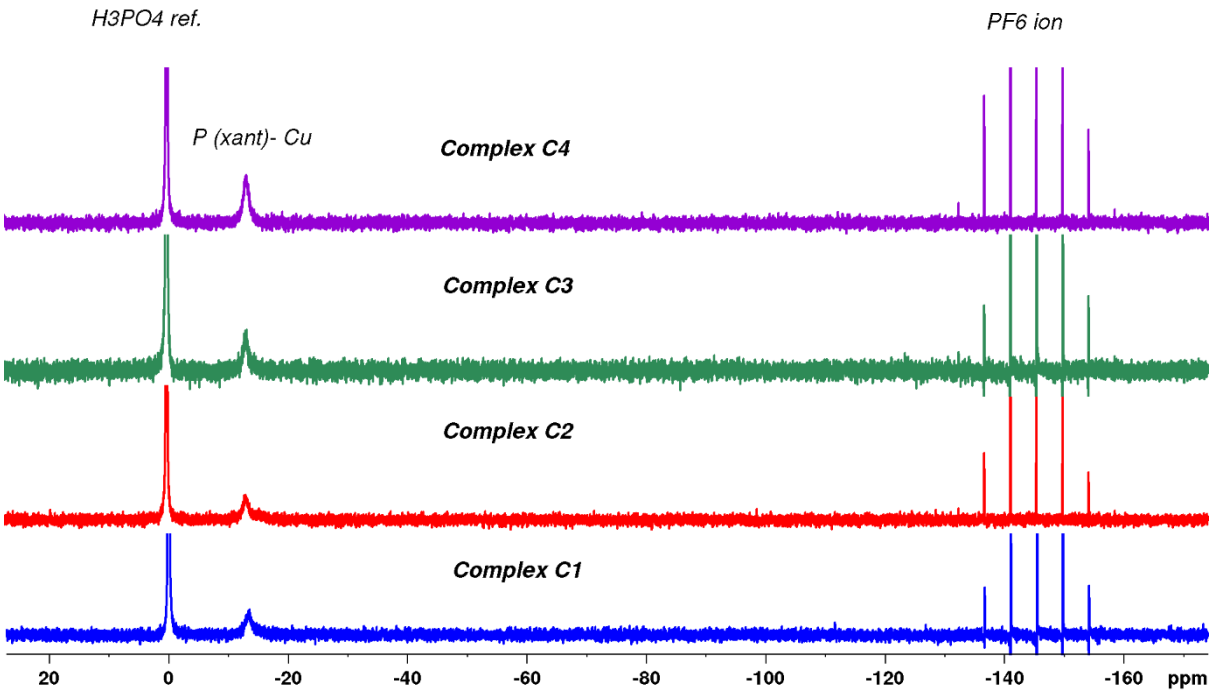

Figure 3.28. Stacked $^{31}P\{1H\}$ NMR (400 MHz, CD_3CN, ref: H_3PO_4= 0.00 ppm) of xantphos-based Copper complexes (**C1 – C4**).

There was an obvious change in the shift of the phosphorus upon varying the backbone of the (P^P) ligand with the phosphorus atoms of complex **C5** showing a shift of -10.04 ppm (**Figure 3.29**). The expected broad singlet for the complex **C6** was only identified by ^{31}P HMBC since it was almost overlapped by the reference H_3PO_4 peak (**Figure 3.30**). It showed two $^3J_{PH}$ correlation and one $^4J_{PH}$ correlation to protons of shifts *ca.* 6.6 ppm (integral 2H), 6.8 ppm (1H) and 7.4 ppm (3H) respectively. Hence, the final chemical shift value of the singlet for **C6** phosphorus atoms were determined to be in the range *ca.* + 0.91 – 1.20 ppm. It should be noted that the entire structure demonstrated a C_{2v} symmetry despite its atropisomeric nature which implies that the protons of the two phenyl groups on $\mathbf{P^1}$ have similar chemical environment as the phenyl protons on $\mathbf{P^2}$ (**Figure 3.30**).

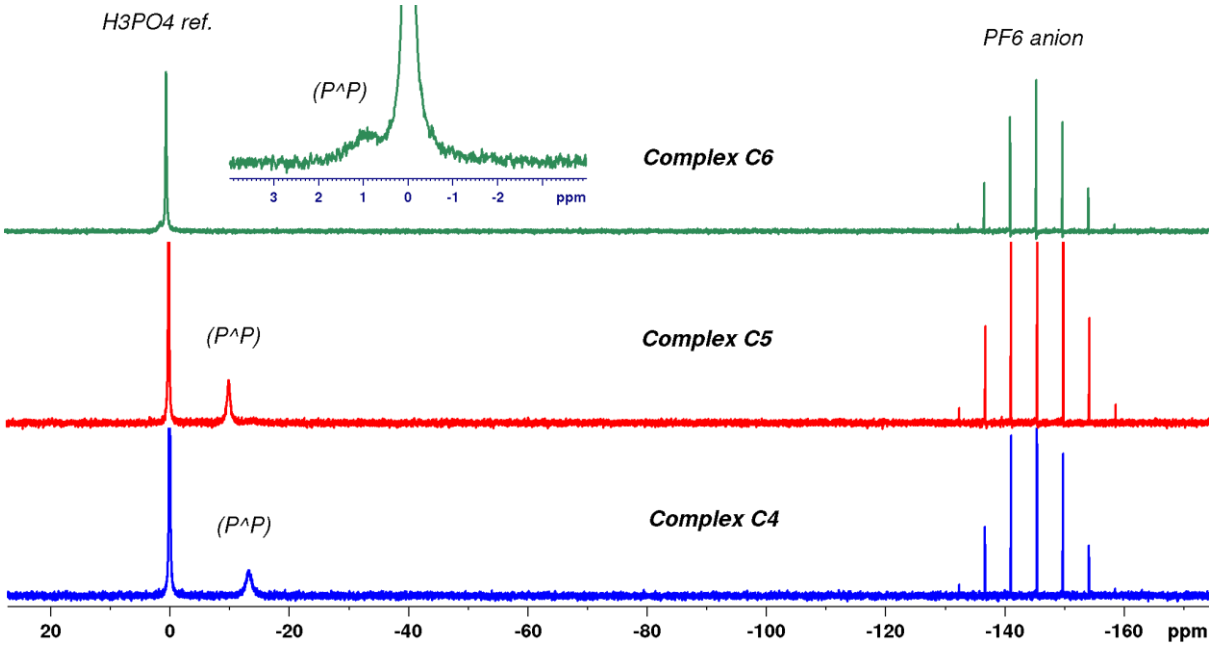

Figure 3.29. Stacked $^{31}P\{1H\}$ NMR (400 MHz, CD_3CN, ref: H_3PO_4= 0.00 ppm) of xantphos-based Copper complexes (**C4 – C6**) showing the differences in chemical shifts for the corresponding diphosphine groups.

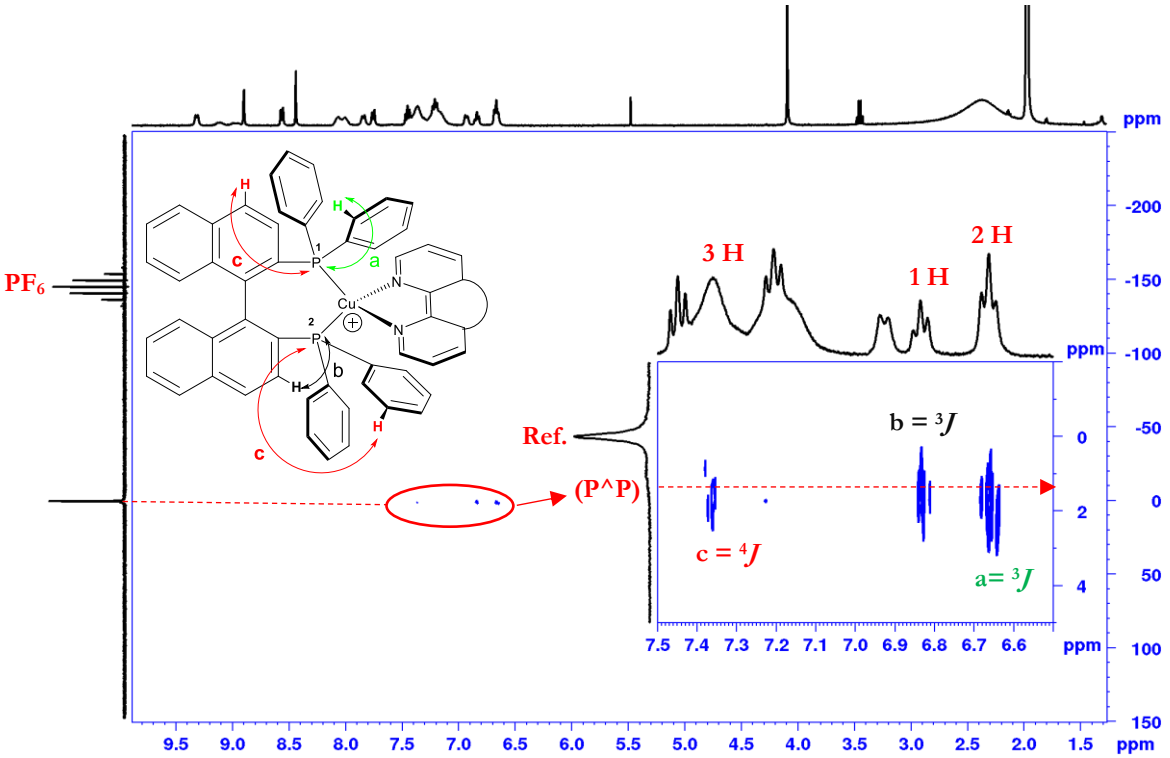

Figure 3.30. ^{1}H - $^{31}P\{^{1}H\}$ HMBC NMR (400 MHz, CD_3CN, ref: H_3PO_4= 0.00 ppm) of complex **C6** revealing the chemical shift for the diphosphine groups. **n-H** stands for the peak integrals. Colour of spectrum markeers (a, b and c) corresponds with colour of correlation arrows.

A series of DOSY NMR experiments conducted on complexes **C1** to **C6** using non-degassed MeCN-d_3, evidenced the unambiguous formation of pure heteroleptic Cu^{I} species with an average diffusion coefficient (D) of *ca.* **2.0 ± 0.5 ×10^{-9} m^{2}s^{-1}** (**C1** = [1.64 – 1.67]×10^{-9} m^{2}s^{-1}, **C2 =** [1.75 – 1.87]×10^{-9} m^{2}s^{-1}, **C3** = [2.04 – 2.08]×10^{-9} m^{2}s^{-1}, **C4** = [1.75 – 1.79]×10^{-9} m^{2}s^{-1}, **C5** = [1.58 – 1.91]×10^{-9} m^{2}s^{-1}, **C6** = [1.67 – 1.70]×10^{-9} m^{2}s^{-1}). Analyzing the coefficients using the SEGWE (Stokes-Einstein-Gierer-Wirtz Estimation) method resulted in inaccurate output of calculated molecular weights due to the fact that the model was only applicable to small molecules with molecular weight < 1000 gmol^{-1}. For instance, H_2O (**H**OD δ 2.16 ppm with D= 6.77×10^{-9} m^{2}s^{-1}) under the acquisition conditions yielded an estimated molecular weight of 18.51 gmol^{-1}. Complex **C4** (with m/z =1281 Da) on the other hand, yielded an output of 233.34 gmol^{-1}. Fortunately, the various DOSY spectra of **C1** to **C6** also highlighted the absence of a dissociative speciation reaction (**Equation 11**) leading to the formation of undesired homoleptic species (**Figure 3.31**).

$$2CuL'L \rightarrow CuL'L' + CuLL \qquad (11)$$

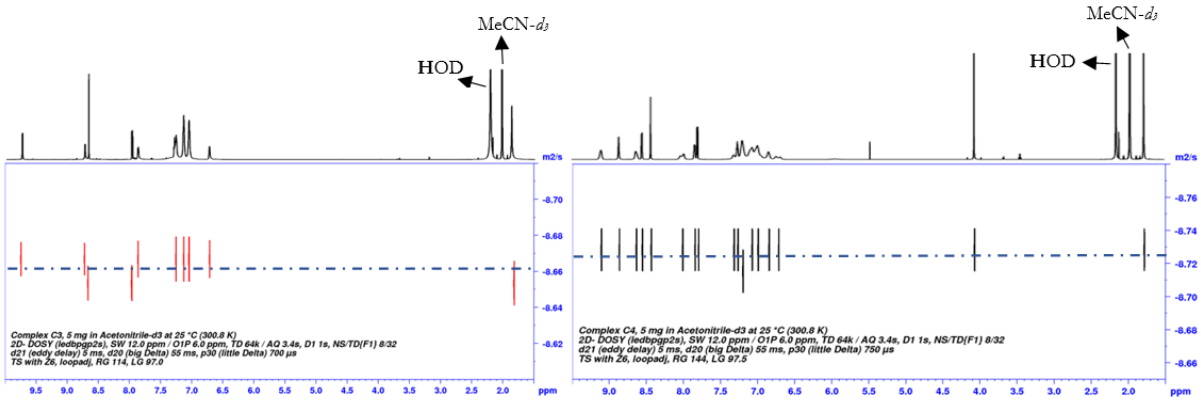

Figure 3.31. Zoomed-in DOSY NMR (800 MHz, CD_3CN) of complex **C3 (left)** and **C4 (right)** at 300.8 K. Dashed blue line through the cross peaks indicates that all the peaks originate from their respective complexes. The same phenomenon occurs for all the other complexes.

Besides the integral values of the aromatic protons of (P^P) ligand matching the dppz protons, the *AA'BB'* split pattern present in complex **C1** (peak 22–**H** with shift 8.13 ppm and 23–**H** with shift 8.47 ppm) as elucidated for the benzothiadiazole groups (**Section 3.2**), resolves into singlets in **C2** and **C3** (peak 23–**H** δ 8.32 ppm and 8.66 ppm respectively) due to the presence of the bromo and cyano groups (**Figure 3.32**).

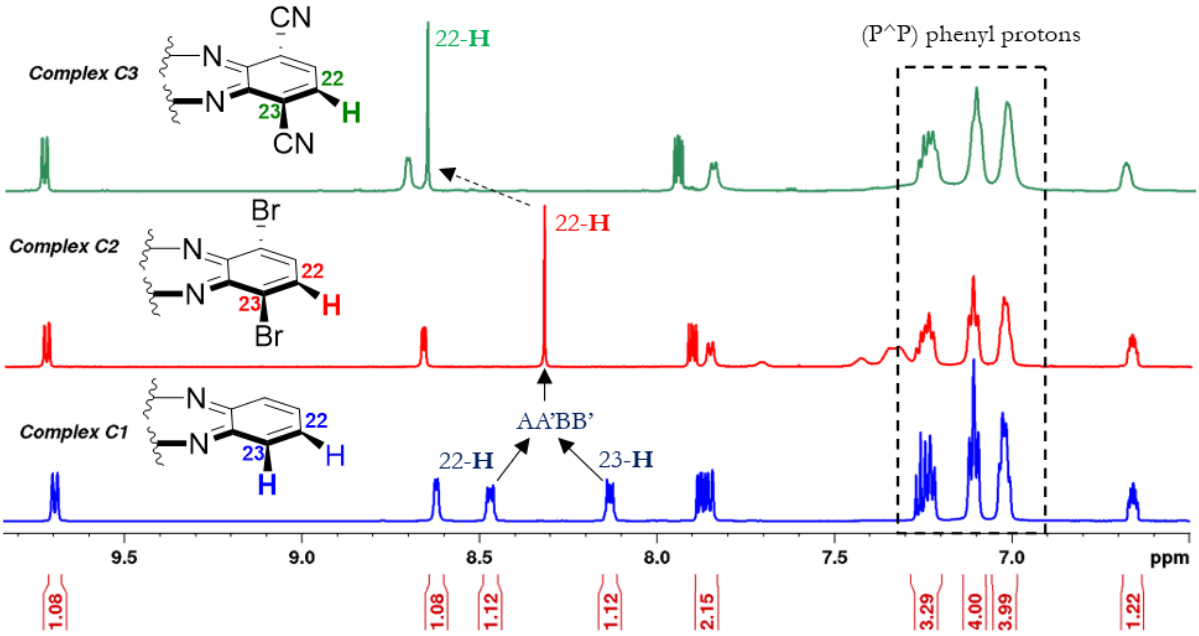

Figure 3.32. Aromatic region of stacked ^{1}H NMR (600 MHz, CD_3CN) of complex **C1** to **C3** showing the resolution of the AA'BB' peaks into singlets including the presence of the diphosphine groups.

The electron-rich cyclopentadienyl protons 1–**H** and 2–**H** of **C5** appear in an upfield region with δ 4.43 ppm and 4.57 ppm respectively (**Figure 3.33**). The distinction between 1–**H** and 2–**H** was based on correlations observed in the acquired ^{31}P{^{1}H} HMBC spectrum which indicated a $^{3}J_{P-H}$ cross peak for 2–**H** with no correlation for 1–**H (Figure 3.34)**. Long–range spin–spin couplings as large as a $^{6}J_{P-H}$ constants between 11–**H** and the phosphorus atom were also observed in addition to $^{4}J_{P-H}$ and $^{5}J_{P-H}$ for 9–**H** and 10–**H** respectively. Such inter–ligand coupling effect proves the presence of a diamagnetic Cu^{I} centre. The mechanism for the large couplings for complex **C5** specifically is unknown. However, published reports pertaining to long-range phosphorus–hydrogen constants $^{n}J_{P-H}$ (n = 3 – 7) in organophosphorus compounds have suggested a hybridization and angle-dependent mechanism as an explanation. Applying this model to complex **C5** means that there exists a connection between the $^{n}J_{P-H}$ constant to the angle between the N–Cu^{I}–P bonds and the plane of the π–electronic system directly attached to the phosphorus, with *n* of $^{n}J_{P-H}$ reducing to a minimum at angle 0 °.[80, 81] Hence, such large couplings though not certain, might be evidence of a possible tetrahedral geometry around the copper centre.

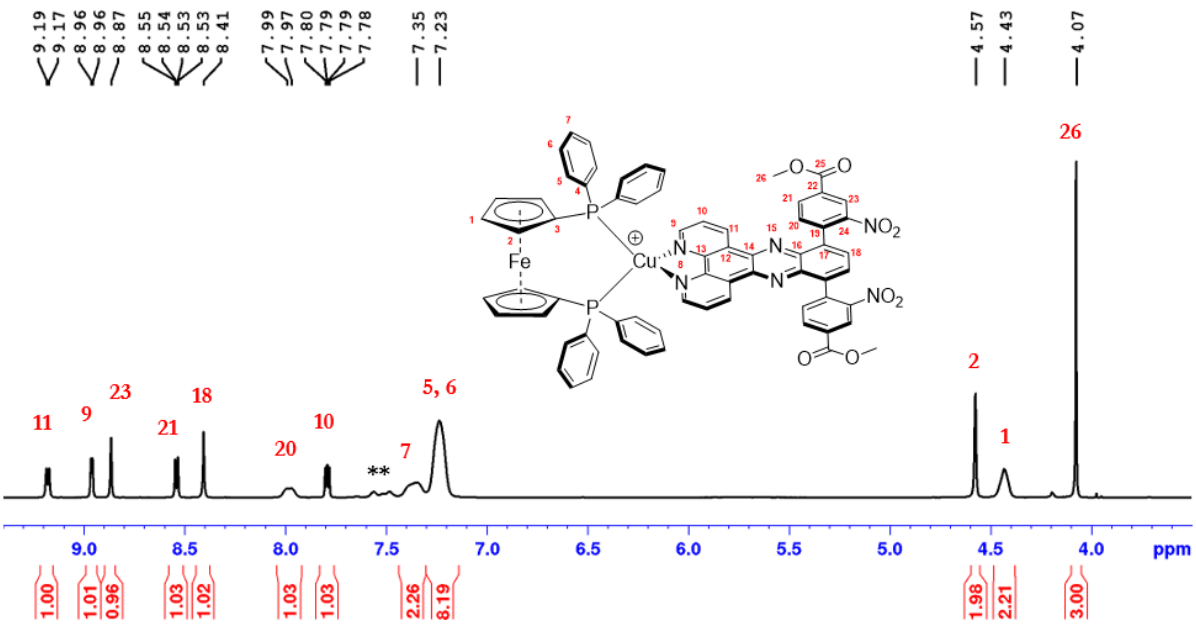

Figure 3.33. ^{1}H NMR (600 MHz, CD_3CN) of complex **C5** with various proton assignments based on acquired HSQC and HMBC spectra. **** unknown.

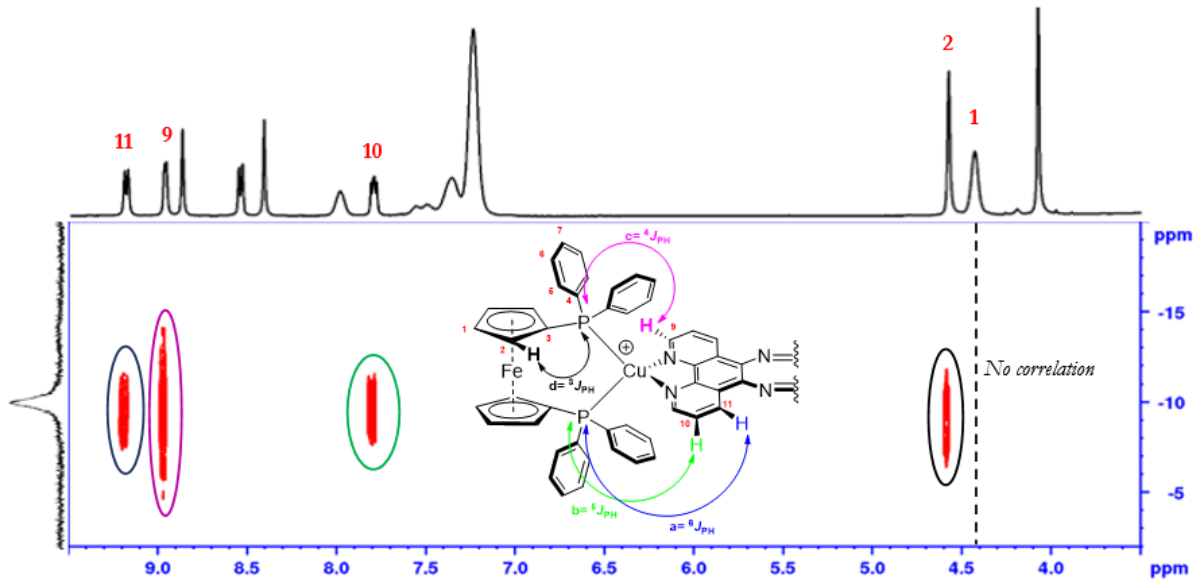

Figure 3.34. ^{1}H – ^{31}P{^{1}H} HMBC (600 MHz, CD_3CN) of complex **C5** with with an embedded structure of the various correlations of protons to the phosphorus atoms. Numbering of structure is based on **Figure 3.33**.

With a high number of acquisition scans for the ^{31}P{^{1}H} HMBC, this large P–H coupling effect was not only limited to complex **C5** but was also observed in complex **C2** with protons 5–**H** (δ 6.68 ppm, $^{4}J_{P-H}$= **β**), 10–**H** (δ 7.02 ppm, $^{3}J_{P-H}$ = **α**), 11–**H** (δ 7.11 ppm, $^{4}J_{P-H}$= **ε**) and 12–**H** (δ 7.28 ppm, $^{5}J_{P-H}$= **δ**) revealing intra-ligand correlations and 14–**H** (δ 8.66 ppm, $^{4}J_{P-H}$= **ϕ**) and 16–**H** (δ 9.72 ppm, $^{6}J_{P-H}$= **χ**) showing inter–ligand correlations with the phosphorus atoms (Figure

3.35). 12–**H** was assigned amongst (12 + 6) since it befits a weaker correlation with a relatively larger $^{n}J_{P-H}$ coupling.

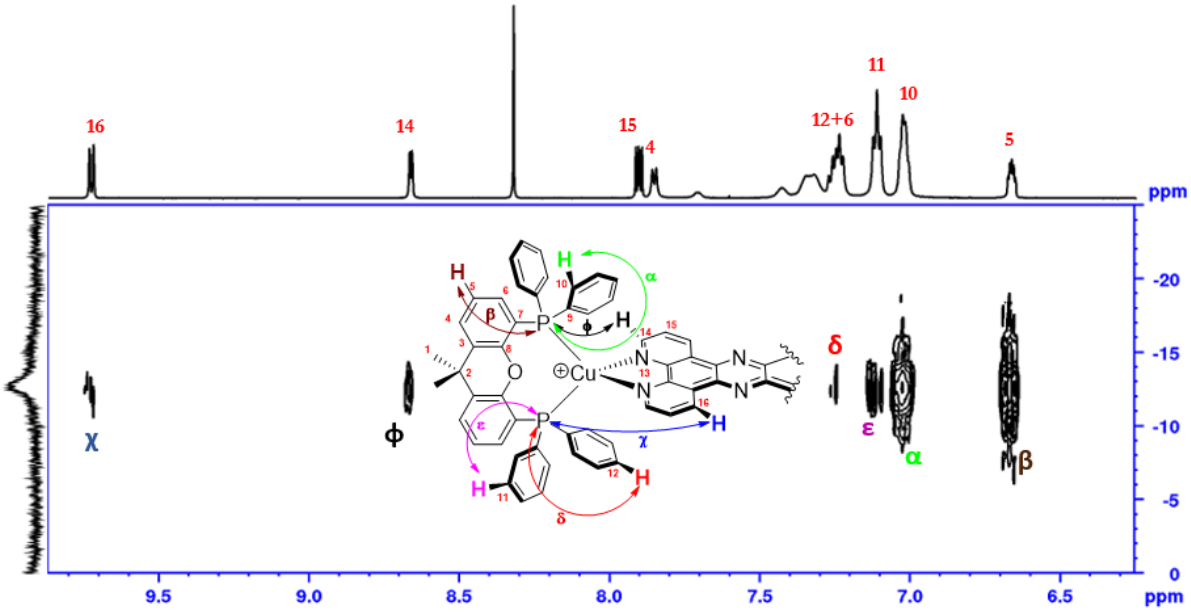

Figure 3.35. Aromatic region of ^{1}H - $^{31}P\{^{1}H\}$ HMBC (600 MHz, CD_3CN) of complex **C2** with an embedded structure of the various correlations of protons to the phosphorus atoms.

Besides the phosphorus-hydrogen coupling in complex **C5**, the presence of a Cu^{I}-center was further confirmed by correlations within an acquired phase–sensitive ROESY spectrum (**Figure 3.36**). A through-space (TS) ROE coupling between 5–**H** + 6–**H** (δ 7.23 ppm) of the diphosphine and 9–**H** (δ 8.96 ppm) of the dppz ligand means that the two target rings have to be in proximity to establish such correlation (green circle in **Figure 3.36**). This implies a possible π–π stacking interactions which might cause the [Cu(P^P)]- moiety to slightly deviate from the phenazine axis (**Scheme 3.16**). It should be noted that this observation was not limited to **C5** alone but was present in all the complexes (**C1** to **C6**). In addition to the stacking effect, an insight into the 3D orientation of the terphenyl ring is revealed by a ROE coupling between 18–**H** and 20–**H** (blue circle in **Figure 3.36**)**.** The two 10, 13–phenyl substituents conform into an almost perpendicular orientation to the flat dppz plane for the two protons to be in proximity to establish the coupling effect without steric interference from the nitro groups with the phenazine ring **(Scheme 3.17)**.

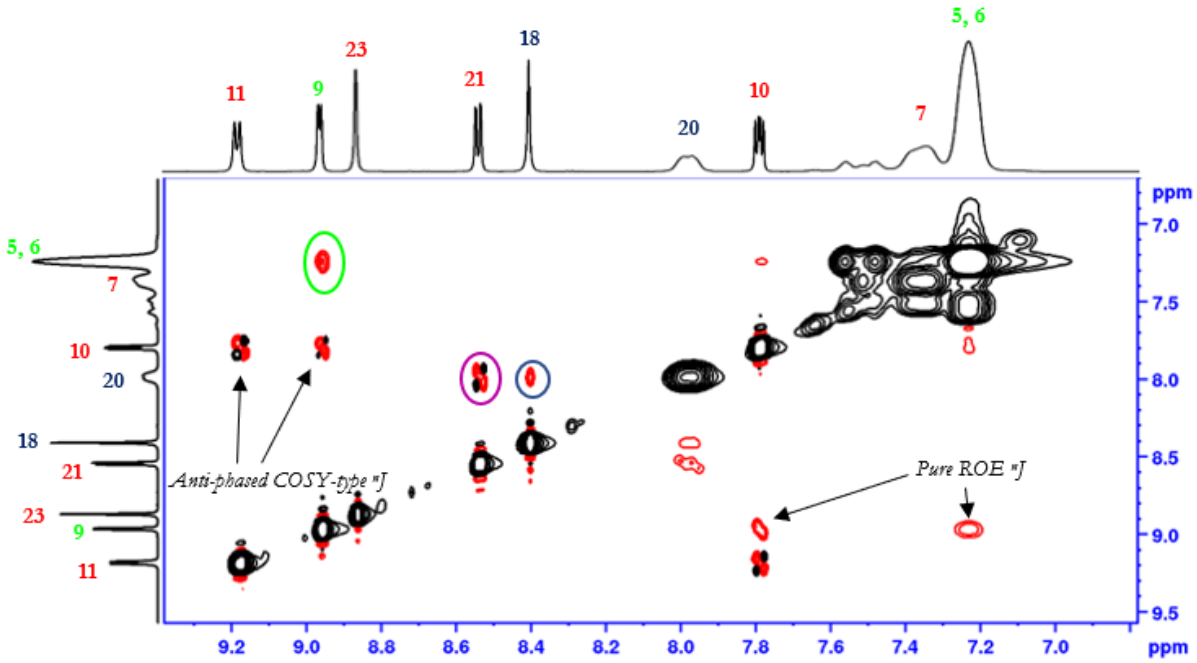

Figure 3.36. Aromatic region of ROESY (600 MHz, CD_3CN) of complex **C5** with an embedded structure of the various correlations of protons to the phosphorus atoms. Numbering is in accordance with structure in **Figure 3.33**.

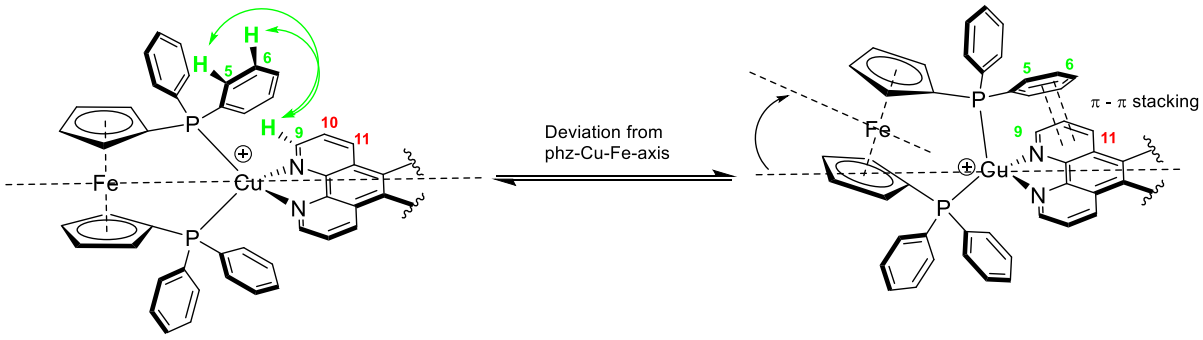

Scheme 3.16. Conformational change in complex **C5**: Deviation from the phenazine axis caused by the necessity for proximity of the rings to establish a strong ROE coupling (5-**H**+6-**H** and 9-**H**) encircled in green in **Figure 3.36**.

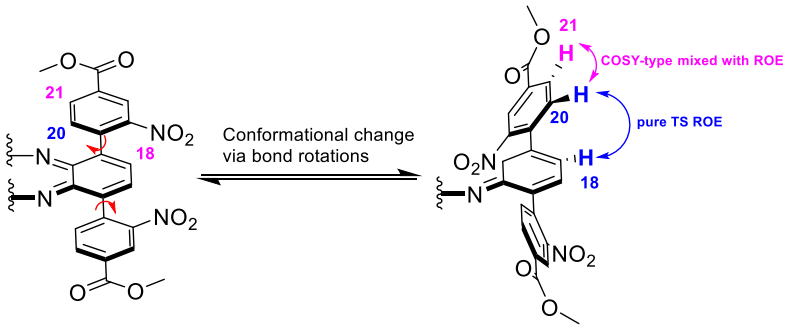

Scheme 3.17. Possible conformational change of the terphenyl ring indicated by a ROE coupling between 18-**H** and 20-**H** of complex **C5** (Encircled in blue in **Figure 3.36**).

The terphenyl conformational changes shown in **Scheme 3.17** is not limited to **C5** but occurs in all complexes with the same aromatic moiety (i.e., **C4** – **C6**). From a phase–sensitive NOESY spectrum of **C6** for instance, is there evidence of NOE coupling effects between 27–**H**, 25–**H** and 28–**H** (pink markers in **Figure 3.38** with assignment reference from **Figure 3.37**). Moreover, other dynamic processes highlighted include the atropisomerization of the coordinated BINAP ligand with the two naphthyl environments corresponding to one facing the dppz ligand and the other away (**Scheme 3.18**). EXSY peaks amongst protons from the naphthyl environment close to the diagonal is indication for exchange between the two chemically non-equivalent environment (green markers in **Figure 3.38**). However, this process coupled with other solution dynamics (such as rotation of C_{phenyl}–P bond) are too fast on the NMR timescale to lead to distinct resonances. Hence, the resonances are revealed as broad overlapped peaks making specific assignments to the phenyl environment and naphthyl backbone complicated.

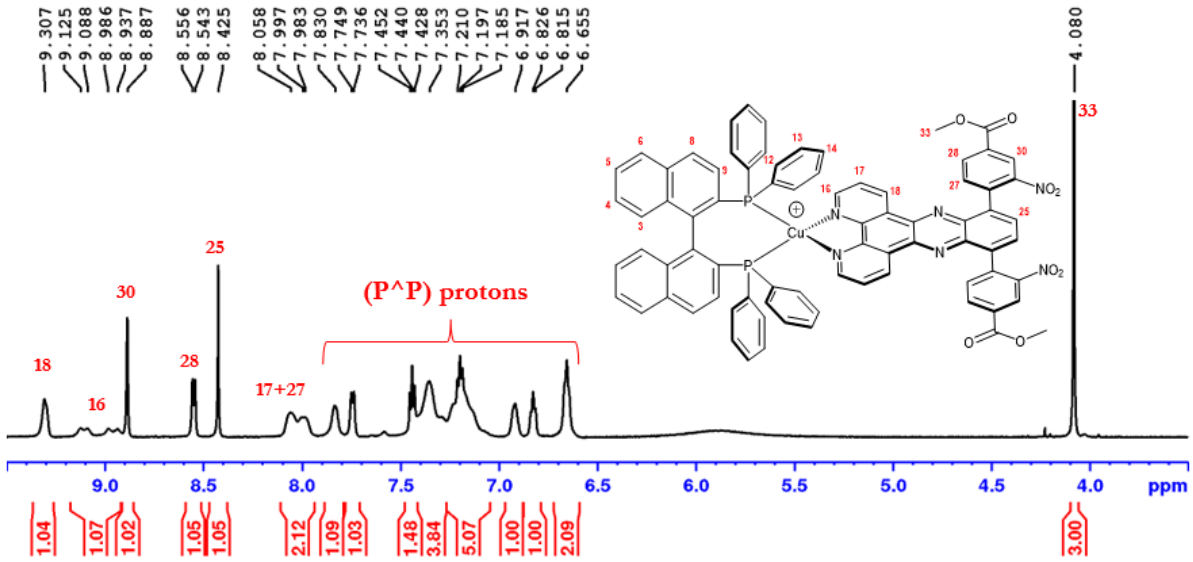

Figure 3.37. ^{1}H NMR (600 MHz, CD_3CN) of complex **C6** with various proton assignments based on acquired HSQC and HMBC spectra.

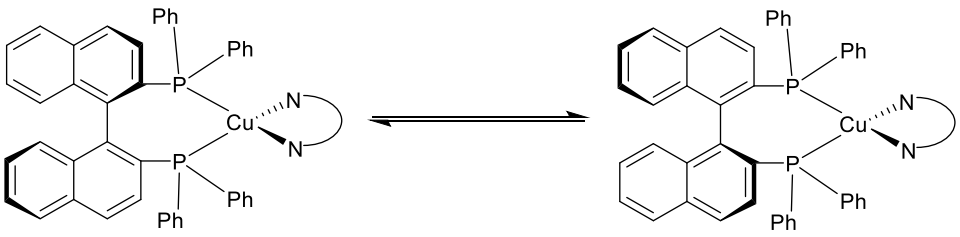

Scheme 3.18. Atropisomerization of coordinated (P^P) ligand as a dynamic process in complex **C6.**

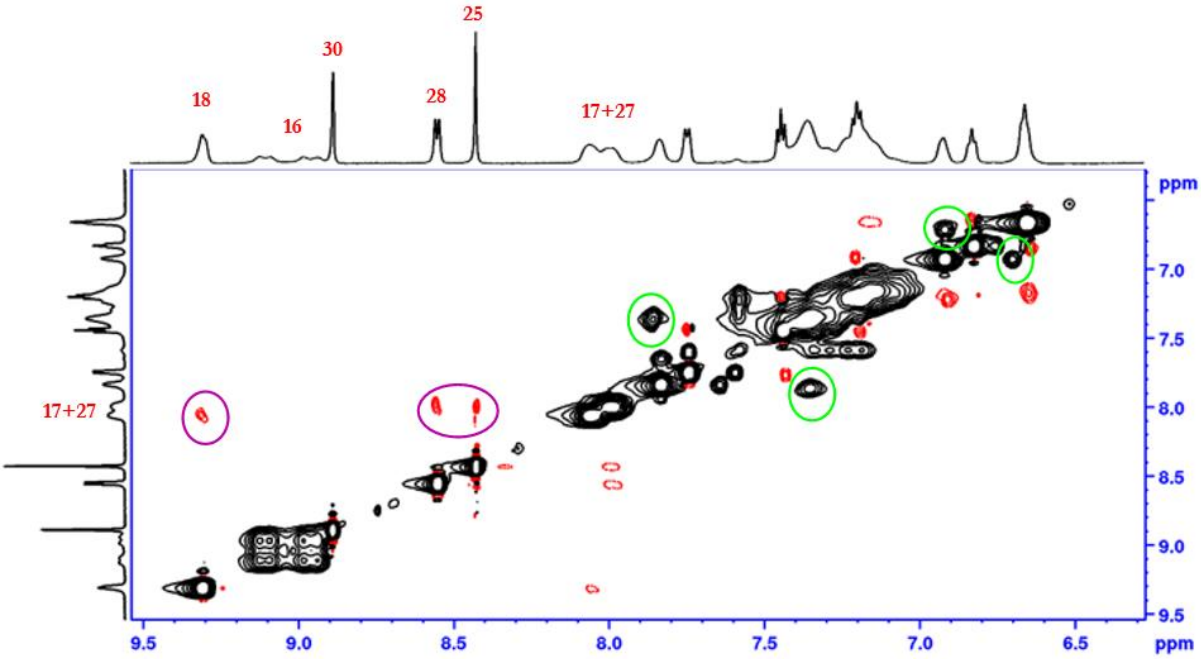

Figure 3.38. Aromatic region of phase-sensitive NOESY (600 MHz, CD_3CN) of complex **C6**. Green circles indicate EXSY peaks which highlights the dynamic process of the diphosphine ligand (**Scheme 3.18**). Pink circles indicate NOE correlations which highlights the terphenyl conformational changes similar to **Scheme 3.17**.

In addition to the terphenyl orientations (pink circles in **Figure 3.40**) of complex **C4**, there was also NOE coupling (green circle) between 4–**H** (xanthene arene proton δ 7.83 ppm) and 1–**H** (δ 1.77 ppm; singlet from xanthene CMe_2 group). Published reports on the NMR dynamics of this CMe_2 group within desymmetrized xantphos-bipyridine coordinated Cu^I-complexes suggested the C_2 symmetry of these complexes are attributed to inversions of the xanthene backbone, making the methyl groups appear as one unit on an NMR timescale (**Scheme 3.19**).[82] The absence of EXSY peaks stemming from two distinct methyl resonances and the presence of a NOE coupling effect in **Figure 3.40** proves this dynamic behaviour. The methyl groups are able orient themselves in greater proximity to 4–**H** to establish such a strong NOE effect. If the oxygen unit and the quartenary carbon were in the same plane, 1–**H** will point away from 4–**H** causing the coupling effect to not appear (**Scheme 3.20**).

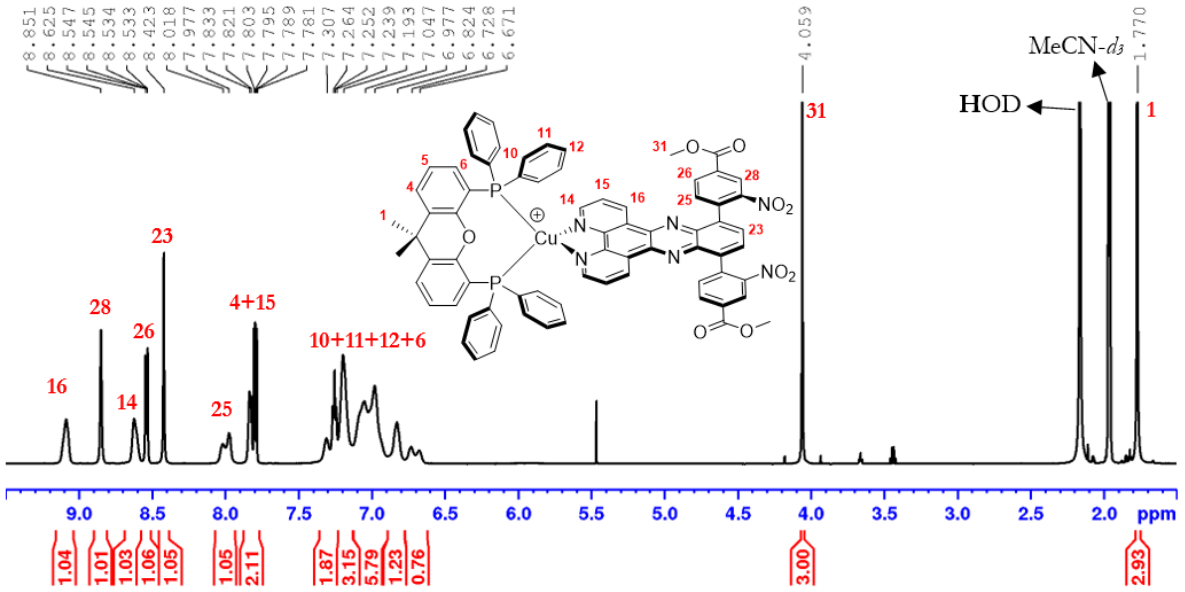

Figure 3.39. ^{1}H NMR (600 MHz, CD_3CN) of complex **C4** with various proton assignments based on correlations from acquired HSQC and HMBC spectra.

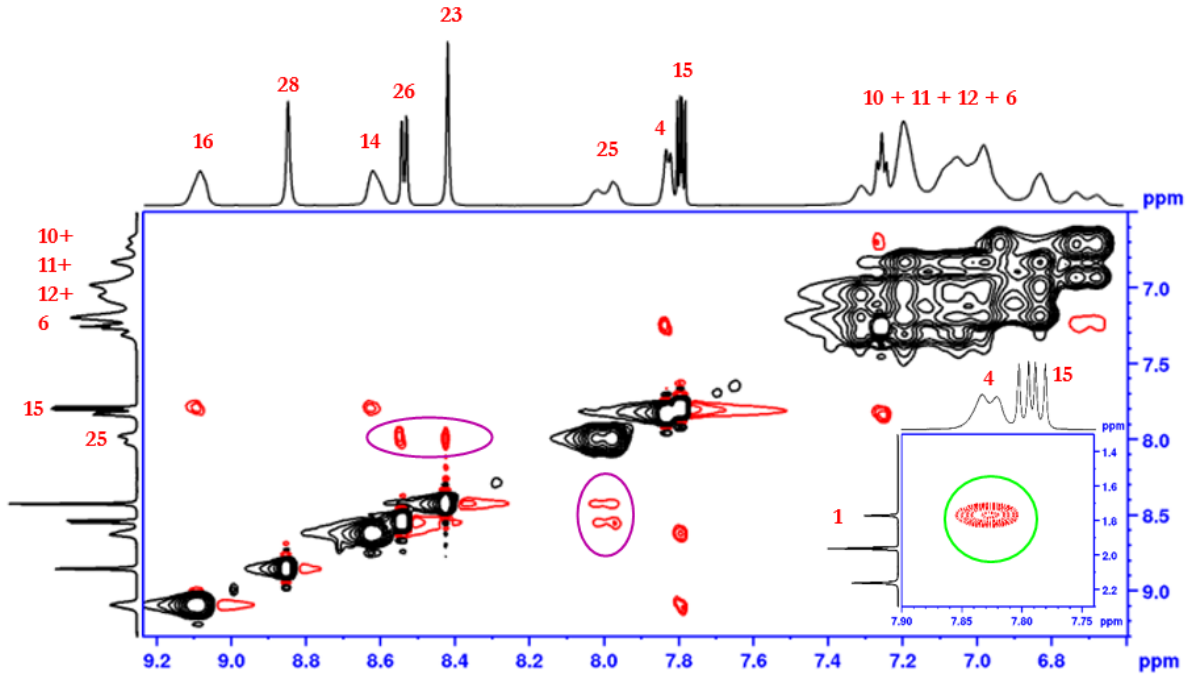

Figure 3.40. Aromatic region of phase-sensitive NOESY (600 MHz, CD_3CN) of complex **C4** with an embedded zoom-in of aliphatic region in the bottom right of spectrum. Pink circles indicate the terphenyl conformational changes similar to **Scheme 3.17**. Green indicates 1-**H** to 4-**H** correlation. Numbering in accordance with **Figure 3.39**.

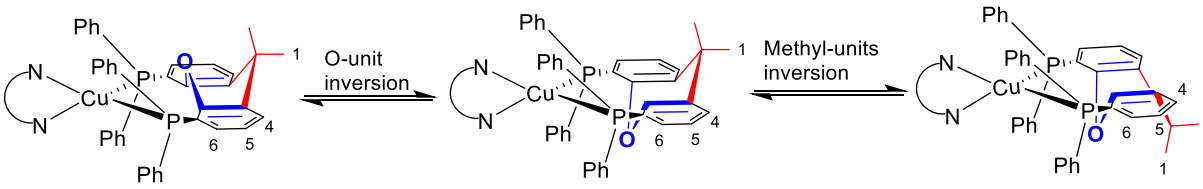

Scheme 3.19. Dynamic process in xantphos-based complexes **C1 – C4**: Inversions of the xanthene backbone into boat-like conformations causes the methyl groups to appear as one unit and renders C_2 symmetry on complex.

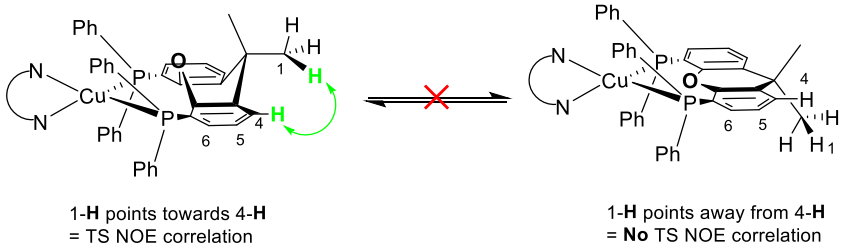

Scheme 3.20. Establishment of a NOE correlation as a result of dynamic process in **Scheme 22**. Colour of correlation arrow corresponds to marker in **Figure 3.40**.

As expected in all the complexes, carbons in close proximity to the phosphorus atoms experience $^{n}J_{P-C}$ (n= 1 – 3) coupling effects (**Figure 3.41**) with $^{1}J_{P-C}$, $^{2}J_{P-C}$ and $^{3}J_{P-C}$ within the ranges of 14 – 20 Hz, 6 – 8 Hz and 4 – 5 Hz respectively. Though each coupled peaks were also expected to be doublets, they were revealed as triplets (highlights in **Figure 3.41).** Considering the defined *C*$_2$ symmetry of the complexes, it was uncertain as to whether the split pattern can be attributed to a combination of one of the phosphorus of the (P^P) ligand and the counter anion PF_6^- (chemical inequivalence). How the counter anion might exactly contribute to this is unknown as counter anion identity effects were not investigated. Another explanation might be possible magnetic inequivalence between the two phosphorus atoms due to asymmetry of the (P^P) ligand with the through-bond coupling effect conveyed via $C^{coupled}$–P^{A}–Cu^{I}–P^{B} bonds. However, this is also unlikely as identified distinct triplets appeared with perfect 1: 2: 1 ratio. Note that previous discussions of the acquired 1D and 2D NMR had already supported the symmetric nature of the (P^P) ligands. If magnetic inequivalence was the case, then the 1:2:1 triplet can be attributed to the solution dynamics of the C_{phenyl}–P bond rotating very rapidly on the solution NMR timescale at room temperature. Nevertheless, it was observed that as the complexes became structurally complicated with 10, 13–substituents and change in the (P^P) ligand, the triplets resolve into broad singlets with reduced intensity. Regardless, phosphorus–coupled quaternary carbons of these complexes were capable of being elucidated due to the respective peaks establishing single cross correlations in acquired ^{1}H–^{13}C HSQC and HMBC spectra.

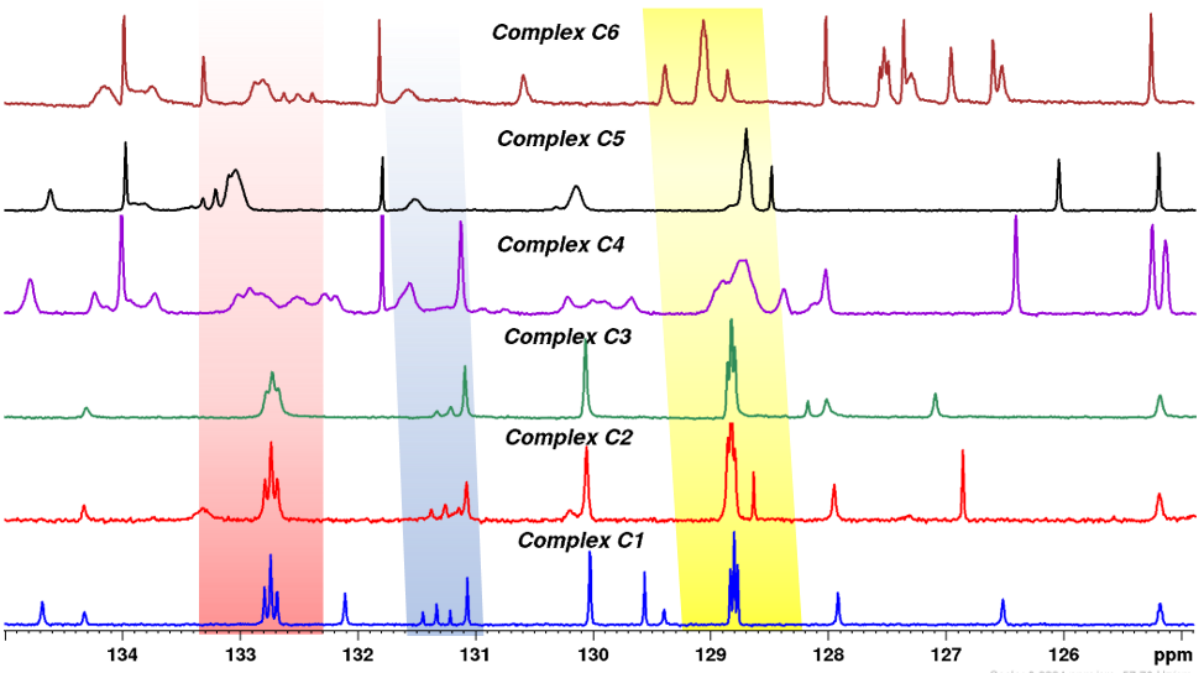

Figure 3.41. Stacked ^{13}C NMR (600 MHz, CD_3CN) of complexes **C1** to **C6** with coloured highlights indicating the triplet splitting patterns of $^{n}J_{P\text{-}C}$ coupling.

3.8.2. Example NMR elucidation of quaternary(q.) carbons and nitrogens of an arbitrarily chosen complex: C1.

From **Figure 3.42**, δ 1.83 ppm (the only aliphatic peak) integrating to 3H stem from the CMe_2 group of the xanthene backbone (1–**H**). Besides the HSQC artefact **C**^{1} (δ 134.3 ppm), it shared a ^{2}J and ^{3}J coupling with aliphatic q. carbon **C**^{2} (δ 27.5 ppm) and aromatic q. carbon **C**^{3} (δ 134.3 ppm) respectively (**Figure 3.43. a**). The AA'BB' peaks 22–**H** and 23–**H** shared HSQC correlation to aromatic carbons **C**^{22}(δ 129.6 ppm) and **C**^{23}(δ 132.1 ppm). Proximity to **N**^{20} (δ –62.3 ppm) was indicated by cross peak with only 22–**H** ($^{3}J_{NH}$) with CNST13= 7.5Hz (**Figure 3.43. b**). Q. carbon **C**^{21} was confirmed by correlations from both 22–**H** and 23–**H** (**Figure 3.44**). **N**^{13} (δ –117.1 ppm) was also confirmed from **Figure 3.43. b** by proximity to 14–**H** ($^{2}J_{NH}$) and 15–**H** ($^{3}J_{NH}$).

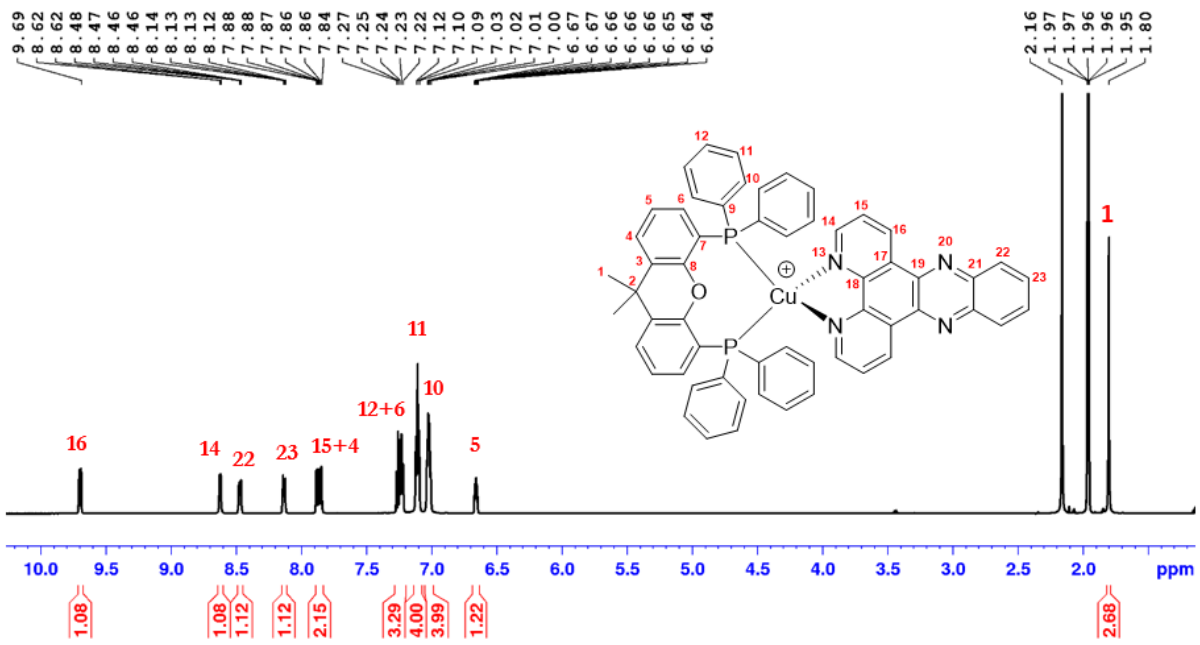

Figure 3.42. ^{1}H NMR (600 MHz, CD_3CN) of complex **C1**

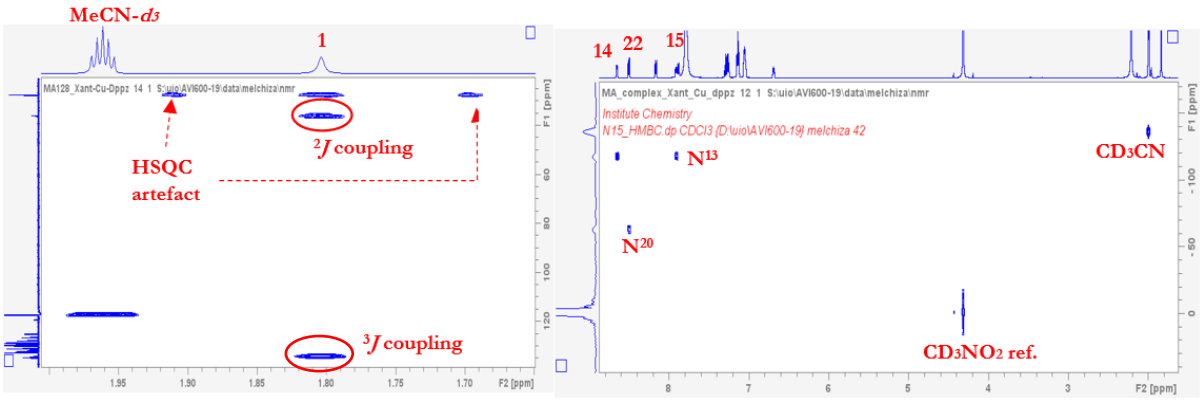

Figure 3.43.a (left): Aliphatic region ^{1}H - ^{13}C HMBC (600 MHz, CD_3CN) of complex **C1. b. (right):** zoomed–in ^{1}H–^{15}N HMBC (600 MHz, CD_3CN) of complex **C1.**

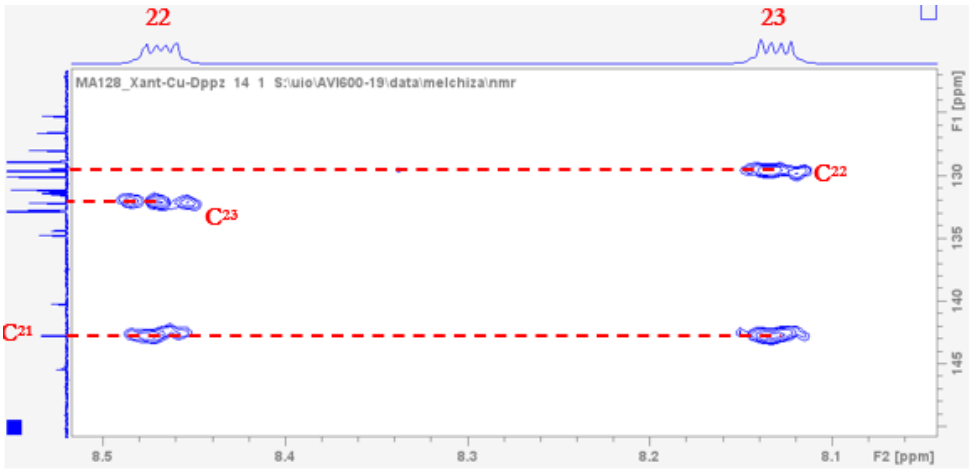

Figure 3.44. Zoomed in ^{1}H–^{13}C HMBC (600 MHz, CD_3CN) of complex **C1** showing correlations of 22–**H** and 23–**H.**

Q. carbon **C**[18] (δ 145.8 ppm) was identified by $^{3}J_{C–H}$ coupling with both 14–**H** and 16–**H** (**Figure 3.45**). Q. carbon **C**[17] (δ 129.4 ppm) was confirmed by $^{3}J_{C–H}$ coupling with 15–**H** whereas **C**[19] was by by $^{3}J_{C–H}$ coupling with only 16–**H (Figure 3.45). C**[7] (δ 119.3 ppm, $^{1}J_{CP}$ = 13.97 Hz), **C**[8] (δ 154.9, $^{2}J_{CP}$ = 6.4 Hz), and C[9] (δ 131.3 ppm, $^{1}J_{CP}$ = 17.5 Hz) were confirmed based on their triplet patterns with C8 sharing a $^{3}J_{CH}$ coupling with 4–**H**, **C**[7] coupled by 6–**H** and **C**[9] by phenyl protons 10–**H**, 11–**H** and 12–**H**.

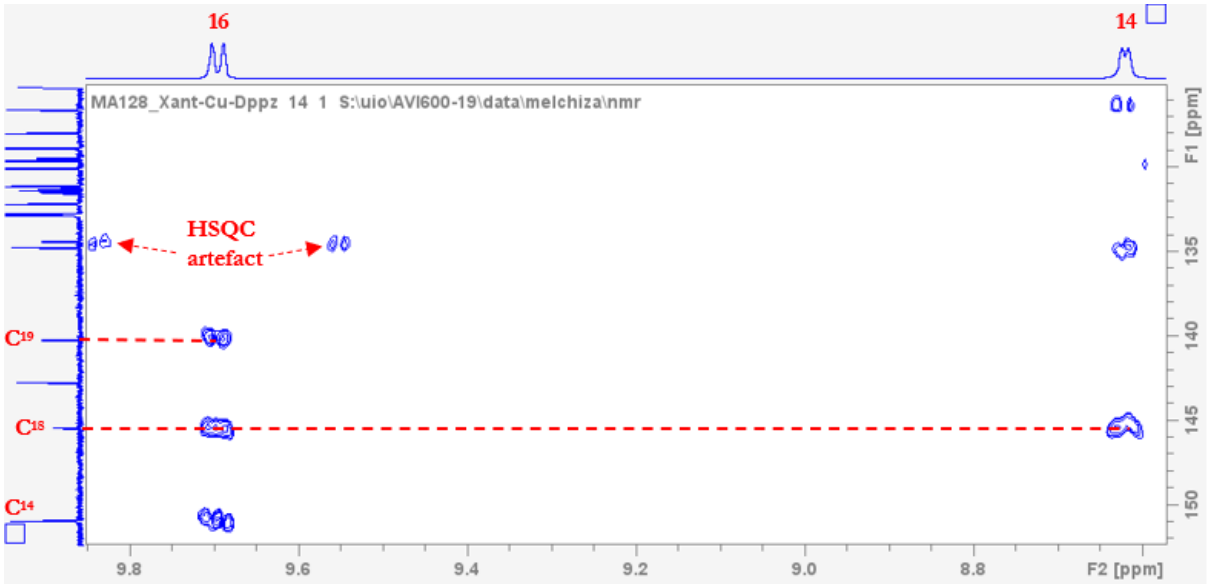

Figure 3.45. Zoomed in $^{1}H–^{13}C$ HMBC (600 MHz, CD_3CN) of complex **C1** showing correlations of 16–**H** and 14–**H.**

3.8.3. FTIR–ATR spectra of solid–state complexes C1 to C6

It should be noted from the ^{1}H NMR spectra that the complexes were intrinsically hygroscopic. Hence, υ (O–H) vibrational of absorbed atmospheric water molecules *ca.* 3700 cm^{-1} were removed during post-acquisition data refinement. However, this process could not be applied to the asymmetrical stretching υ (C–O) of atmospheric CO_2 with bands at 2340 cm^{-1} – 2372 cm^{-1}, which are present in complexes **C1** to **C3** (**Figure 3.46**). Complexes **C1** to **C3** showed very similar vibrational bands with only subtle differences in the appearance of very weak bands. υ (P–F) stretching modes of the counter anion were also observed with very significant bands at 856 cm^{-1}, 837 cm^{-1}, and 839 cm^{-1} for **C1**, **C2** and **C3** respectively, in addition to the diphenyl phosphane C–H rocking (ϱ (C_{phenyl}–H)) at *ca.* 1400 – 1430 cm^{-1}. Stretching modes υ (C–Br) of **C2**

and υ (C≡N) of **C3** could not be easily distinguished as done for compounds **3a** and **3b** (**Figure 3.13**), and ligands **L2** and **L3** (**Figure 3.26**). It was observed that intensity of the υ (C≡N) stretching mode reduces as the structures became more complicated from compound **3a** to ligand **L3** to complex **C3** (**Figure 3.47**).

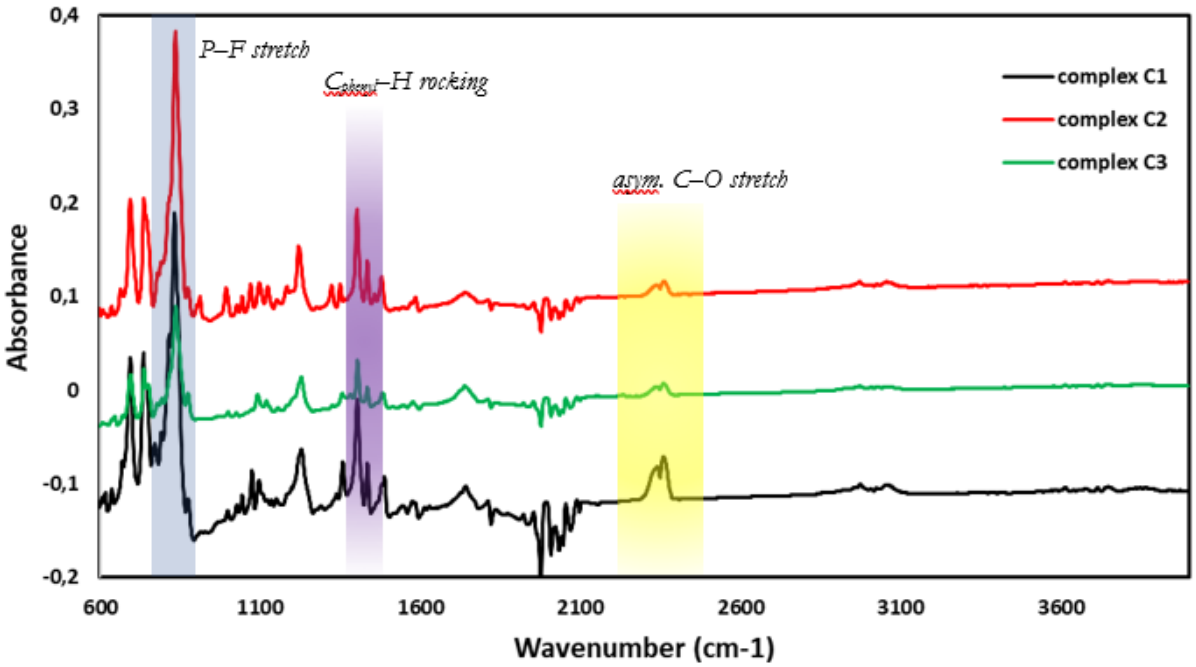

Figure 3.46. Stacked FTIR spectra of complexes **C1** to **C3**. **Blue** highlight = PF_6 counteranion vibrational band. **Violet** highlight = Diphenyl C-H rocking. **Yellow** highlight = atmospheric CO_2 asymmetrical stretching.

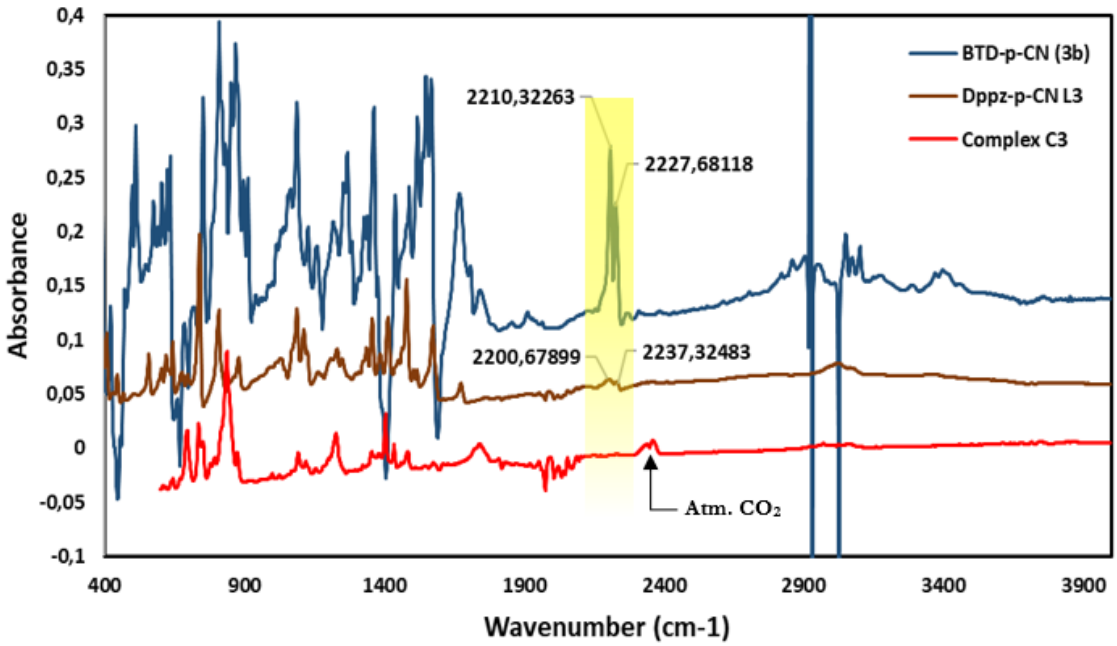

Figure 3.47. Stacked FTIR spectra of compound **3b**, ligand **L3** and Complex **C3.** **Yellow** highlight the reduction in the intensity of υ (C≡N) stretching mode.

Complexes **C4** to **C6** also exhibited the same behaviour as complexes **C1** to **C3** with very similar FTIR bands, the presence atmospheric CO_2 vibrational stretch υ(C–O) at *ca.* 2370 cm^{-1} and υ(P–F) of the counter anion PF_6^- at *ca.* 837 cm^{-1} (**Figure 3.48**). Other identified vibrational bands common amongst the three complexes included υ(C=O) stretch of the ester groups at *ca.* 1726 cm^{-1}, υ(N–O) stretch of the nitro groups at 1533 cm^{-1} and very weak bands of aromatic υ(C–H) stretch at *ca.* 3000 – 3100 cm^{-1}. Characteristic frequencies indicating *Cu–N* and *Cu–P* stretching modes were not accessible.

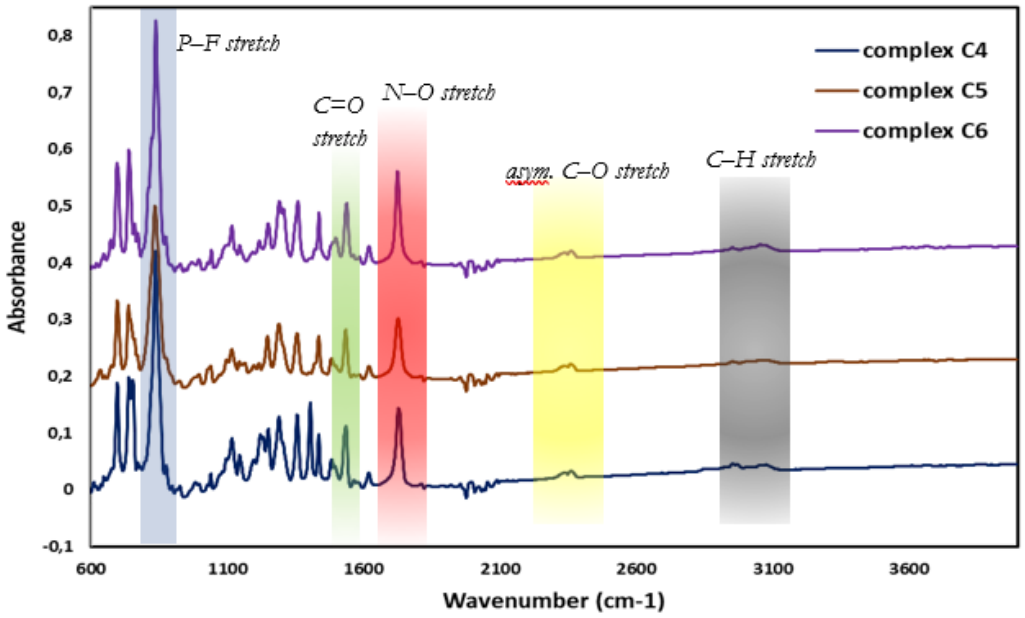

Figure 3.48. Stacked FTIR spectra of complexes **C1** to **C3**. **Blue** highlight = PF_6 counteranion vibrational band. **Green** highlight = (C=O) stretch of ester groups, **Red** highlight = N-O stretch of nitro groups . **Yellow** highlight = atmospheric CO_2 asymmetrical stretching, **Black** highlight = Aromatic C–H stretch.

3.8.4. Single Crystal X-Ray Diffraction studies of Cu(I) complexes

Slow diffusion of a layer of *n*–hexane or diethyl ether into a solution of **C1** to **C6** in dichloromethane or vapour diffusion with the same solvent systems afforded crystals for complexes **C1**, **C2**, **C4** and **C5** suitable for structure resolution by SC–XRD. Crystals for complexes **C3** and **C6** could not be obtained, with reasons for **C6** attributed to its atropisomeric nature. Discussions will be limited to the crystal structures of **C1** and **C5** because SC–XRD measurements were successful for only those. Since the xantphos moiety was present in **C1** to **C4** and the coordinated ligand **L4** in complexes **C4** to **C6,** observations derived from these structural analyses can be extended to all the other complexes.

3.8.4.1. Complex C1

The crystallographic determined structure of complex **C1** showed a monoclinic symmetry with a $P2_1/m$ space group and an R-factor of 5.33 % (**Figure 3.49**). It also revealed the hypothesized deviation from the ideal tetrahedral D_{2d} geometry to a distorted tetrahedral coordination around the Cu^{I} metal centre. The distortion was as a result of the difference in the size (due to the backbone) and bite angles of the diphosphine (P2B–Cu1B–P1B = 122.56(2)º) and the **L1** ligand (N4B–Cu1B–N3B = 80.54(7)º). More importantly, an obvious π–stacking is indicated between one phenyl group of the diphosphine (labelled **α**) and the phen moiety of coordinated **L1** with a distance of *ca.* 3.7 Å – 3.9 Å. This observation was in agreement with the results from the NOESY correlations similar to that in **Scheme 3.16**. The π–stacking though necessary for the stability of the complex, causes the **β** phenyl ring to become remote to interact with phen of **L1 (Figure 3.50)**. In addition to the longitudinal deviation from the phz axis(already shown in **Scheme 3.16**), a transverse deviation can also be observed (**Scheme 3.21**) causing the phenyl to be directly facing the mid portion of the phen moiety. Hence, the two deviation modes influence the dihedral angles between the π–stacking phenyl ring **α** and remote phenyl ring **β,** and the **L1** plane to differ significantly (97.9º for **α** and 128.1º for **β**). A more interesting observation is the π – π interactions between one **L1** ligand and another **L1** ligand of a neighbouring complex. The phen moiety of one complex directly stacks upon the phz moiety of the other centrosymmetrically with an interplanar distance of *ca.* 3.2 Å – 3.5 Å.

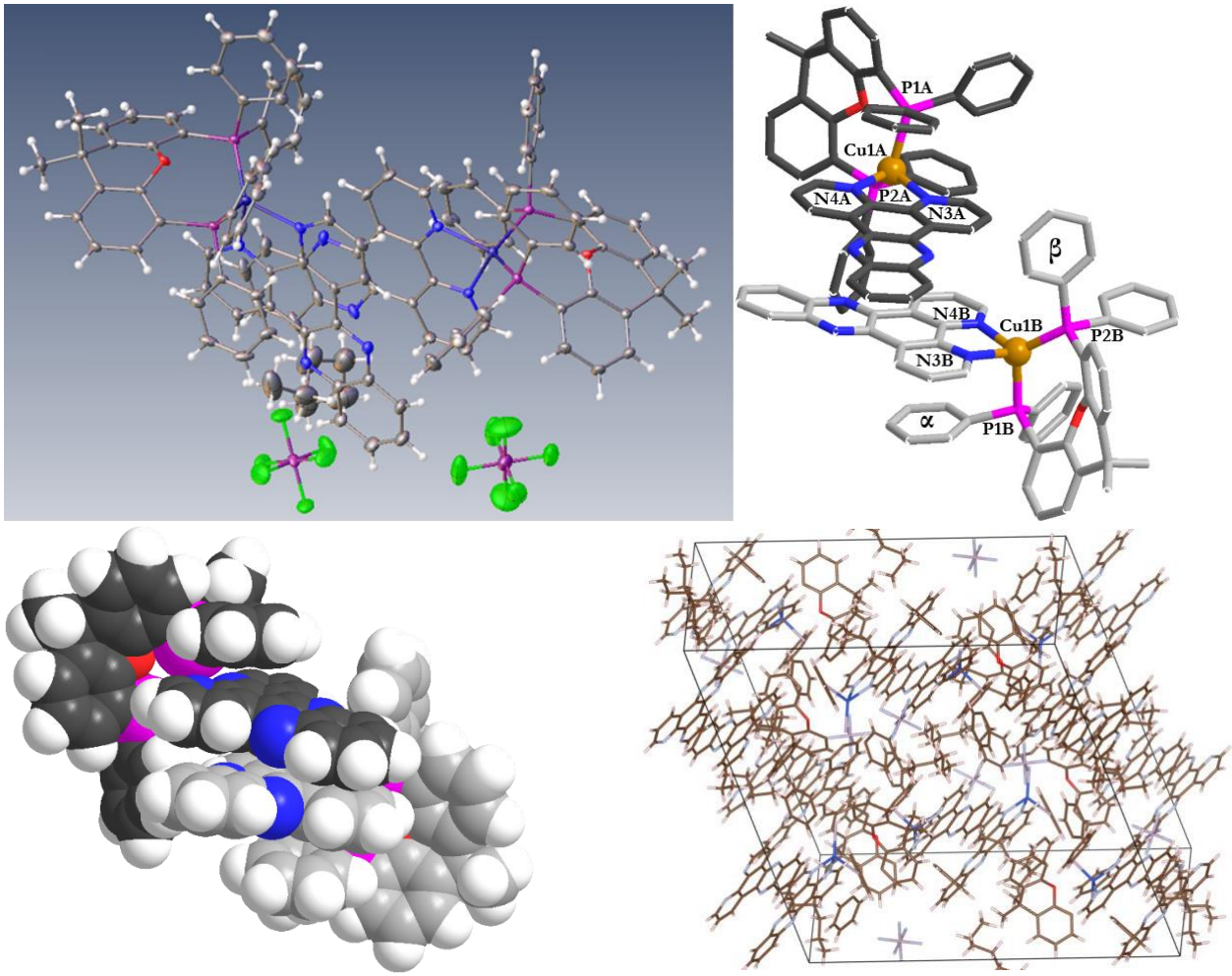

Figure 3.49. a (Top Left): ORTEP plot for solid–state structure complex **C1** with co–crystallized counter anion PF_6 and solvent molecules (*n*–hexane) with thermal ellipsoids at a probability of 50 %. Colour codes: dark blue= copper, blue= nitrogen, red= oxygen, violet= phosphorus, green= fluorine, white= hydrogen, grey= carbon. **b. (Top Right):** Crystallographically rendered sticks structure of complex **C1** (with counter anions, hydrogens and solvent molecules omitted for clarity) showing coordination around the Cu^{I} metal. **c. (Bottom left)** CPK space–filling representation of complex C1 highlighting the intra and intermolecular π – π interactions. **d. (Bottom right)** 3D unit cell showing monoclinic space group arrangement of complex **C1.**

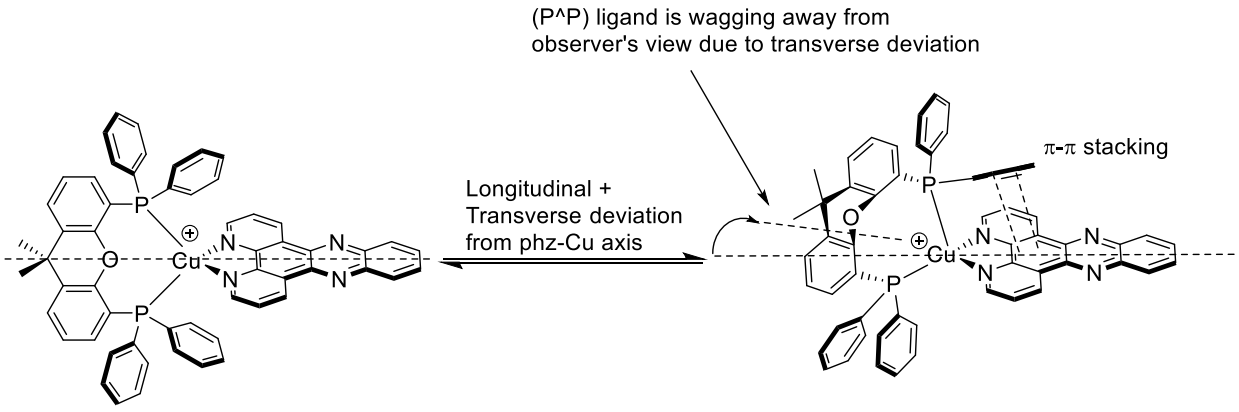

Scheme 3.21. Longitudinal and transverse deviation of the (P^P) ligand from the phenazine spacer axis.

3.8.4.2. Complex C5

SC–XRD for complex **C5** was performed at 298 K (**C1** was performed at 100 K) Measurements resulted in A-level alerts with low number of reflections and a high R–factor due to poor scattering ability of the crystal. Nevertheless, the symmetry revealed was triclinic $P\bar{1}$. A clear picture of the Cu^{I} coordination showed a distorted tetrahedral geometry similar to complex **C1 (Figure 3.50)**. The P1–Cu–P2 angle was expectedly smaller (= 113.2º) due to the reduced size of the ferrocene backbone compared with the xanthene backbone. The N5–Cu–N6 on the other hand was similar to complex **C1** (=79.8º) due to the rigidity of the **L1** and **L4** phen moiety. In addition, neither introducing 10, 13–*para*–substituents on coordinated **L1** nor changing the diphosphine backbone had any effect on the Cu–N bond length (Cu1A–N4A = 2.0715 Å and Cu1A–N3A = 2.0759 Å of complex **C1** compared to Cu–N6 = 2.090 Å and Cu–N5 = 2.105 Å of complex **C5**).

The phenyl (**α**)–phen (**L1**) π stacking effect present in **C1** was also evidenced with the effect redirected towards the pyrido-N5 ring at a similar distance of 3.5 Å. Although an interplanar **L4** – **L4** π–stacking was not observed, the terphenyl conformation justified from NOESY correlations in **Scheme 3.17** and **Figure 3.36** was observed with the distance between the *o*–proton of the phenazine ring (**β**) and the pseudo–perpendicular *o*–proton of the 10, 13–phenyl ring (**γ**) being *ca.* 2.6 Å. The conformation of the (P^P) ligand also revealed the additional transverse deviation effect as seen in **Scheme 3.21** with the planes of the cyclopentadienyl rings being perpendicular to the coordinated **L4** ligand plane.

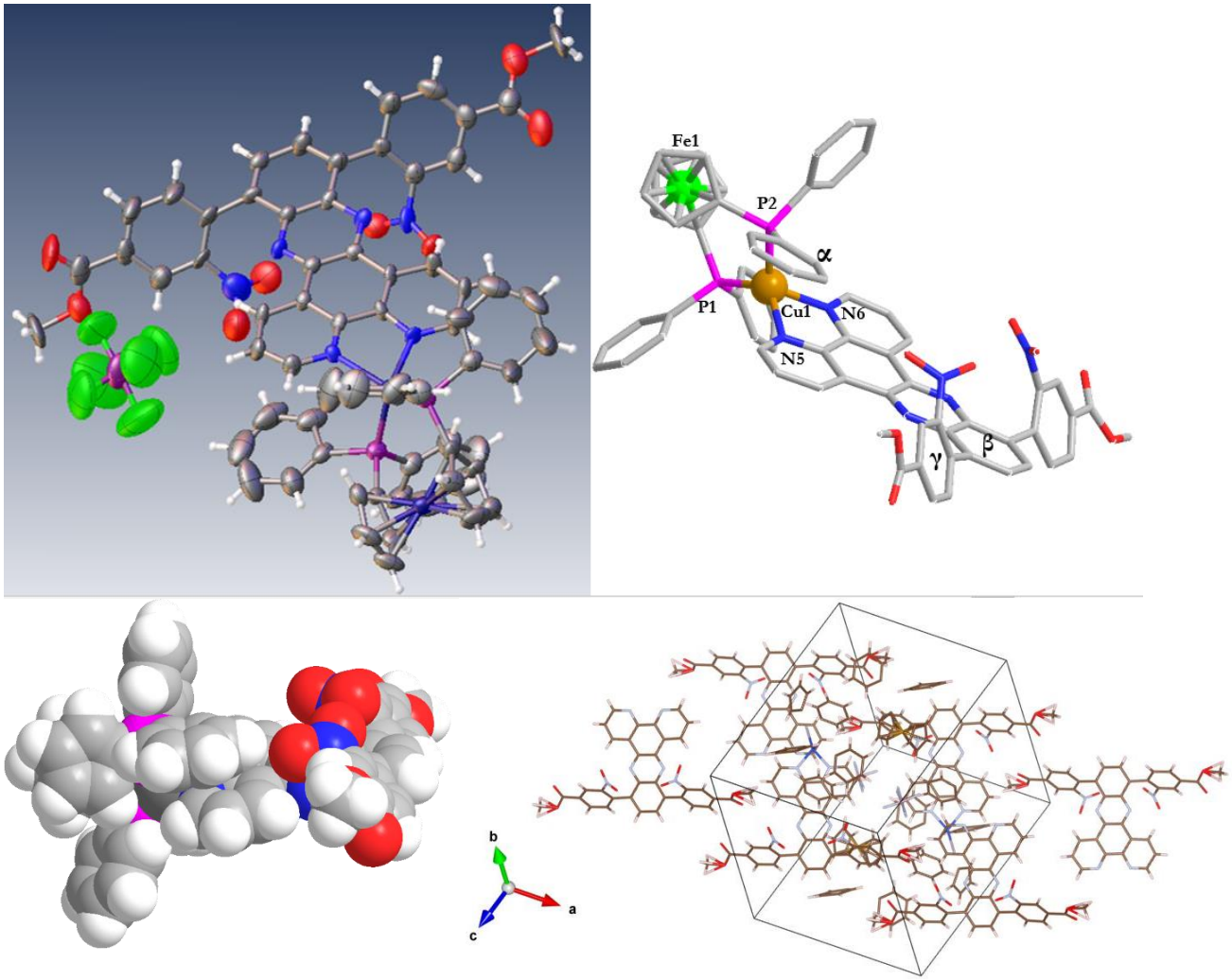

Figure 3.50. a. (Top Left) : ORTEP plot for solid–state structure complex **C5** with co–crystallized counter anion PF_6 and with thermal ellipsoids at an undetermined probability. Colour codes: dark blue= copper, blue= nitrogen, red= oxygen, violet= phosphorus, green= fluorine, white= hydrogen, grey= carbon. **b (Top Right) :** Crystallographically rendered sticks structure of complex **C5** (with counter anions and hydrogens omitted for clarity) showing coordination geometry around Cu^{I} metal. **c. (Bottom left)** CPK space–filling representation of complex **C5** highlighting the intramolecular π interactions. **d. (Bottom right)** 3D unit cell showing triclinic space group arrangement of complex **C5** with no interplanar interactions.

3.8.5. UV–Vis DRS studies of the free ligands and Cu(I) complexes

The choice of the diffuse reflectance spectroscopy was justified not only from the severe solubility issues by the free ligands in common laboratory solvents but most importantly, from the fact that prospective [Cu(N^N)(P^P)]$^+$–incorporated MOF materials which will be solids, will require solid–based UV–Vis studies. As stated in **Section 2.4.**, assessment of the absorption properties did not pertain to the intensity variations amongst the measured samples but on the variations along the wavelength axis. The reflectance (%) was only shown to indicate that the reflectance profiles were lower than that of $BaSO_4$ (100%) with **L3** in **Figure 3.51** exhibiting the highest absorption ability. This is consistent with the dark colour of the sample.

The spectra of the various ligands **L1** to **L4** showed similarities of high absorption at $\lambda^{abs} <$ 430 nm, which might be attributed to intra-ligand phen or phz π → π* transitions (**Figures 3.51** and **3.52**). Ligand **L2** showing its absorption edge $\lambda^{abs}_{edge} = ca.\,430$ nm compared with **L1** and **L4** $\lambda^{abs}_{edge} = ca.\,409$ nm implies that the introduction of electron withdrawing groups on the 10, 13–positions promotes red-shifting of the absorption bands.

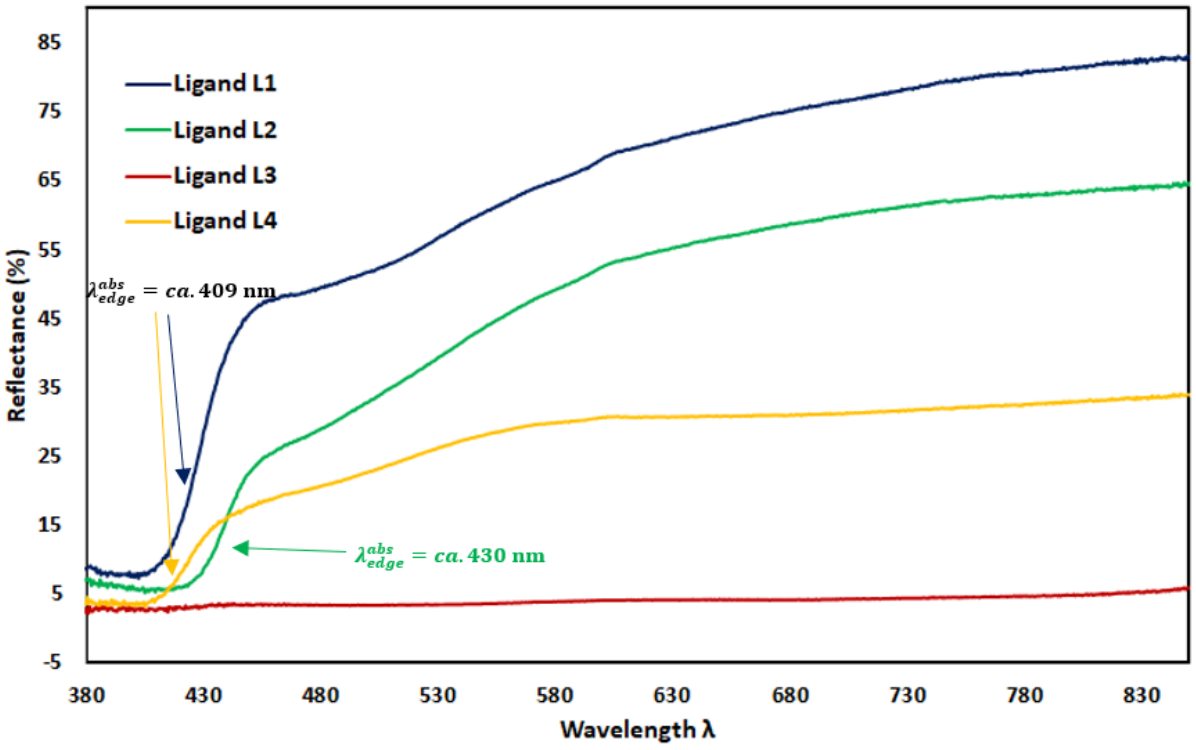

Figure 3.51. Unnormalised UV -Vis DR spectra (stacked, ref. $BaSO_4$) of free ligands **L1** to **L4.**

In addition to the high absorption property at $\lambda^{abs} < 430$ nm, ligand **L3** on the other hand showed $\lambda^{abs}_{max} = ca. 500$ nm and $\lambda^{abs}_{max} = ca. 684$ nm not clearly defined for the other ligands. Whether these were as a result of the relatively strong electron withdrawing character of the cyano groups and its extension of the dppz π conjugation, could not be inferred with certainty.

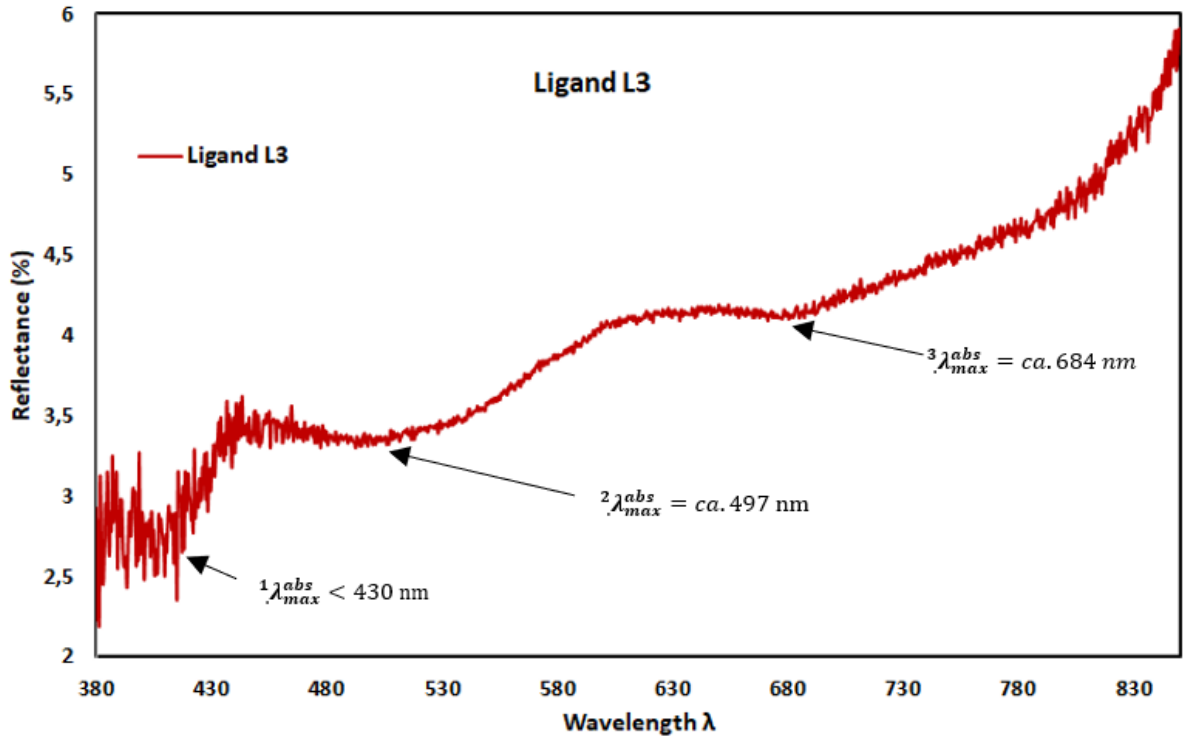

Figure 3.52. Unnormalised UV -Vis DR spectra (ref. $BaSO_4$) of ligand **L3** showing multiple λ^{abs}_{max}.

Complexation of the free ligands was followed by a large red-shift of the absorption edges. An instance is shown in **Figure 3.53** where λ^{abs}_{edge} shifts from *ca.* 409 nm to *ca.* 500 nm (indicated as solid black arrow), implying the presence of charge transitions (MLCT or ILCT). Increasing the electron withdrawing ability of the phenazine moiety shows further red shifting of the absorption edges (dashed arrows) with the order: H (**C1**) < Br (**C2**) < methyl nitrobenzoate (**C4**) < cyano (**C3**). This implies that the band energy gap for the HOMO *d* – LUMO π^* MLCT transition is narrower for complex **C3** than for complexes **C4, C2** and **C1**. This observation was similar to that reported for corresponding *para*-substituted dppz–based Ru^{II} complexes by Aslan *et. al.*[22] where solvated DFT calculations showed that the HOMO *d* → LUMO *phz* π^* energy for ground state $[Ru(phen)_2(dppz–p–CN]^{2+}$ was smaller in eV units than that of $[Ru(phen)_2(dppz–p–Br)]^{2+}$ (**Figure 3.54**).

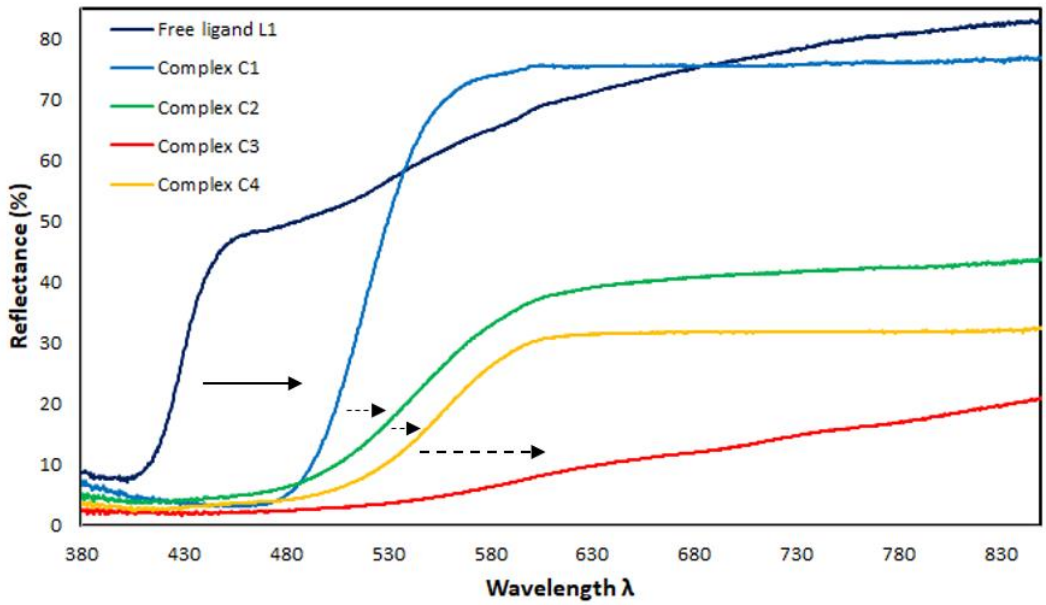

Figure 3.53. Unnormalised UV -Vis DR spectra (stacked, ref. $BaSO_4$) of ligand **L1** and complex **C1** to **C4** with the arrows showing the red shifts for complexation (solid arrow) and increase in the electron-withdrawing character (dashed arrow).

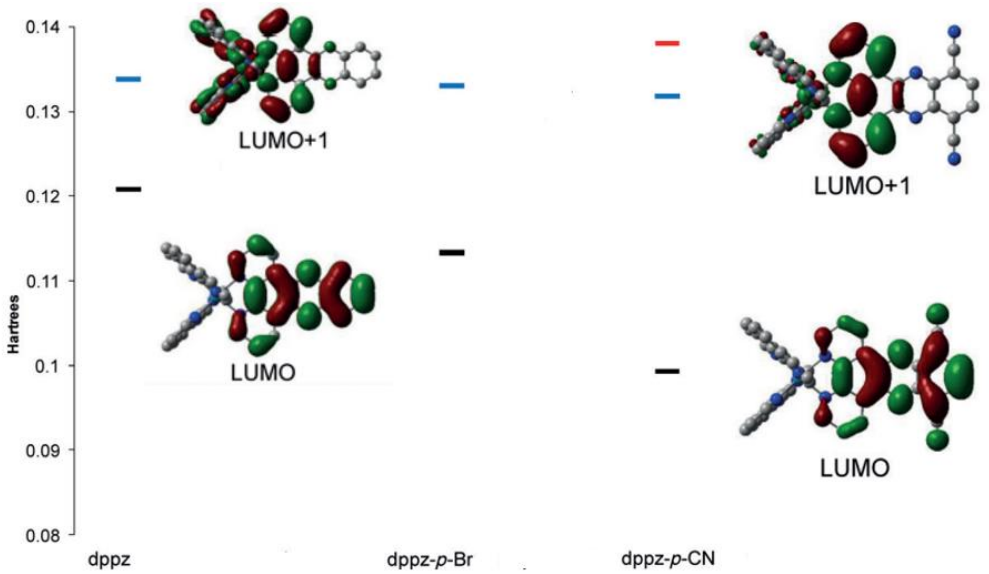

Figure 3.54. Energy level diagram showing the smaller HOMO → LUMO energy gap confirmed by UV-Vis DRS studies (**Figure 3.53**) for coordinated **L3** compared to coordinated **L2** and **L1**. HOMO at 0 Hartree units. LUMO= black dash (phz–centered MOs), LUMO+1= blue dash (phen–centered MOs). DFT calculations (B3LYP level) were conducted specifically on dppz-based Ru^{II} complexes from ref[22].

Similar red-shift effect is observed upon complexation of ligand **L4** with copper (**Figure 3.55**). However, changing the backbone of the coordinated diphosphine ligand from xanthene to ferrocene or binaphthyl seemed to have no effect, as the λ_{edge}^{abs} of the corresponding complexes were in the same region. Only increasing the electron-withdrawing character of the 10, 13-substituents caused an obvious effect. This implies that the major MLCT processes probably occurring are electron transitions from the Cu^{I} centre to the coordinated dppz ligand and not the diphosphine ligand. Based on this observation, it will be more appropriate in cases of prospective MOF incorporation of Cu^{I}-complexes for electron transfer reactions if the dppz ligand is used as the direct linker. Once the cyano groups are transformed into carboxylates, the inorganic Zr–secondary building units (SBU) become the electron accepting components in replacement to the cyano groups.

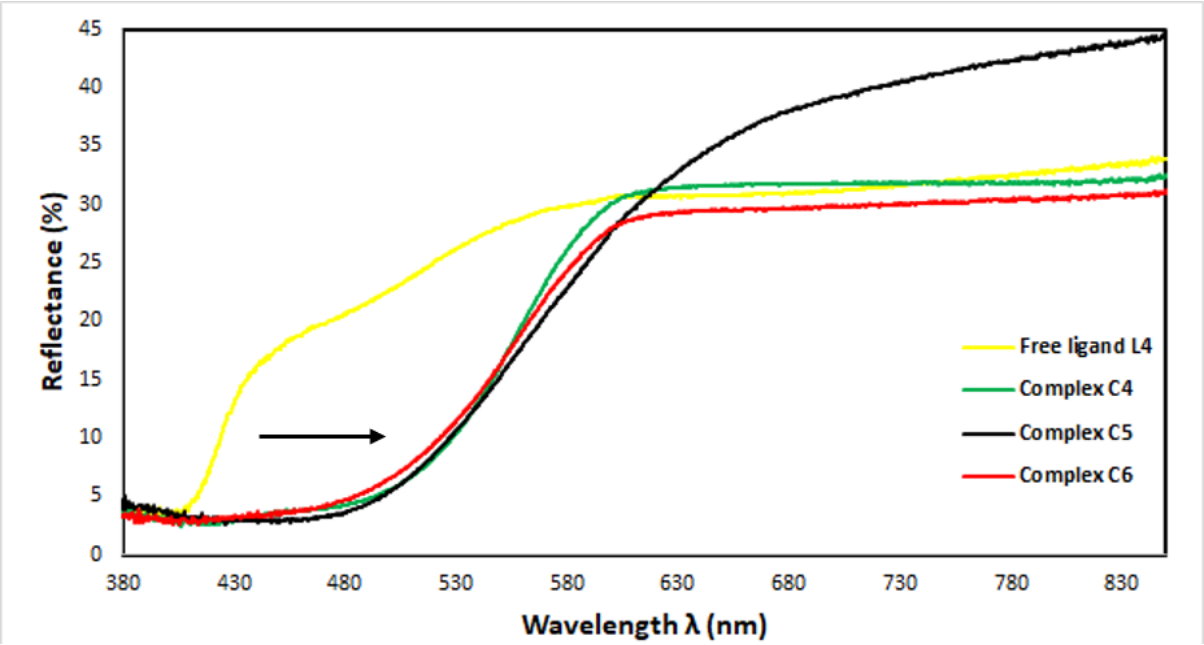

Figure 3.55. Unnormalised UV -Vis DR spectra (stacked, ref. $BaSO_4$) of ligand **L4** and complex **C4** to **C6** with the solid arrow indicating the red shifts for complexation.

4. Conclusion and Prospects

Stated in the rationale (**Section 2.1.2**) is the primary aim of this study which involved the synthesis of the 10, 13–disubstituted dppz analogues. The desired dppz ligands **L1** to **L4** were afforded in quantitative yields via condensation of phenO_2 with the corresponding *o*–phenylenediamines. Prior sulfur extrusion process of the alkyl benzoate–functionalized benzothiadiazoles did not yield the desired product as the reaction conditions were harsh on the ester groups. Applying the same reaction (Co^{II}–$NaBH_4$ system) on bromo– and cyano–benzothiadiazoles afforded the desired diamines. NMR characterization of the ligand structures on the other hand, required the use of trifluoroacetic acid due to solubility issues encountered.

The secondary aim dealt with complexation of the ligands via a one–pot–two step method to produce a series of heteroleptic $[Cu(N^N)(P^P)]^+$ complexes with subsequent detailed structural and spectroscopic studies. The yielded copper(I) complexes showed gratifying stability upon exposure to air with DOSY studies confirming the absence of homoleptic species caused by the speciation reaction (**Equation 11**). The structure of the complexes were elucidated by a number of NMR experiments with ^{31}P HMBC confirming the presence of the counter anion and inter-ligand (P^P)→ **H**–(N^N) correlations. Certain inter-ligand π–stacking properties, axis deviations and coordinated **L4** terphenyl conformations amongst the complexes were deduced by through–space NOE correlations. In addition, the C_2 symmetry of the complexes **C1** to **C4** was as a result of dynamic flipping of the –O and –CMe_2 group of the xanthene backbone. Single crystal structures of complexes C1 and C5 confirmed these conformations in addition to the distorted tetrahedral coordination around the Cu^I metal centre. Even though the presence of 10, 13–EWGs did not affect the Cu–N bond lengths, UV–Vis DRS evaluation indicated their influence in red–shifting the absorption properties of the complexes.

Continuation of this work will require a detailed computational, electrochemical, photoactivation reactions and solution–based photocatalytic CO_2 conversion studies of the complexes. As stated in **Section 2.1.2.**, Zr–based MOF heterogenization of the complexes can also be attempted. For instance, complex **C3** can be incorporated into UiO–66 and **C4** to **C6** into UiO–68 to create a PS–based AP MOF system for photocatalytic testing. Producing UiO–67 and –69 dppz linkers on the other hand will require optimization of the sulfur extrusion process for the alkyl benzoate–functionalized benzothiadiazoles **3f**, **3g** and **3h**.

5. Experimental Section

5.1. General

All reactions were performed in oven-dried (140°C) glassware under argon atmosphere using standard Schlenk technique unless otherwise stated. All reported reaction temperatures correspond to internal temperatures measured with the IKA® IKATRON™ ETS-D4 Temperature Controller. Room temperature (rt) was approximately 19.5 °C.

NMR spectra of samples were recorded on the Bruker Avance AVIIIHD400 (400 MHz, ^{1}H; 100 MHz, ^{13}C; 162 MHz, ^{31}P), Bruker Avance AVI600 or AVII600 (600 MHz, ^{1}H; 151 MHz, ^{13}C) or Bruker Avance AVIIIHD800 (800 MHz, ^{1}H; 201 MHz, ^{13}C) operating at 300 K. The spectra were calibrated against residual $CDCl_3$ (δ_H = 7.26 ppm, δ_C= *ca.* 77 ppm), CD_3CN (δ_H 1.96 ppm, δ_C= *ca.* 1.39 and 118.69 ppm), Pyridine-d_5 (δ_H = 7.19, 7.55 and 8.71 ppm, δ_C= *ca.* 123.5, 135.5 and 149.9 ppm) and Trifluoroacetic acid-d (δ_H = 11.5 ppm, δ_C= *ca.* 116.6 and 164.2 ppm). ^{31}P NMR were referenced against 85% aq. H_3PO_4 (δ_P = 0.00 ppm) and ^{15}N HMBCs against CH_3NO_2 (δ_N = 0.00 ppm). Chemical shifts are reported in parts per million (ppm). Multiplicities are indicated by s (singlet), d (doublet), t (triplet), q (quartet), quin (quintet), hept (heptet), and m (multiplet). Coupling constants, *J*, are reported in Hertz.

DOSY spectra were collected on Bruker Avance AVIIIHD800 with Z-gradient probe with the ledbpgp1s pulse sequence with 16 transitions. The diffusion period Δ was 55 ms and gradient pulse duration (p30, ½ ·δ) was 750 µs. Spinning was off. The data were analysed using the Diffusion option in the Bruker Dynamics Center.

Mass spectra were obtained by Bruker Scion 436-TQ GC-MS (EI) and Bruker maXis II ETD QTOF (ESI and HRMS EI) and are presented as m/z (% rel int). All ESI-spectra were run in positive ion mode. All reported melting points are uncorrected and were recorded using a Stuart SMP10 point apparatus.

Reaction solvents tetrahydrofuran, dimethylformamide, dichloromethane were dried using the MB SPS-800 solvent purification system from MBraun. Methanol and ethanol were dried using molecular sieves before use. Hexanes were redistilled before use. Only Type II distilled water was used for the workup that involved the use of water. Analytical thin-layer chromatography

was performed on Merck silica gel 60 RP-18 F254s plates. Visualization was accomplished with UV light (254 nm). Flash column chromatography was performed using VWR Silica gel (40-63 μm particle size, 230-400 mesh) (SiO2). All the reagents were used as delivered from Sigma Aldrich, Fluorochem and VWR Chemicals unless stated otherwise.

$[Cu(MeCN)_4]PF_6$ as the precursor for the copper (I) complex synthesis was purchased from Sigma Aldrich and used without further purification. All Cu(I) complexes synthesis were conducted using standard Schlenk techniques under argon atmosphere.

Ultraviolet–Visible Diffuse Reflectance Spectroscopy (UV–Vis DRS) measurements were conducted, using a USB2000+ spectrometer from Ocean Optics (FLMS16026). IR spectra were recorded using Vertex 70 Fourier Transform Infrared spectrometer equipped for transmission measurements. All data were recorded at room temperature.

The diffraction intensity data of the complexes for crystal structure determination were collected on a Bruker D8 Venture diffractometer equipped with a Photon 100 detector and using Mo Kα radiation (λ = 0.71073 Å) from an Incoatec iμS microsource. Data reduction was performed with the Bruker Apex3 Suite. Using Olex2 as user interface, the structure was solved with the SHELXT structure solution program using Intrinsic Phasing and refined with the SHELXL refinement package using Least Squares minimisation. X-Ray suitable crystals were grown from DCM/hexane (or Et_2O) solutions.

5.2. Synthesis procedures

5.2.1. Synthesis of 1,10-phenanthroline-5,6-dione (1a).

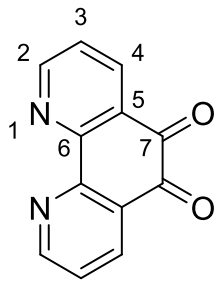

To an oven dried 25 mL round-bottomed flask equipped with a magnetic stirrer and placed in an ice bath was added 60% H_2SO_4 (12 mL; prepared by diluting 7.6 mL 95% H_2SO_4) followed by 1,10-phenanthroline (0.541 g, 3.0 mmol, 1.0 equiv.). After complete dissolution, potassium bromate (0.551 g, 3.3 mmol, 1.1 equiv.) was added in very small batches over a period of 30 minutes to an hour under slow stirring. Thereafter, the reaction flask was fitted with an addition funnel (with tap closed) or condenser with a tube dipped in thiosulfate solution. The red mixture was left to stir at room temperature overnight (> 20 hours). The resulting mixture was poured over ice and neutralized slowly and carefully to pH 5 – 6 using saturated NaOH solution (30% - 50%) in small drops whilst maintaining the solution temperature at 0 ºC. The resulting mixture was extracted thrice with dichloromethane, washed with water and brine, and dried using $MgSO_4$. Solvent was filtrated and removed under reduced pressure resulting in a yellow powder. Crude was purified by recrystallization from methanol to produce **1a** (0.575 g, 91 % yield) as bright yellow powder.

^{1}H NMR (600 MHz, $CDCl_3$): 7.59 (dd, 1H, 3–**H**, ^3J = 7.9 Hz, 4.7 Hz), 8.51 (dd, 1H, 4–**H**, ^3J = 7.8 Hz, ^4J = 1.8 Hz), 9.12 (dd, 1H, 2–**H**, ^3J= 4.7 Hz, ^4J= 1.8 Hz).

^{13}C NMR (151 MHz, $CDCl_3$): 125.6 (**3**), 128.1 (**5**), 137.3 (**4**), 152.9 (**6**), 156.4 (**2**), 178.7 (**7**).

LRMS (ESI, MeCN) m/z (rel. %): 233 ($[M + Na + H]^+$, 100)

HRMS (ESI, MeCN): Measured m/z: 233.0321. Calculated m/z for $[C_{12}H_6N_6O_2 + Na]^+$: 233.0327.

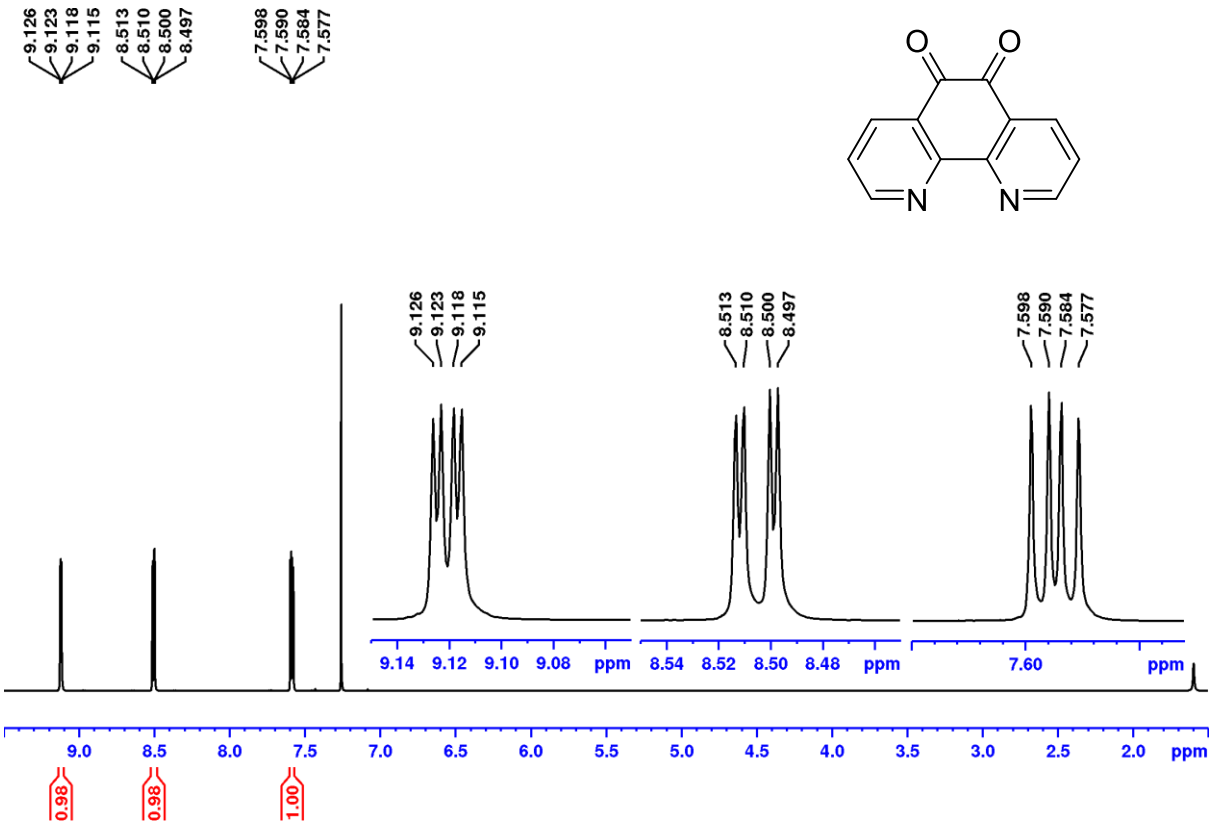

Figure 5.1. ^{1}H NMR (600 MHz, $CDCl_3$) spectrum of **1a.**

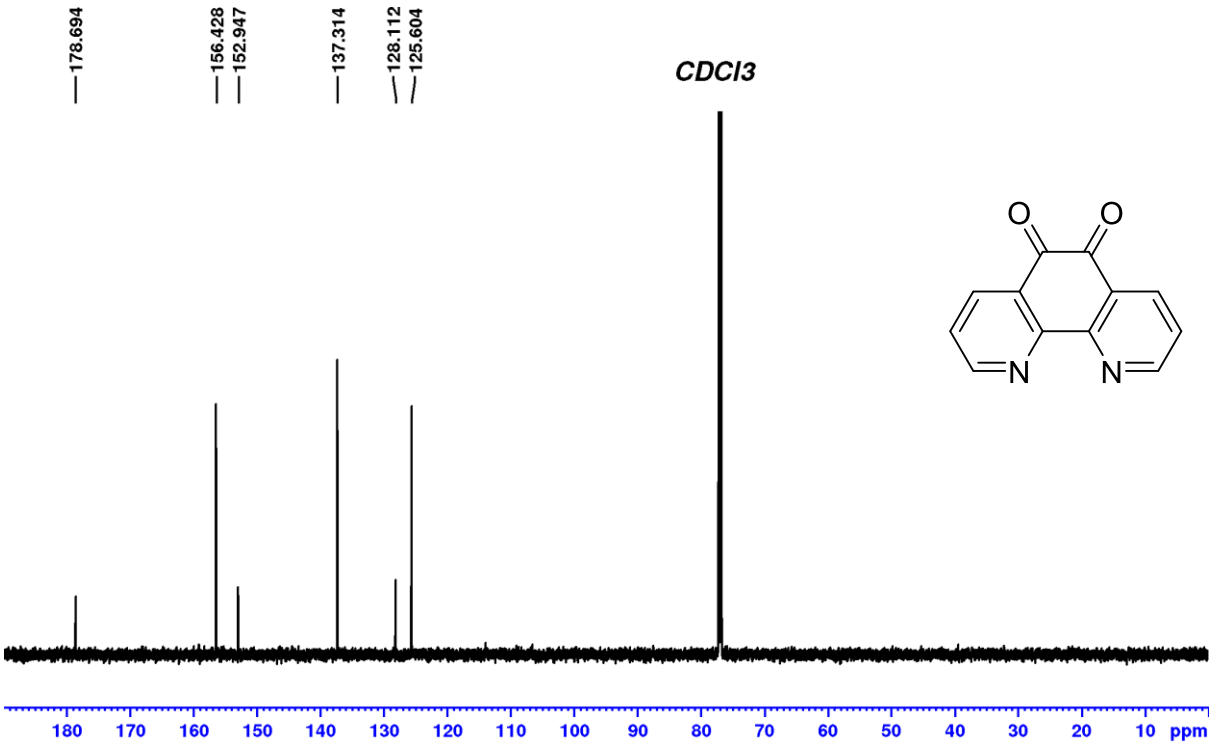

Figure 5.2. ^{13}C NMR (151 MHz, $CDCl_3$) spectrum of **1a.**

5.2.2. Synthesis of benzo[c][1,2,5]thiadiazole (2)

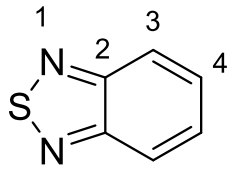

To a 50 mL round-bottomed flask equipped with a magnetic stirrer was added grounded *o*–phenylenediamine **1b** (1.00 g, 9.25 mmol, 1.0 equiv.), dichloromethane (20 mL) and triethylamine (5.20mL, 37.00 mmol, 4.0 equiv.) and the reaction mixture stirred until complete dissolution. Under ice, thionyl chloride (1.00 mL, 13.88 mmol, 1.50 equiv.) was added dropwise very slowly and the mixture refluxed (55 ºC) for 5 hours. The solvent was removed in vacuo and distilled water (100 mL) was added to the residue. Concentrated HCl was added dropwise until final pH of 1. Extra water was added and purification was conducted by steam distillation (99 ºC with vacuum). The distillate was extracted with dichloromethane (5 × 25 mL), washed with water and dried with $MgSO_4$. The solvent was filtered and removed under reduced pressure to afford **2** (0.80g, 63 %) as orange-yellow solid pure by ^{1}H NMR.

^{1}H NMR (600 MHz, $CDCl_3$): 7.49(m *ortho*-[AA'XX'], 1H , 4–**H** [X/X'], |N|: $|^3J_{XA} + {}^4J_{XA'}|$ d = 10.0 Hz), 7.90 (m *ortho*-[AA'XX'], 1H, 3–**H** [A/A'], |N|: $|^3J_{AX} + {}^4J_{AX'}|$ d = 10.1 Hz).

^{13}C NMR (151 MHz, $CDCl_3$): 121.5 (**3**), 129.3 (**4**), 154.8 (**2**).

LRMS (APCI, MeCN) m/z (rel. %): 136 ($M^{\bullet+}$, 100).

HRMS (APCI, MeCN): Measured m/z: 136.0064. Calculated m/z for $[C_6H_4N_2S]^{\bullet+}$: 136.0095

M_p: 42 – 44 °C.

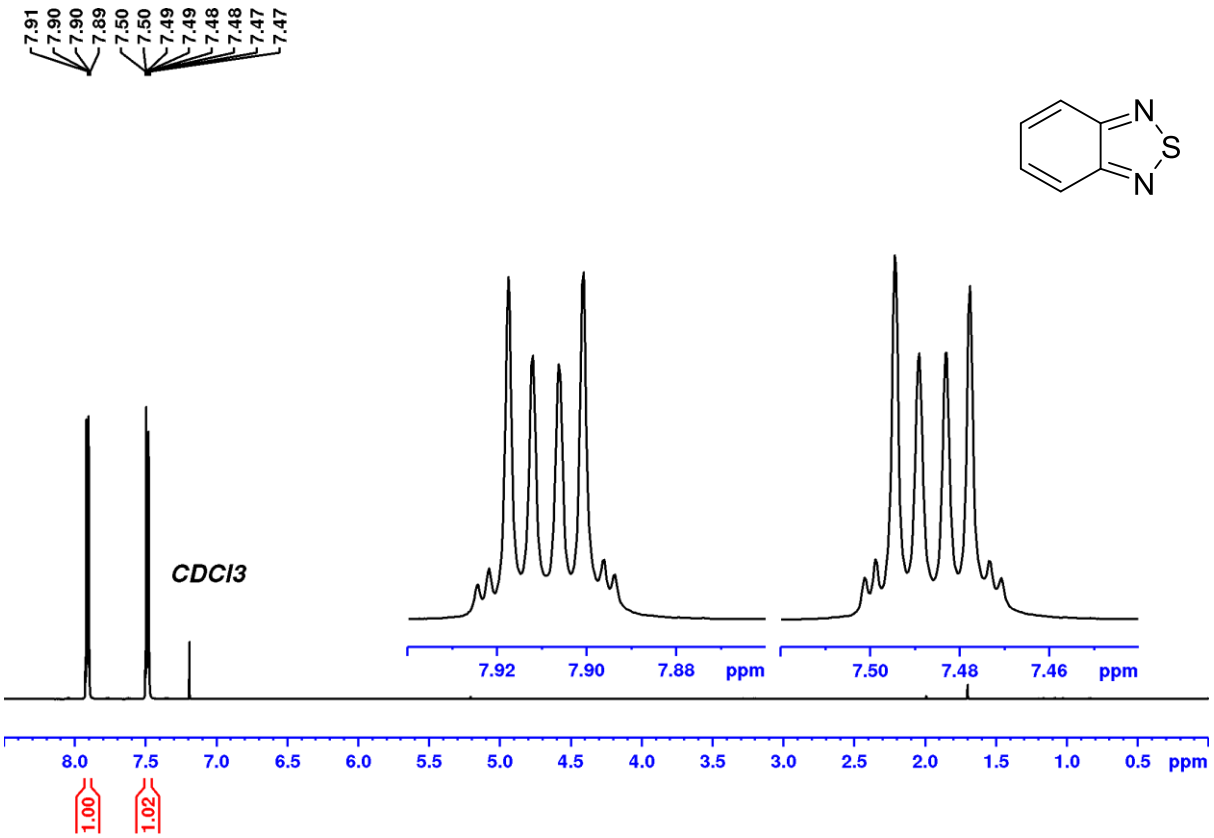

Figure 5.3. ^{1}H NMR (600 MHz, $CDCl_3$) spectrum of **2.**

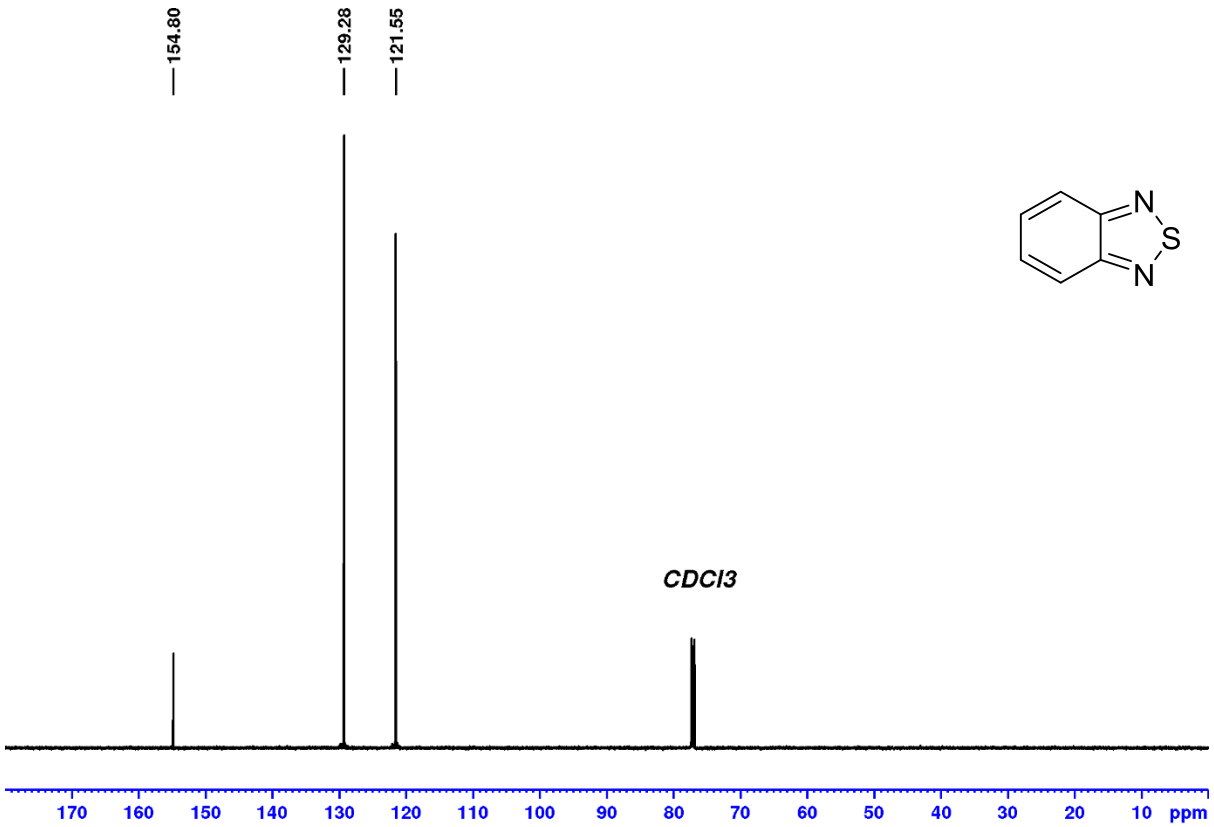

Figure 5.4. ^{13}C NMR (151 MHz, $CDCl_3$) spectrum of **2.**

5.2.3. Synthesis of 4,7-dibromobenzo[c][1,2,5]thiadiazole (3a)

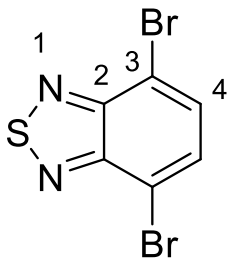

To an oven dried two-necked round-bottomed flask equipped with magnetic stirrer and under argon atmosphere was added concentrated H_2SO_4 (10 mL), **2** (1.00 g, 7.34 mmol, 1.0 equiv.) and *N*–bromosuccinimide (2.70 g, 15.40 mmol, 2.1 equiv.) and the resulting mixture stirred at 65 ºC for 3 hours. The reaction mixture was cooled to room temperature and placed in an ice bath. Cold distilled water (60 mL) was added dropwise slowly and the resulting white mixture extracted with toluene (3 × 50 mL). The organic layers were washed with water, brine and dried with $MgSO_4$. Solvents were filtered and removed *in vacuo* and the product recrystallized from chloroform: hexane (1:2) affording **3a** (1.81 g, 84 % yield) as off-white crystals.

^{1}H NMR (600 MHz, $CDCl_3$): 7.72 (s, 2H , 4–**H**).

^{13}C NMR (151 MHz, $CDCl_3$): 113.9 (**3**), 132.4(**4**), 153 (**2**).

LRMS (APCI, MeCN) m/z (rel. %): 292.8366 ($[M+H]^{\bullet+}$, 51.4), 214.9226 ($[M - Br]^{\bullet+}$, 3.9), 374.7448 ($[M + Br + H]^{\bullet+}$, 6.0)

HRMS (APCI, MeCN): Measured m/z: 292.8366. Calculated m/z for $[C_6H_3Br_2N_2S]^{\bullet+}$: 292.8383.

FTIR (ATR) ν_{max}/cm^{-1} : 486 – 671 (range of C^3–Br stretch)

M_p: 183 – 185 °C.

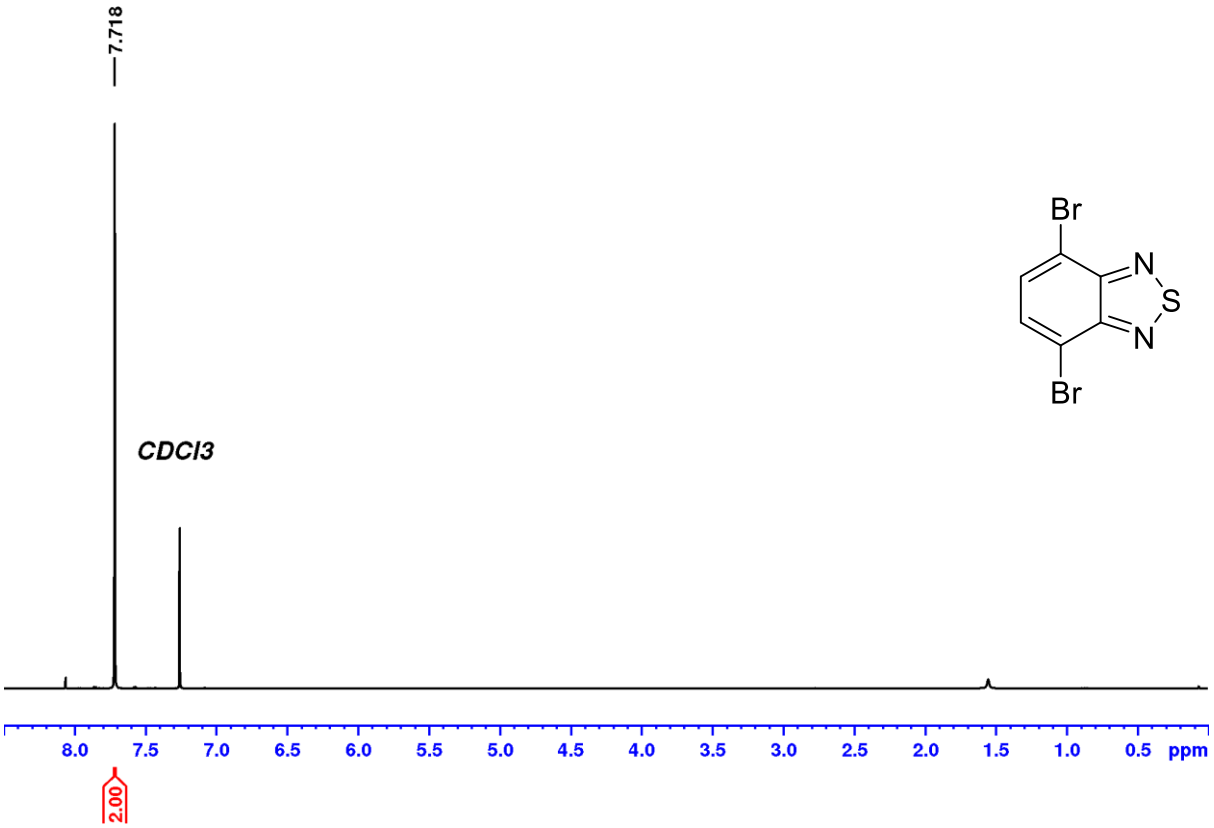

Figure 5.5. ^{1}H NMR (600 MHz, $CDCl_3$) spectrum of **3a.**

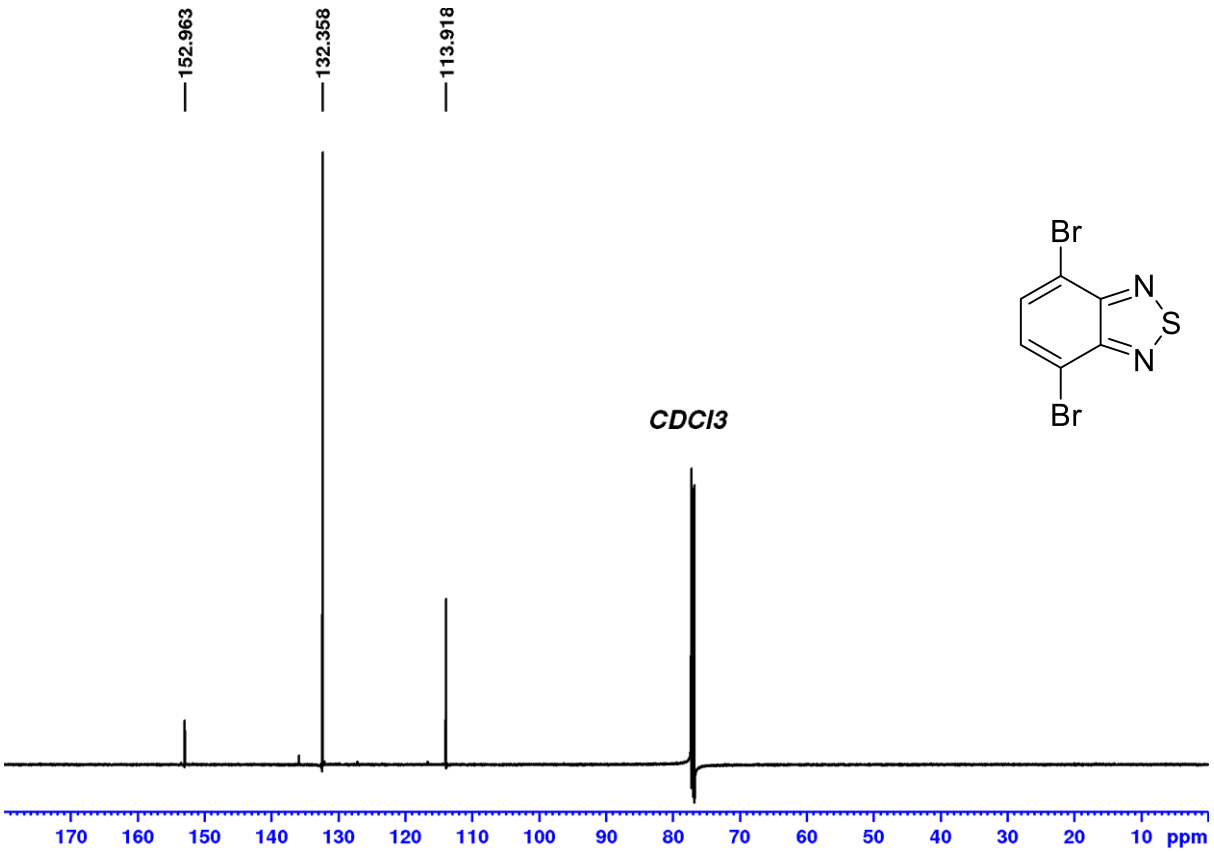

Figure 5.6. ^{1}H NMR (600 MHz, $CDCl_3$) spectrum of **3a.**

5.2.4. Synthesis of benzo[c][1,2,5]thiadiazole-4,7-dicarbonitrile (3b)

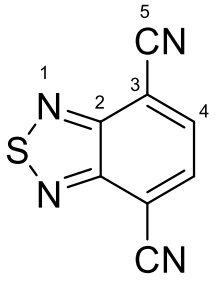

To a two-necked round bottomed flask equipped with a magnetic stirrer was added **3a** (1.00 g, 3.40 mmol, 1.00 equiv.) and copper(I) cyanide (0.99 g, 11.06 mmol, 3.25 equiv.). The flask was flushed and fitted with a septa-enclosed condenser and maintained under argon flow. Dry DMF (30 mL) was added and the reaction was refluxed (170 ºC) for 3.5 hours under argon atmosphere. A separate solution was prepared by stirring $FeCl_3 \cdot 6H_2O$ (4.53 g, 16.76 mmol, 4.93 equiv.) in 1.74 M HCl solution (23.5 mL). Once the refluxed mixture cooled to room temperature, the $FeCl_3 \cdot 6H_2O$ solution was added and the reaction mixture was further stirred for 1 hour at room temperature. The mixture was then extracted with dichloromethane (4 × 50 mL). The combined organic layers were washed with 6M HCl (3 × 75 mL), distilled water (3 × 50 mL), brine (3 × 50 mL) and dried with $MgSO_4$. Solvents were removed under reduced pressure to afford **3b** (0.52 g, 82 %) as an orange solid.

^{1}H NMR (600 MHz, $CDCl_3$): 8.07 (s, 1H , 4–**H**).

^{13}C NMR (151 MHz, $CDCl_3$): 110.7 (**5**), 113.8 (**3**), 134.5 (**4**), 152.4 (**2**).

LRMS (APCI, MeCN) m/z (rel. %): 187.0074 ($[M+H]^{\bullet+}$, 33)

HRMS (APCI, MeCN): Measured m/z: 187.0074. Calculated m/z for $[C_8H_3N_4S]^{\bullet+}$: 187.0073.

FTIR (ATR) ν_{max}/cm^{-1} : 2213, 2229 ($C^5 \equiv N$ stretch)

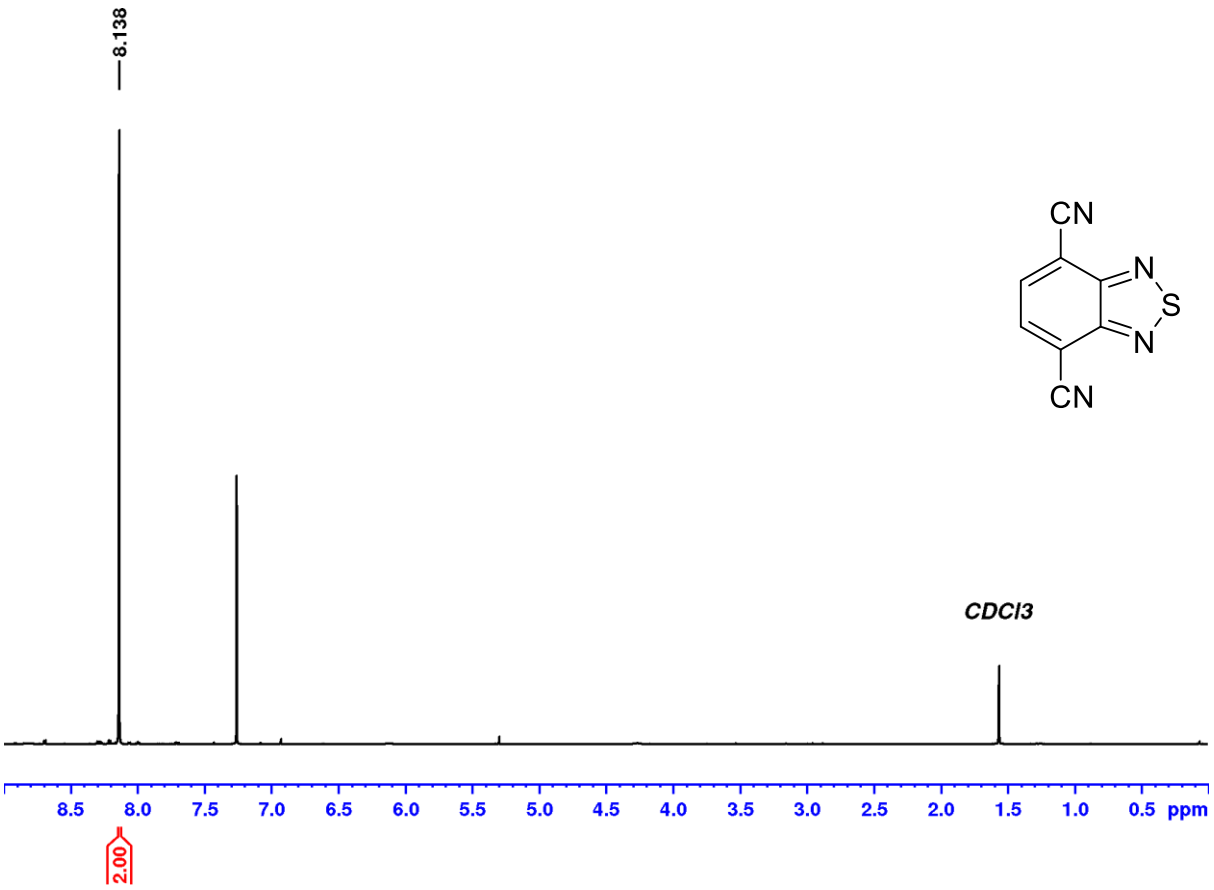

Figure 5.7. ^{1}H NMR (600 MHz, $CDCl_3$) spectrum of **3b.**

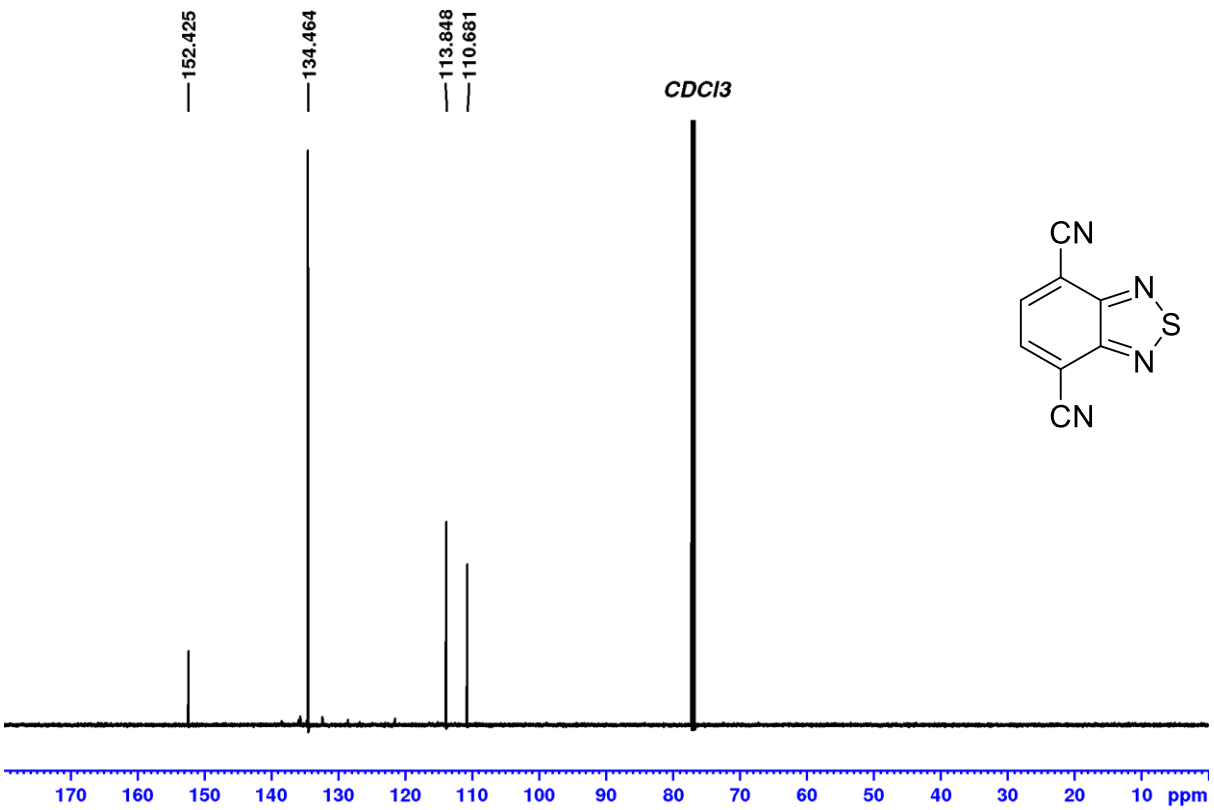

Figure 5.8. ^{13}C NMR (151 MHz, $CDCl_3$) spectrum of **3b.**

5.2.5. Procedure for the synthesis of terphenyls 3c, 3e and quaterphenyl 3h

To an oven–dried two-necked round-bottomed flask was added **3a** (1.0 equiv.), corresponding boronic acid (2.2 equiv.) and grounded $KF \cdot 2H_2O$ (4.1 equiv.). The flask was flushed with argon, fitted with a septa-enclosed condenser and maintained under argon flow. Dry THF (0.25 M with respect to **3a**) was added and the suspension bubbled with argon for 20 minutes. Pd_2dba_3 (0.5 mol%) and $HBF_4 \cdot P(t\text{–Bu})_3$ (1.2 mol%) was added and the suspension bubbled further for 2 minutes before a magnetic stirrer was added. The reaction was allowed to stir at room temperature overnight. The reaction mixture was then extracted with chloroform thrice. The organic layer was washed with water followed by brine and dried with MgSO4. Solvents were filtered and removed in vacuo, and the product recrystallized from toluene (or an MeCN **:** MePh mixture) yielding both **3c** (86 %) and **3e** (80 %) as yellow powders.

3h: was the by-product of the same reaction which yields **3e** with **3a** (1.0 equiv.), corresponding boronic acid (3.0 equiv.), $Pd(OAc)_2$ (0.05 equiv.), PPh_3 (0.2 equiv.), K_2CO_3 (6 equiv.) and DMF under heating at 100 ºC overnight. Reaction mixture was extracted with dichloromethane followed by evaporation *in vacuo*. The residue was purified by flash chromatography (Hexane/DCM/EtOAc).

5.2.5.1. Dimethyl 4,4'-(benzo[c][1,2,5]thiadiazole-4,7-diyl)dibenzoate (3c)

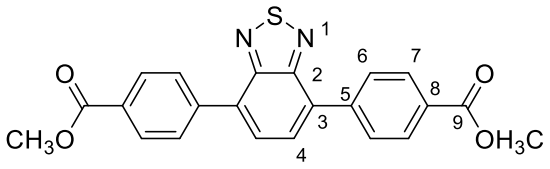

^{1}H NMR (600 MHz, $CDCl_3$): 3.97 (s, 3H, –O**H**$_3$C), 7.87 (s, 1H, 4–**H**), 8.06 (m *para*-[AA'XX'], 2H, 6–**H** [A/A'], |N|: $|^3J_{AX} + {}^5J_{AX'}|$ d = 8.5 Hz, |K|: $|^4J_{AA'} + {}^4J_{XX'}|$ ax q = 3.8 Hz), 8.21 (m *para*-[AA'XX'], 2H, 7–**H** [X/X'], |N|: $|^3J_{XA} + {}^5J_{XA'}|$ d = 8.5 Hz, |K|: $|^4J_{XX'} + {}^4J_{AA'}|$ ax q = 3.8 Hz).

^{13}C NMR (151 MHz, $CDCl_3$): 52.3 (–OH_3**C**), 128.5 (**4**), 129.3 (**6**), 129.9 (**7**), 133.0 (**3**), 135.6 (**8**), 141.6 (**5**), 153.8 (**2**), 166.8 (**9**).

LRMS (ESI, MeCN) m/z (rel. %): 427 ($[M + Na]^+$, 100)

HRMS (ESI, MeCN): Measured m/z: 427.0723. Calculated m/z for $[C_{22}H_{16}N_2O_4S + Na]^+$: 427.0728.

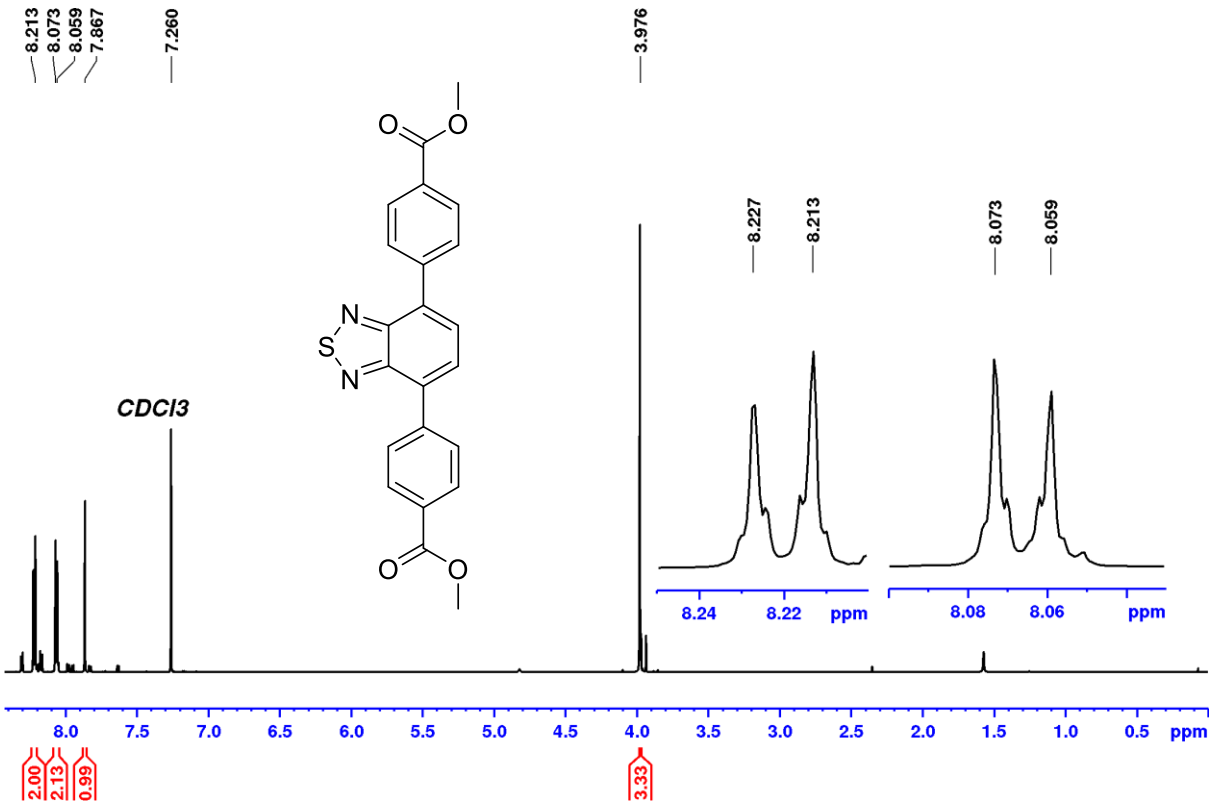

Figure 5.9. ^{1}H NMR (600 MHz, $CDCl_3$) spectrum of **3c.**

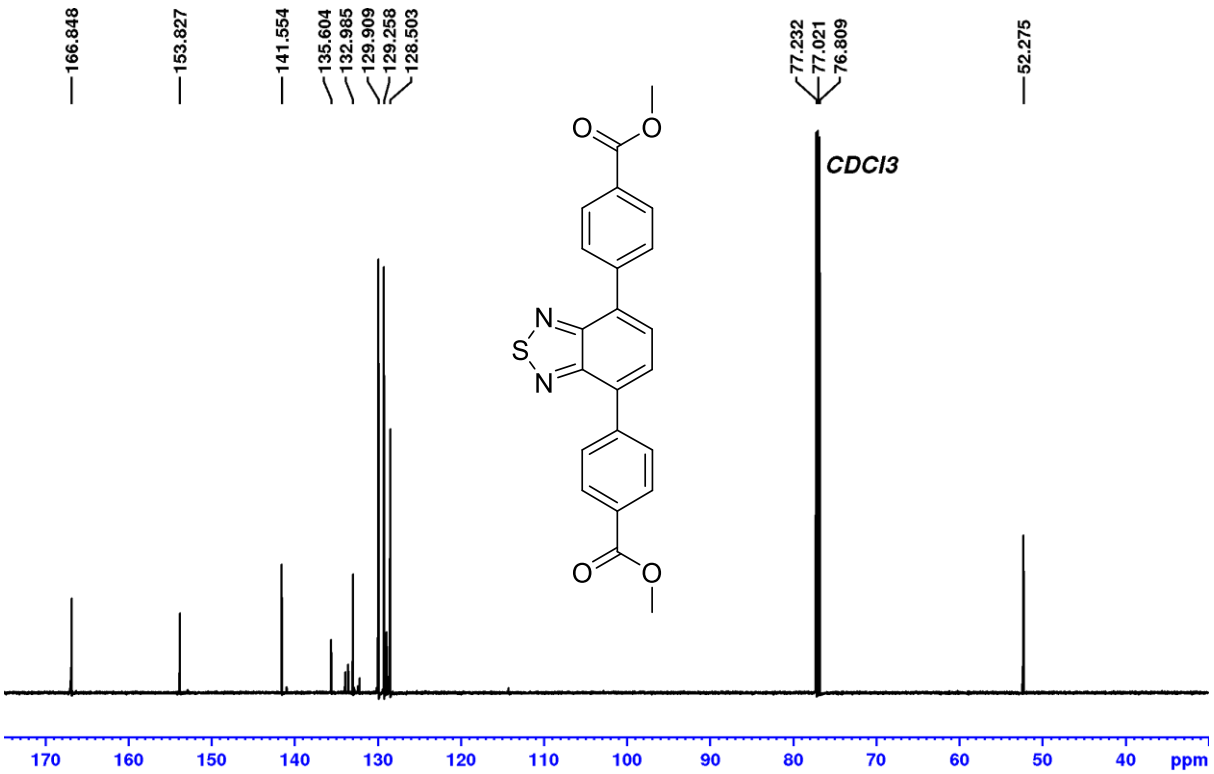

Figure 5.10. ^{13}C NMR (151 MHz, $CDCl_3$) spectrum of **3c.**

5.2.5.2. Diethyl 4,4'-(benzo[c][1,2,5]thiadiazole-4,7-diyl)dibenzoate (3e)

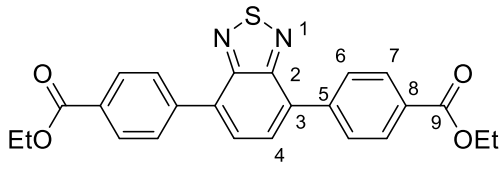

^{1}H NMR (600 MHz, $CDCl_3$): 1.44 (t, 3H, $–OH_2C\mathbf{H_3}C$, ^{3}J =7.2 Hz), 4.44 (q, 2H, $–O\mathbf{H_2}CH_3C$, ^{3}J =7.1 Hz), 7.87 (s, 1H, 4–**H**), 8.06 (m *para*-[AA'XX'], 2H, 6–**H** [A/A'], |N|: $|^{3}J_{AX} + {}^{5}J_{AX'}|$ d = 8.4 Hz, |K|: $|^{4}J_{AA'} + {}^{4}J_{XX'}|$ ax q = 3.8 Hz), 8.23 (m *para*-[AA'XX'], 2H, 7–**H** [X/X'], |N|: $|^{3}J_{XA} + {}^{5}J_{XA'}|$ d = 8.4 Hz, |K|: $|^{4}J_{XX'} + {}^{4}J_{AA'}|$ ax q = 3.8 Hz).

^{13}C NMR (151 MHz, $CDCl_3$): 14.3 ($–OH_2CH_3\mathbf{C}$), 61.1 ($–OH_2\mathbf{C}H_3C$), 128.5 (**4**), 129.3 (**6**), 129.9 (**7**), 130.3 (**8**), 133.0 (**3**), 141.5 (**5**), 153.9 (**2**), 166.4 (**9**).

LRMS (ESI, MeCN) m/z (rel. %): 455 ($[M + Na]^+$, 100)

HRMS (ESI, MeCN): Measured m/z: 455.1036. Calculated m/z for $[C_{22}H_{16}N_2O_4S + Na]^+$: 455.1041.

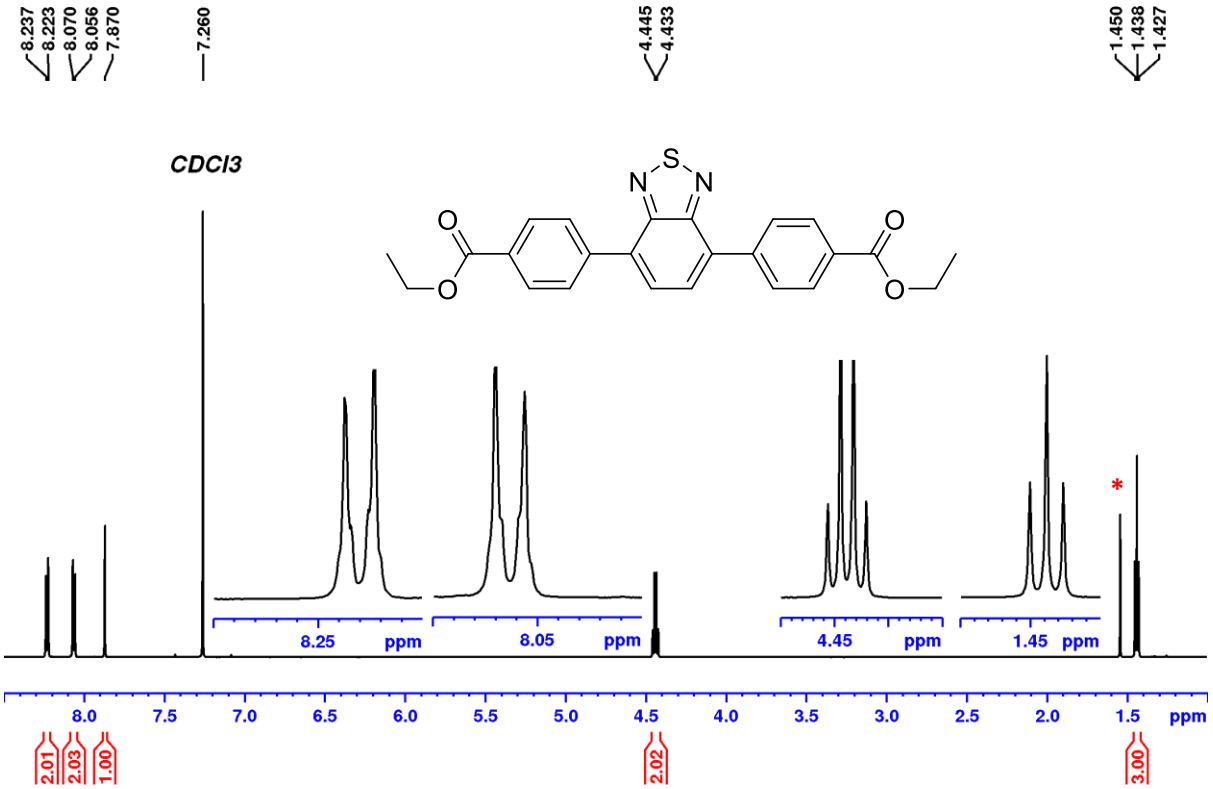

Figure 5.11. ^{1}H NMR (600 MHz, $CDCl_3$) spectrum of **3e.** * residual MeCN from recrystallization solvent.

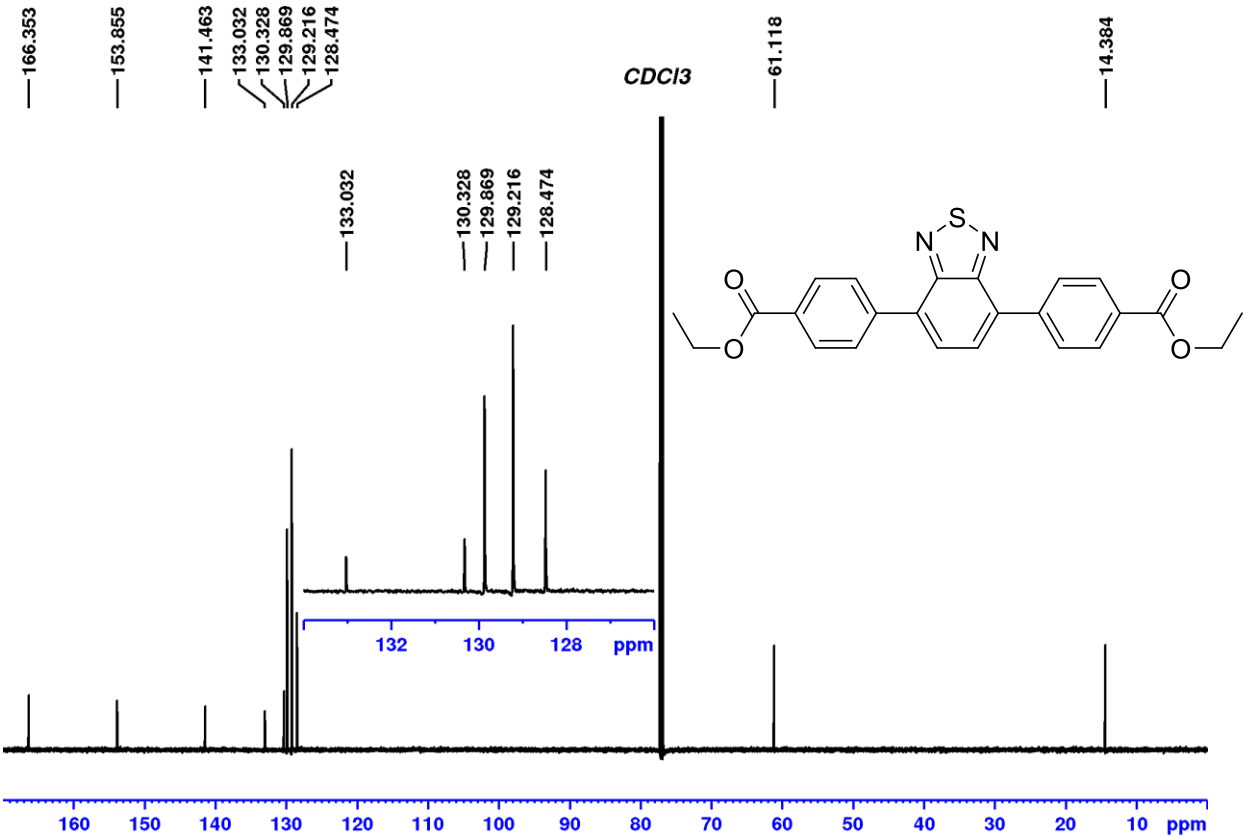

Figure 5.12. ^{13}C NMR (151 MHz, $CDCl_3$) spectrum of **3e.**

5.2.5.3. Diethyl 4,4'-([4,4'-bibenzo[c][1,2,5]thiadiazole]-7,7'-diyl)dibenzoate (3h)

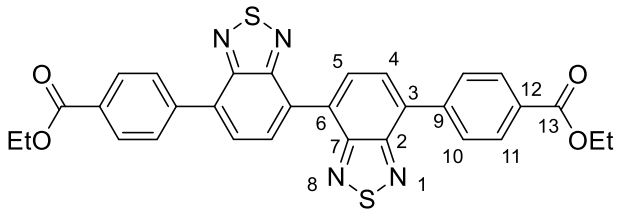

3h; yield= n.d.

^{1}H NMR (600 MHz, $CDCl_3$): 1.44 (t, 3H, –OH_2 C**H_3**C, ^{3}J =7.2 Hz), 4.45 (q, 2H, –O**H_2**CH_3C, ^{3}J =7.1 Hz), 7.98 (d, 1H, 4–**H,** ^{3}J =7.4 Hz), 8.10 (m *para*-[AA'XX'], 2H, 10–**H** [A/A'], |N|: $|^{3}J_{AX} + {}^{5}J_{AX'}|$ d = 8.4 Hz), 8.25 (m *para*-[AA'XX'], 2H, 11–**H** [X/X'], |N|: $|^{3}J_{XA} + {}^{5}J_{XA'}|$ d = 8.4 Hz), 8.47 (d, 1H, 5–**H,** ^{3}J =7.3 Hz).

^{13}C NMR (151 MHz, $CDCl_3$): 14.4 (–OH_2CH_3**C**), 61.1 (–OH_2**C**H_3C), 128.4 (**4**), 129.3 (**10**), 129.4 (**6**), 129.9 (**11**), 130.4 (**12**), 131.2 (**5**), 133.4 (**3**), 141.5 (**9**), 153.8 (**2**), 154.2 (**7**), 166.4 (**13**).

LRMS (ESI, MeOH) m/z (rel. %): 589 ($[M + Na]^+$, 54), 1155 ($[2M + Na]^+$, 51)

HRMS (ESI, MeOH): Measured m/z: 589.0978. Calculated m/z for $[C_{30}H_{22}N_4O_4S_2 + Na]^+$: 589.0975.

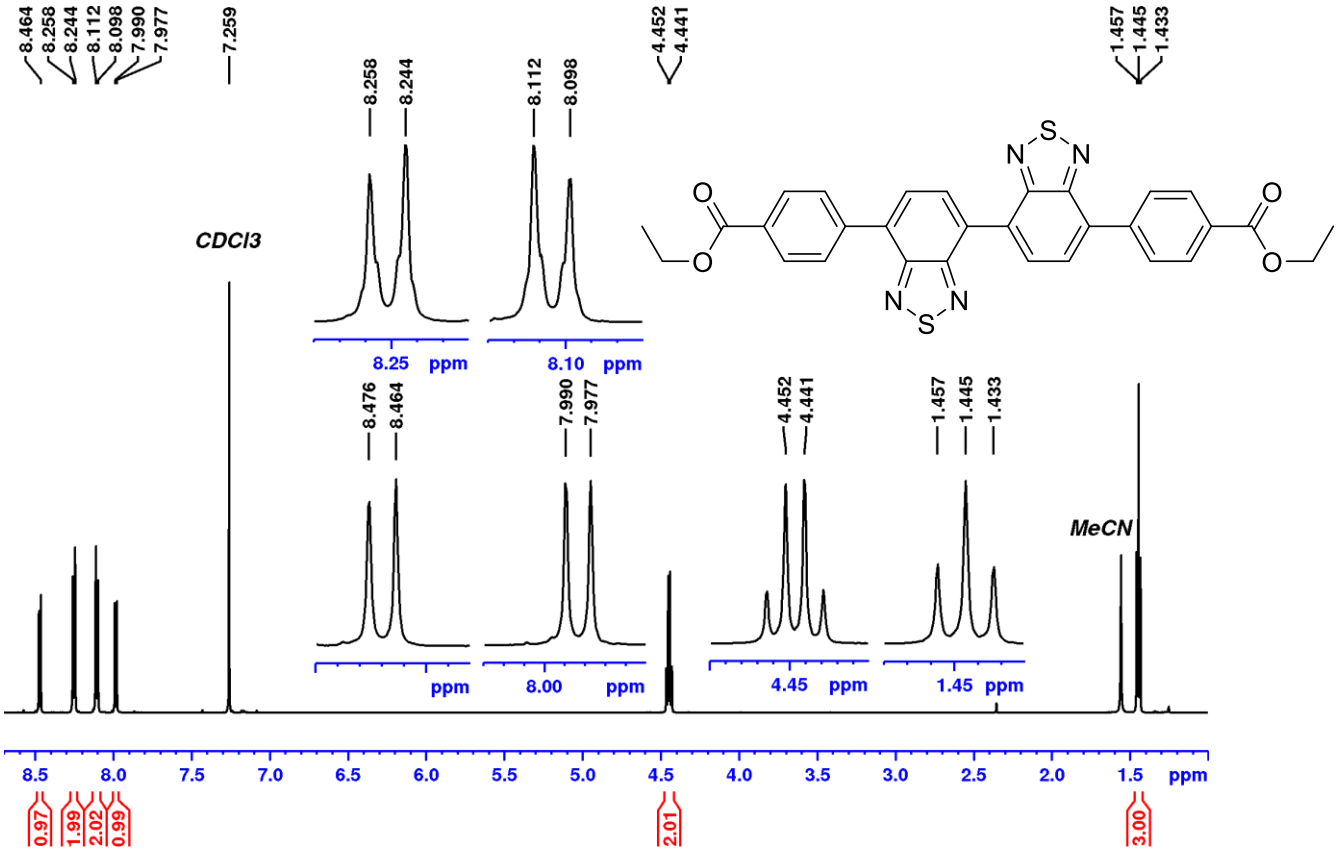

Figure 5.13. ^{1}H NMR (600 MHz, $CDCl_3$) spectrum of **3h.**

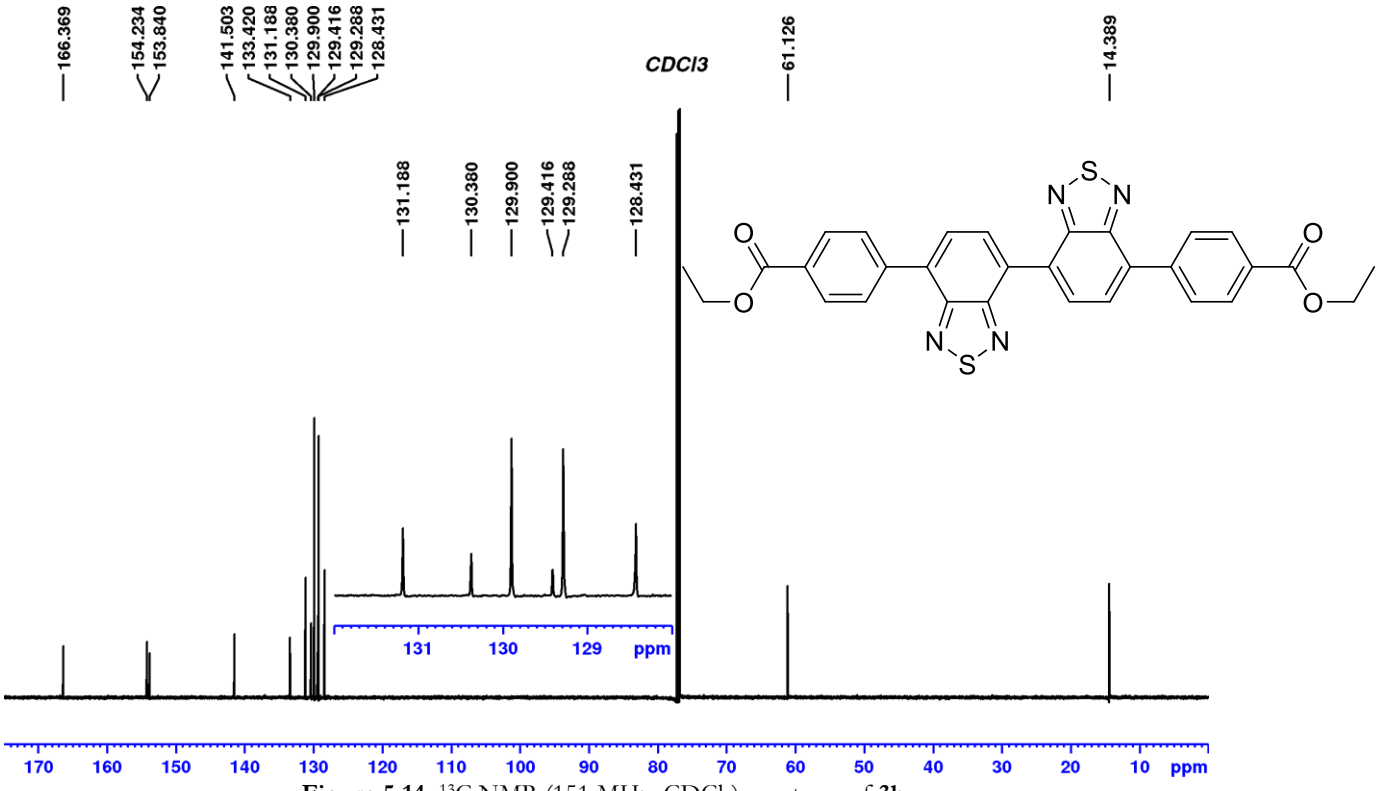

Figure 5.14. ^{13}C NMR (151 MHz, $CDCl_3$) spectrum of **3h.**

5.2.6. Synthesis of dimethyl 4,4'-(benzo[c][1,2,5]thiadiazole-4,7-diyl)bis(3-nitrobenzoate) (3d)

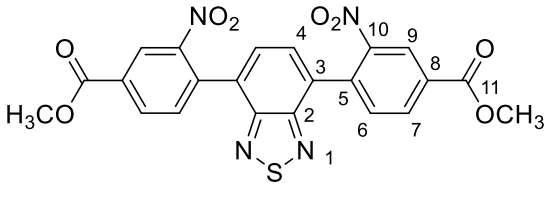

To an oven–dried two-necked round-bottomed flask was added **3a** (1.15 g, 3.90 mmol, 1.0 equiv.), corresponding boronic acid (3.0 equiv.) and grounded $KF{\cdot}2H_2O$ (9.0 equiv.). The flask was flushed with argon, fitted with a septa-enclosed condenser and maintained under argon flow. Dry THF (0.25 M with respect to **3a**) was added and the suspension bubbled with argon for 20 minutes. Pd_2dba_3 (0.0154 g, 0.0168 mmol, 0.4 mol%) and $HBF_4{\cdot}P(t\text{–}Bu)_3$ (0.0124 g, 0.0427 mmol, 1.1 mol%) was added and the suspension bubbled further for 2 minutes before a magnetic stirrer was added. The reaction was refluxed for one hour under argon atmosphere. After cooling to room temperature, MeOH (5× the initial THF volume) was added under stirring for 30 minutes. Thereafter, the reaction flask was cooled in the fridge overnight followed by filtration. The solids were washed with extra cold methanol, dried and redissolved in DCM. The mixture was vacuum filtered with DCM through a short silica plug. DCM was removed in vacuo and the residue recrystallized with MeCN: MePh to yield **3d** (1.66 g, 3.35 mmol, 86%) as a yellow solid.

^{1}H NMR (600 MHz, $CDCl_3$): 4.04 (s, 3H, –O**H$_3$**C), 7.75 (d, 1H, 6–**H**, ^3J =8.2 Hz), 7.76 (s, 1H, 4–**H**), 8.42 (dd, 1H, 7–**H,** ^3J =7.9 Hz, ^4J =1.6 Hz), 8.81 (d, 1H, 9–**H**, ^4J =1.6 Hz),.

^{13}C NMR (151 MHz, $CDCl_3$): 52.9 (–OH_3**C**), 126.1 (**9**), 128.2 (**4**), 131.5 (**3**), 131.8 (**8**), 133.0 (**6**), 133.8 (**7**), 135.9 (**5**), 149.3 (**10**), 152.5 (**2**), 164.7 (**11**).

LRMS (ESI, MeOH) m/z (rel. %): 517 ($[M + Na]^+$, 100), 1011 ($[2M + Na]^+$, 12)

HRMS (ESI, MeOH): Measured m/z: 517.0424. Calculated m/z for $[C_{22}H_{14}N_4O_8S + Na]^+$: 517.0429.

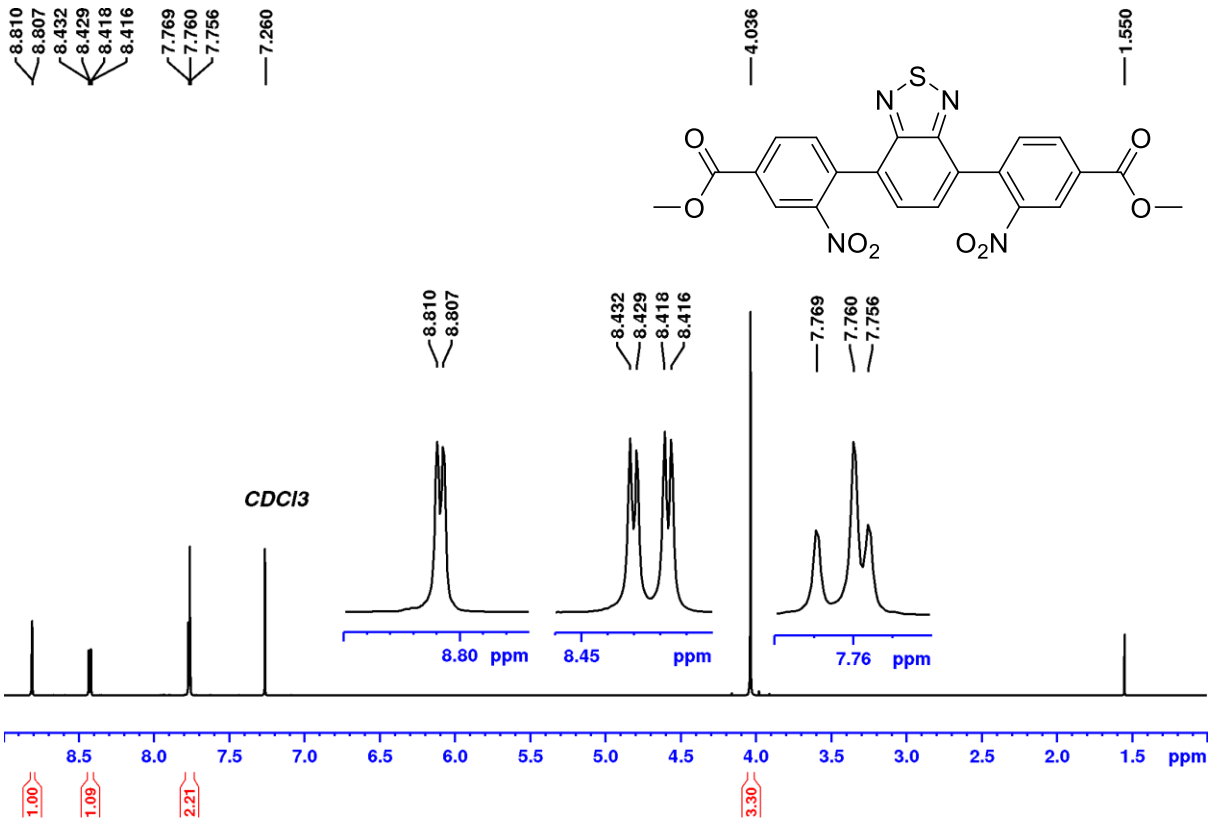

Figure 5.15. ^{1}H NMR (600 MHz, $CDCl_3$) spectrum of **3d.**

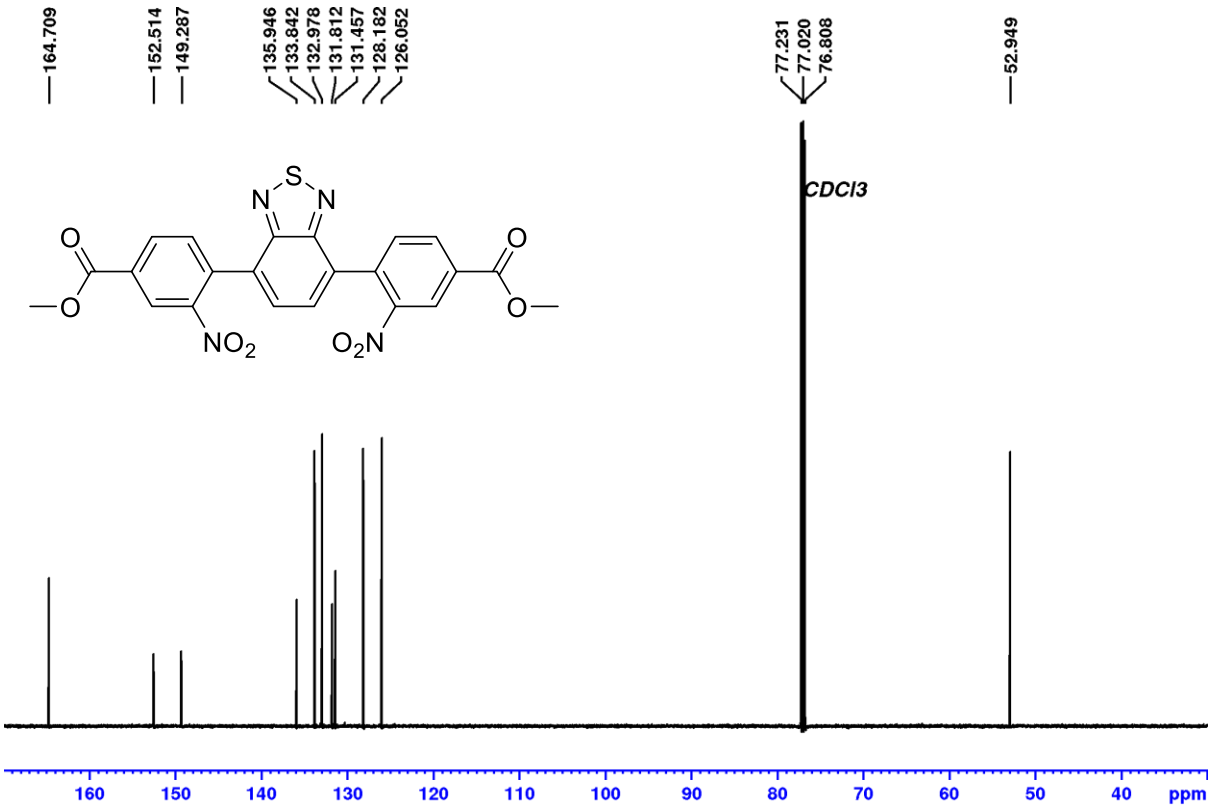

Figure 5.16. ^{13}C NMR (151 MHz, $CDCl_3$) spectrum of **3d.**

5.2.7. Procedure for the synthesis of heteroaryl-fused biphenyls 3f and 3g

To an oven–dried two-necked round-bottomed flask was added **3a** (1.0 equiv.), corresponding boronic acid (1.0 equiv.) and grounded $KF{\cdot}2H_2O$ (4.5 equiv.). The flask was flushed with argon, fitted with a septa-enclosed condenser and maintained under argon flow. Dry THF (0.25 M with respect to **3a**) was added and the suspension bubbled with argon for 20 minutes. Pd_2dba_3 (0.5 mol%) and $HBF_4{\cdot}P(t\text{–}Bu)_3$ (1.2 mol%) was added and the suspension bubbled further for 2 minutes before a magnetic stirrer was added. The reaction was refluxed for one hour under argon atmosphere. After cooling to room temperature, the reaction mixture was extracted with DCM thrice and the solvent was removed under reduced pressure. The residue was purified by flash chromatography with Hex: EtOAc (8:2).

3f and **3g** were isolated in yields of 30% and 31% respectively as white-fluffy and yellow solids.

5.2.7.1. Methyl 4-(7-bromobenzo[c][1,2,5]thiadiazol-4-yl)-3-nitrobenzoate (3f)

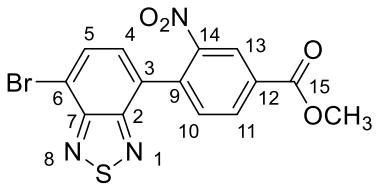

^{1}H NMR (600 MHz, $CDCl_3$): 4.02 (s, 3H, –O**H**$_3$C), 7.52 (d, 1H, 4–**H**, ^3J =7.4 Hz), 7.65 (d, 1H, 10–**H**, ^3J =7.9 Hz), 7.97 (d, 1H, 5–**H,** ^3J =7.4 Hz), 8.38 (dd, 1H, 11–**H,** ^3J =7.9 Hz, ^4J =1.7 Hz) 8.78 (d, 1H, 13–**H**, ^4J =1.6 Hz).

^{13}C NMR (151 MHz, $CDCl_3$): 52.9 (–OH_3**C**), 126.1 (**9**), 128.2 (**4**), 131.5 (**3**), 131.8 (**8**), 133.0 (**6**), 133.8 (**7**), 135.9 (**5**), 149.3 (**10**), 152.5 (**2**), 164.7 (**11**).

LRMS (ESI, MeOH) m/z (rel. %): 415.9 ($[M + Na]^+$, 96)

HRMS (ESI, MeOH): Measured m/z: 415.9311. Calculated m/z for $[C_{14}H_8BrN_3O_4S + Na]^+$: 415.9217.

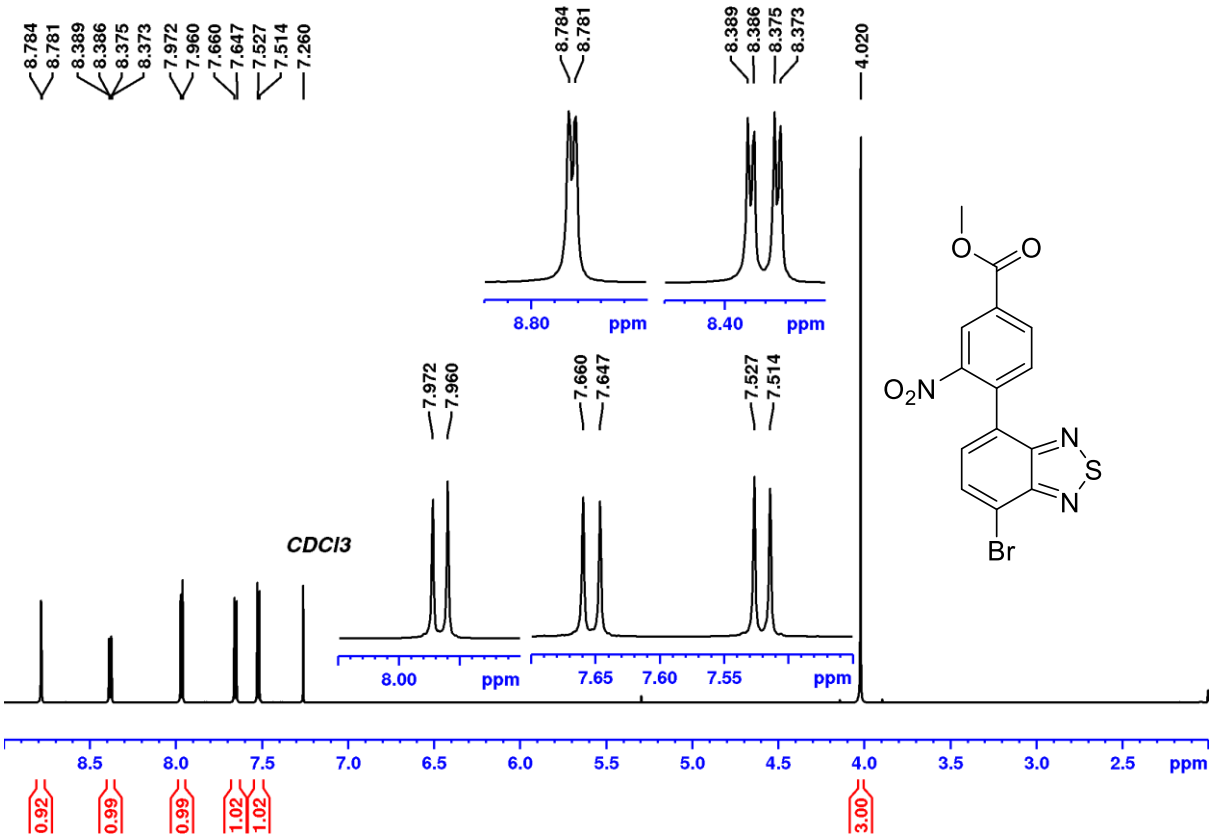

Figure 5.17. ^{1}H NMR (600 MHz, $CDCl_3$) spectrum of **3f.**

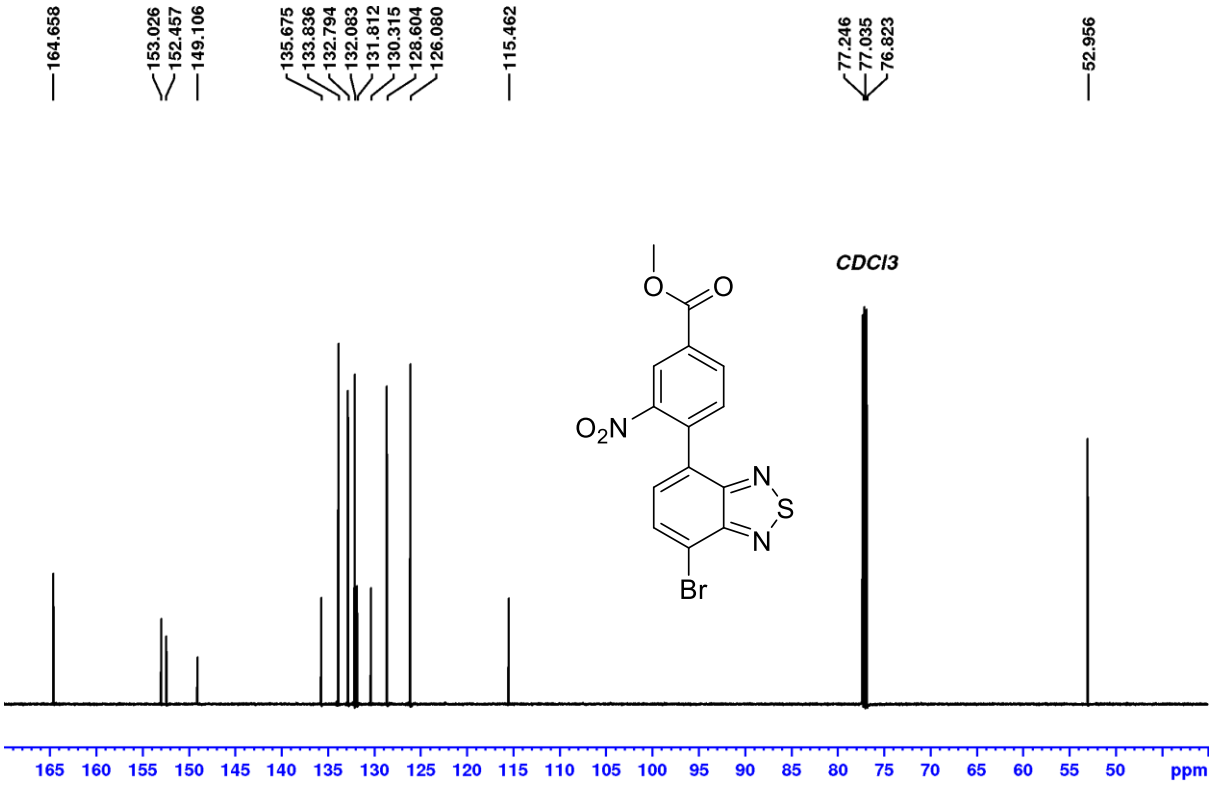

Figure 5.18. ^{13}C NMR (151 MHz, $CDCl_3$) spectrum of **3f.**

5.2.7.2. Ethyl 4-(7-bromobenzo[c][1,2,5]thiadiazol-4-yl)benzoate (3g)

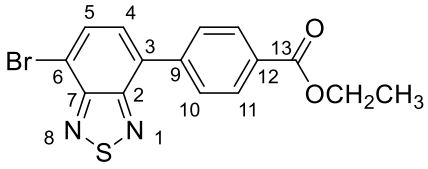

^{1}H NMR (600 MHz, $CDCl_3$): 1.42 (t, 3H, $–OH_2C\mathbf{H_3}C$, ^{3}J =7.1 Hz), 4.43 (q, 2H, $–O\mathbf{H_2}CH_3C$, ^{3}J =7.1 Hz), 7.63 (d, 1H, 4–**H**, ^{3}J =7.5 Hz), 7.95 (d, 1H, 5–**H**, ^{3}J =7.5 Hz), 7.98 (m *para*-[AA'XX'], 2H, 10–**H** [A/A'], |N|: $|^{3}J_{AX} + {}^{5}J_{AX'}|$ d = 8.5 Hz), 8.20 (m *para*-[AA'XX'], 2H, 11–**H** [X/X'], |N|: $|^{3}J_{XA} + {}^{5}J_{XA'}|$ d = 8.4 Hz).

^{13}C NMR (151 MHz, $CDCl_3$): 14.4 ($–OH_2CH_3\mathbf{C}$), 61.2 ($–OH_2\mathbf{C}H_3C$), 114.2 (**6**), 128.4 (**4**), 129.1 (**10**), 129.9 (**11**), 130.5 (**3**), 132.2 (**5**), 132.9 (**12**), 140.8 (**9**), 152.5 (**2**), 153.9 (**7**), 166.3 (**13**).

LRMS (ESI, MeOH) m/z (rel. %): 387 ($[M + Na + 2H]^+$, 100), 385 ($[M + Na]^+$, 95)

HRMS (ESI, MeOH): Measured m/z: 384.9616. Calculated m/z for $[C_{15}H_{11}BrN_2O_2S + Na]^+$: 384.9622.

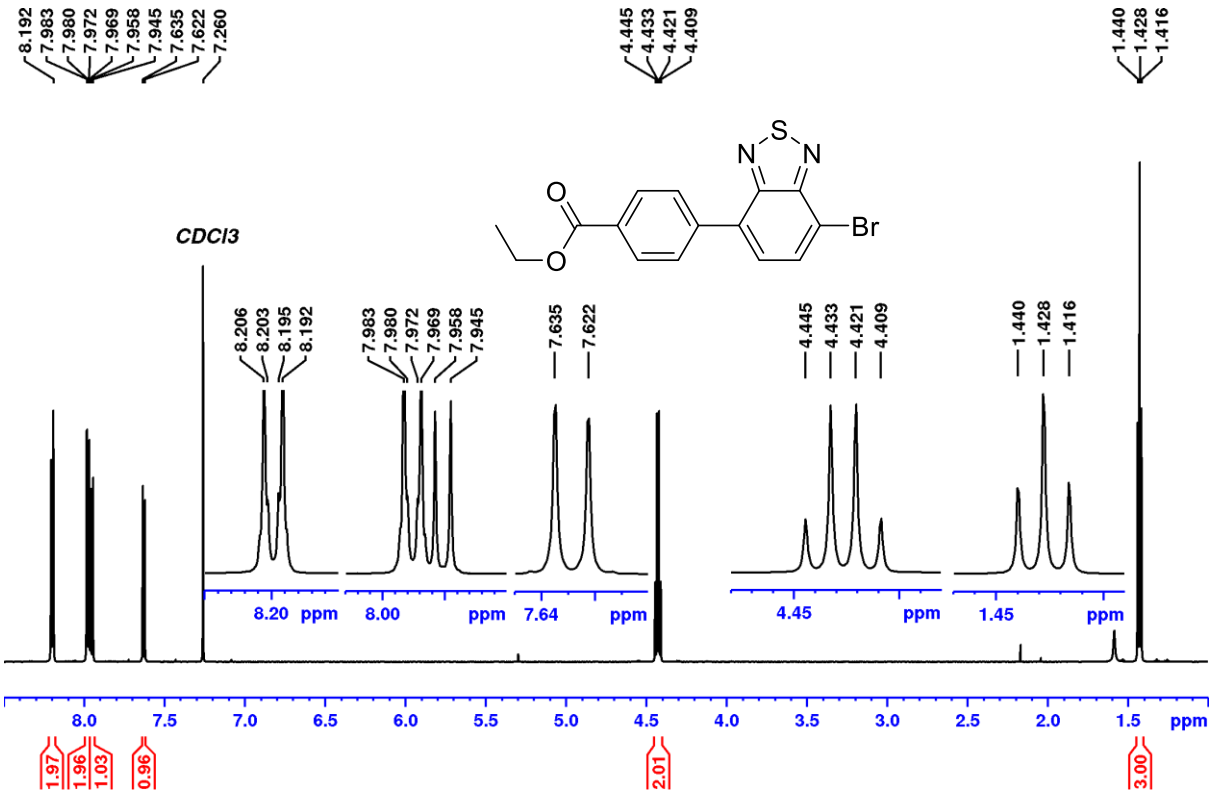

Figure 5.19. ^{1}H NMR (600 MHz, $CDCl_3$) spectrum of **3g.**

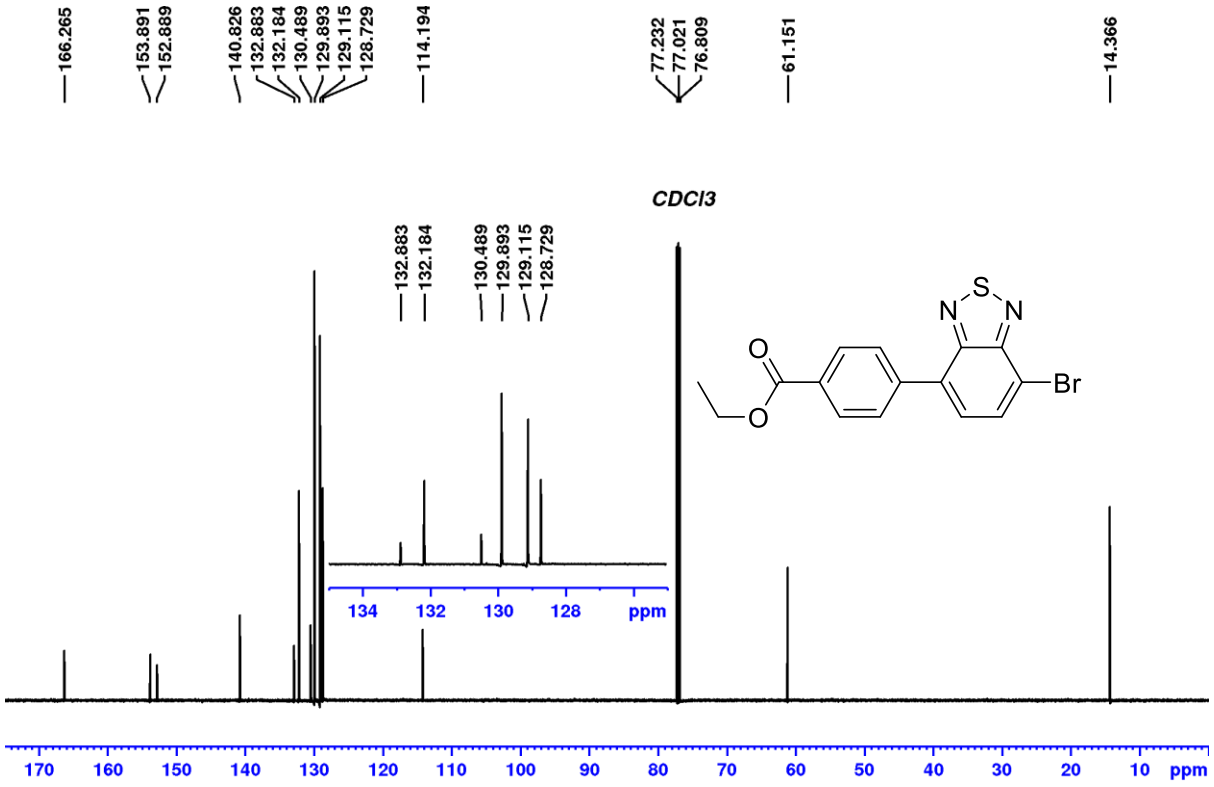

Figure 5.20. ^{13}C NMR (151 MHz, $CDCl_3$) spectrum of **3g.**

5.2.8. Procedure for the synthesis of disubstituted o-phenylene diamines 4a and 4b

To an oven dried round-bottomed flask equipped with a magnetic stirrer was added the 10, 13–disubstituted benzothiadiazoles (**3a** or **3b**) (1.0 equiv.), THF (15 mL) and ethanol (25 mL). In an ice-bath, $NaBH_4$ (7 equiv.) was added to the cooled solution in small portions under stirring. Catalytic amounts of $CoCl_2 \cdot 6H_2O$ (1 mol%) was added releasing H_2S gas. The open mixture was stirred at room temperature overnight. Thereafter, the mixture was diluted with THF/ethanol and then vacuum filtered through a filter paper and Celite. The solvents were then evaporated. Water was added to the residue and the mixture extracted with DCM thrice. The organic phases were washed with water and dried using $MgSO_4$. Solvents were removed *in vacuo* yielding **4a** (96 %) as purple-violet flakes and **4b** (60 %) as yellow solid.

5.2.8.1. 3,6–dibromobenzene–1,2–diamine 4a

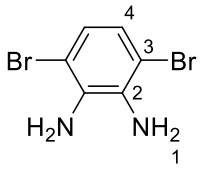

^{1}H NMR (600 MHz, $CDCl_3$): 3.90 (br s, 4H, **H**–N^1), 6.84 (s, 2H, **H**–4).

^{13}C NMR (151 MHz, $CDCl_3$): 109.7 (**3**), 123.3 (**4**), 133.7 (**2**).

..

5.2.8.2. 2,3-diaminoterephthalonitrile 4b

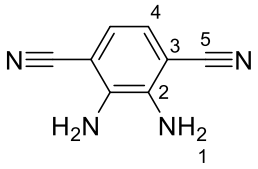

^{1}H NMR (600 MHz, $CDCl_3$): 4.25 (br s, 4H, **H**–N^1), 6.93 (s, 2H, **H**–4).

^{13}C NMR (151 MHz, $CDCl_3$): 100.9 (**5**), 116.3 (**3**), 121.5 (**4**), 138.9 (**2**).

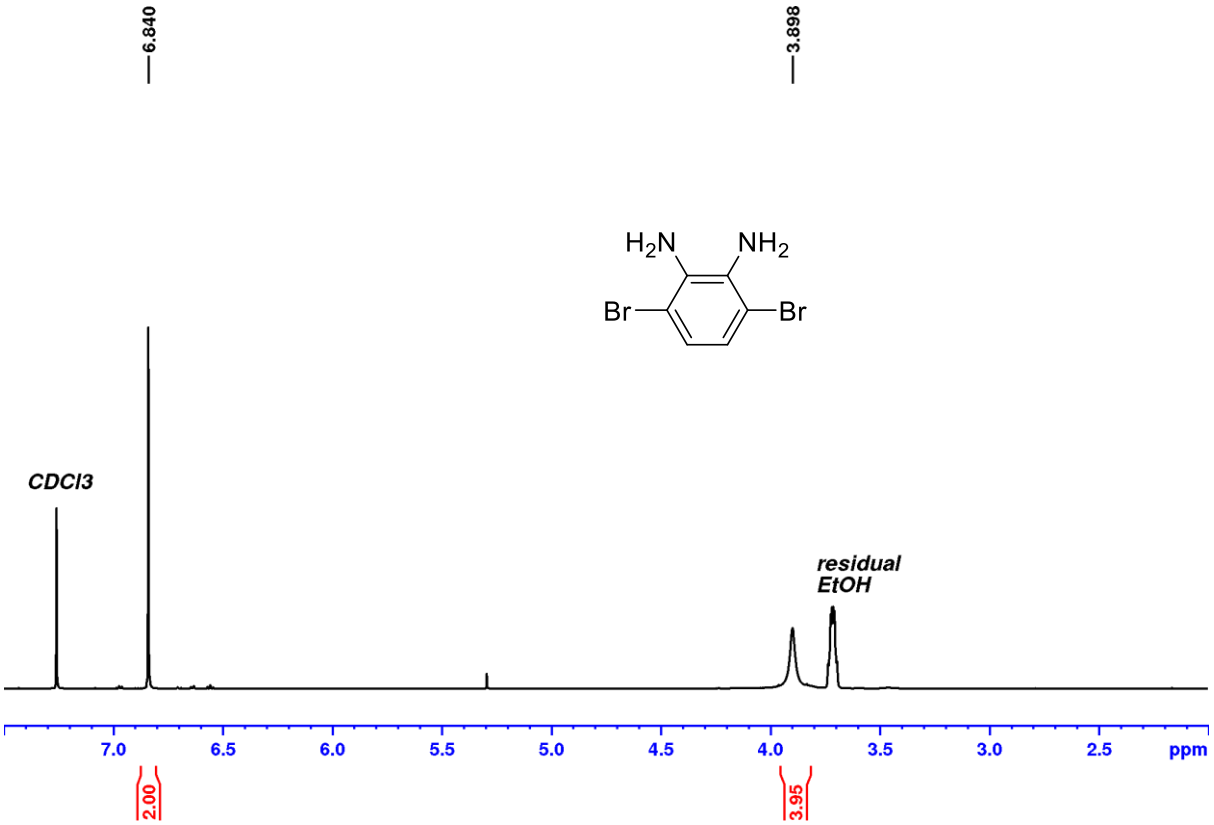

Figure 5.21. ^{1}H NMR (600 MHz, $CDCl_3$) spectrum of **4a.**

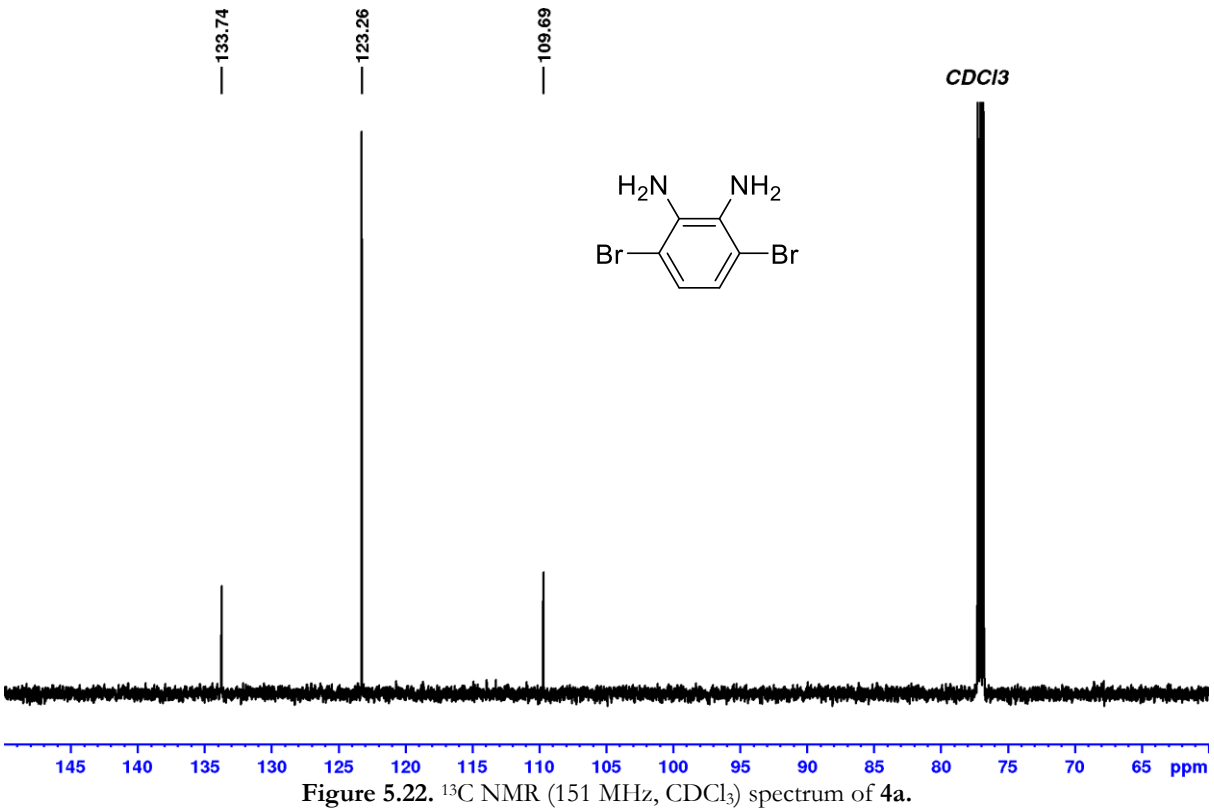

Figure 5.22. ^{13}C NMR (151 MHz, $CDCl_3$) spectrum of **4a.**

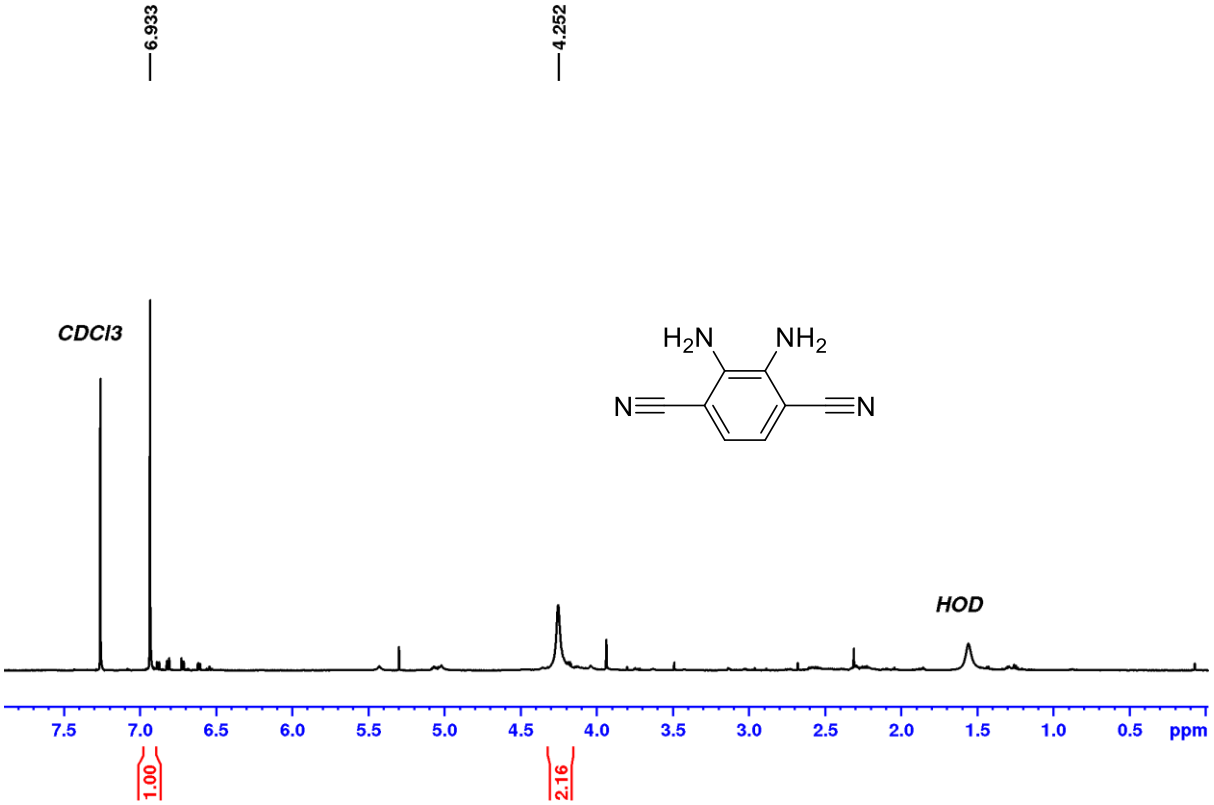

Figure 5.23. ^{1}H NMR (600 MHz, $CDCl_3$) spectrum of **4b.**

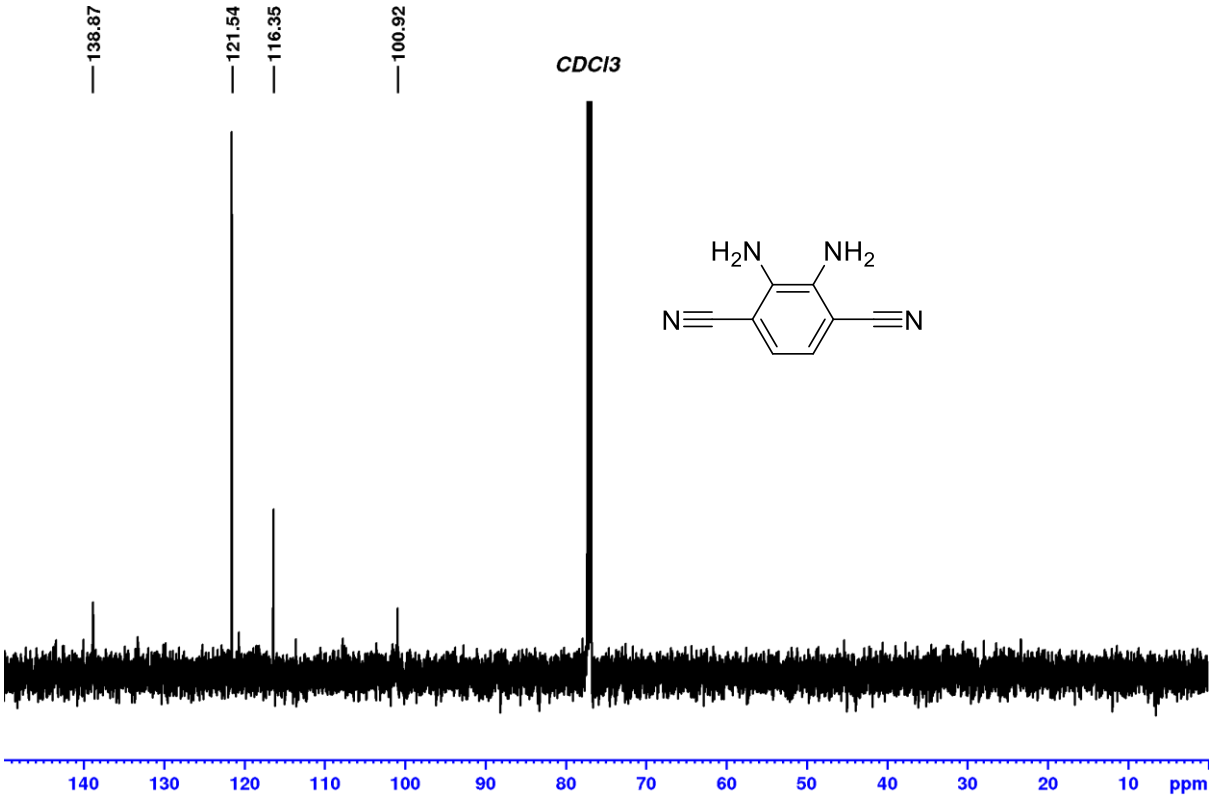

Figure 5.24. ^{13}C NMR (151 MHz, $CDCl_3$) spectrum of **4b.**

5.2.9. Synthesis of dimethyl 2',3'-diamino-2,2''-dinitro-[1,1':4',1''-terphenyl]-4,4''-dicarboxylate (4c)

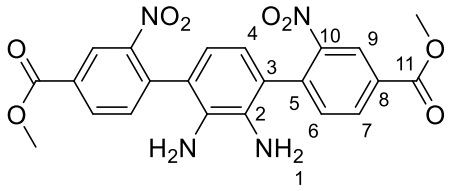

To an oven–dried two-necked round-bottomed flask was added **4a** (1.0 equiv.), corresponding boronic acid (3.0 equiv.) and grounded $KF{\cdot}2H_2O$ (9.0 equiv.). The flask was flushed with argon, fitted with a septa-enclosed condenser and maintained under argon flow. Dry THF (0.25 M with respect to **3a**) was added and the suspension bubbled with argon for 20 minutes. Pd_2dba_3 (0.5 mol%) and $HBF_4{\cdot}P(t\text{–Bu})_3$ (1.2 mol%) was added and the suspension bubbled further for 2 minutes before a magnetic stirrer was added. The reaction was refluxed for one hour under argon atmosphere. After cooling to room temperature, the reaction mixture was extracted with DCM thrice and the solvent was removed under reduced pressure. The residue was purified by flash chromatography with Hex: DCM: EtOAc. The product was further recrystallized using MeCN to obtain **4c** (69%) as orange crystals.

^{1}H NMR (600 MHz, $CDCl_3$): 3.36 (br s, 2H, **H**–N^1), 4.01 (s, 3H, –O**H**$_3$C), 6.59 (major s) + 6.61 (minor s) (1H, 4–**H**), 7.76 (s, 1H, 4–**H**), 7.58 (minor d, ^3J =7.9 Hz) + 7.65 (major d, ^3J =7.9 Hz) (1H, 6–**H**), 8.32-8.33 (major + minor dd, ^3J =7.9 Hz, ^4J =1.6 Hz) (1H, 7–**H**), 8.60 (major d, ^4J =1.4 Hz) + 8.62 (minor br s) (1H, 9–**H**).

^{13}C NMR (151 MHz, $CDCl_3$): 52.9 (–OH_3**C**), 119.9 (**4**), 124.3 (major) + 124.5 (minor) (**3**), 125.5 (major) + 125.7 (minor) (**9**), 131.1 (**8**), 132.5 (**2**), 132.9 (minor) + 133.2 (major) (**6**), 133.39 (minor) + 133.43 (major) (**7**), 137.7 (**5**), 149.70 (minor) + 149.75 (major) (**10**), 164.8 (**11**)

LRMS (ESI, MeOH) m/z (rel. %): 489 ($[M + Na]^+$, 100)

HRMS (ESI, MeOH): Measured m/z: 489.1017. Calculated m/z for $[C_{22}H_{18}N_4O_8 + Na]^+$: 489.1022.

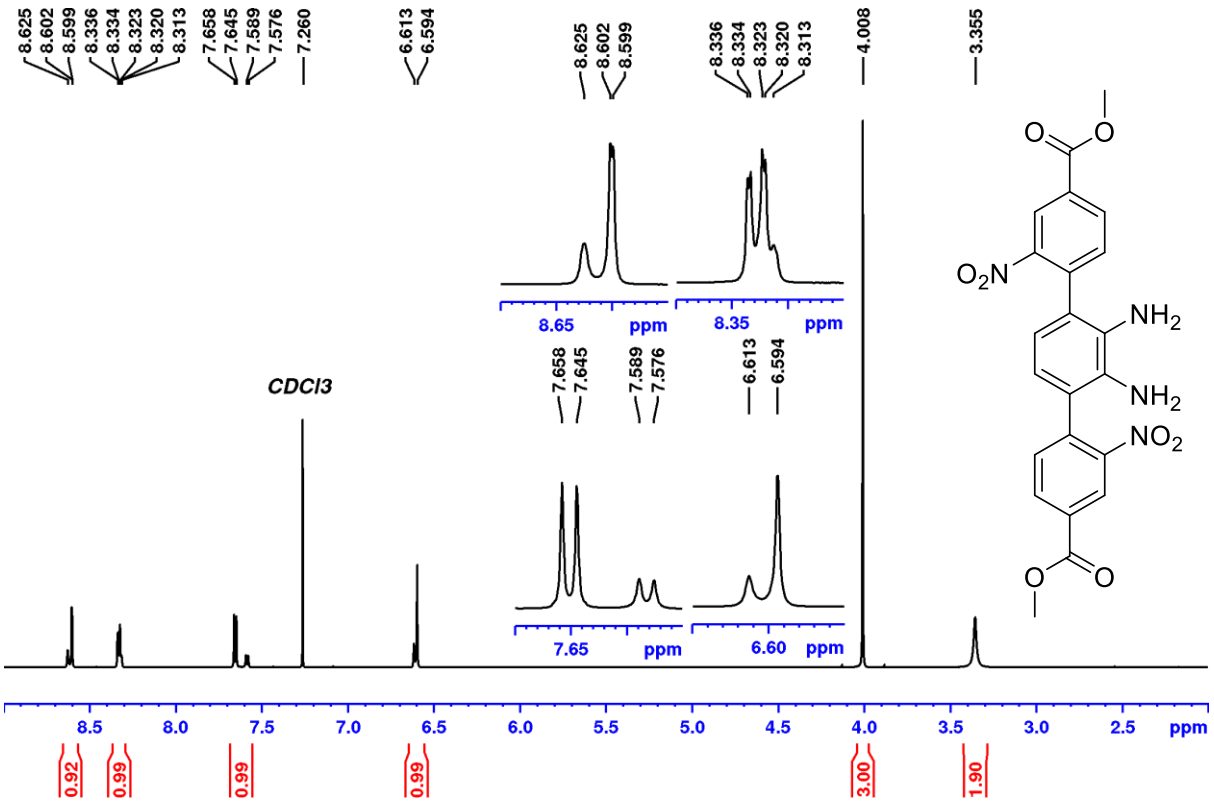

Figure 5.25. ^{1}H NMR (600 MHz, $CDCl_3$) spectrum of **4c.**

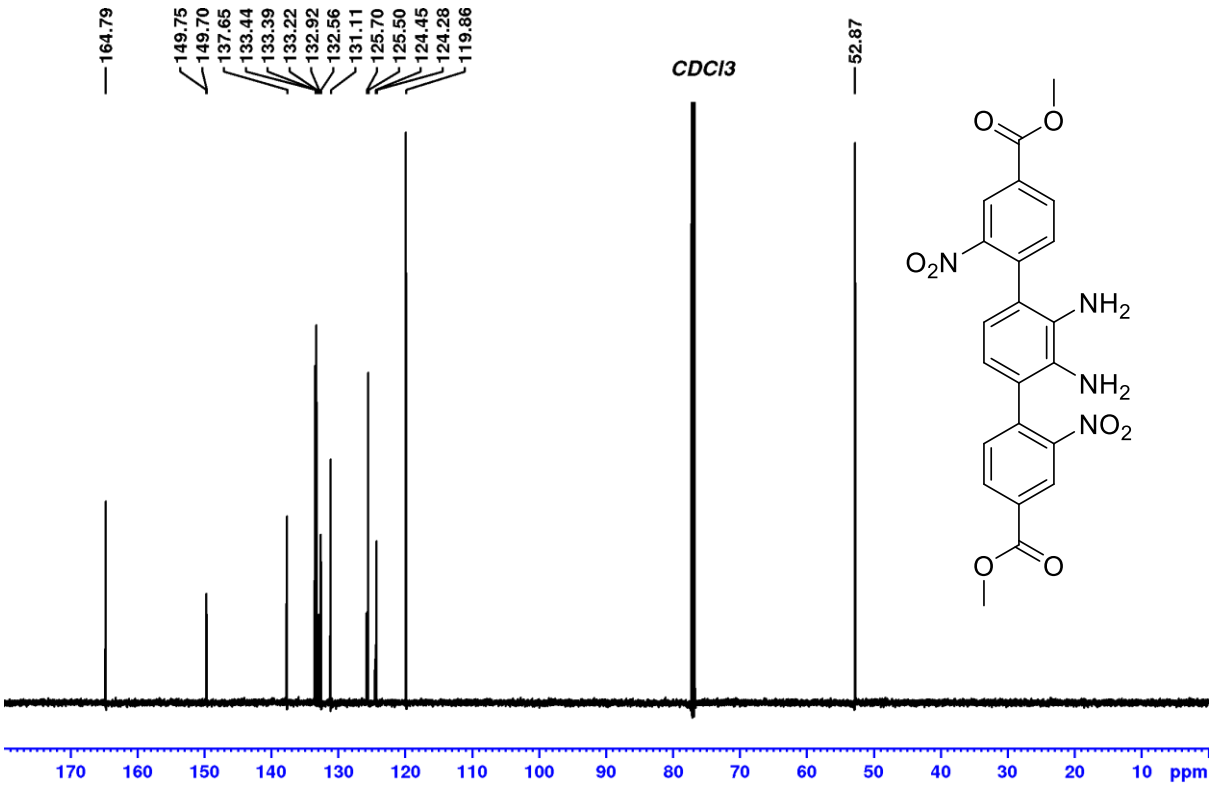

Figure 5.26. ^{13}C NMR (151 MHz, $CDCl_3$) spectrum of **4c.**

5.2.10. Procedure for the synthesis of Ligands L1 – L4.

5.2.10.1. For L1, L4

To an oven-dried two-necked round-bottomed flask equipped with a magnetic stirrer was added phendione **1a** (1.0 equiv.) and the phenylene diamine **1b** or **4c** (1.0 equiv.). The flask was flushed and fitted with a septa-enclosed condenser and maintained under argon flow. Sieve-dried MeOH was syringed into the flask followed by degassing with argon gas for 10 minutes, The mixture was then refluxed overnight under argon atmosphere. The precipitate was vacuum-filtered, washed with cold MeOH followed by water and dried *in vacuo* at 70 ºC overnight yielding **L1** (97 %) as white-brown crystals and **L4** (89 %) as grey solid.

5.2.10.2. For L2 and L3

To an oven-dried two-necked round-bottomed flask equipped with a magnetic stirrer was added phendione **1a** (1.0 equiv.), the phenylene diamine **4a** or **4b** (1.0 equiv.) and K_2CO_3 (0.4 equiv.). The flask was flushed and fitted with a septa-enclosed condenser and maintained under argon flow. Sieve-dried EtOH was syringed into the flask followed by degassing with argon gas for 10 minutes, The mixture was then refluxed overnight under argon atmosphere. The precipitate was vacuum-filtered, washed with hot water, acetone and diethyl ether, followed by drying *in vacuo* at 70 ºC overnight yielding **L2** (66 %) as yellow powder and **L3** (64 %) as black charcoal-like solid.

5.2.10.3. Dipyrido[3,2-a:2',3'-c]phenazine L1

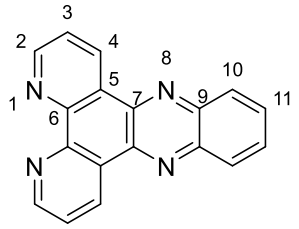

^{1}H NMR (600 MHz, Py-d_5): 7.69 (dd, 1H, 3–**H**, ^{3}J =8.0 Hz, ^{3}J =4.3 Hz), 7.88 (m *ortho*-[AA'XX'], 1H, 11–**H** [X/X'], |N|: $|^{3}J_{XA} + {}^{4}J_{XA'}|$ d = 9.8 Hz), 8.41 (m *ortho*-[AA'XX'], 1H, 10–**H** [A/A'], |N|: $|^{3}J_{AX} + {}^{4}J_{AX'}|$ d = 9.8 Hz), 9.32 (dd, 1H, 2–**H**, ^{3}J =4.1Hz, ^{4}J =1.4 Hz), 9.52 (dd, 1H, 4–**H**, ^{3}J =8.1 Hz, ^{4}J =1.4 Hz).

^{13}C NMR (151 MHz, Py-d_5): 125.6 (**3**), 129.1 (**5**), 131.1 (**10**), 132.3 (**11**), 134.7 (**4**), 142.8 (**7**), 143.9 (**9**), 150.4 (**6**), 153.9 (**2**).

LRMS (ESI, MeOH) m/z (rel. %): 283 ($[M + H]^+$, 100), 587 ($[2M + Na]^+$, 53.5),

HRMS (ESI, MeOH): Measured m/z: 283.0978. Calculated m/z for $[C_{18}H_{10}N_4 + H]^+$: 283.0983.

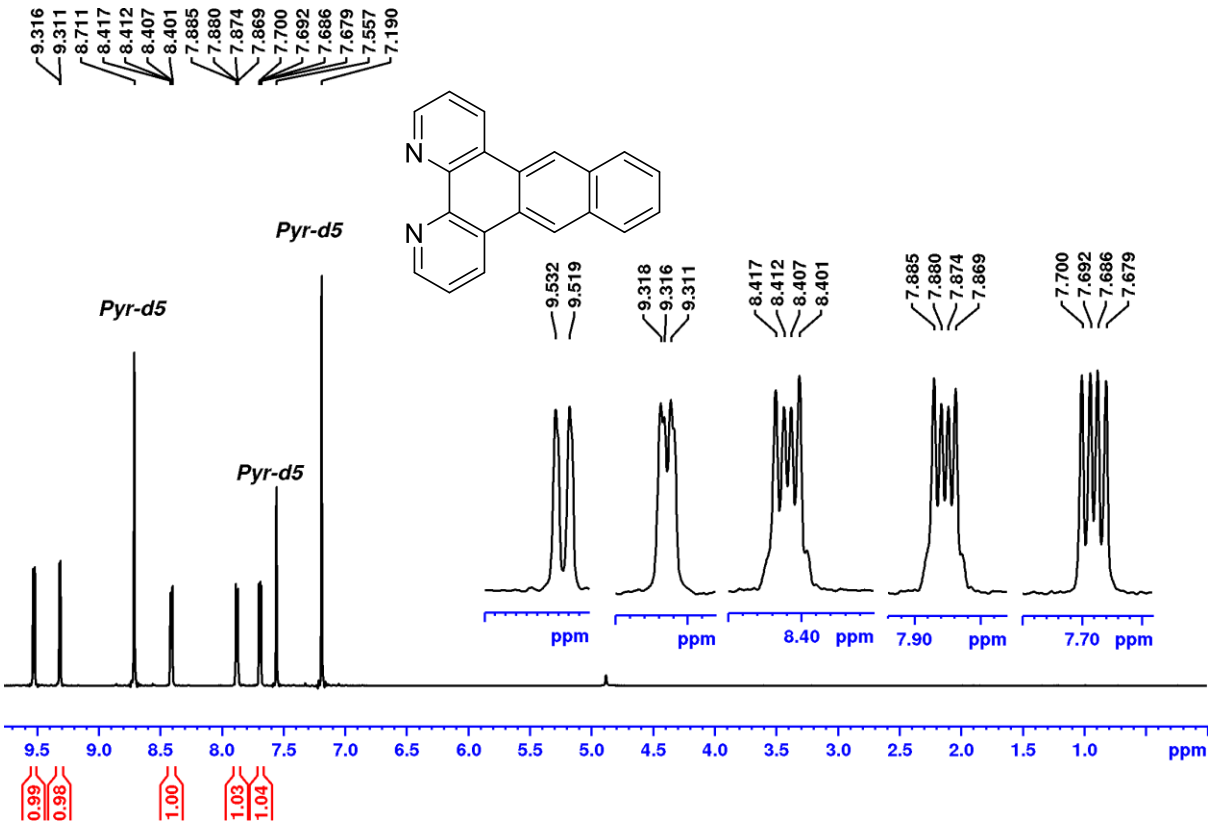

Figure 5.27. ^{1}H NMR (600 MHz, Pyr-d_5) spectrum of **L1.**

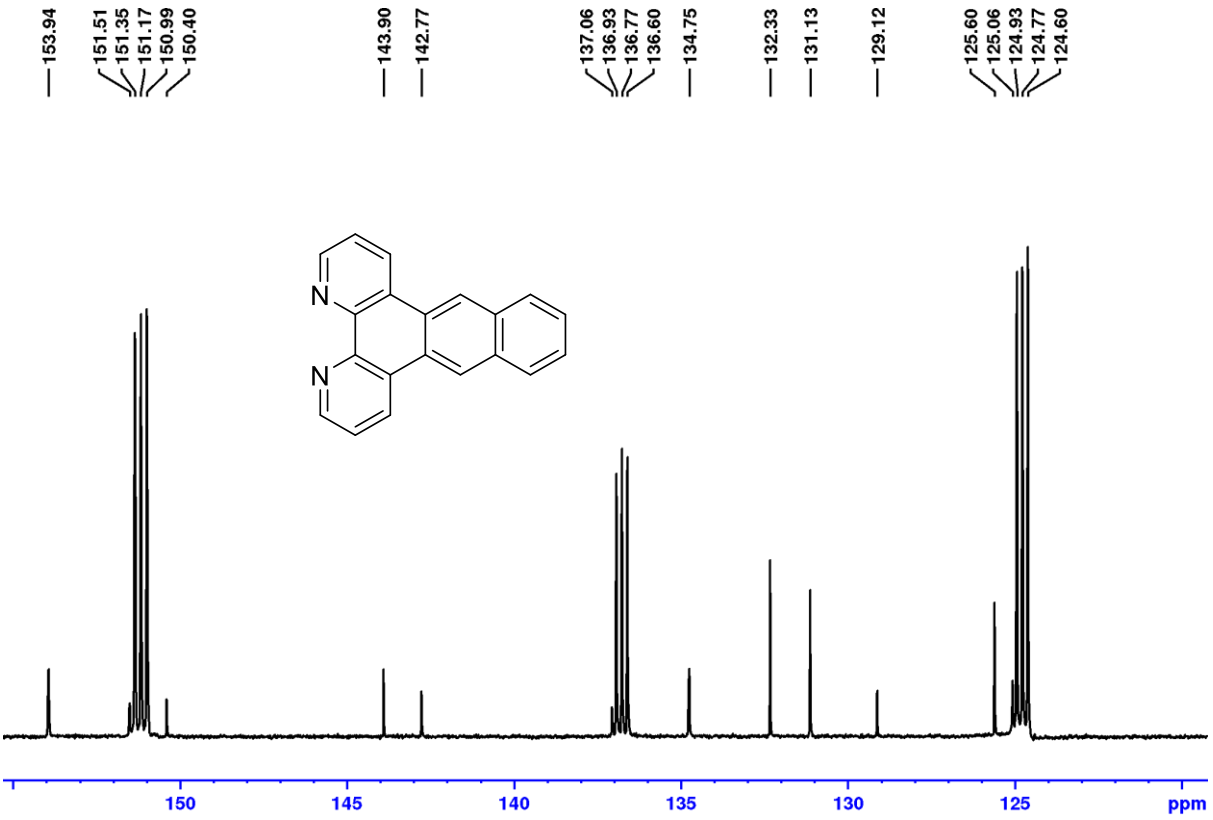

Figure 5.28. ^{13}C NMR (151 MHz, Pyr-d_5) spectrum of **L1.**

5.2.10.4. 10, 13-Dibromodipyrido[3,2-a:2',3'-c]phenazine L2

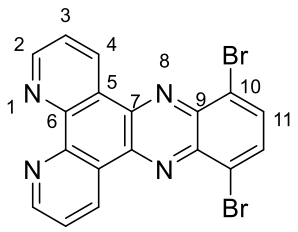

^{1}H NMR (600 MHz, $CDCl_3$ with TFA–*d*): 8.28 (s, 1H, 11–**H**), 8.33 (dd, 1H, 3–**H**, ^{3}J =8.2 Hz, ^{3}J =5.1 Hz), 9.40 (dd, 1H, 2–**H**, ^{3}J = 5.0 Hz, ^{4}J =1.4 Hz), 10.13 (dd, 1H, 4–**H**, ^{3}J = 8.2 Hz, ^{4}J =1.5 Hz).

^{13}C NMR (151 MHz, $CDCl_3$ with TFA–*d*): 124.6 (**10**), 127.5 (**3**), 129.1 (**5**), 135.8 (**11**), 139.4 (**7**), 140.0 (**4**), 141.4 (**9**), 149.1 (**2**), ? (**6**).

LRMS (ESI, MeOH) m/z (rel. %): 462.9 ($[M + Na + 2H]^+$, 100), 460.9 ($[M + Na]^+$, 50.8)

HRMS (ESI, MeOH): Measured m/z: 460.9008. Calculated m/z for $[C_{18}H_8Br_2N_4 + Na]^+$: 460.9013.

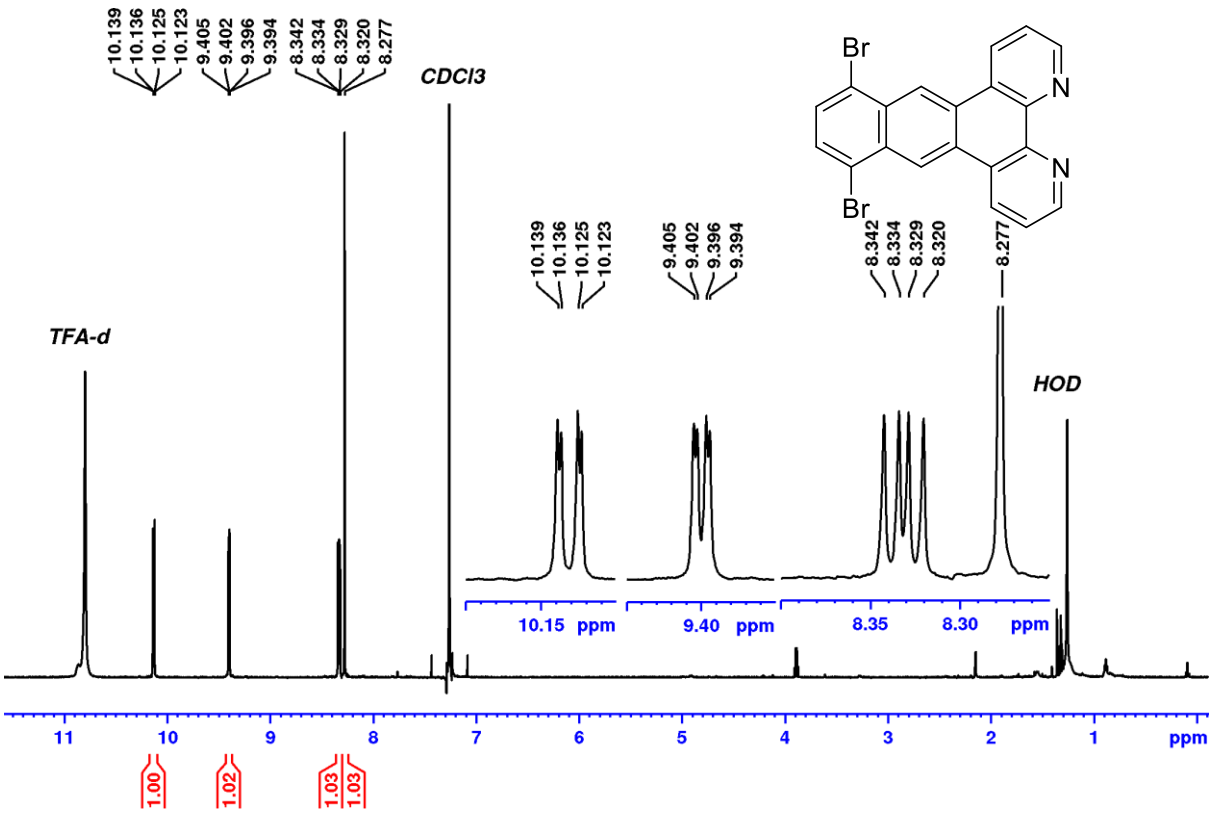

Figure 5.29. ^{1}H NMR (600 MHz, CDCl3 + TFA-*d*) spectrum of **L2.**

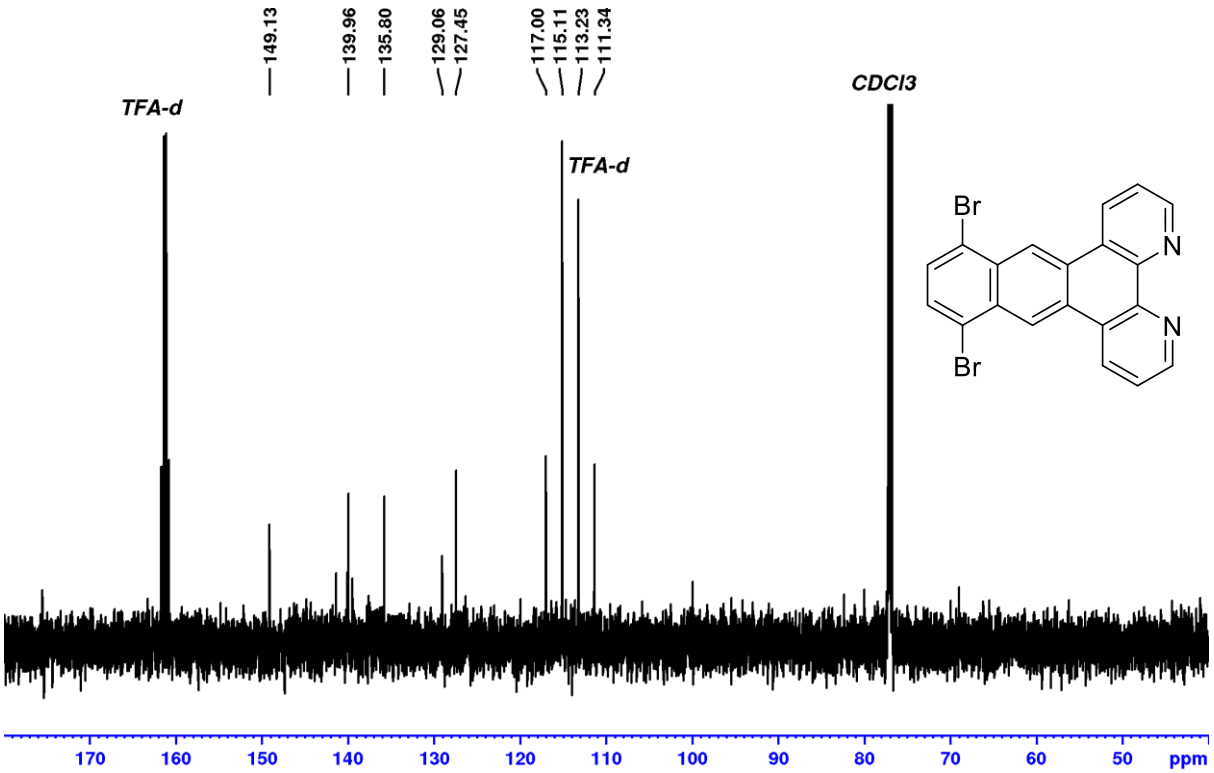

Figure 5.30. ^{13}C NMR (151 MHz, CDCl3 + TFA-*d*) spectrum of **L2.** Complete assignment based on ^{1}H - ^{13}C HMBC correlations.

5.2.10.5. 10, 13–Dicyanodipyrido[3,2-a:2',3'-c]phenazine L3

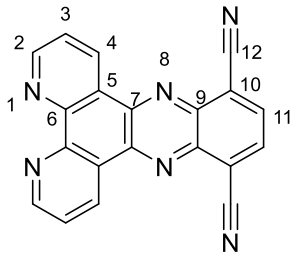

^{1}H NMR (600 MHz, $CDCl_3$ with TFA–*d*): 8.40 (dd, 1H, 3–**H**, ^{3}J =7.9 Hz, ^{3}J =5.2 Hz), 8.65 (s, 1H, 11–**H**), 9.40 (d, 1H, 2–**H**, ^{3}J = 4.5 Hz), 10.19 (d, 1H, 4–**H**, ^{3}J = 8.0 Hz).

^{13}C NMR (151 MHz, $CDCl_3$ with TFA–*d*): 117.7 (**12**), 128.0 (**3**), 128.3 (**5**), 137.3 (**11**), 140.5 (**6**), 140.6 (**4**), 141.3 (**7**), 141.7 (**9**), 149.1 (**2**), ? (**10**).

LRMS (ESI, MeOH) m/z (rel. %): 355 ($[M + Na]^+$, 100)

HRMS (ESI, MeOH): Measured m/z: 355.0702. Calculated m/z for $[C_{20}H_8N_6 + Na]^+$: 355.0707.

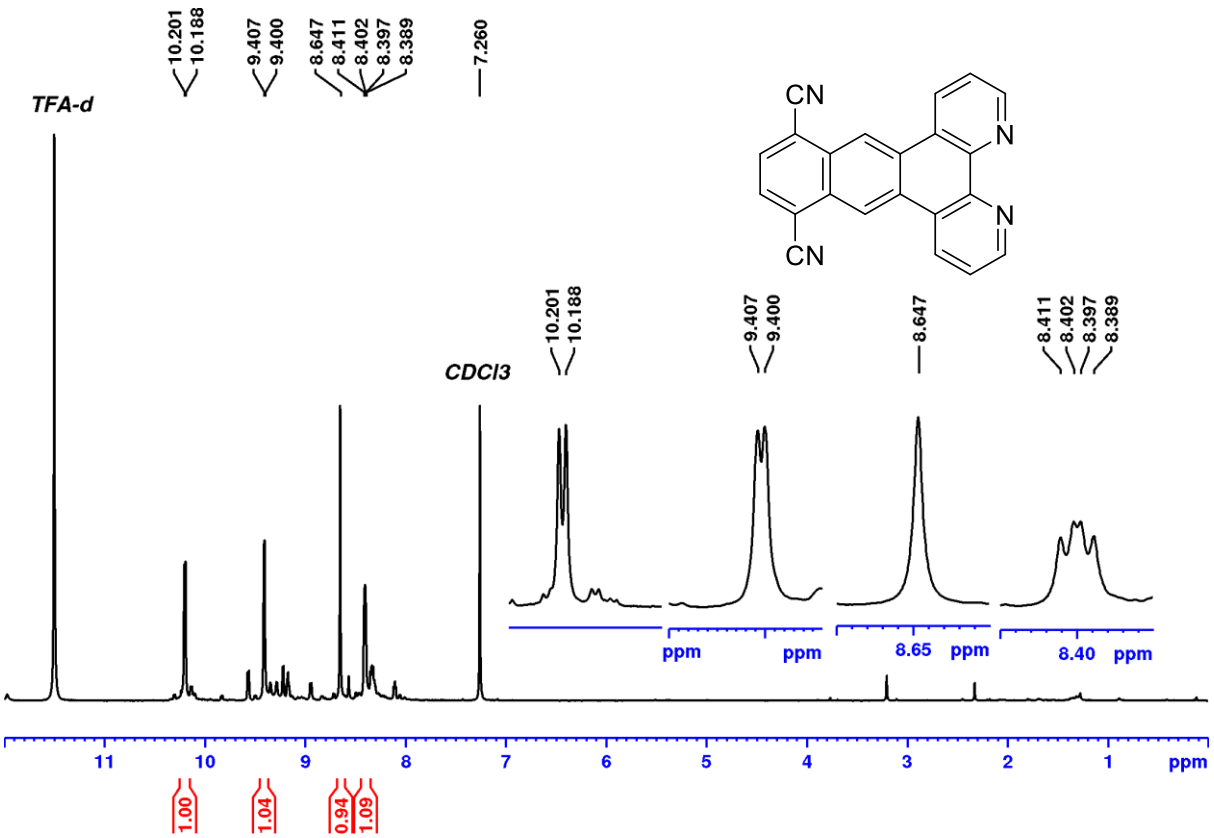

Figure 5.31. ^{1}H NMR (600 MHz, $CDCl_3$ + TFA-*d*) spectrum of **L3**

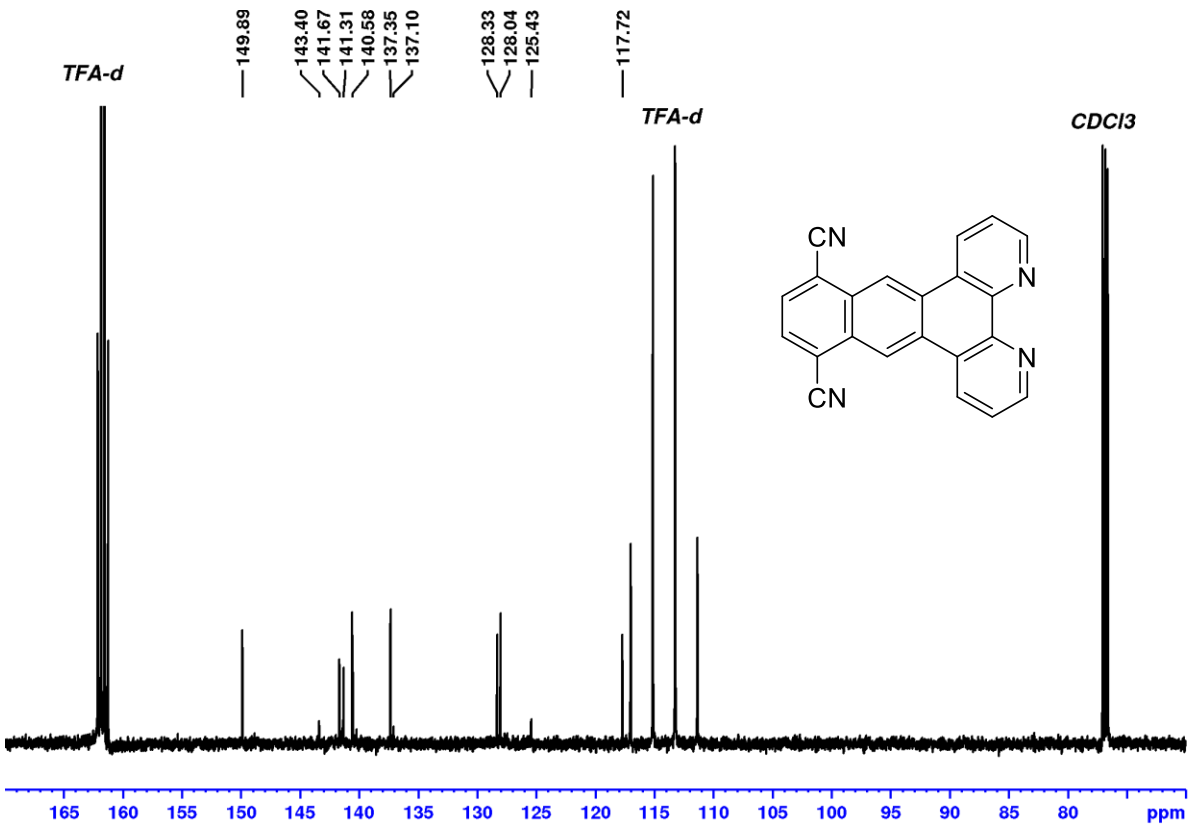

Figure 5.32. ^{13}C NMR (151 MHz, $CDCl_3$ + TFA-*d*) spectrum of **L3**

5.2.10.6. Dimethyl 4,4'-(dipyrido[3,2-a:2',3'-c]phenazine-10,13-diyl)bis(3-nitrobenzoate) L4

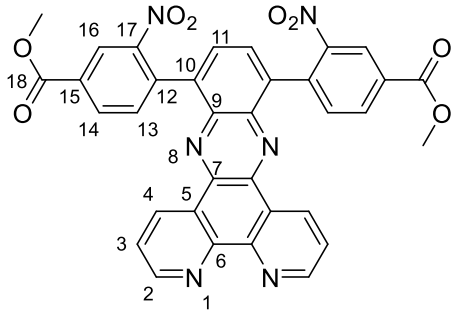

^{1}H NMR (600 MHz, $CDCl_3$): 4.10 (s, 3H, –O**H**$_3$C), 7.75 (br m, 1H, 3–**H**), 7.85 (br s, 1H, 13–**H**), 8.16 (s, 1H, 11–**H**), 8.51 (d, 1H, 14–**H**, ^{3}J = 7.7 Hz), 8.93 (d, 1H, 16–**H**, ^{4}J = 1.5 Hz), 9.08 (d, 1H, 4–**H**, ^{3}J = 8.0 Hz), 9.23 (br s, 1H, 2–**H**).

^{13}C NMR (151 MHz, $CDCl_3$): 53.0 (–OH_3**C**), 124.4 (**3**), 125.3 (**16**), 126.7 (**5**), 129.9 (**11**), 131.6 (**17**), 133.5 (1**3**), 133.9 (**14**), 134.1 (**2**), 136.8 (**12**), 138.1 (**10**), 138.9 (**9**), 141.4 (**7**), 148.8 (**6**), 150.6 (**15**), 153.1 (**4**), 165.0 (**18**).

LRMS (ESI, MeOH) m/z (rel. %): 663 ($[M + Na]^+$, 100)

HRMS (ESI, MeOH): Measured m/z: 663.1232. Calculated m/z for $[C_{34}H_{20}N_6O_8 + Na]^+$: 663.1240.

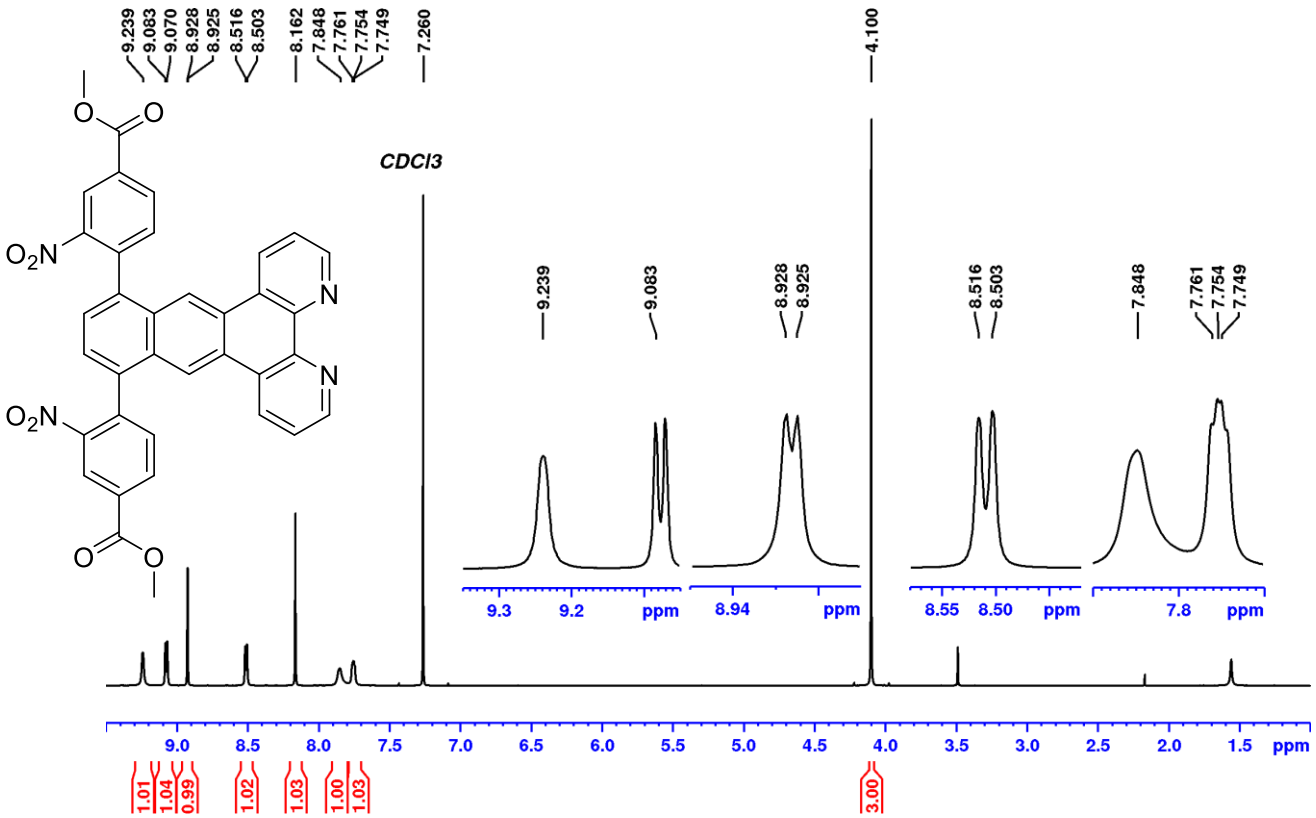

Figure 5.33. ^{1}H NMR (600 MHz, $CDCl_3$) spectrum of **L4**

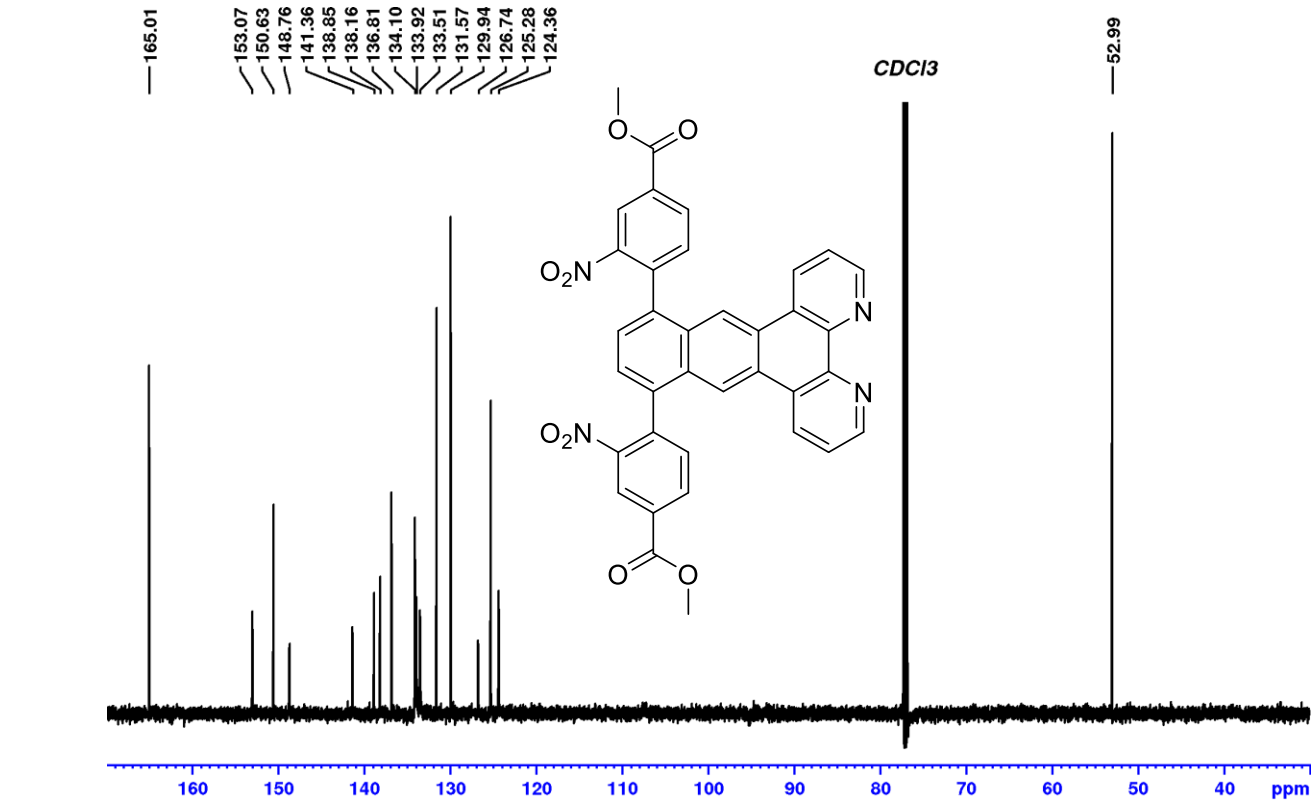

Figure 5.34. ^{13}C NMR (151 MHz, $CDCl_3$) spectrum of **L4**

5.2.11. General one-pot two-step procedure for the synthesis of Copper (I) complexes C1 – C6.

To an oven-dried 50 mL Schlenk flask equipped with a magnetic stirrer was added $[Cu(MeCN)_4]PF_6$ (1.00 equiv.) and diphosphine co-ligand (1.00 equiv.) followed by a few vacuum/argon purge-and-refill cycles. Dry DCM (15 mL) was syringed into the flask and the resultant mixture refluxed overnight under argon atmosphere. A solution of the diimine dppz ligand **L1 – L4** (1.00 equiv.) in dry DCM (5 – 10 mL) was syringed into the reaction mixture at room temperature. The mixture further refluxed for 3 hours and cooled to room temperature. NH_4PF_6 (4.00 equiv.) and *n*–hexane (excess) were finally added to the mixture under stirring at 0 ºC. The precipitate was vacuum-filtered off, washed with *n*–hexane, water and diethyl ether, and finally dried *in vacuo* at 70 ºC. This yielded **C1** (48 %) as a bright yellow powder, **C2** (90 %) as an orange powder, **C3** (42 %) as a burgundy powder, **C4** (84 %), **C5** (85 %), **C6** (83 %) as bright orange/red powders.

5.2.11.1. [Cu(xant)(dppz)]PF_6 (C1)

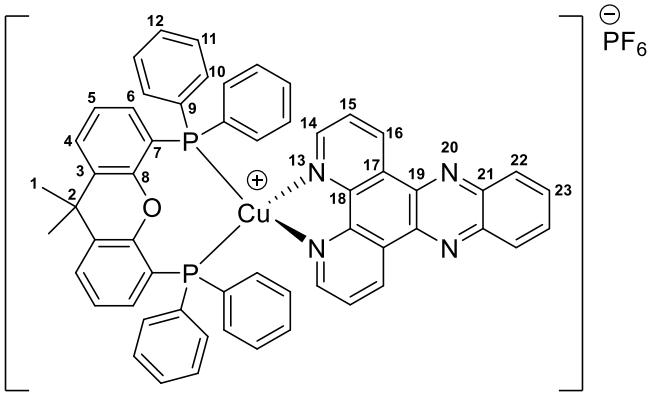

^{1}H NMR (600 MHz, MeCN–d_3): 1.80 (s, 3H, 1–**H**), 6.64 – 6.67 (m, 1H, 5–**H**), 7.01 (m, 4H, 10–**H**), 7.11 (m, 4H, 11–**H**), 7.22 – 7.27 (m, 3H, 12–**H** + 6–**H**), 7.84 – 7.88 (m, 2H, 15–**H** + 4– **H**), 8.13 (m *ortho*-[AA'XX'], 1H, 23–**H** [A/A'], |N|: $|^3J_{AX} + {}^4J_{AX'}|$ d = 9.9 Hz), 8.47 (m *ortho*-[AA'XX'], 1H, 22–**H** [X/X'], |N|: $|^3J_{XA} + {}^4J_{XA'}|$ d = 9.8 Hz), 8.62 (d, 1H, 14–**H**, ^3J = 4.4 Hz), 9.69 (br d, 1H, 16–**H**, ^4J = 8.1 Hz).

^{13}C NMR (151 MHz, MeCN–d_3): 27.5 (**1**), 36.1 (**2**), 119.3 (t, **7,** $^1J_{CP}$ = 13.97 Hz), 125.2 (br t, **6**), 126.5 (**15**), 127.9 (**4**), 128.8 (t, **11,** $^3J_{CP}$ = 5.2 Hz) 129.4 (**17**), 129.6 (**22**), 130.0 (**12**), 131.1 (**5**), 131.3 (t, **9,** $^1J_{CP}$ = 17.5 Hz), 132.1 (**23**), 132.7 (t, **10,** $^2J_{CP}$ = 8.0 Hz), 134.3 (**3**), 134.7 (**16**), 140.2 (**19**), 142.9 (**21**), 145.4 (**18**), 150.9 (**14**), 154.9 (t, **8,** $^2J_{CP}$ = 6.4 Hz).

^{31}P {^{1}H} NMR (162 MHz, MeCN–d_3, ref: H_3PO_4): -13.53 (br s, **P** – Cu), -145.47 (sept, **P** – F, $^1J_{PF}$ = 706.2 Hz)

LRMS (ESI, MeOH) m/z (rel. %): 641 ($[Cu(P\hat{}P)]^+$, 22.1), 923 ($[M - PF_6]^+$, 100),

HRMS (ESI, MeOH): Measured m/z: 923.2146. Calculated m/z for $[C_{57}H_{42}{}^{63}CuN_4OP_2]^+$: 923.2142.

Crystal data for complex C1: $C_{126}H_{112}Cu_2F_{12}N_8O_2P_6$ (M =2311.13 g/mol): monoclinic, space group $P2_1/n$ (no. 14), a = 26.844(3) Å, b = 15.9625(19) Å, c = 27.110(3) Å, β = 106.750(3)°, V = 11123(2) Å^3, Z = 4, T = 100.00 K, μ(Mo Kα) = 0.546 mm^{-1}, $Dcalc$ = 1.380 g/cm^3, 313128 reflections measured (4.018° ≤ 2Θ ≤ 58.26°), 29894 unique (R_{int} = 0.0373, R_{sigma} = 0.0176) which were used in all calculations. The final R_1 was 0.0533 (I > 2σ(I)) and wR_2 was 0.1643 (all data).

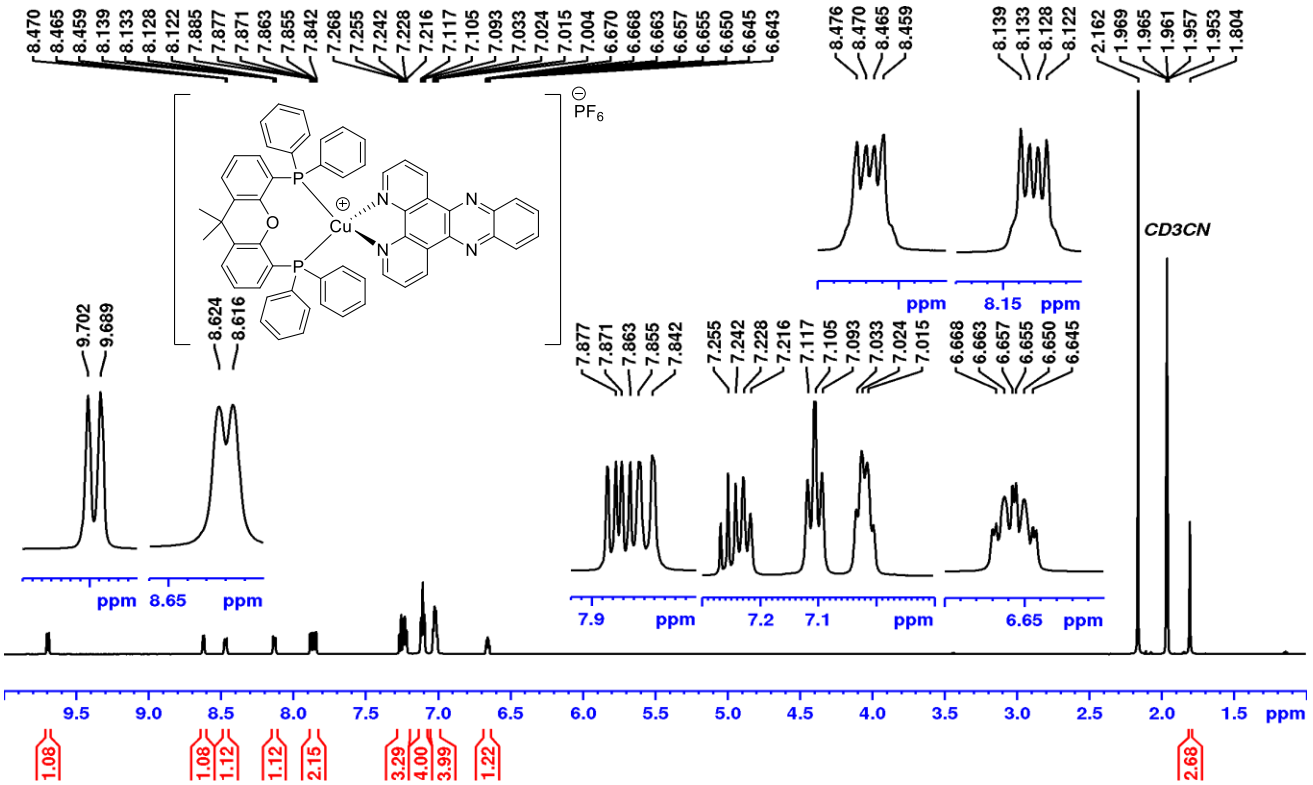

Figure 5.35. ^{1}H NMR (600 MHz, $CDCl_3$) spectrum of complex **C1.**

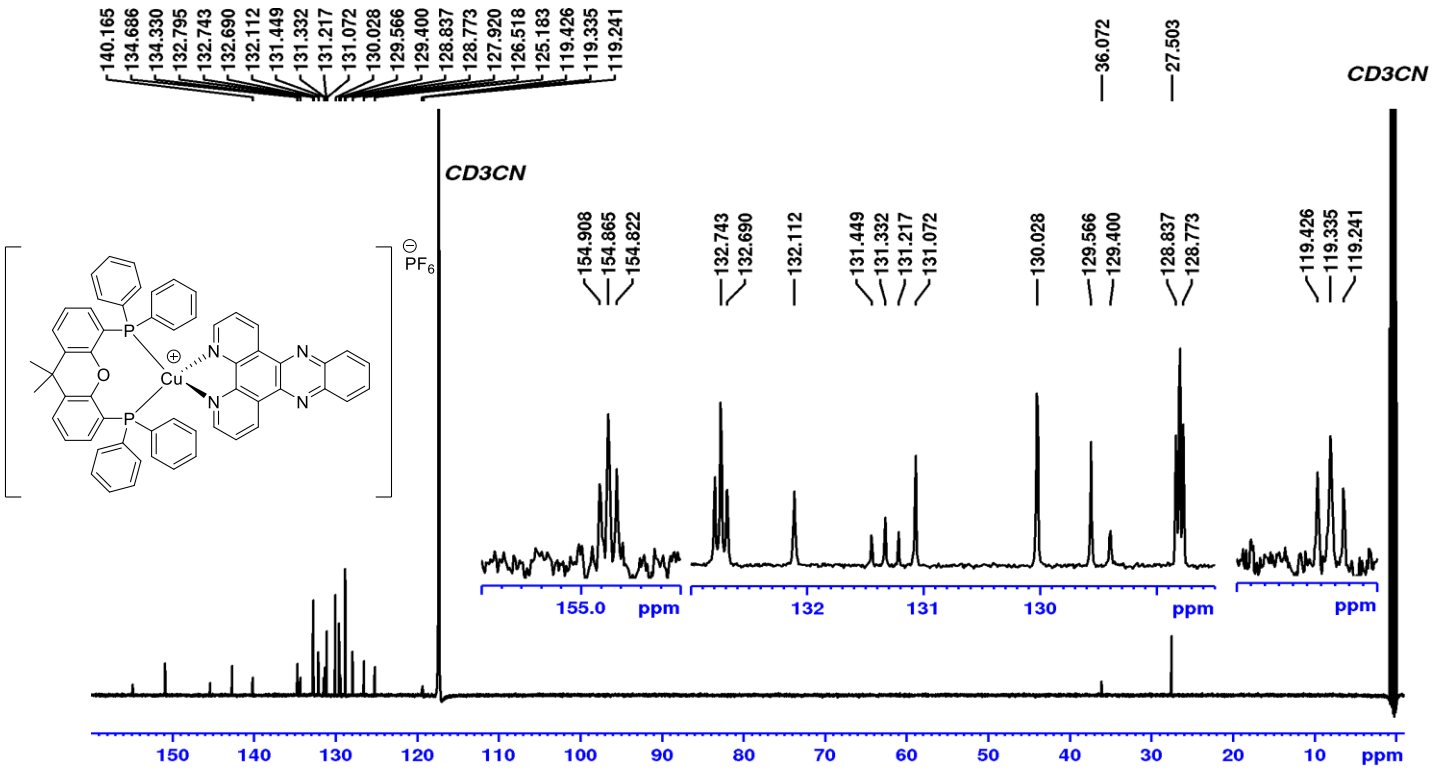

Figure 5.36. ^{13}C NMR (151 MHz, $CDCl_3$) spectrum of complex **C1.**

5.2.11.2. [Cu(xant)(dppz–*p*–Br)]PF_6 (C2)

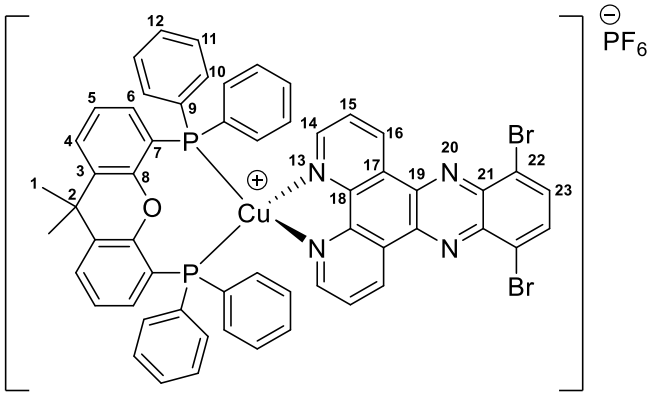

^{1}H NMR (600 MHz, MeCN–d_3): 1.80 (s, 3H, 1–**H**), 6.65 – 6.68 (m, 1H, 5–**H**), 7.02 (m, 4H, 10–**H**), 7.11 (m, 4H, 11–**H**), 7.23 – 7.32 (m, 3H, 12–**H** + 6–**H**), 7.85 (d, 1H, 4–**H**, ^3J = 7.7 Hz), 7.91 (dd, 1H, 15–**H**, ^3J = 7.7, 4.80 Hz), 8.32 (s, 1H, 23–**H**), 8.66 (dd, 1H, 14–**H**, ^3J = 4.8 Hz, ^4J = 1.7 Hz), 9.72 (dd, 1H, 16–**H**, ^3J = 8.0 Hz, ^4J = 1.4 Hz).

^{13}C NMR (151 MHz, MeCN–d_3): 27.5 (**1**), 36.1 (**2**), 119.3 (t, **7,** $^1J_{CP}$ = 14.4 Hz), 123.8 (**22**), 125.2 (br s, **6**), 126.9 (**15**), 128.0 (**4**), 128.6 (**17**), 128.8 (t, **11,** $^3J_{CP}$ = 4.5 Hz), 130.1 (**12**), 131.1 (**5**), 131.3 (t, **9,** $^1J_{CP}$ = 17.8 Hz), 132.7 (t, **10,** $^2J_{CP}$ = 7.8 Hz), 134.3 (**3**), 135.16 (**23**), 134.24 (**16**), 140.8 (**21**), 141.1 (**19**), 145.8 (**18**), 151.6 (**14**), 154.8 (t, **8,** $^2J_{CP}$ = 6.6 Hz).

^{31}P {^{1}H} NMR (162 MHz, MeCN–d_3, ref: H_3PO_4): -13.14 (br s, **P** – Cu), -145.45 (sept, **P** – F, $^1J_{PF}$ = 706.3 Hz)

LRMS (ESI, MeOH) m/z (rel. %): 641 ([Cu(P^P)]$^+$, 100), 1081 ([M – PF_6 + 2H]$^+$, 74.4), 1079 ([M – PF_6]$^+$, 29)

HRMS (ESI, MeOH): Measured m/z: 1079.0312 Calculated m/z for [$C_{57}H_{40}{}^{63}CuBr_2N_4OP_2$]$^+$: 1079.0335.

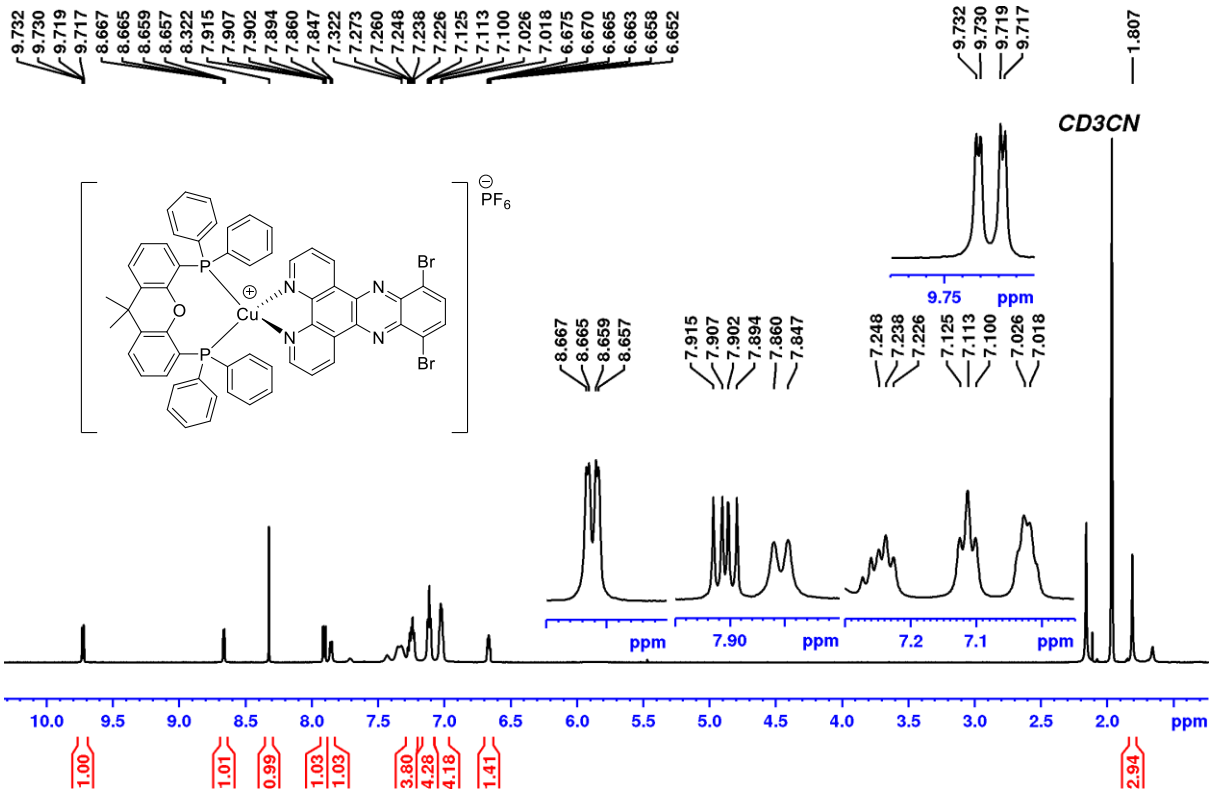

Figure 5.37. ^{1}H NMR (600 MHz, $CDCl_3$) spectrum of complex **C2.**

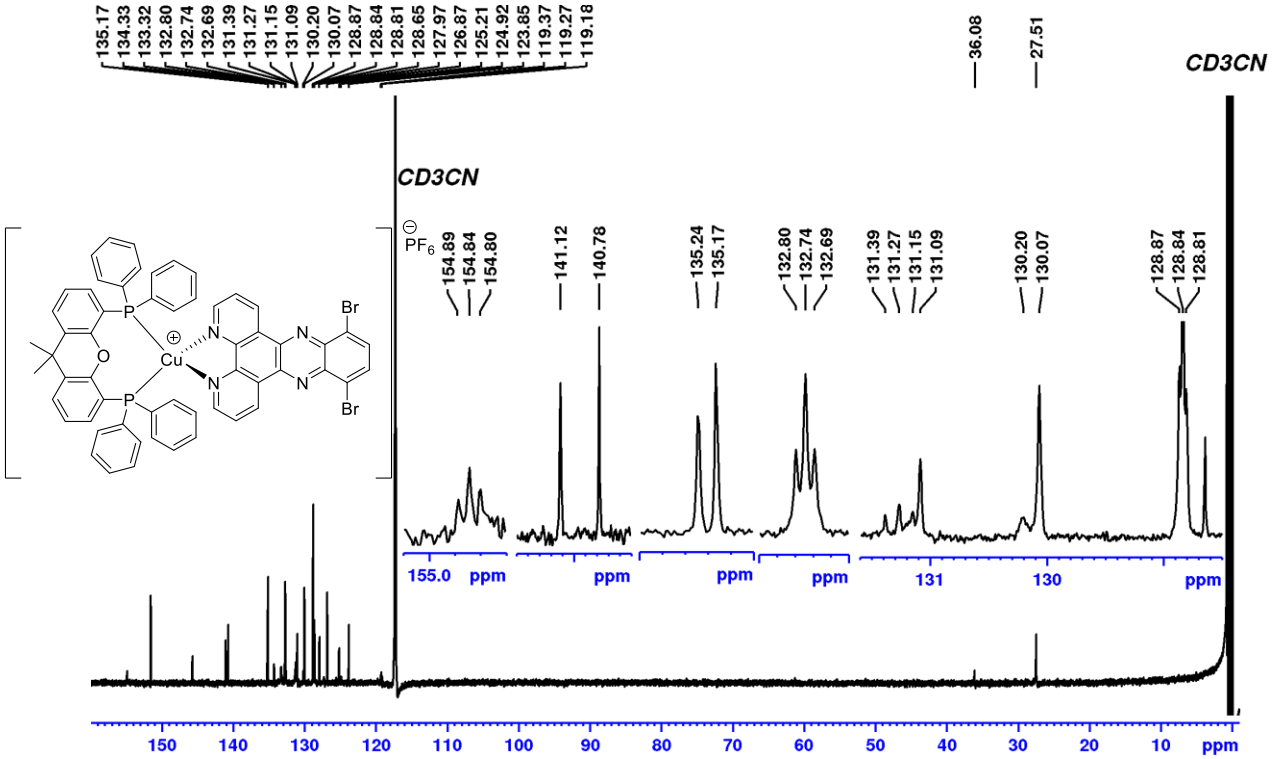

Figure 5.38. ^{13}C NMR (151 MHz, $CDCl_3$) spectrum of complex **C2**

5.2.11.3. [Cu(xant)(dppz–*p*–CN)]PF_6 (C3)

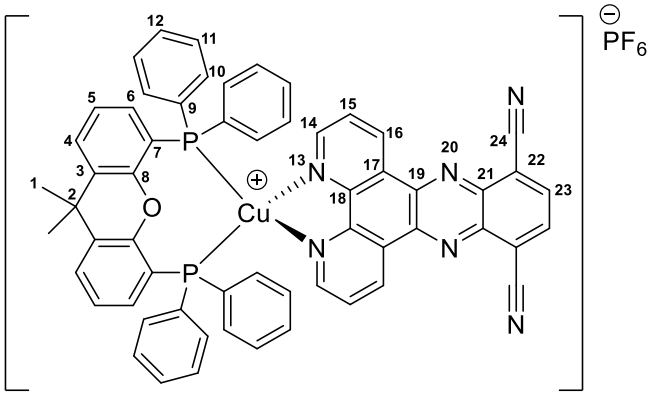

^{1}H NMR (600 MHz, MeCN–d_3): 1.80 (s, 3H, 1–**H**), 6.69 (m, 1H, 5–**H**), 7.02 (m, 4H, 10–**H**), 7.11 (m, 4H, 11–**H**), 7.22 – 7.28 (m, 3H, 12–**H** + 6–**H**), 7.85 (d, 1H, 4–**H**, ^3J = 7.2 Hz), 7.95 (dd, 1H, 15–**H**, ^3J = 8.2, 4.80 Hz), 8.66 (s, 1H, 23–**H**), 8.71 (br d, 1H, 14–**H**, ^3J = 4.0 Hz), 9.72 (dd, 1H, 16–**H**, ^3J = 8.1 Hz, ^4J = 1.4 Hz).

^{13}C NMR (151 MHz, MeCN–d_3): 27.6 (**1**), 36.1 (**2**), 114.9 (**24**), 117.1 (**22**), 119.2 (t, **7,** $^1J_{CP}$ = 14.8 Hz), 125.2 (**6**), 127.1 (**15**), 128.0 (**17**), 128.2 (**4**), 128.8 (t, **11,** $^3J_{CP}$ = 4.6 Hz), 130.1 (**12**), 131.1 (**5**), 131.2 (t, **9,** $^1J_{CP}$ = 17.4 Hz), 132.7 (t, **10,** $^2J_{CP}$ = 7.7 Hz), 134.3 (**3**), 135.4 (**16**), 137.2 (**23**), 141.3 (**21**), 142.6 (**19**), 146.0 (**18**), 152.2 (**14**), 154.8 (br s, **8**).

^{31}P {^{1}H} NMR (162 MHz, MeCN–d_3, ref: H_3PO_4): -13.33 (br s, **P** – Cu), -145.45 (sept, **P** – F, $^1J_{PF}$ = 706.2 Hz)

LRMS (ESI, MeOH) m/z (rel. %): 641 ([Cu(P^P)]$^+$, 25.3), 973 ([M – PF_6]$^+$, 100).

HRMS (ESI, MeOH): Measured m/z: 973.2025 Calculated m/z for [$C_{59}H_{40}{}^{63}CuN_6OP_2$]$^+$: 973.2025.

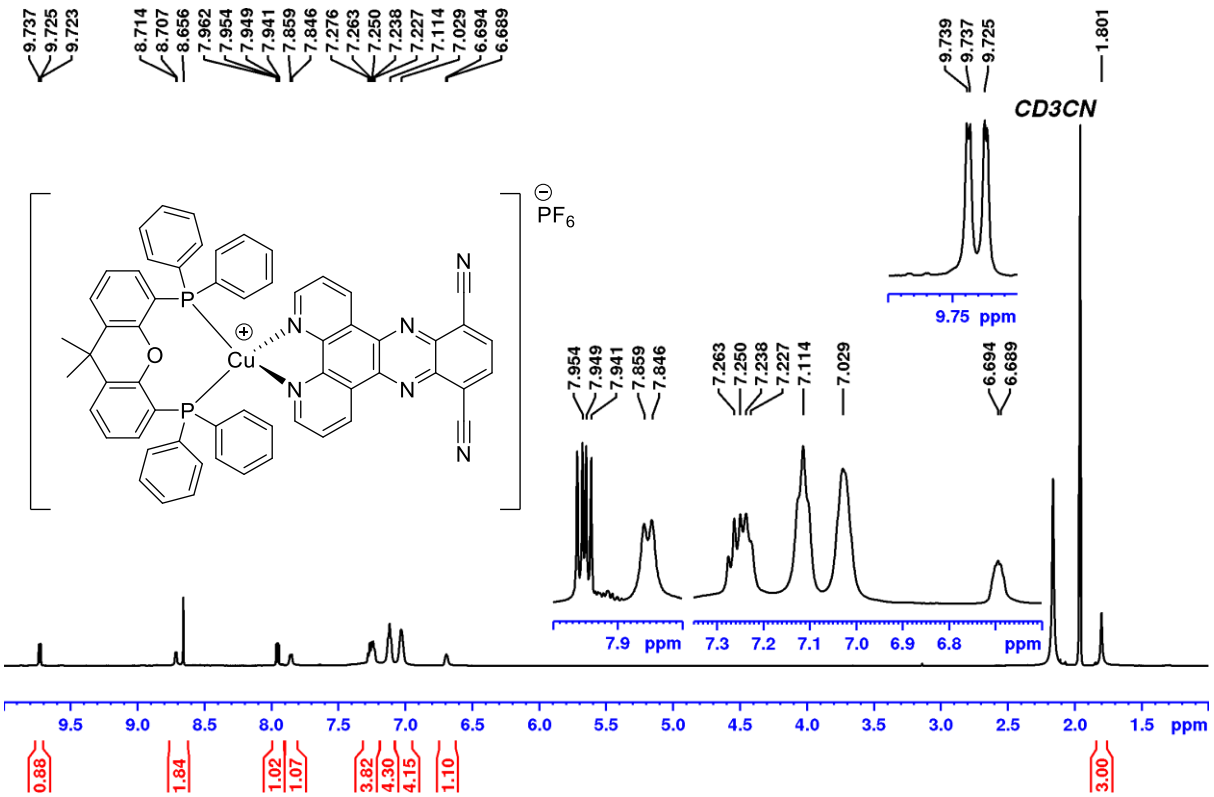

Figure 5.39. ^{1}H NMR (600 MHz, $CDCl_3$) spectrum of complex **C3.**

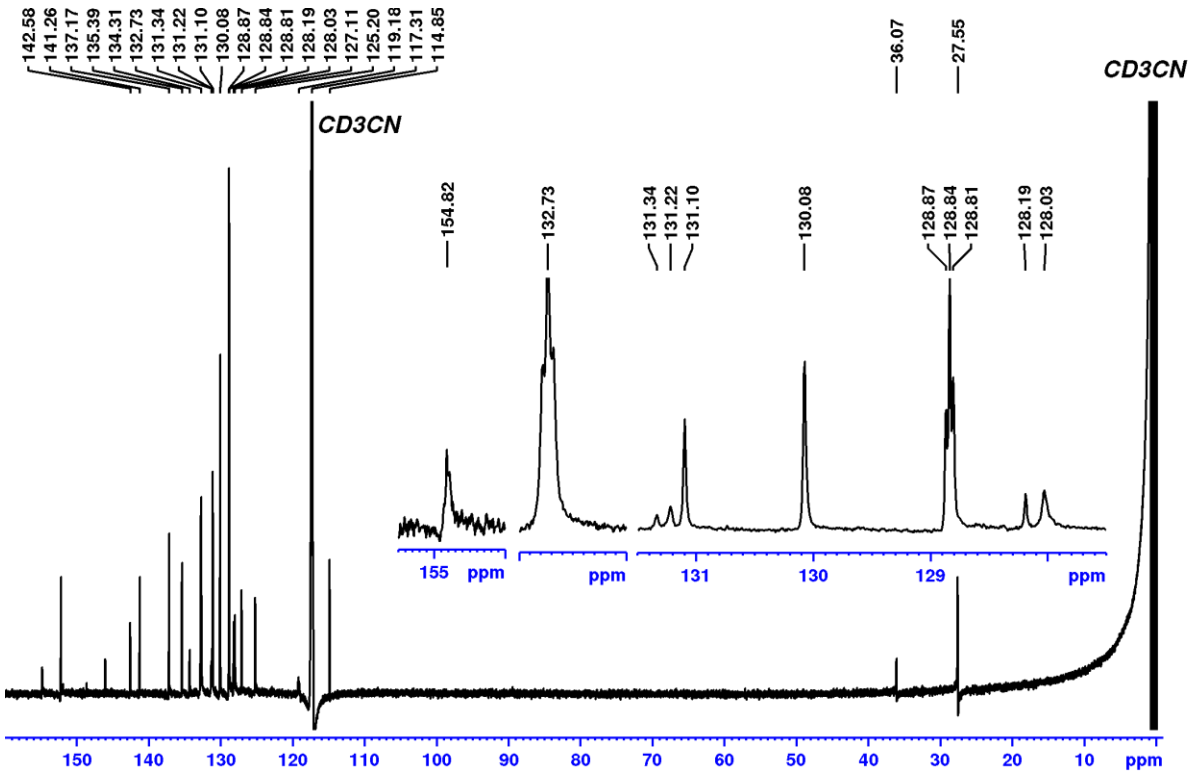

Figure 5.40. ^{13}C NMR (151 MHz, $CDCl_3$) spectrum of complex **C3**

5.2.11.4. [Cu(xant)(dppz–*p*–BzNO$_2$Me)]PF$_6$ (C4)

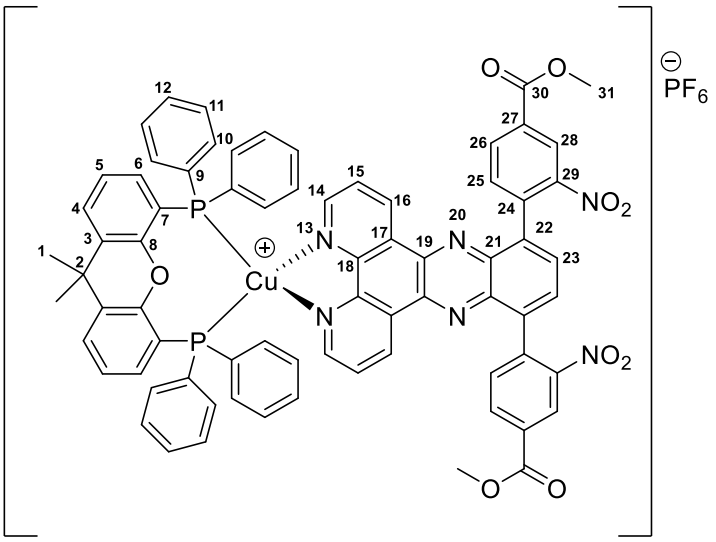

^{1}H NMR (600 MHz, MeCN–d_3): 1.80 (s, 3H, 1–**H**), 4.06 (s, 3H, 31–**H**), 6.67 – 6.72 (m, 1H, 5–**H**), 6.82 – 7.31 (m, 11H, 10–**H** + 11–**H** + 12–**H** + 6–**H**), 7.79 (dd, 1H, 15–**H**, ^3J = 8.2, 4.8 Hz), 7.83 (d, 1H, 4–**H**, ^3J = 7.2 Hz), 8.00 (d, 1H, 25–**H**), 8.42 (s, 1H, 23–**H**), 8.54 (dd, 1H, 26–**H**, ^3J = 7.9 Hz, ^4J = 1.8 Hz), 8.62 (br s, 1H, 14–**H**), 8.85 (br s, 1H, 28–**H**), 9.09 (br s, 1H, 16–**H**).

^{13}C NMR (151 MHz, MeCN–d_3): 27.7 (**1**), 36.0 (**2**), 52.6 (**31**), 119.3 (t, **7**), 125.2 (**6**), 125.3 (**28**), 126.4 (**15**), 128.0 (**4**), 128.4 (**17**), 128.7 (**12**), 130.0 (t, **11**), 131.1 (**5**), 131.6 (**23**), 131.8 (**22**), 132.3 (t, **9**), 133.0 (t, **10**), 133.7 (**25**), 134.0 (**26**), 134.2 (**3**), 134.8 (**16**), 136.0 (**24**), 138.0 (**29**), 139.9 (**19**), 145.6 (**18**), 150.5 (**27**), 151.2 (**14**), 154.8 (**8**), 164.9 (**30**).

^{31}P {^{1}H} NMR (162 MHz, MeCN–d_3, ref: H_3PO_4): -13.27 (br s, **P** – Cu), -145.45 (sept, **P** – F, $^1J_{PF}$ = 706.3 Hz)

LRMS (ESI, MeOH) m/z (rel. %): 641 ([Cu(P^P)]$^+$, 12.3), 1281.3 ([M – PF_6]$^+$, 100)

HRMS (ESI, MeOH): Measured m/z: 1281.2558. Calculated m/z for [$C_{73}H_{52}{}^{63}CuN_6O_9P_2$]$^+$: 1281.2562.

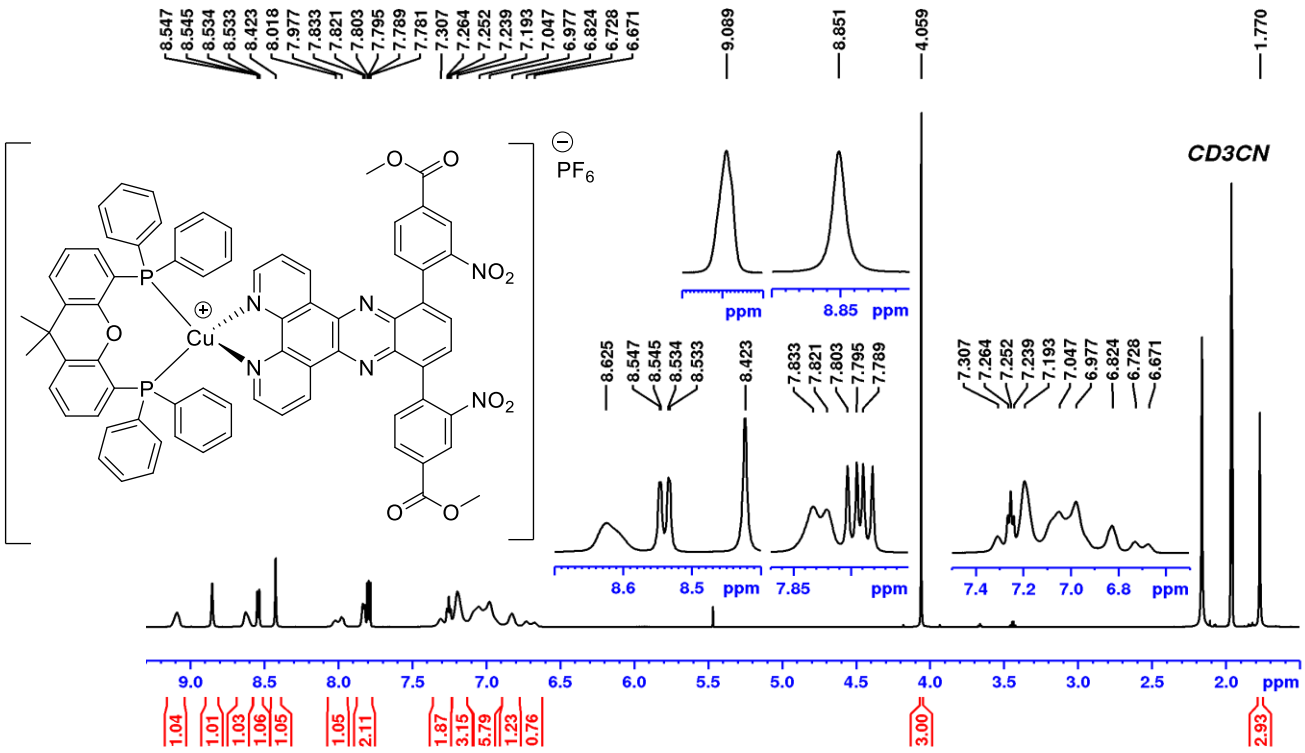

Figure 5.41. ^{1}H NMR (600 MHz, $CDCl_3$) spectrum of complex **C4.**

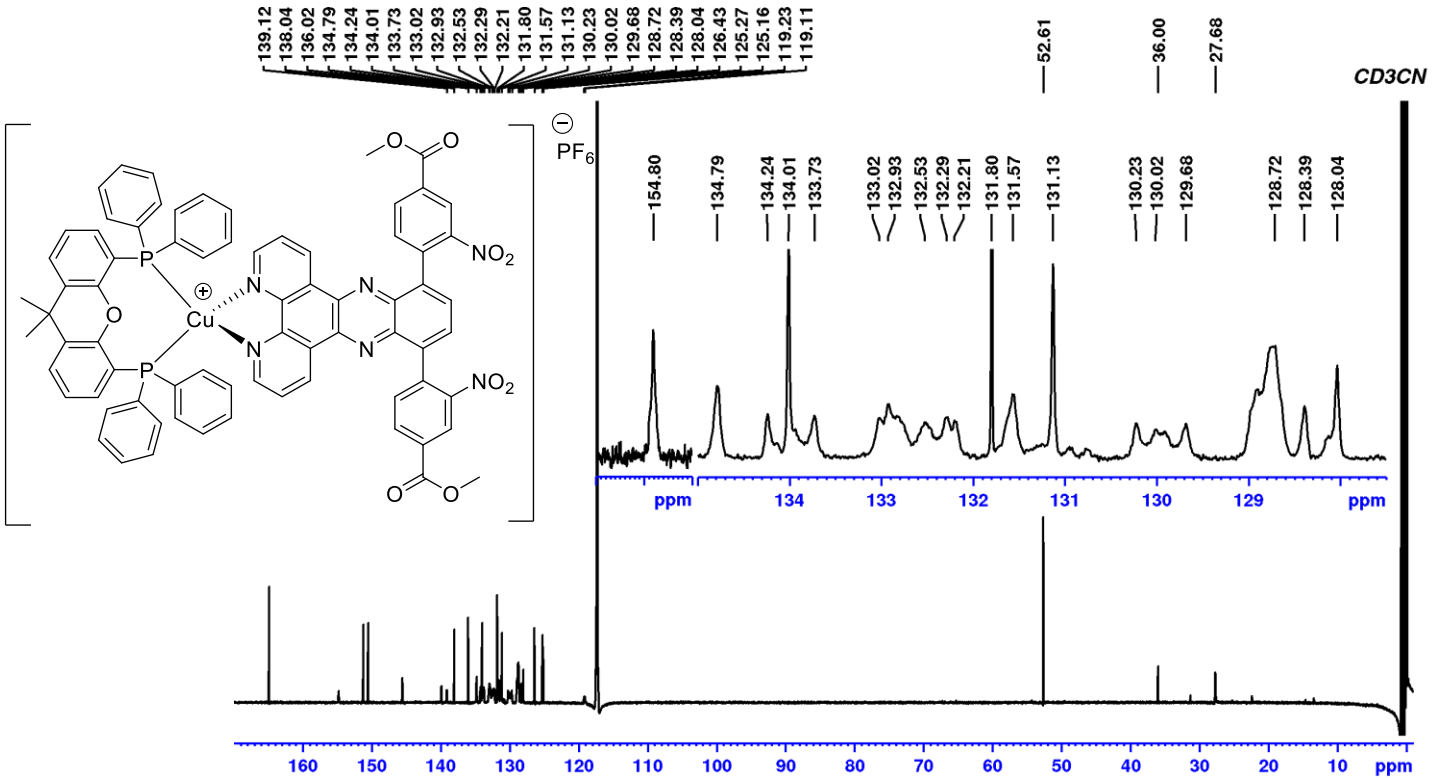

Figure 5.42. ^{13}C NMR (151 MHz, $CDCl_3$) spectrum of complex **C4.**

5.2.11.5. [Cu(dppf)(dppz–*p*–BzNO$_2$Me)]PF$_6$ (C5)

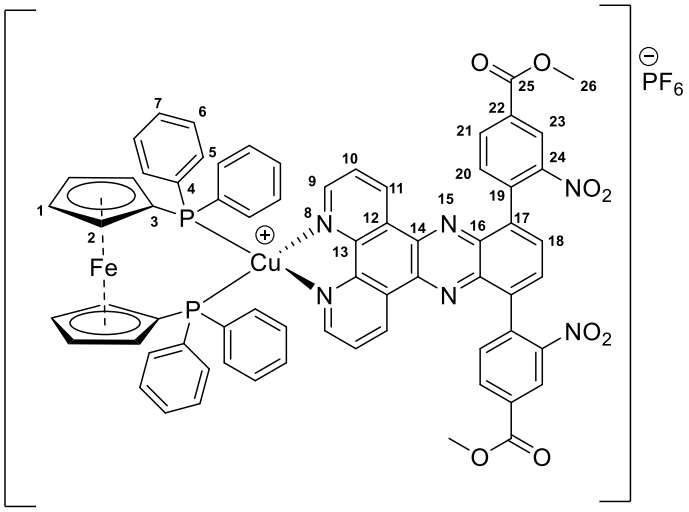

^{1}H NMR (600 MHz, MeCN–d_3): 4.07 (s, 3H, 26–**H**), 4.43 (br s, 2H, 1–**H**), 4.57 (s, 2H, 2–**H**), 7.23 (br s, 8H, 5–**H** + 6–**H**), 7.35 (br m, 2H, 7–**H**), 7.79 (dd, 1H, 10–**H**, ^3J = 8.1, 4.9 Hz), 7.98 (d, 1H, 20–**H**), 8.41 (s, 1H, 18–**H**), 8.54 (dd, 1H, 21–**H**, ^3J = 7.9 Hz, ^4J = 1.9 Hz), 8.87 (s, 1H, 23–**H**), 8.96 (d, 1H, 9–**H**, ^3J = 4.5 Hz), 9.18 (dd, 1H, 11–**H**, ^3J = 8.0 Hz).

^{13}C NMR (151 MHz, MeCN–d_3): 52.6 (**26**), 72.8 (br s, **1**), 74.5 (t, **2**), 125.2 (**23**), 126.1 (**10**), 128.5 (**12**), 128.7 (**6**), 130.2 (**7**), 130.3 (**17**), 131.5 (**3**), 131.8 (**18**), 133.1 (br m, **5**), 133.3 (t, **4**), 133.9 (**21**), 134.0 (**20**), 134.6 (**11**), 136.1 (**19**), 138.0 (**24**), 139.1 (**16**), 140.2 (**14**), 146.1 (**13**), 150.5 (**22**), 152.4 (**9**), 164.9 (**25**).

^{31}P {^{1}H} NMR (162 MHz, MeCN–d_3, ref: H_3PO_4): -10.04 (br s, **P** – Cu), -145.45 (sept, **P** – F, $^1J_{PF}$ = 706.2 Hz)

LRMS (ESI, MeOH) m/z (rel. %): 1257 ([M – PF_6]$^+$, 100)

HRMS (ESI, MeOH): Measured m/z: 1257.1651. Calculated m/z for [$C_{68}H_{48}{}^{63}CuFeN_6O_8P_2$]$^+$: 1257.1649.

Crystal data for complex C5: $C_{136}H_{96}Cu_2F_{12}Fe_2N_{12}O_{16}P_6$ (M = 2806.84 g/mol): triclinic, space group $P\bar{1}$, a = 14.694(8) Å, b = 15.623(9) Å, c = 19.907(11) Å, α = 98.926(7)°, β = 105.048(7)°, γ = 116.315(7) Å, V = 3758(4) Å^3, Z =1, T = 299 K, μ(Mo Kα) = 0.607 mm^{-1}, $Dcalc$ = 1.240 g/cm^3, 7184 reflections measured (4.018° ≤ 2Θ ≤ 40.556°). The final R_1 was 0.1400 (I > 2σ(I)) and wR_2 was 0.4143 (all data).

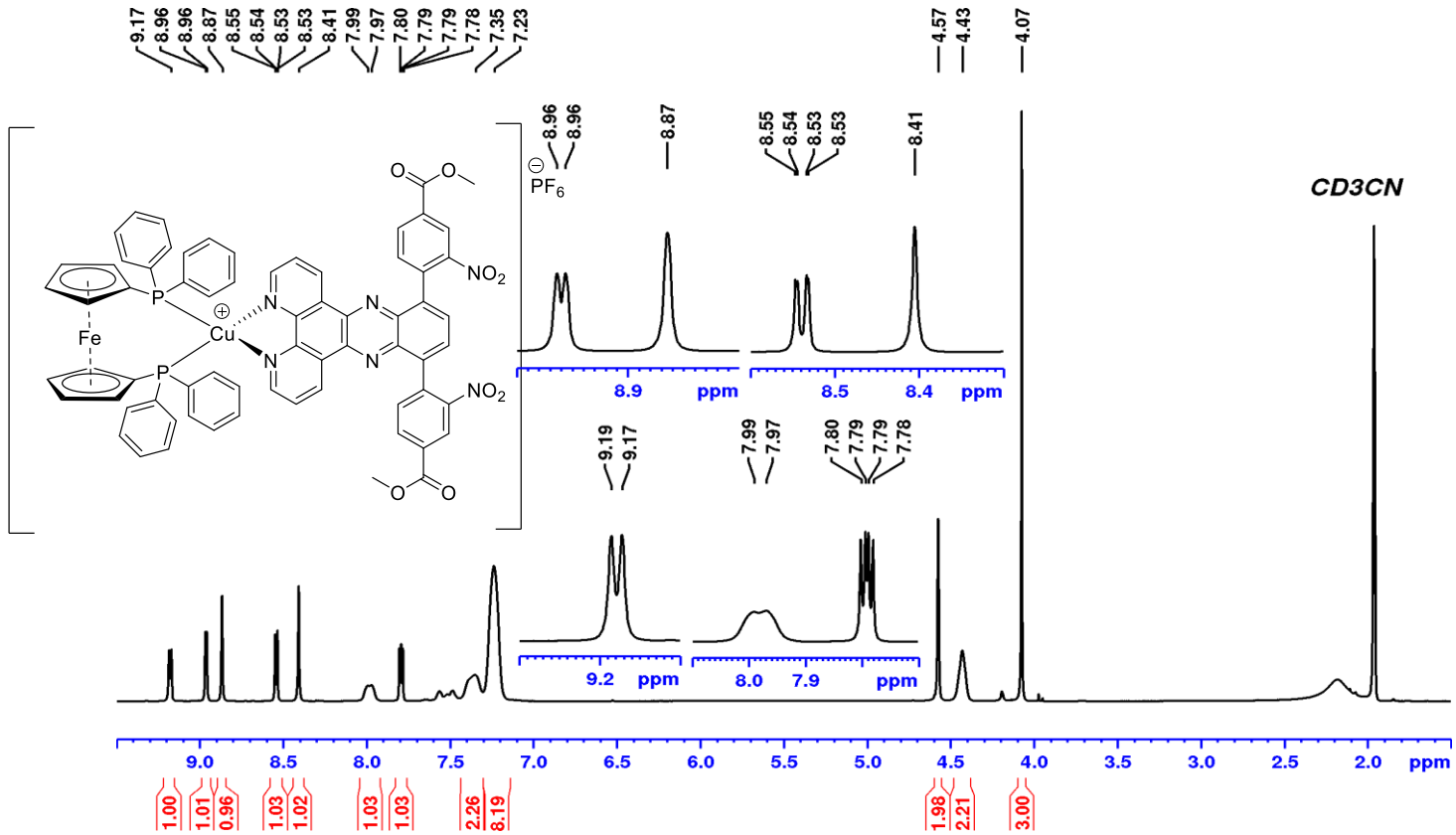

Figure 5.43. ^{1}H NMR (600 MHz, $CDCl_3$) spectrum of complex **C5.**

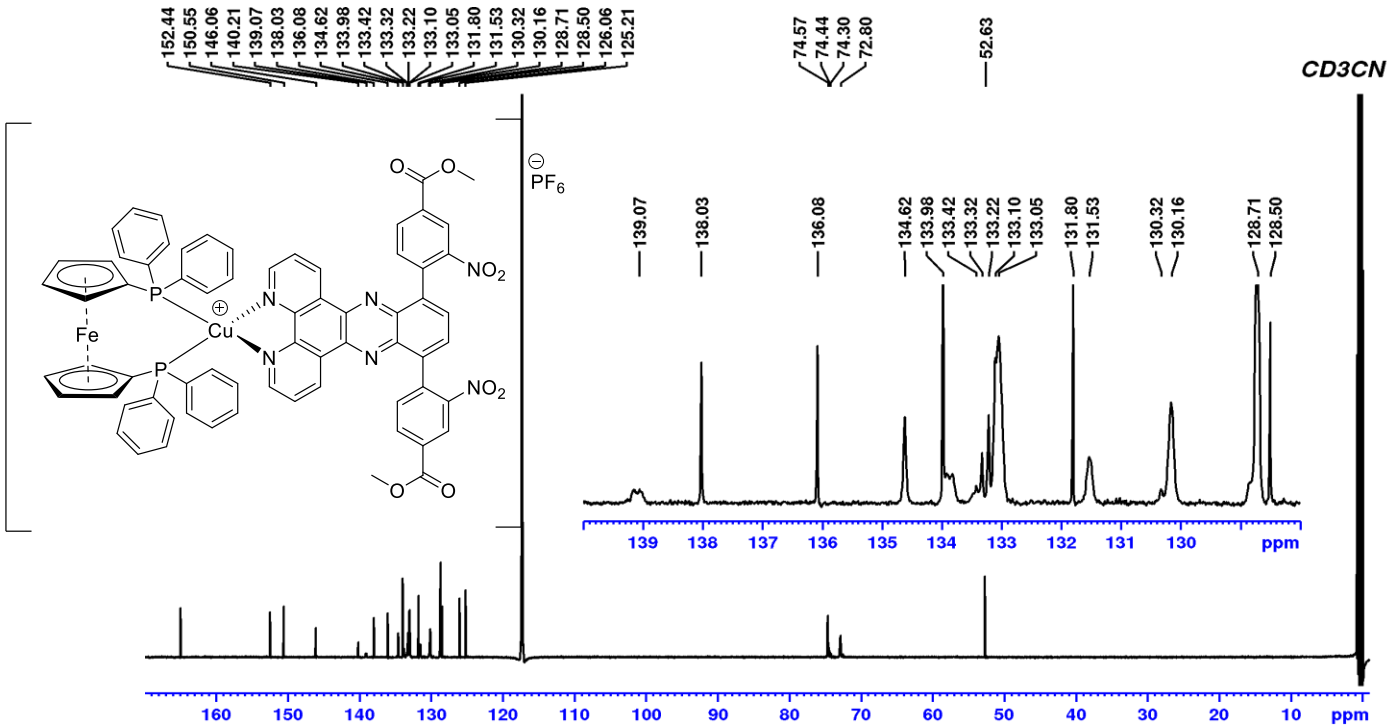

Figure 5.44. ^{13}C NMR (151 MHz, $CDCl_3$) spectrum of complex **C5.**

5.2.11.6. [Cu(BINAP)(dppz–*p*–BzNO$_2$Me)]PF$_6$ (C6)

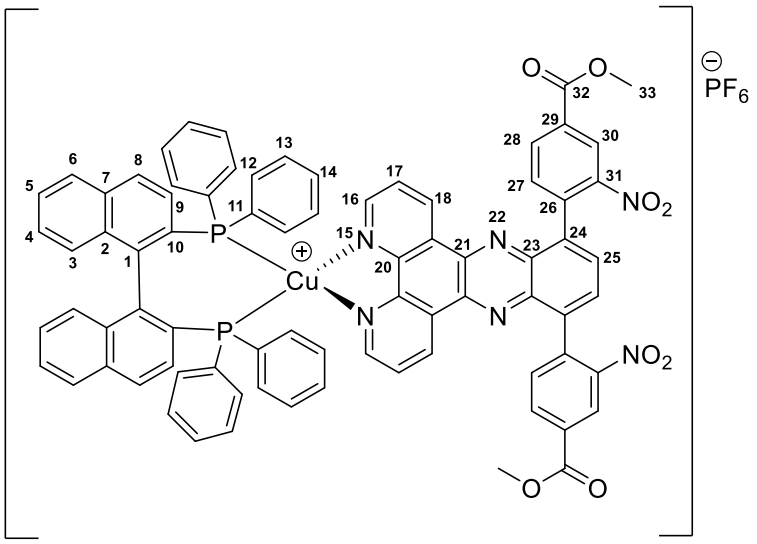

^{1}H NMR (600 MHz, MeCN–d_3): 4.08 (s, 3H, 33–**H**), [6.66 (br s, 2H), 6.82 (br s, 1H), 6.92 (br s, 1H), 7.20 – 7.44 (br m, 10 H), 7.74 (d, 1H), 7.83 (br s, 1H) (3–**H,** 4–**H,** 5–**H,** 6–**H,** 8–**H,** 9–**H,** 12–**H,** 13–**H,** 14–**H**)], 7.99 (br m, 2H, 17–**H +** 27–**H**), 8.43 (s, 1H, 25–**H**), 8.55 (d, 1H, 28–**H**), 8.89 (s, 1H, 30–**H**), 9.05 (br dd, 1H, 16–**H**), 9.31 (br s, 1H, 18–**H**),.

^{13}C NMR (151 MHz, MeCN–d_3): 52.6 (s), 125.3 (s), 126.5 + 126.6 (d), 126.9 (s), 127.3 (br m), 127.4 (s), 127.5 (br t), 128.0 (s), 128.9 (s), 129.1 (s), 129.4 (s), 130.6 (br s), 131.6 (br m), 131.8 (s), 132.5 (br t), 132.8 (br m), 133.3 (s), 133.8 (s), 133.9 (br m), 134.0 (s), 134.2 (br m), 135.1 (s), 136.1 (s), 138.1 (s), 139.3 (br m), 140.3 (s), 146.2 (s), 150.5 (s), 152.6 (br m), 164.9 (s).

^{31}P {^{1}H} NMR (162 MHz, MeCN–d_3, ref: H_3PO_4): + 0.91 (br s, **P** – Cu), -145.45 (sept, **P** – F, $^1J_{PF}$ = 706.3 Hz)

LRMS (ESI, MeOH) m/z (rel. %): 1325 ([M – PF_6]$^+$, 100),

HRMS (ESI, MeOH): Measured m/z: 1325.2605. Calculated m/z for [$C_{78}H_{52}{}^{63}CuN_6O_8P_2$]$^+$: 1325.2612.

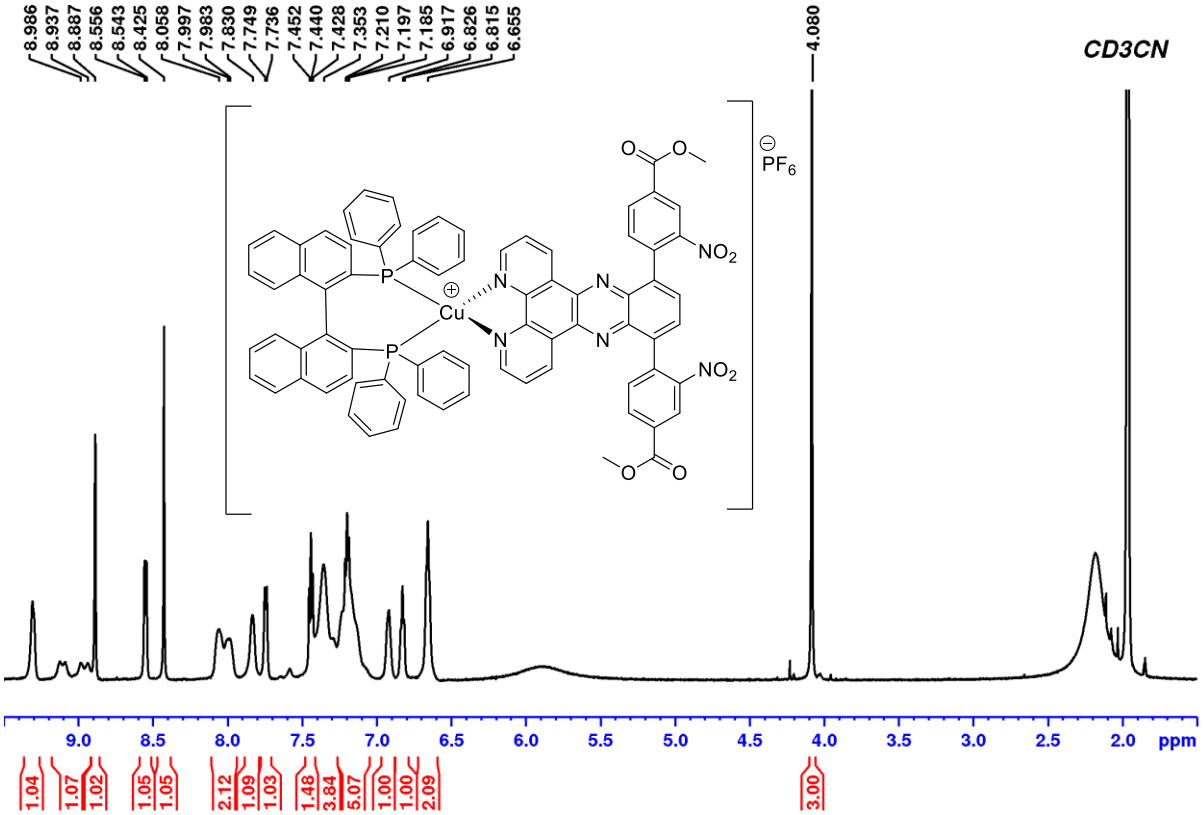

Figure 5.45. ^{1}H NMR (600 MHz, $CDCl_3$) spectrum of complex **C6.**

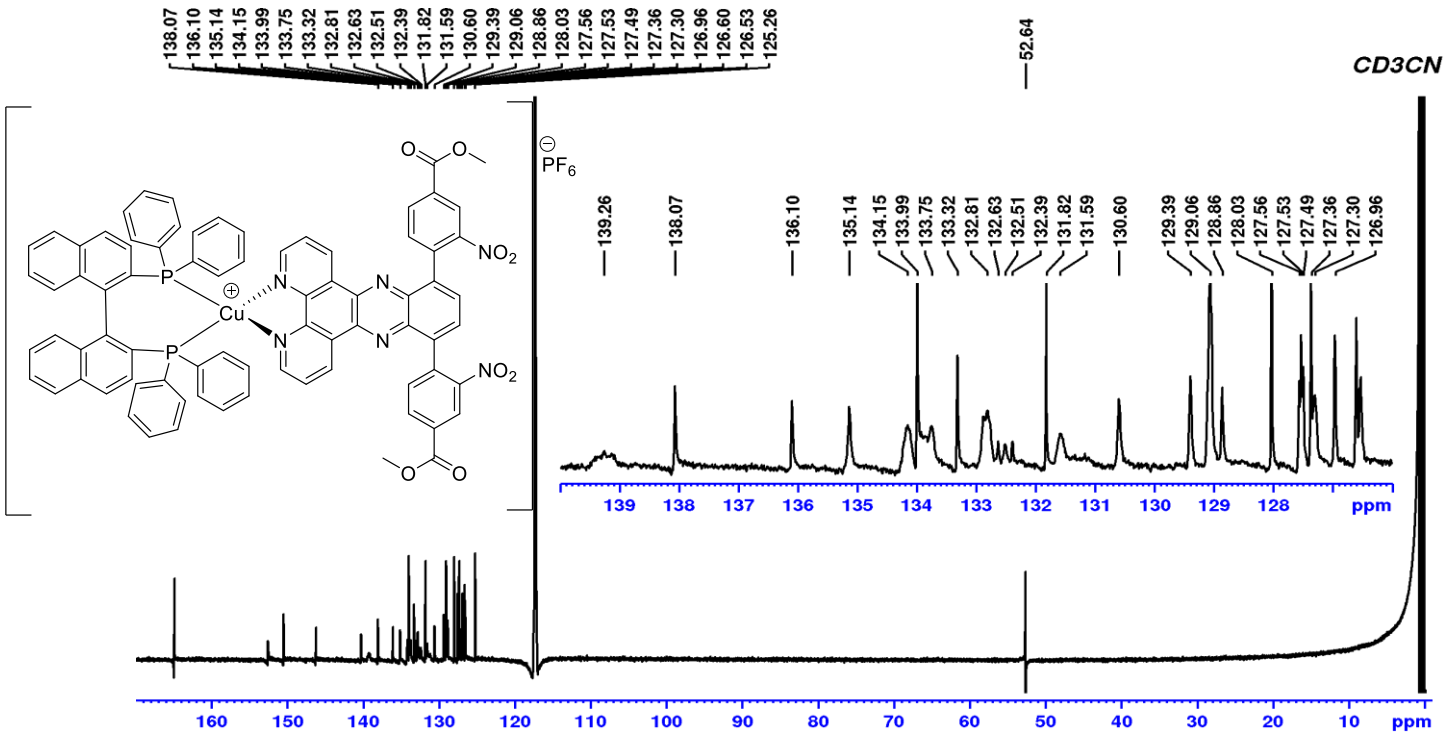

Figure 5.46. ^{13}C NMR (151 MHz, $CDCl_3$) spectrum of complex **C6.**

6. Bibliography

[1] Kim D., Sakimoto K. K., Heng D., Yang P., *Angew. Chem. Int. Ed.* **2015**, 54, 3259 – 3266.

[2] Wang L., *Catal. Rev.* **2022**, *12*(8), 919.

[3] Yuan Y. J., Yu Z. T., Chen D. Q., Zhou Z. G., *Chem. Soc. Rev.* **2017**, 46, 603–631.

[4] Wenger O. S., *Coord. Chem. Rev.,* **2009**, 253, 1439–1457.

[5] Wang, H., Zhang, L., Chen, Z., Hu, J., Li, S., Wang, Z., Liu, J., Wang, X.. *Chem. Soc. Rev.* **2014**, 43, 5234–5244.

[6] Tran, T.T., Pino, T., Ha-Thi, M.H., *J. Phys. Chem. C* **2019**, 123, 28651–28658.

[7] Chen H.C., Hetterscheid D.G., Williams R.M., van der Vlugt J.I., Reek J.N., Brouwer A.M., *Energy Environ.* **2015**, 8, 975–982.

[8] Andreiadis E.S., Chavarot-Kerlidou M., Fontecave M., Artero V., *Photochem. Photobiol.* **2011**, 87, 946–964.

[9] Irikura M., Tamaki Y., Ishitani O., *Chem. Sci.* **2021**, 12, 13888–13896.

[10] Kobayashi A., Takizawa S.Y., Hirahara M., *Coord. Chem. Rev.* **2022**, 467, 214624.

[11] Armaroli N., *Chem. Soc. Rev.* 2001, **30**, 113–124.

[12] C. R. Bock, J. A. Connor, A. R. Gutierrez, T. J. Meyer, D. G. Whitten, B. P. Sullivan and J. K. Nagle, *J. Am. Chem. Soc.,* **1979**, 101, 4815–4824.

[13] H. D. Gafney and A. W. Adamson, *J. Am. Chem. Soc.,* **1972**, 94, 8238–8239.

[14] C. R. Bock, T. J. Meyer and D. G. Whitten, *J. Am. Chem. Soc.,* **1975**, 97, 2909–2911.

[15] J. M. Lehn and J. P. Sauvage, Nouv. *J. Chim.,* **1977**, 1, 449–451.

[16] J. Kiwi and M. Gratzel, *J. Am. Chem. Soc.,* **1979,** 101, 657–658.

[17] L. A. Kelly and M. A. J. Rodgers, *J. Phys. Chem.,* **1995**, 99, 13132–13140.

[18] E. H. Yonemoto, R. L. Riley, Y. I. Kim, S. J. Atherton, R. H. Schmehl and T. E. Mallouk, *J. Am. Chem. Soc.,* **1992,** 114, 8081–8087.

[19] T. Hiraishi, T. Kamachi and I. Okura, *J. Mol. Catal. A: Chem.,* **2000**, 151, 7–15.

[20] K. Kitamoto, M. Ogawa, G. Ajayakumar, S. Masaoka, H. B. Kraatz and K. Sakai, *Inorg. Chem. Front.,* **2016**, 3, 671–680.

[21] K. Kitamoto and K. Sakai, *Chem. – Eur. J.,* **2016**, 22, 12381–12390.

[22] Aslan, J. M., Boston, D. J., MacDonnell, F. M., *Chem.–Eur. J.* **2015**, 21, 17314–17323.

[23] Brennaman M. K., Meyer T. J., and Papanikolas J. M., *J. Phys. Chem. A,* **2004**, 108, 9938–9944.

[24] Van der Salm H., Larsen C. B., McLay J. R. W., Fraser M. G., Lucasa N. T., and Gordon K. C., *Dalton Trans.*, **2014**, 43, 17775-17785.

[25] Van der Salm H., Anastasia B.S., Gordon K. C., *Coord. Chem. Rev.*, **2015**, 282–283, pp 33-49.

[26] J. D. Aguirre, H. T. Chifotides, A. M. Angeles-Boza, A. Chouai, C. Turro, K. R. Dunbar, *Inorg. Chem.* **2009**(48) 4435–4444.

[27] N. J. Lundin, P. J. Walsh, S. L. Howell, A. G. Blackman, K. C. Gordon, *Chem. Eur. J.* 14 (**2008**) 11573–11583.

[28] N. J. Lundin, P. J. Walsh, S. L. Howell, A. G. Blackman, McGarvey J. J., K. C. Gordon, *Inorg. Chem.* **2005***,* 44, 3551−3560.

[29] B. Schafer, H. Gorls, M. Presselt, M. Schmitt, J. Popp, W. Henry, J. G. Vos, S. Rau, *Dalton Trans.* (**2006**) 2225–2231.

[30] Tinker L. L., McDaniel N. D. and Bernhard S., *J. Mater. Chem.,* **2009**, 19, 3328–3337.

[31] Zhang Y., Schulz M., Wächtler M., Karnahl K., Dietzek B., *Coord. Chem. Rev.* **2018**, 356 127–146

[32] Moonshiram D., Garrido B. P., Picón A., Liu C., Zhang X., Karnahl M., Llobet A., *Chem. Eur. J.* **2018**, 24, 6464 –6472.

[33] Mara M. W., Fransted K. A., Chen L. X., *Coord. Chem. Rev.* **2015,** 282–283, 2–18.

[34] Sandroni M., Pellegrin Y., Odobel F., *C. R. Chim.* **2016**, 19, 79–93.

[35] Kamer P.C.J., Van Leeuwen P.W.N.M., Phosphorus(III) Ligands in Homogeneous Catalysis: Design and Synthesis, *John Wiley & Sons*, 2012.

[36] Casey C.P., Whiteker G.T., *Isr. J. Chem.* **1990**, 30, 299–304.

[37] Crabtree R.H., The Organometallic Chemistry of the Transition Metals, 4th ed., *John Wiley & Sons, Inc., Hoboken*, New Jersey, **2005**.

[38] Freixa Z., Van Leeuwen P.W.N.M., *Dalton Trans.* **2003**, 10, 1890–1901.

[39] Tolman C.A., *Chem. Rev.* **1977**, 77, 313–348.

[40] Keller S., Prescimone A., Constable E. C., and Housecroft C. E., *Photochem. Photobiol. Sci.*, **2018**, 17, 375.

[41] Thoresen E. M., Tilset M., Lillerud K. P., Øien-Ødegaard S., Kaur G., and Amedjkouh M. *RSC Adv.*, **2020**, 10, 9052-9062.

[42] Thoresen E. M., Tilset M., Balcells D., Øien-Ødegaard S., Hylland T. K., and Amedjkouh M. Dalton Trans. **2018**, 47 (8), 2589-2601.

[43] Schmittel M. and Ganz A., *Chem. Commun.*, **1997**, 999– 1000.

[44] Saha M. L., Neogi S. and Schmittel M. *Dalton Trans.*, **2014**, 43, 3815-3834.

[45] DaSilveira Neto B. A., Lopes A. S., Wuest M., Costa V. E. U., Ebeling G., Dupont J., *Tetrahedron Lett.* **2005**, 46, 6843 – 6846

[46] Mancilha F. S., DaSilveira Neto B. A., Lopes A. S., Moreira P. F., Quina F. H., Gonçalves R. S., Dupont J., *Eur. J. Org. Chem.* **2006**, 4924 – 4933.

[47] Hylland K., Øien S., & Tilset M. *Eur. J. Org. Chem.* **2020**, 27, 4208-4226.

[48] Yamada M., Tanaka Y., Yoshimoto Y., Kuroda S., Shimao I., *Bull. Chem. Soc. Jpn.*, **1992**, 651006-1011.

[49] Inglett G.E., Smith G.F., *J. Am. Chem. Soc.,* **1950**, 72, 842-844.

[50] Ferretti F., Gallo E., Ragaini F., *J. Org. Chem.* **2014**, 771, 59 – 67.

[51] Miltov. A. S., Karavan V. S., Borin V. A. *Russ. J. Gen. Chem.,* **2019**, 89 (5), 1055 – 1057.

[52] Herrero C., Quaranta A., Fallahpour R. A., Leibl W., and AukaulooA. *J. Phys. Chem.*, **2013**, 117 (19), 9605.

[53] Cardinaels T., Ramaekers J., Nockemann P., Driesen K., Van Hecke K., Van Meervelt L., Lei S., De Feyter S., Guillon D., Donnio B., and Binnemans K. *Chem. Mater.* **2008**, 20 (4), 1278-1291.

[54] Zhao Y–L, Hu L., Grüner G., and Stoddart J. F., *J. Am. Chem. Soc.* **2008** 130 (50), 16996-17003.

[55] Wendlandt A.E., Stahl S. S., *J. Am. Chem. Soc.,* **2014**, 136 (1), 506-512.

[56] Ettedgui J., Diskin-Posner Y., Weiner L., and Neumann R., *J. Am. Chem. Soc.,* **2011**, 133 (2), 188 – 190.

[57] Zhong C., Huang H., He A., and Zhang H., *Dyes Pigm.,* **2008**, 77 (3), 578.

[58] Zheng R. H., Guo H. C., Jiang J. H., Xu K. H., Liu B. B., Sun W. L., Shen Z. Q., *Chin. Chem. Lett.*, **2010**, 21, 1270 – 1272.

[59] Ong C. W., Liao S. C., Chang T. H., Hsu H. F., *J. Org. Chem.* **2004**, 69, 3181.

[60] Suzuki T., Okubo T., Okada A., Yamashita Y., Miyashi T., *Heterocycles* **1993**, 35, 395.

[61] Tao Y–M., Li H. Y., Xu Q. L., Zhu Y. C., Kang L. C., Zheng X. Y., Zuo J. L., You X. Z., *Synthetic Metals*, **2011**, 161 (9–10), 718-723.

[62] Reich Hans, Collection; NMR Spectroscopy, *ACS Div. Org. Chem.,* **2020**. URL: https://organicchemistrydata.netlify.app/hansreich/resources/nmr/?page=05-hmr-15-aabb/. (02-06-2023).

[63] Wu J., Lai C., Li Z., Lu Y., Leng T., Shen Y., Wang C., *Dyes Pigm.* **2016**, 124, 268 – 276.

[64] Pilgram K., Zupan M., Skiles R., J. Het. Chem. **1970**, 7(3), 629 – 633.

[65] Blouin N., Michaud A., Gendron D., Wakim S., Blair E., Neagu–Plesu R., Belletete M., Durocher G., Tao Y., Leclerc M., *J. Am. Chem. Soc.* **2008**, 130 (2), 732 – 742.

[66] Helgesen M., Gevorgyan S. A., Krebs F. C., Janssen R. A. J., *Chem. Mater.* **2009.** 21 (19), 4669 – 4675.

[67] Wong X. L., Sarjadi M. S., *J. Phys: Conf. Ser.* **2019**, 1358, 012006.

[68] Tan S. E., Sarjadi M. S., *Mal. J. Fund. Appl. Sci.* **2017**, 13 (4), 760 – 763.

[69] Heiskanen J. P., Vivo P., Saari N. M., Hukka T. I., Kastinen T., Kaunisto K., Lemmetyinen H. J., Hormi O. E. O. *J. Org. Chem.* **2016** *81* (4), 1535-1546.

[70] Ito Y., Kojima Y., Suginome M., Murakami M., *Heterocycles* **1996**, 42, 597–615.

[71] Naef R., Balli H., *Helv. Chim. Acta* **1978,** 61, 2958–2973.

[72] Corey E. J., Kuhnle F. N. M., *Tetrahedron Lett.* **1997**, 38, 8631– 8634.

[73] Mataka S., Eguchi H., Takahashi K., Hatta T., Tashiro M., *Bull. Chem. Soc. Jpn.* **1989**, 62, 3127–3131.

[74] Mataka S., Ikezaki Y., Takahashi K., Torii A., Tashiro M., *Heterocycles* **1992**, 33, 791–800.

[75] Dyachenko E. K., Pesin V. G., Papirnik M. P., *Zh. Org. Khim.* **1986**, 22, 421–424.

[76] Prashad M., Liu Y., Repic O., *Tetrahedron Lett.* **2001**, 42, 2277–2279.

[77] Ganem B., Heinzman S. W., *J. Am. Chem. Soc.* **1982**, 104, 6801.

[78] Baird D. B., Baxter I., Cameron D. W., Phillips W. R. J. *Chem. Soc. Chem. Commum*. **1971**, 31.

[79] Zhang Y., Traber P., Zedler L., Kupfer S., Gräfe S., Schulz M., Frey W., Karnahl M. and Dietzek B., *Phys. Chem. Chem. Phys.*, **2018**,**20**, 24843-24857.

[80] Griffin C. E., Gordon M., *J. Am. Chem. Soc.* **1967**, 89, 17, 4427–4431

[81] (a) Khaleeludin K., Scott J. M. W., *Chem. Commun. (London),* **1966**, 511-512. (b) Griffin C. E., Davison R. B., Gordon M. *Tetrahedron* **1966**; 22: 561-565.

[82] (a) Keller S., Pertegás A., Longo G., Martinez L., Cerdá J., Junquera-Hernández J.M.; Prescimone A., Constable E.C., Housecroft C.E., Ortí E., *J. Mater. Chem. C* **2016**, *4*, 3857–3871. (b) Brunner F., Graber S., Baumgartner Y., Häussinger D., Prescimone A., Constable E.C., Housecroft C.E., *Dalton Trans.* **2017**, *46*, 6379–6391.

[83] Claridge, T. D. W., *High-resolution NMR techniques in organic chemistry.* **2016**, 3rd ed., Amsterdam: Pergamon.

[84] Kwan E. E., *NMR Manual Course notes*. **2019.** URL: https://ekwan.github.io/notes.html #nmr -spectroscopy. (18.06.2023).

[85] Kühl O., *Phosphorus-31 NMR Spectroscopy, A Concise Introduction for the Synthetic Organic and Organometallic Chemist.* **2008**, Springer-Verlag Berlin Heidelberg.

[86] Morozzi P., Ballarin B., Arcozzi S., Brattich E., Lucarelli F., Nava S., Tositti L., *Atmospheric Environment,* **2021**, 252, 118297.

[87] Blitz P. J., Mirabella F. M., *Chapter 5: Diffuse Reflectance Spectroscopy; Modern Techniques in Applied Molecular Spectroscopy.* **1998,** 1st ed., John Wiley & Sons Inc., 185 – 219.

[88] S. Lou and G. C. Fu, *Adv. Synth. Catal*, **2010**, 352, 2081– 2084.

7. Appendix

Table of Contents

7.1. Supplementary NMR spectra of synthesized compounds

7.1.1. Compound 1a

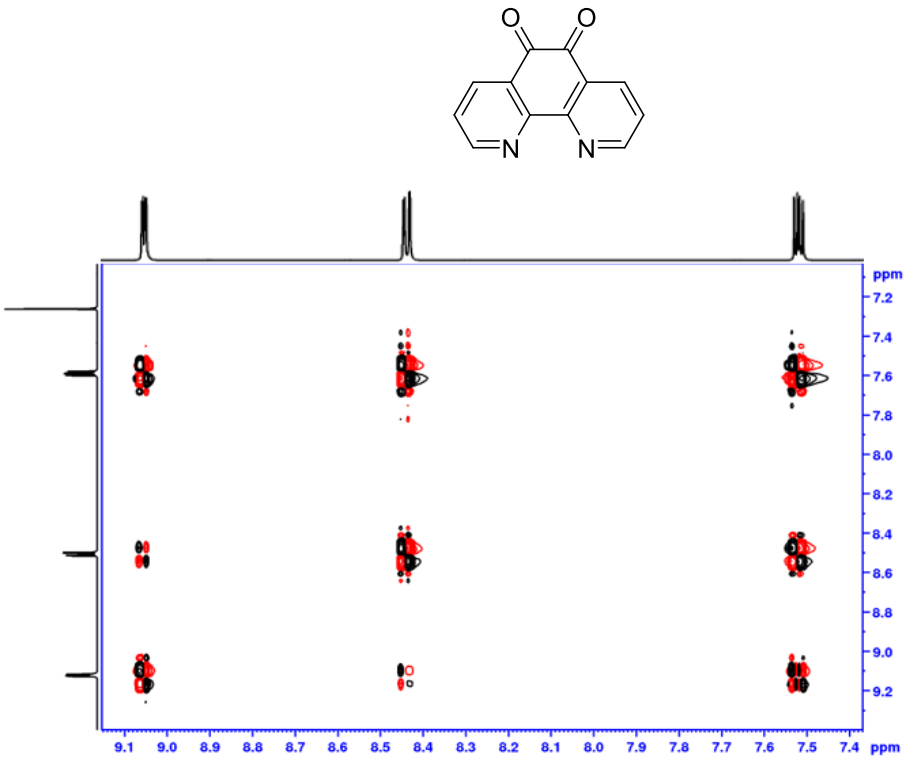

Figure 7.1. DQF–COSY (600 MHz, $CDCl_3$) spectrum of compound **1a.**

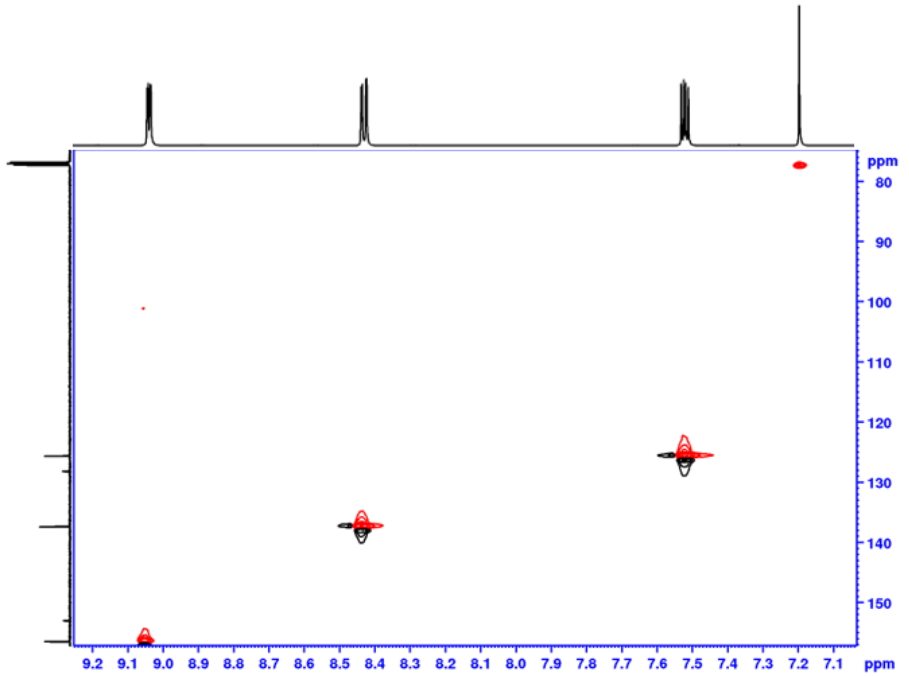

Figure 7.2. ^{1}H–^{13}C HSQC (600 – 151 MHz, $CDCl_3$) spectrum of compound **1a**.

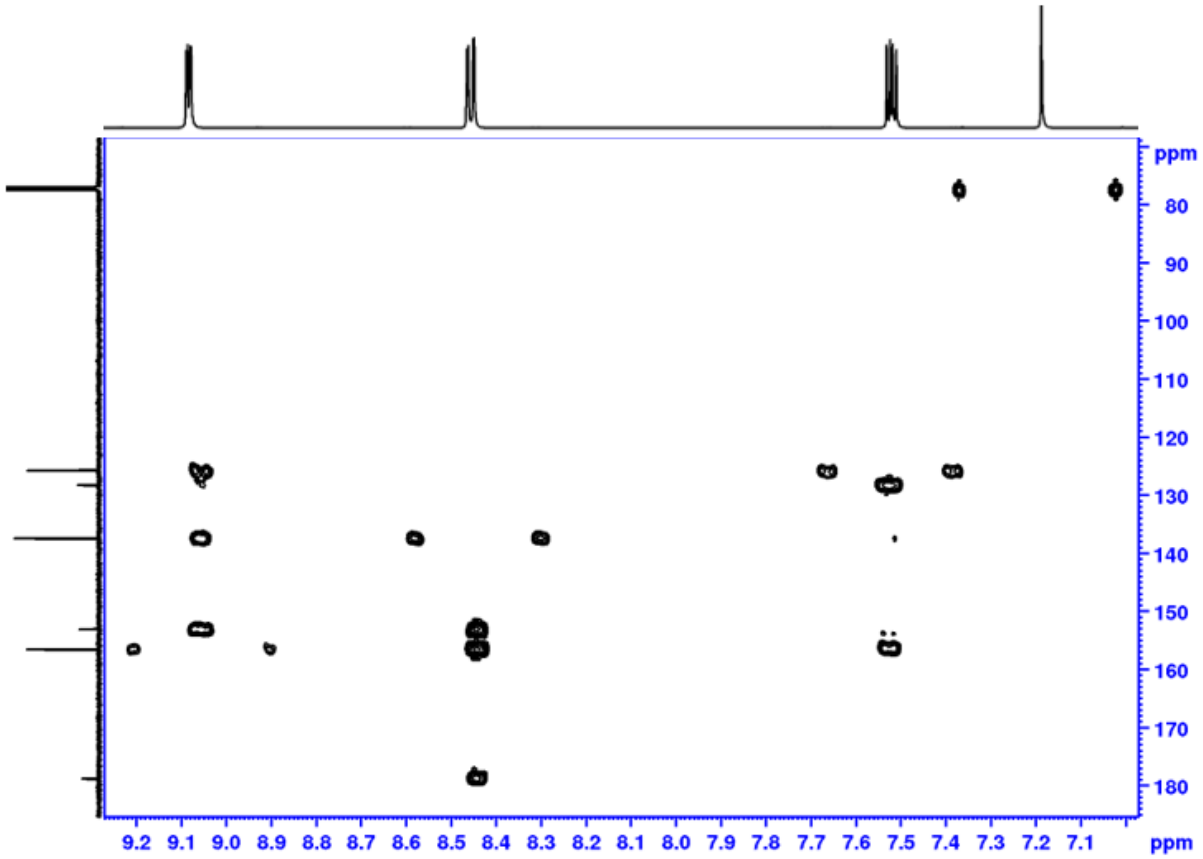

Figure 7.3. $^{1}H–^{13}C$ HMBC (600 – 151 MHz, $CDCl_3$) spectrum of compound **1a**.

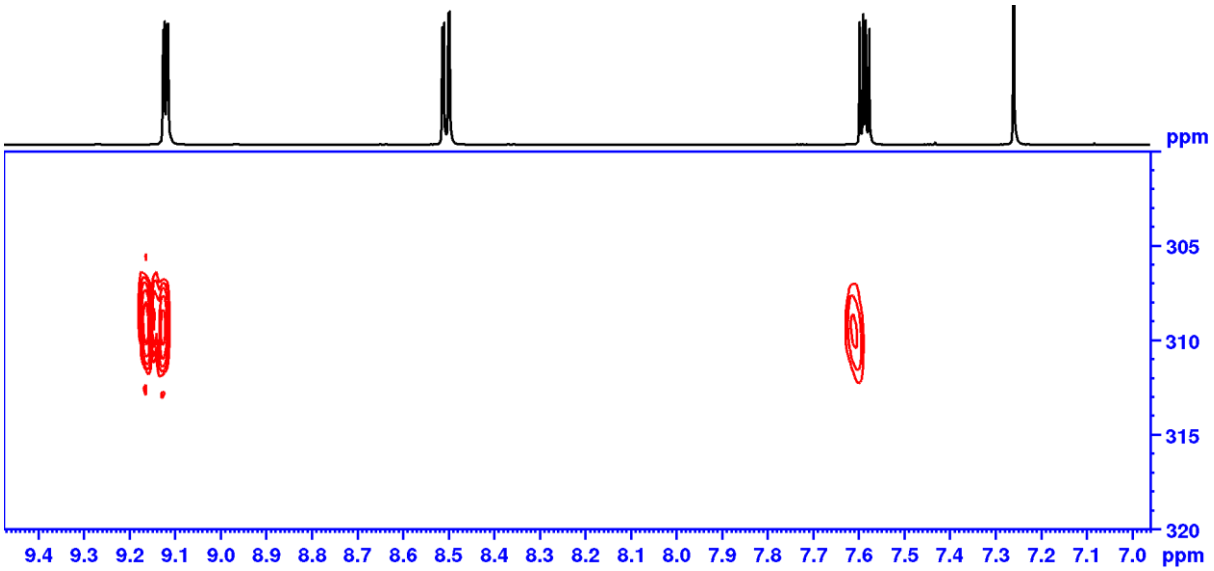

Figure 7.4. Unreferenced $^{1}H–^{15}N$ HMBC (600 – 61 MHz, $CDCl_3$) spectrum of compound **1a**. CNST13 (Default)= 10 Hz.

7.1.2. Compound 2

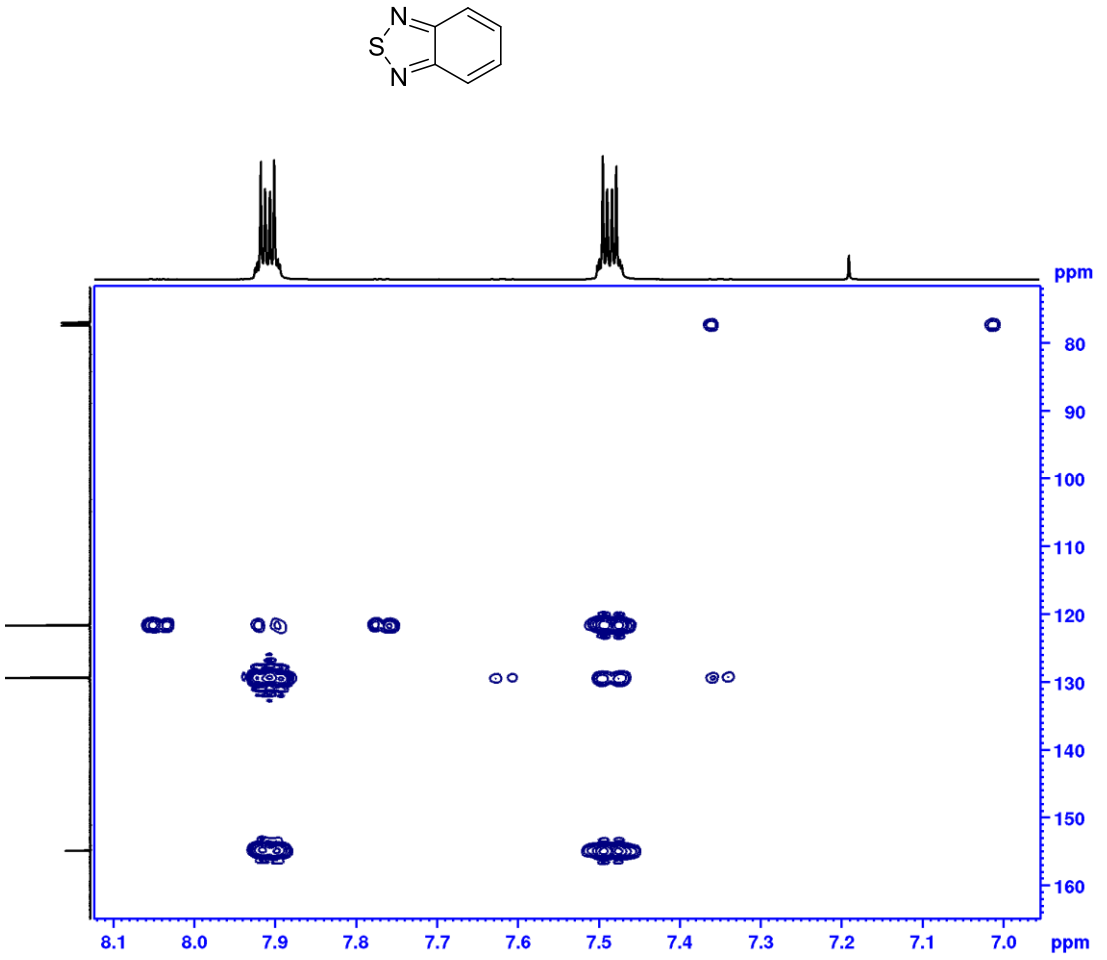

Figure 7.5. $^{1}H–^{13}C$ HMBC (600 – 151 MHz, $CDCl_3$) spectrum of compound **2.**

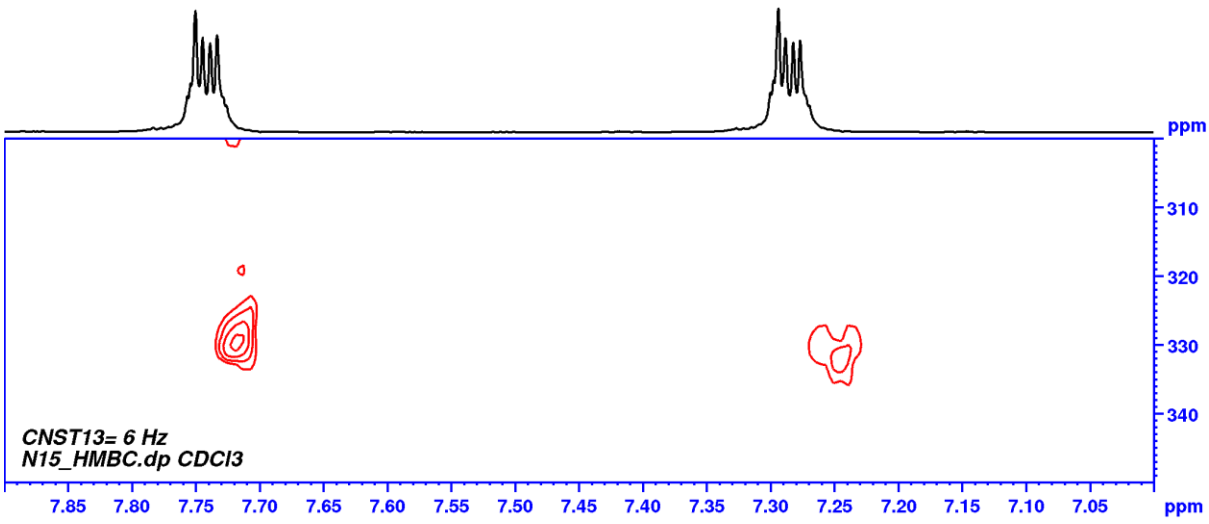

Figure 7.6. Unreferenced $^{1}H–^{15}N$ HMBC (600 – 61 MHz, $CDCl_3$) spectrum of compound **2**.

7.1.3. Compound 3a

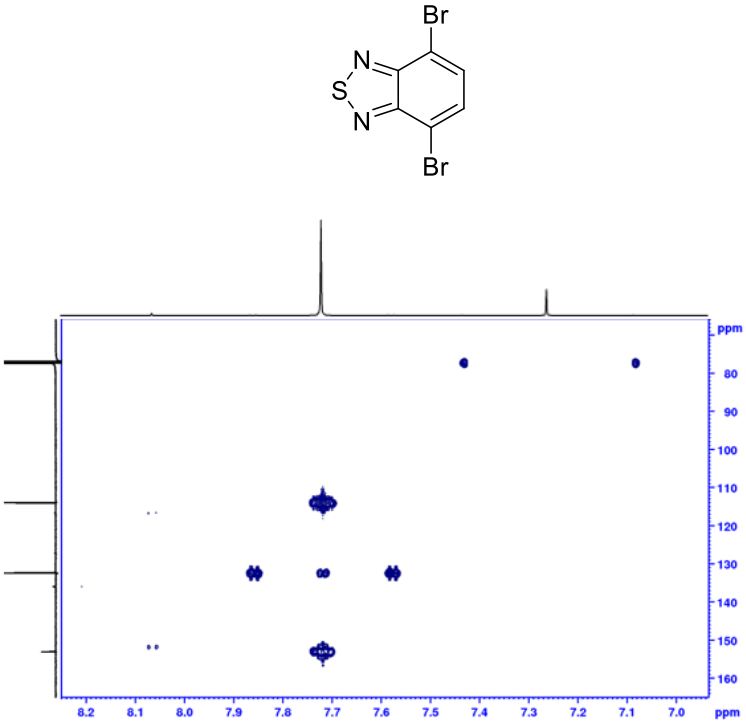

Figure 7.7. $^{1}H–^{13}C$ HMBC (600 – 151 MHz, $CDCl_3$) spectrum of compound **3a.**

7.1.4. Compound 3b

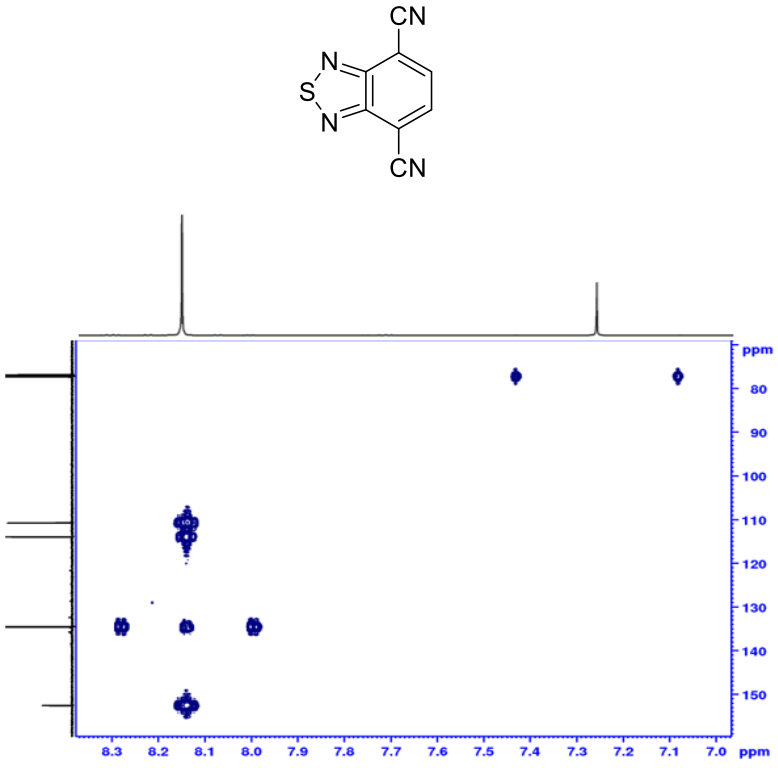

Figure 7.8. $^{1}H–^{13}C$ HMBC (600 – 151 MHz, $CDCl_3$) spectrum of compound **3b.**

7.1.5. Compound 3c

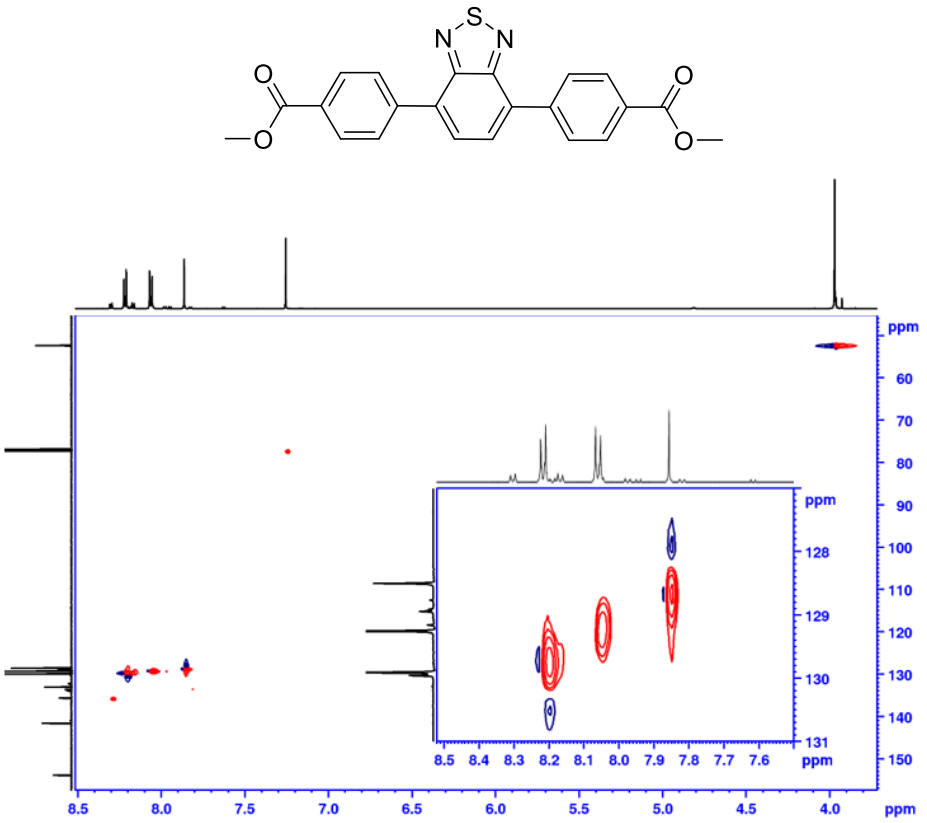

Figure 7.9. Edited $^{1}H–^{13}C$ HSQC (600 – 151 MHz, $CDCl_3$) spectrum of compound **3c**

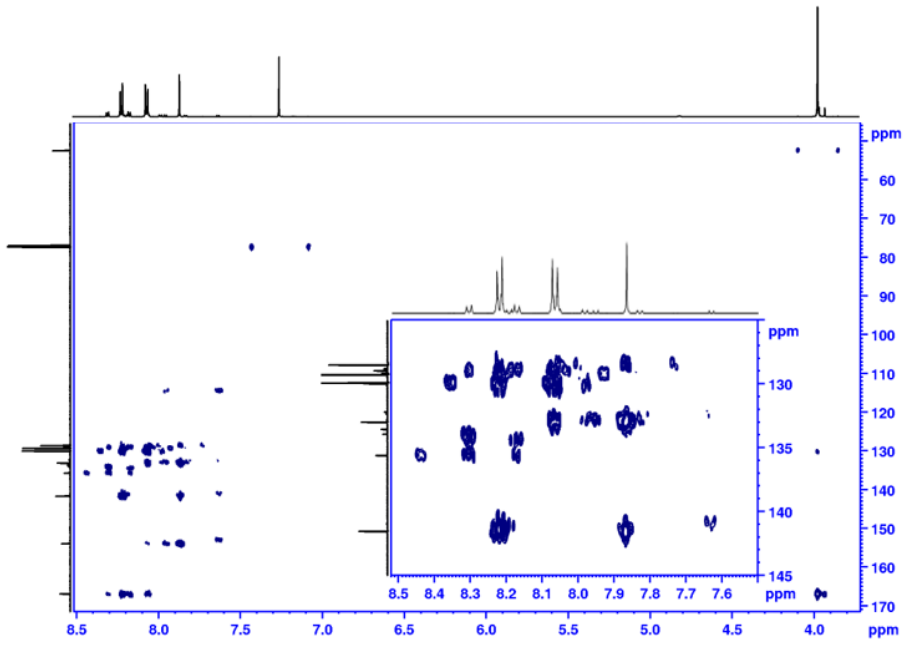

Figure 7.10. $^{1}H–^{13}C$ HMBC (600 – 151 MHz, $CDCl_3$) spectrum of compound **3c**

7.1.6. Compound 3d

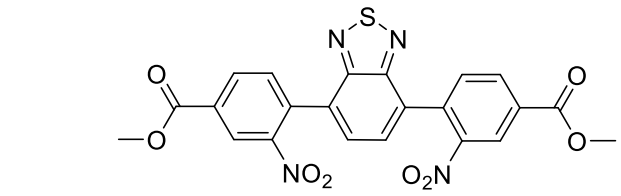

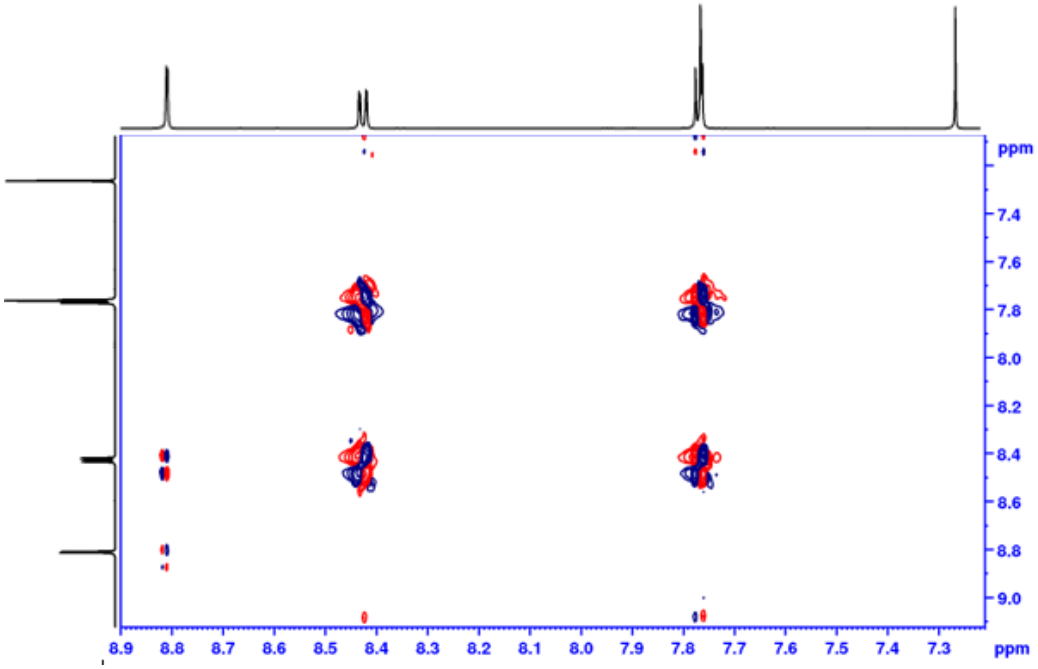

Figure 7.11. COSY–DQF (600 MHz, $CDCl_3$) spectrum of compound **3d**

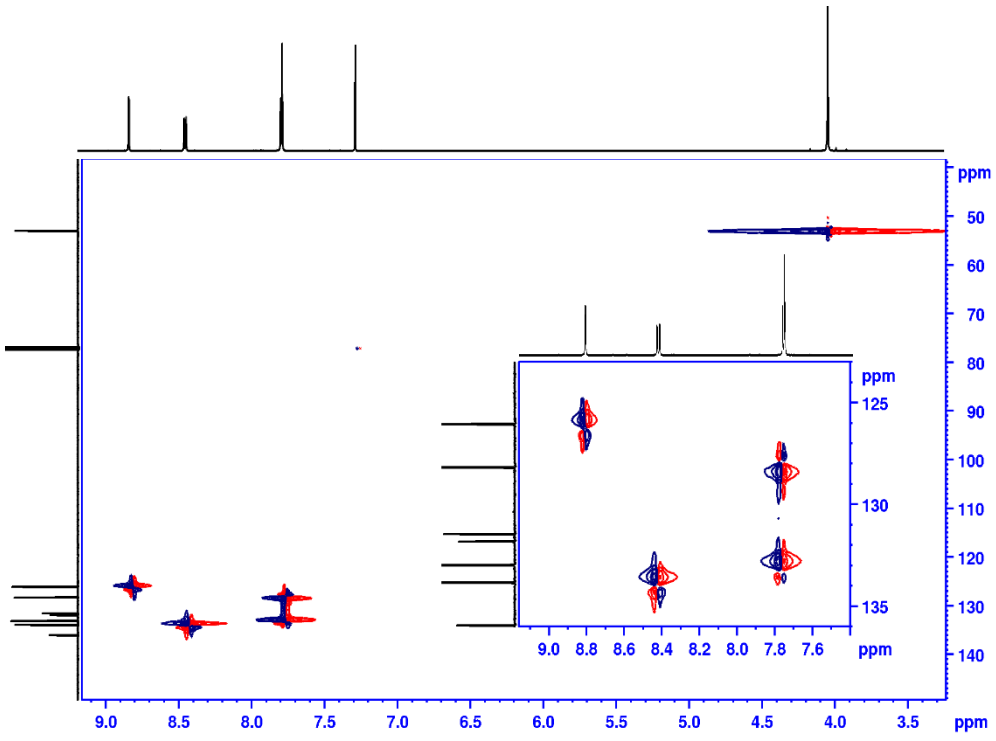

Figure 7.12. ^{1}H–^{13}C HSQC (600 – 151 MHz, $CDCl_3$) spectrum of compound **3d**

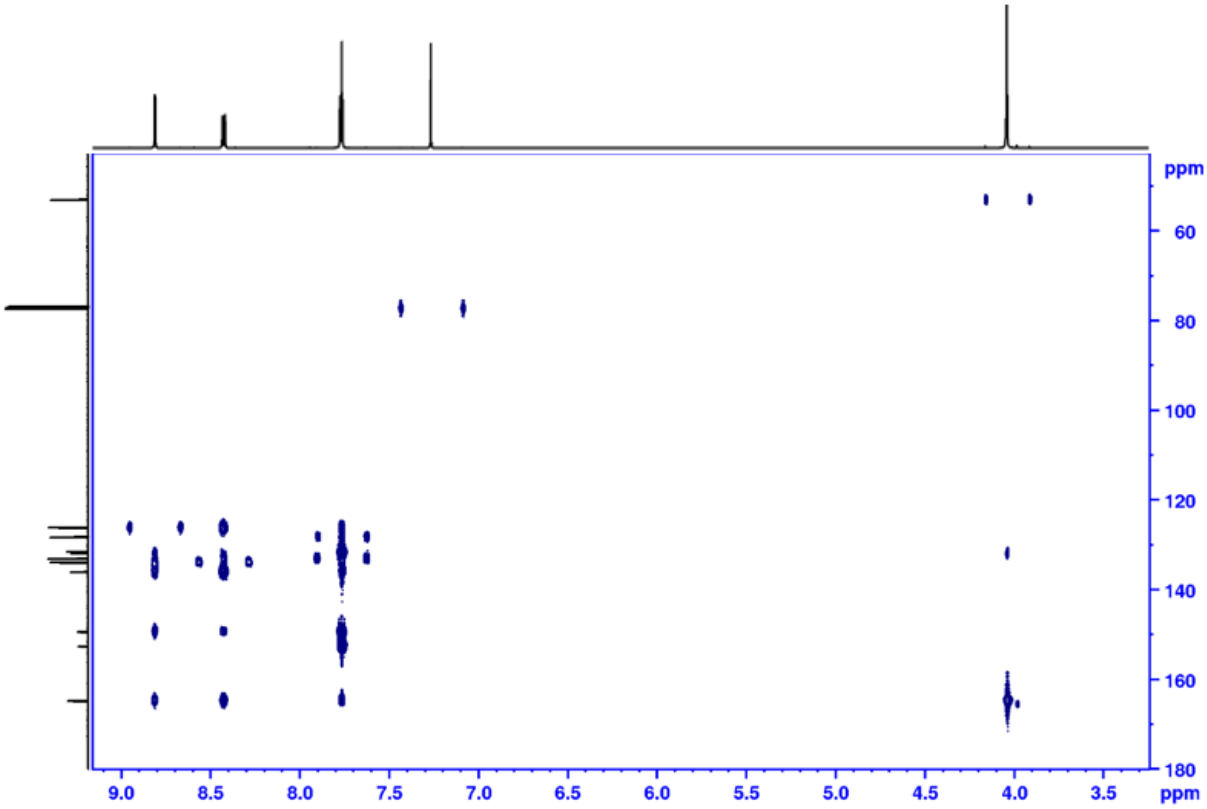

Figure 7.13. $^{1}H–^{13}C$ HMBC (600 – 151 MHz, $CDCl_3$) spectrum of compound **3d**

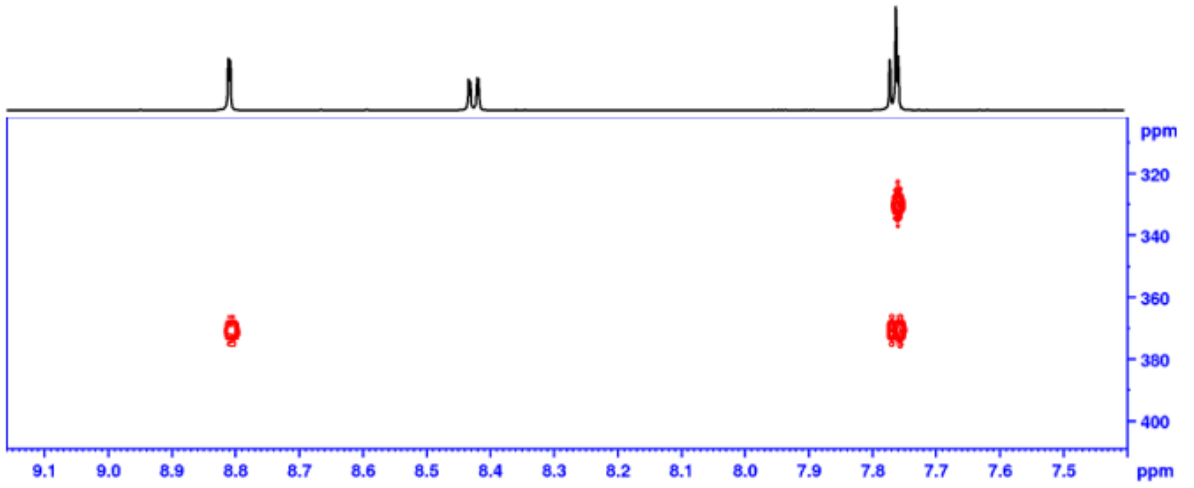

Figure 7.14. Unreferenced $^{1}H–^{15}N$ HMBC (600 – 61 MHz, $CDCl_3$) spectrum of compound **3d.**

7.1.7. Compound 3e

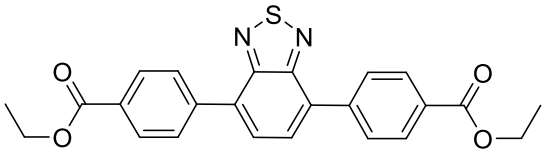

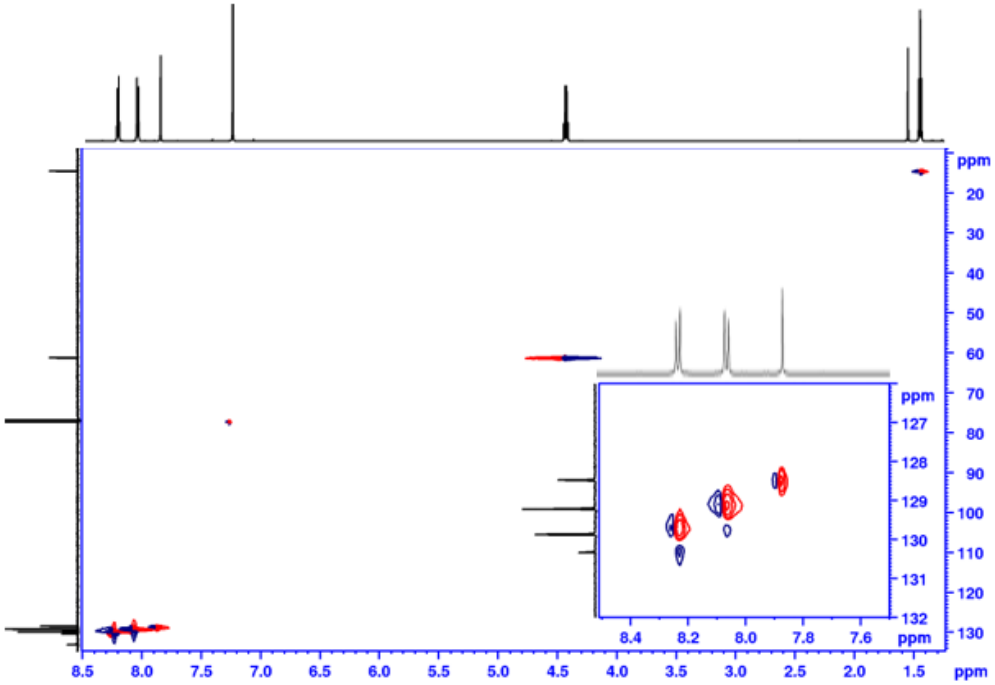

Figure 7.15. $^{1}H–^{13}C$ HSQC (600 – 151 MHz, $CDCl_3$) spectrum of compound **3e.**

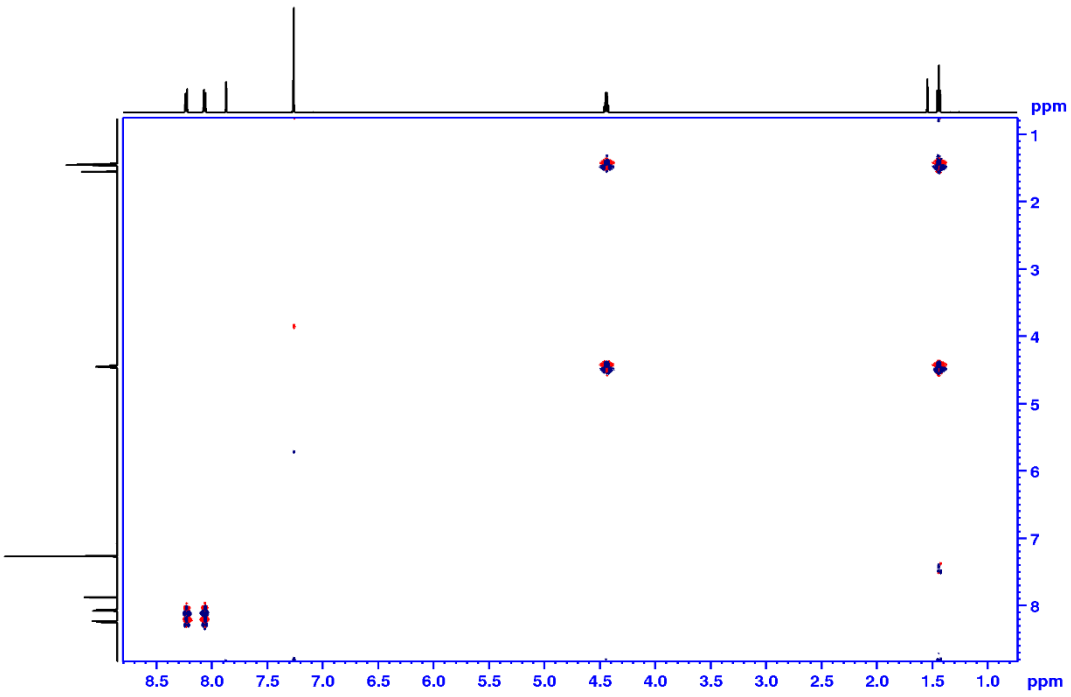

Figure 7.16. COSY–DQF (600 MHz, $CDCl_3$) spectrum of compound **3e.**

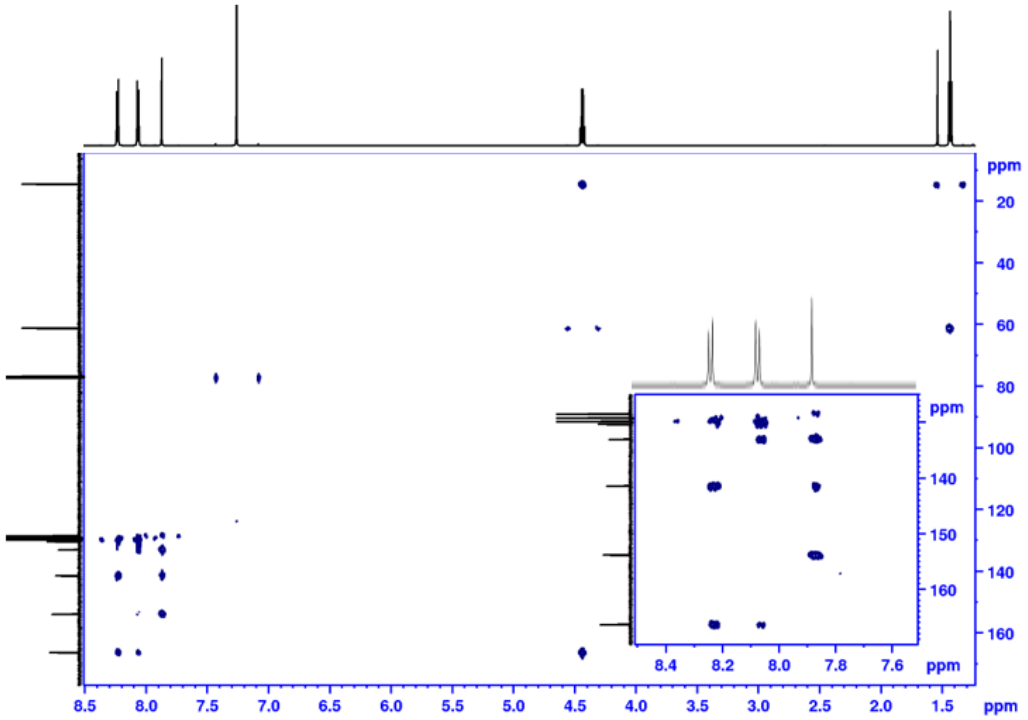

Figure 7.17. $^{1}H–^{13}C$ HMBC (600 MHz, $CDCl_3$) spectrum of compound **3e**

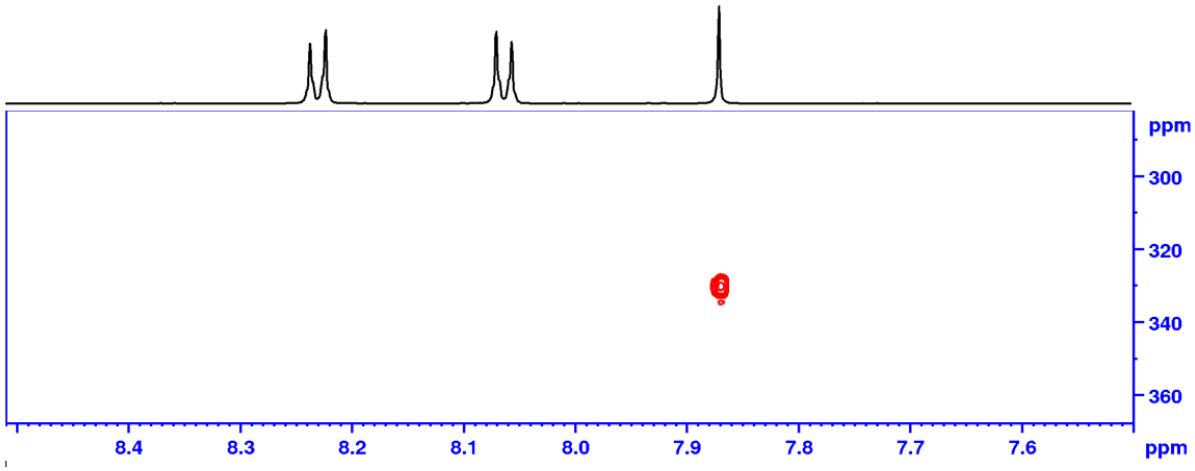

Figure 7.18. $^{1}H–^{15}N$ HMBC (600 MHz, $CDCl_3$) spectrum of compound **3e**

7.1.8. Compound 3f

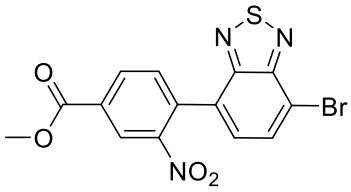

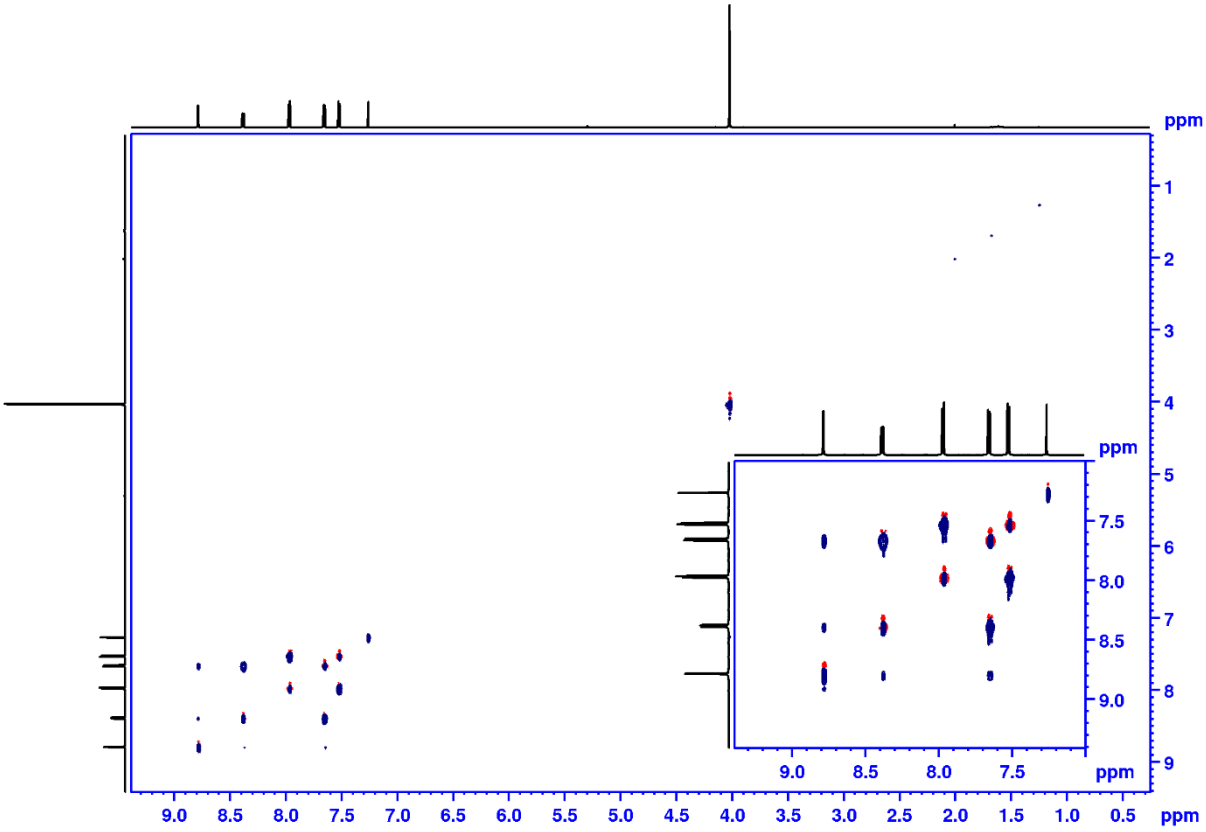

Figure 7.19. TOCSY (600 MHz, $CDCl_3$) spectrum of compound **3f**

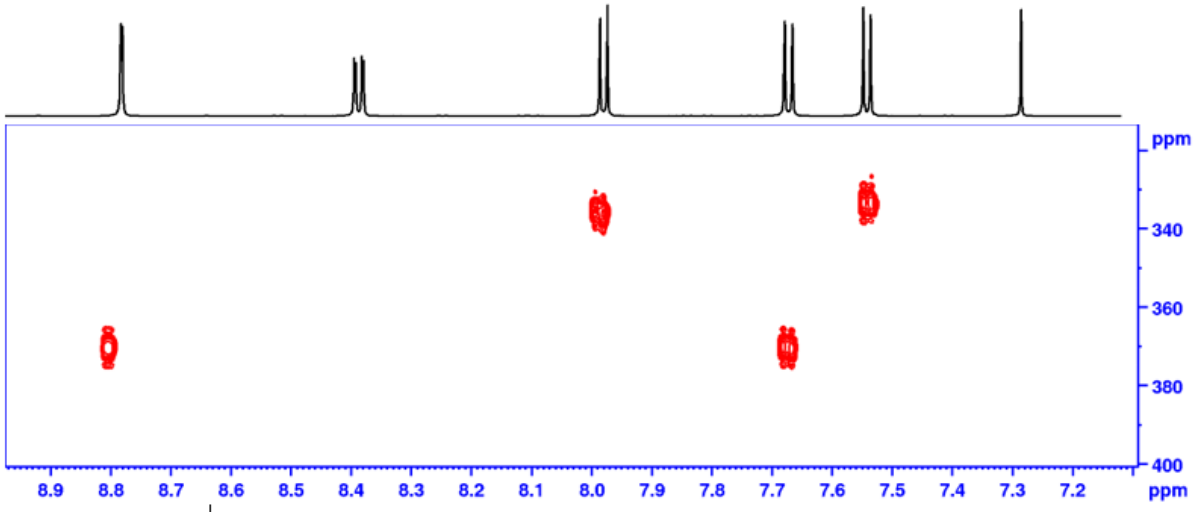

Figure 7.20. Unreferenced ^{1}H – ^{15}N HMBC (600 – 61 MHz, $CDCl_3$) spectrum of compound **3f.**

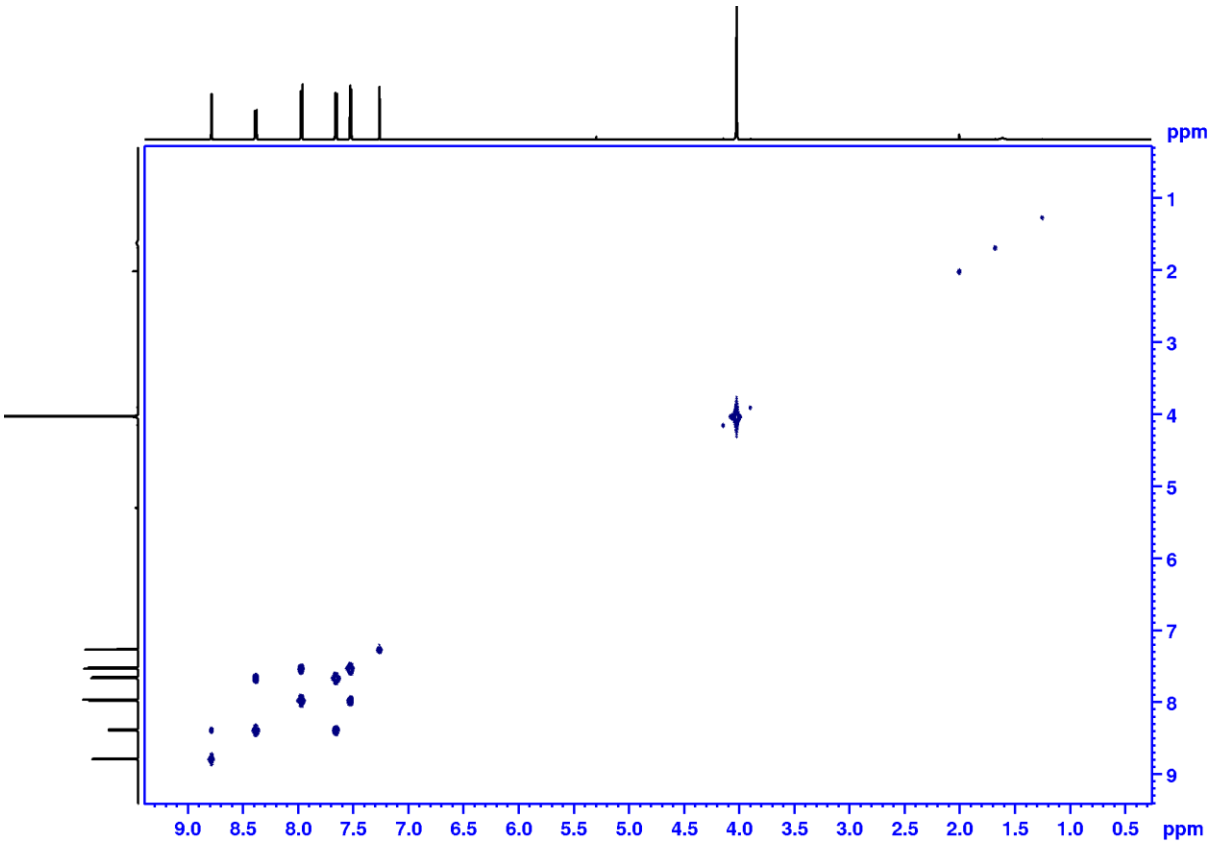

Figure 7.21. COSY-GPSW (600 MHz, $CDCl_3$) spectrum of compound **3f.**

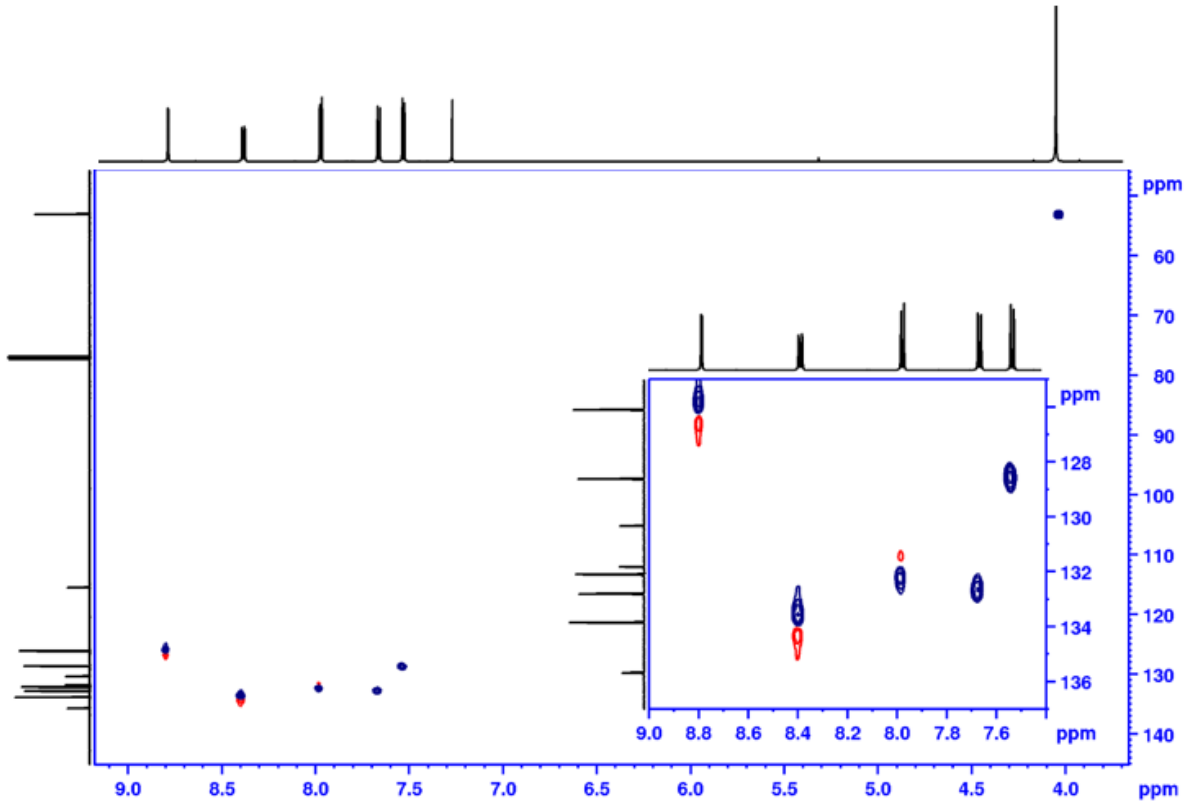

Figure 7.22. ^{1}H – ^{13}C HSQC (600 – 151 MHz, $CDCl_3$) spectrum of compound **3f.**

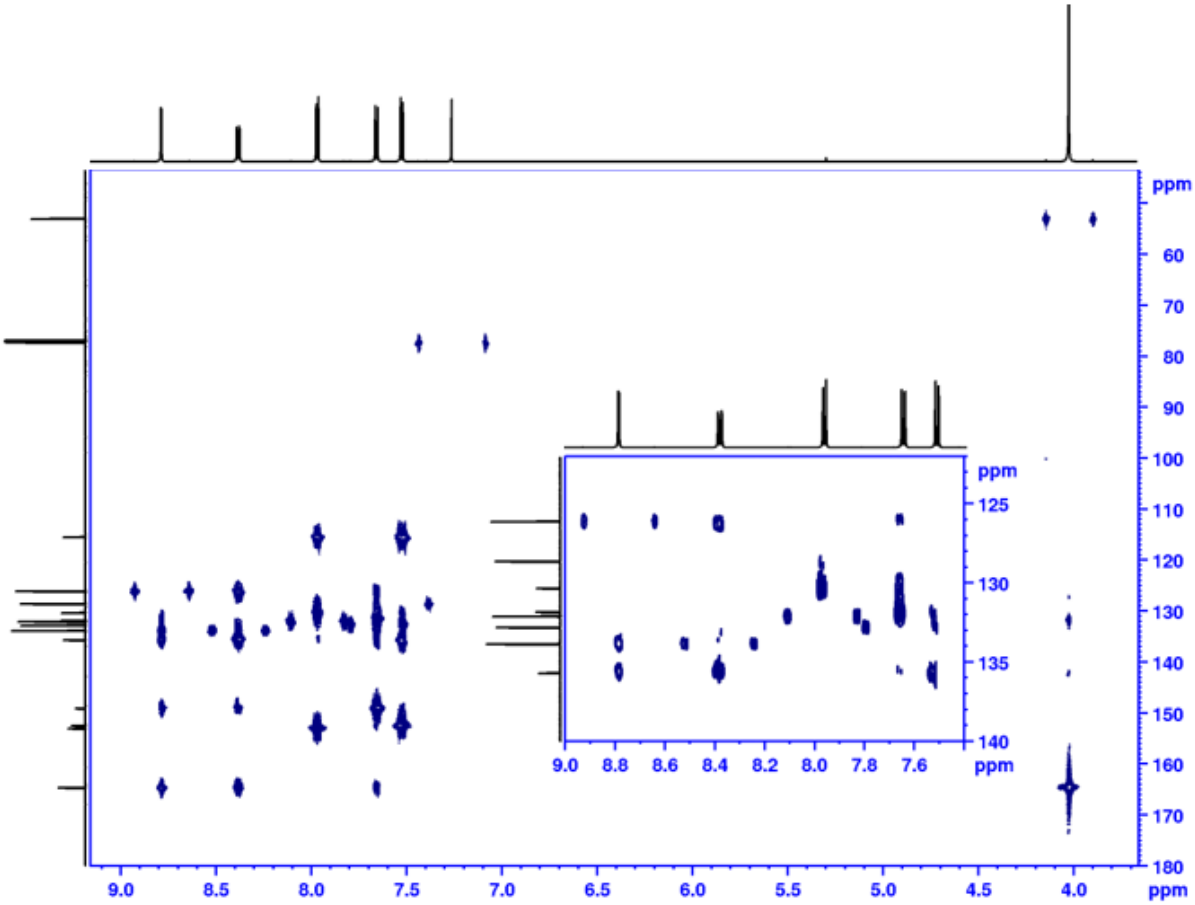

Figure 7.23. $^{1}H - ^{13}C$ HMBC (600 – 151 MHz, $CDCl_3$) spectrum of compound **3f.**

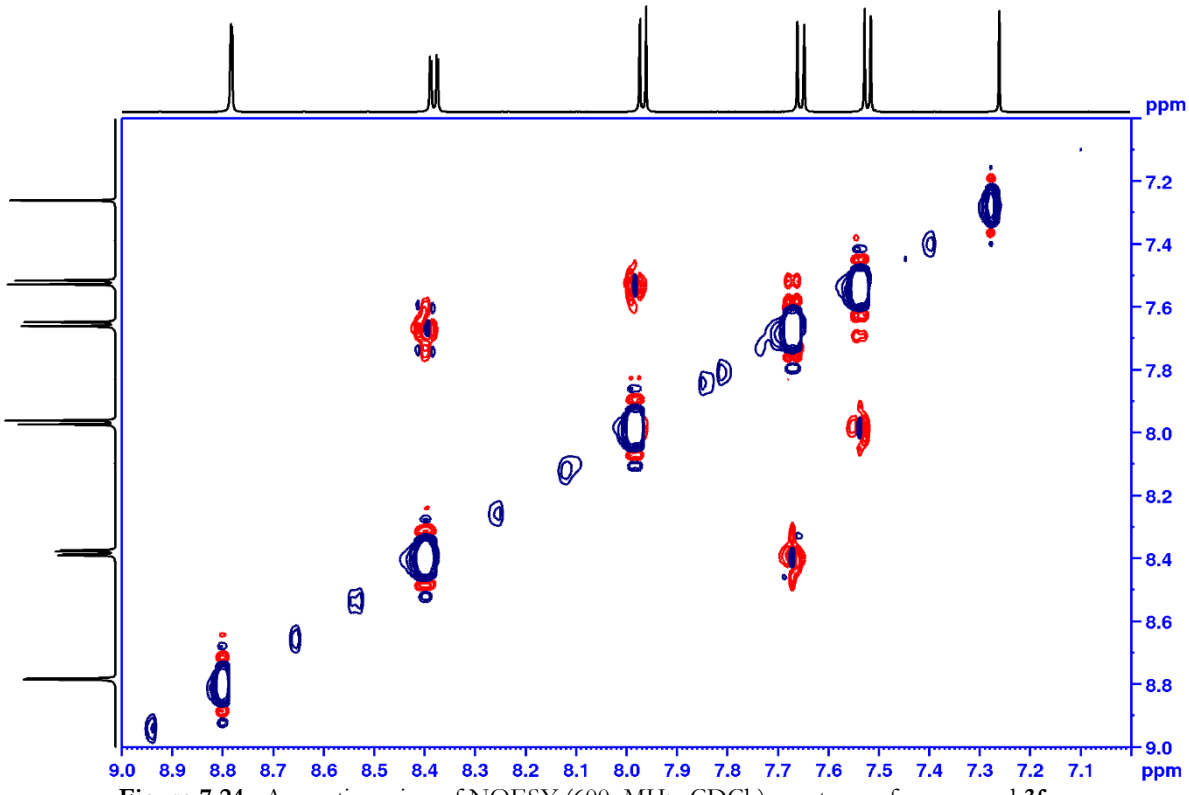

Figure 7.24. Aromatic region of NOESY (600 MHz, $CDCl_3$) spectrum of compound **3f.**

7.1.9. Compound 3g

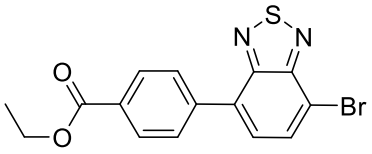

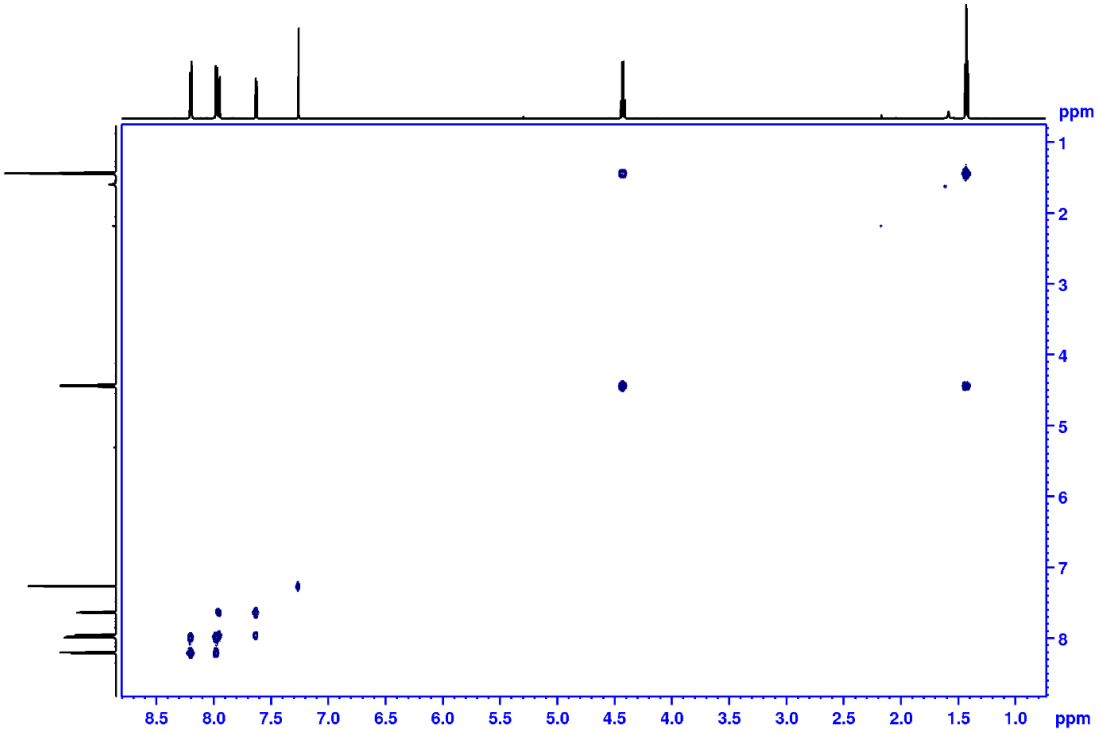

Figure 7.25. COSY–GPSW (600 MHz, $CDCl_3$) spectrum of compound **3g.**

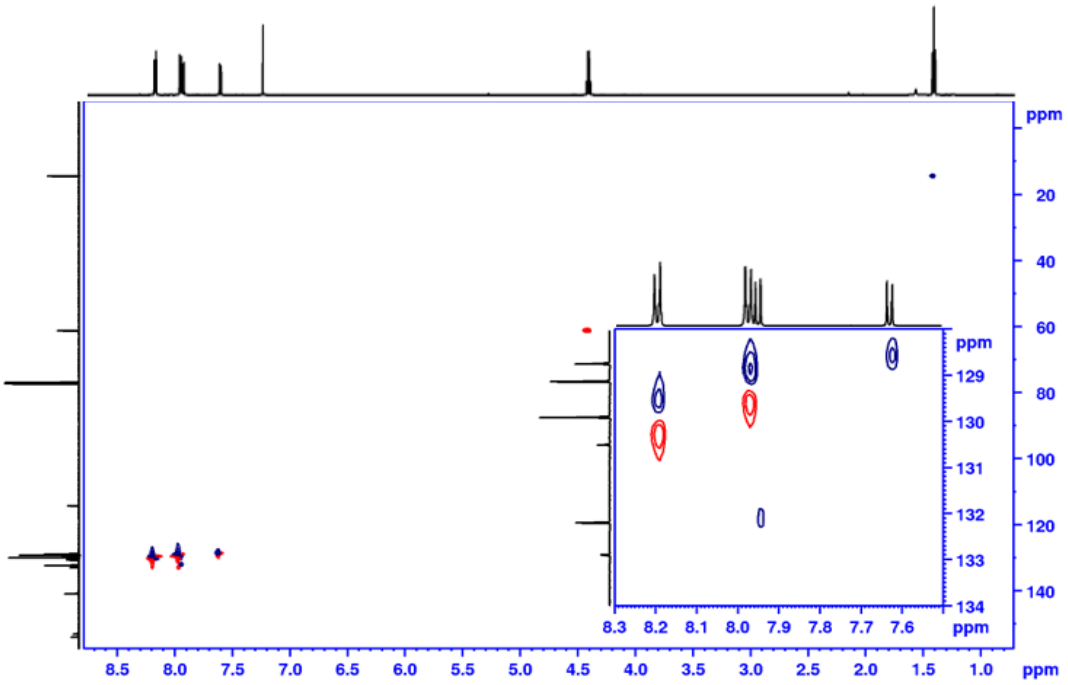

Figure 7.26. ^{1}H – ^{13}C Edited HSQC (600 – 151 MHz, $CDCl_3$) spectrum of compound **3g.**

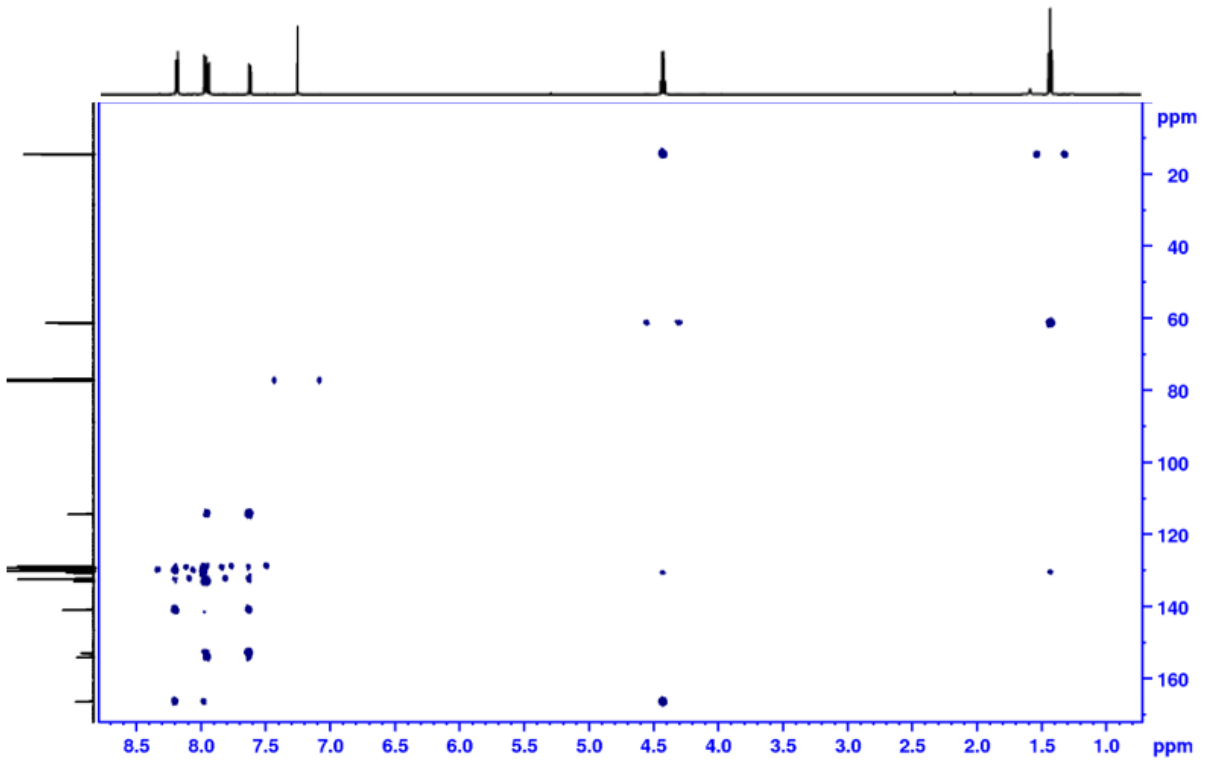

Figure 7.27. ^{1}H – ^{13}C HMBC (600 – 151 MHz, $CDCl_3$) spectrum of compound **3g.**

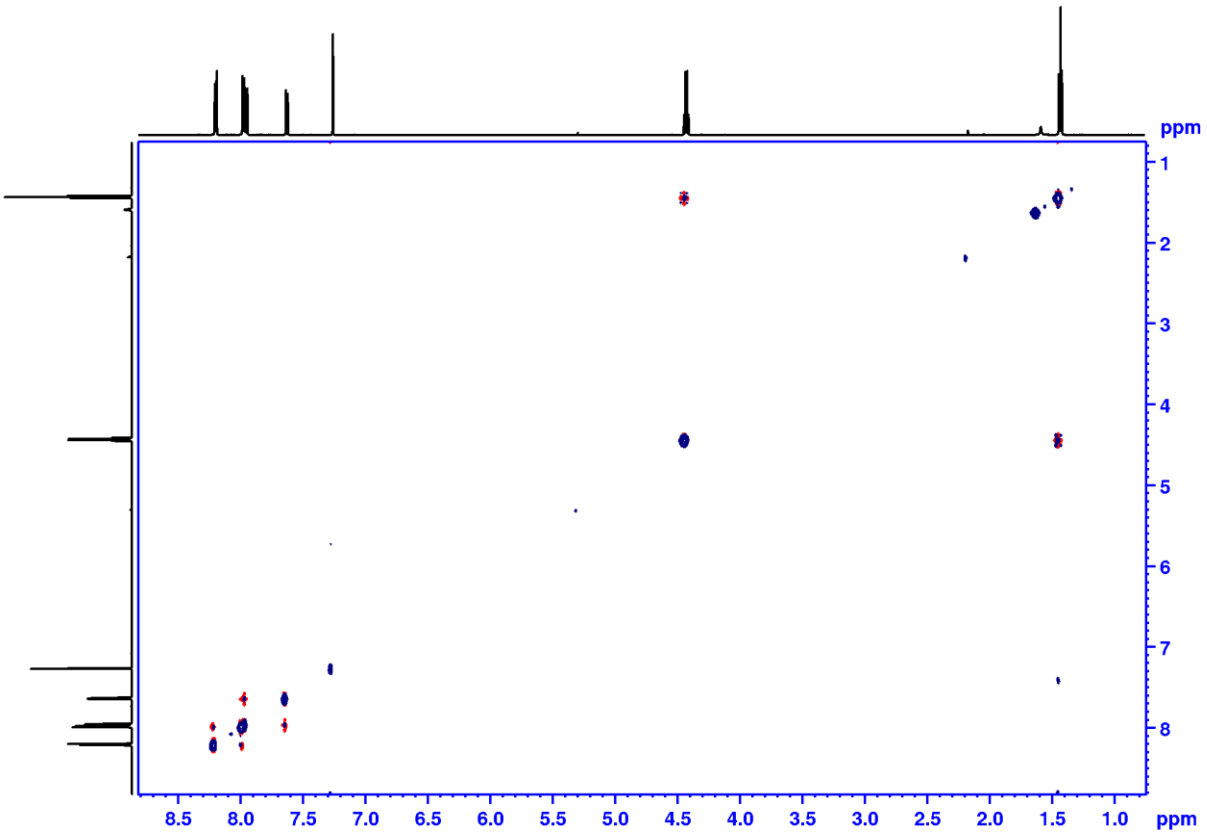

Figure 7.28. NOESY (600 MHz, $CDCl_3$) spectrum of compound **3g**

7.1.10. Compound 3h

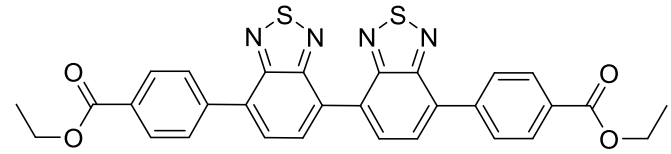

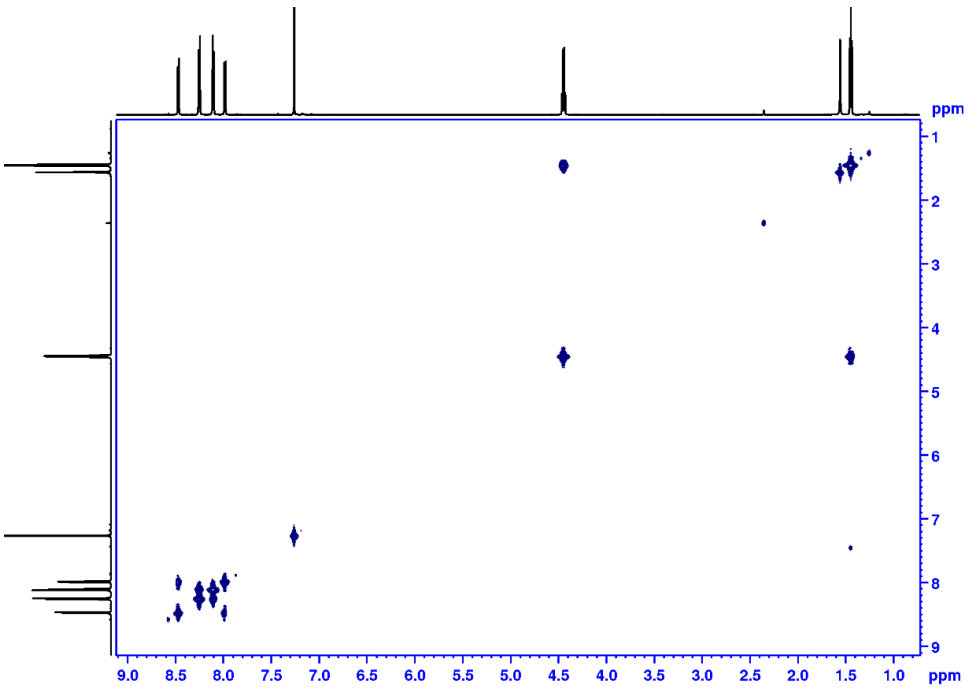

Figure 7.29. COSY-GPSW (600 MHz, $CDCl_3$) spectrum of compound **3h**

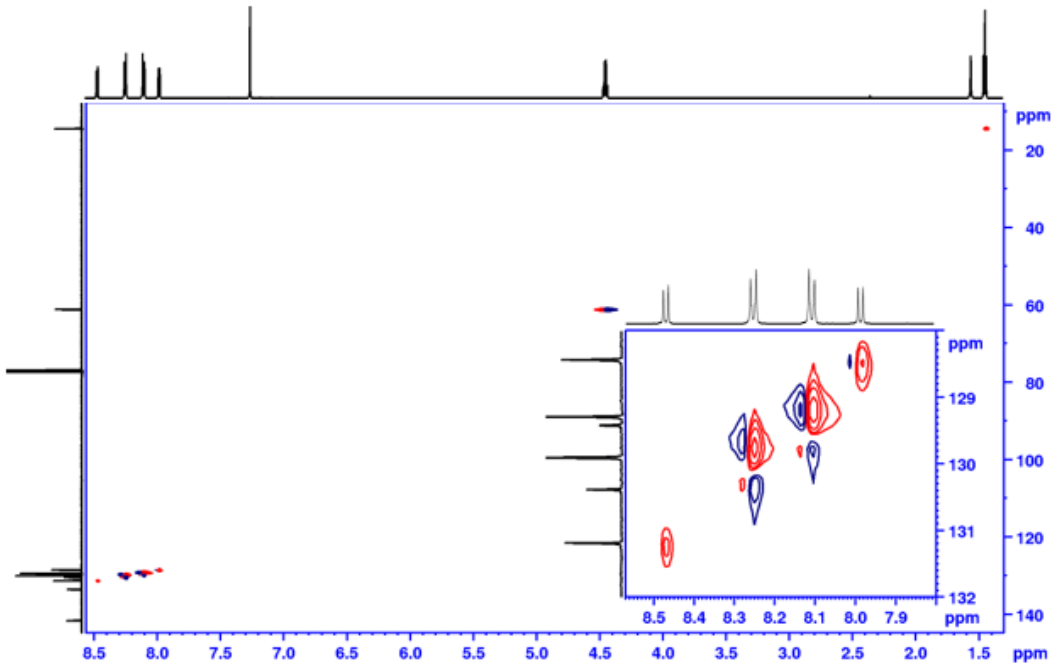

Figure 7.30. ^{1}H–^{13}C HSQC (600 – 151 MHz, $CDCl_3$) spectrum of compound **3h.**

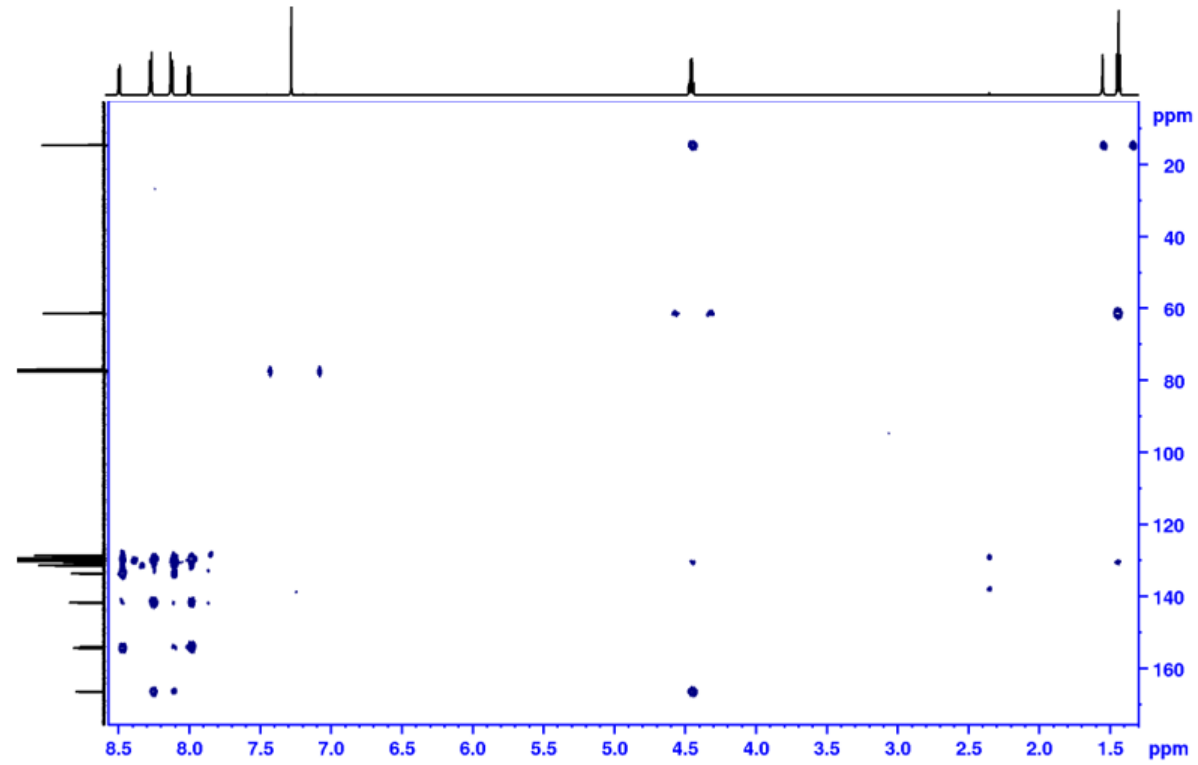

Figure 7.31. $^{1}H–^{13}C$ HMBC (600 – 151 MHz, $CDCl_3$) spectrum of compound **3h.**

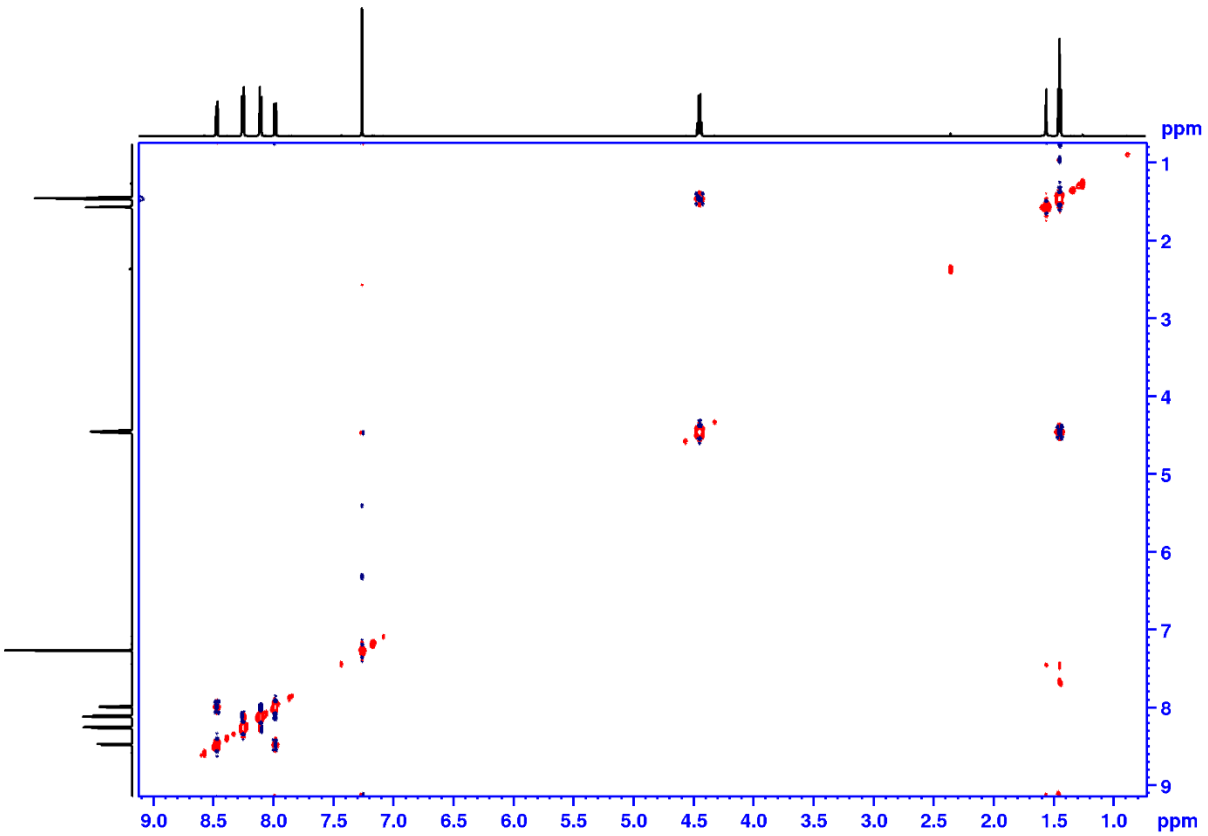

Figure 7.32. NOESY (600 MHz, $CDCl_3$) spectrum of compound **3h.**

7.1.11. Compound 4a

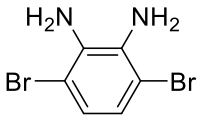

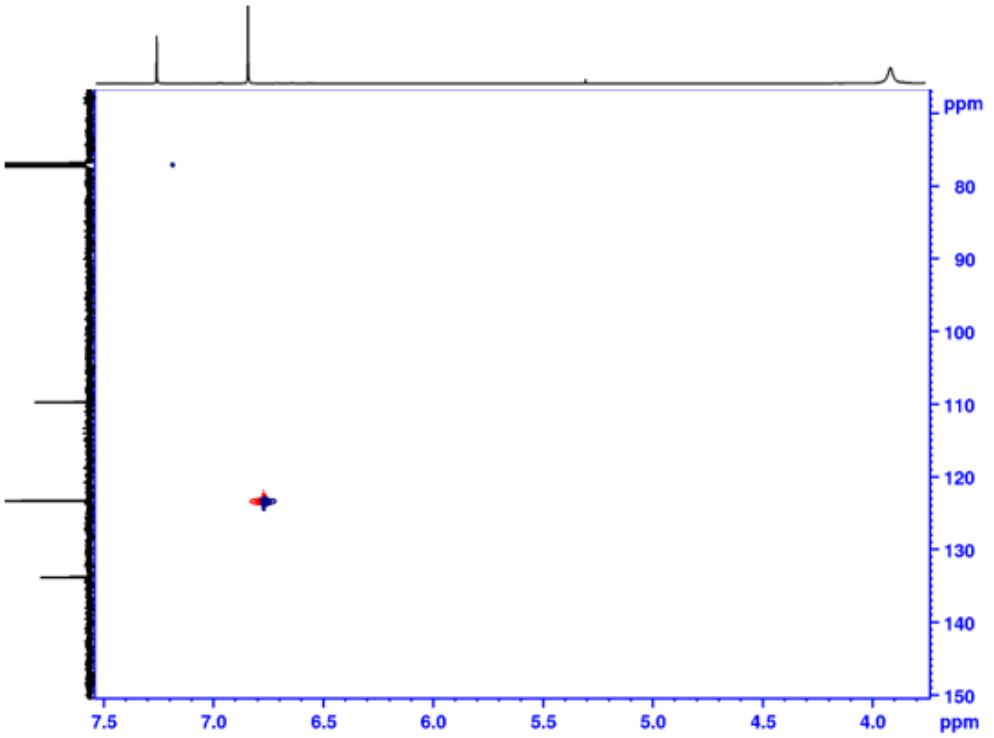

Figure 7.33. ^{1}H -^{13}C HSQC (600 MHz, $CDCl_3$) spectrum of compound **4a.**

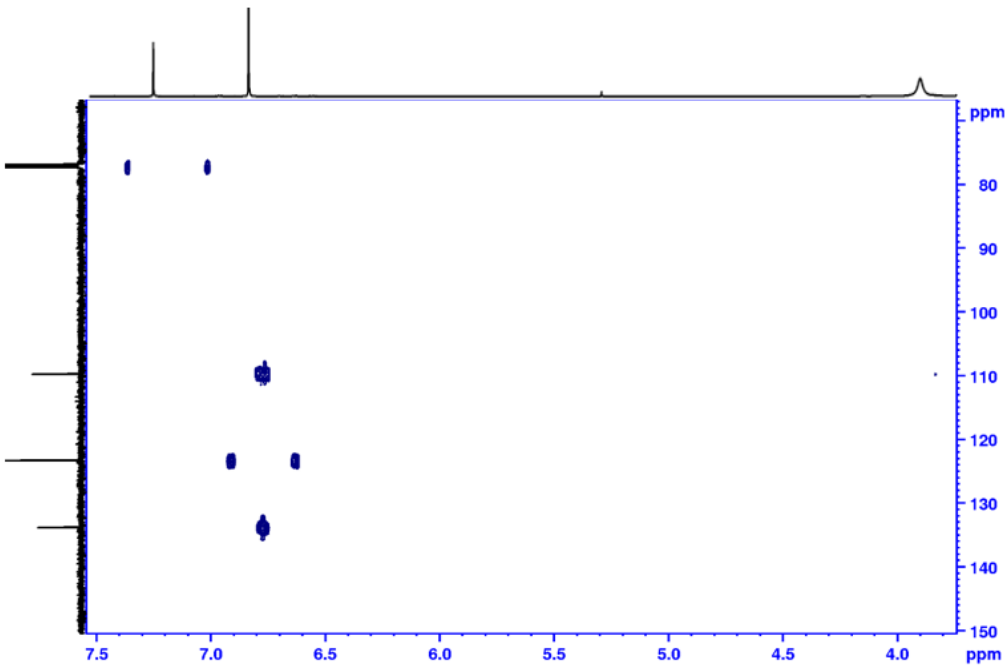

Figure 7.34. ^{1}H -^{13}C HMBC (600 MHz, $CDCl_3$) spectrum of compound **4a.**

7.1.12. Compound 4b

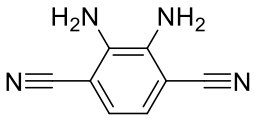

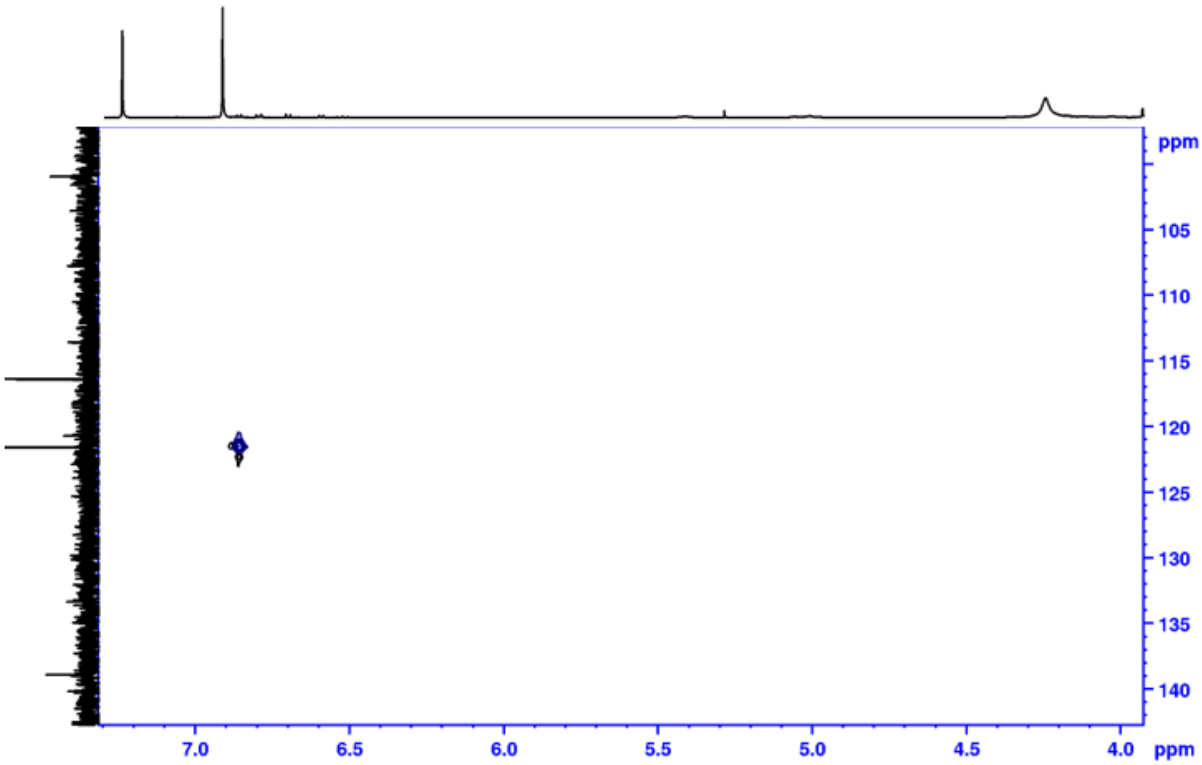

Figure 7.35. ^{1}H -^{13}C HSQC (600 MHz, $CDCl_3$) spectrum of compound **4b.**

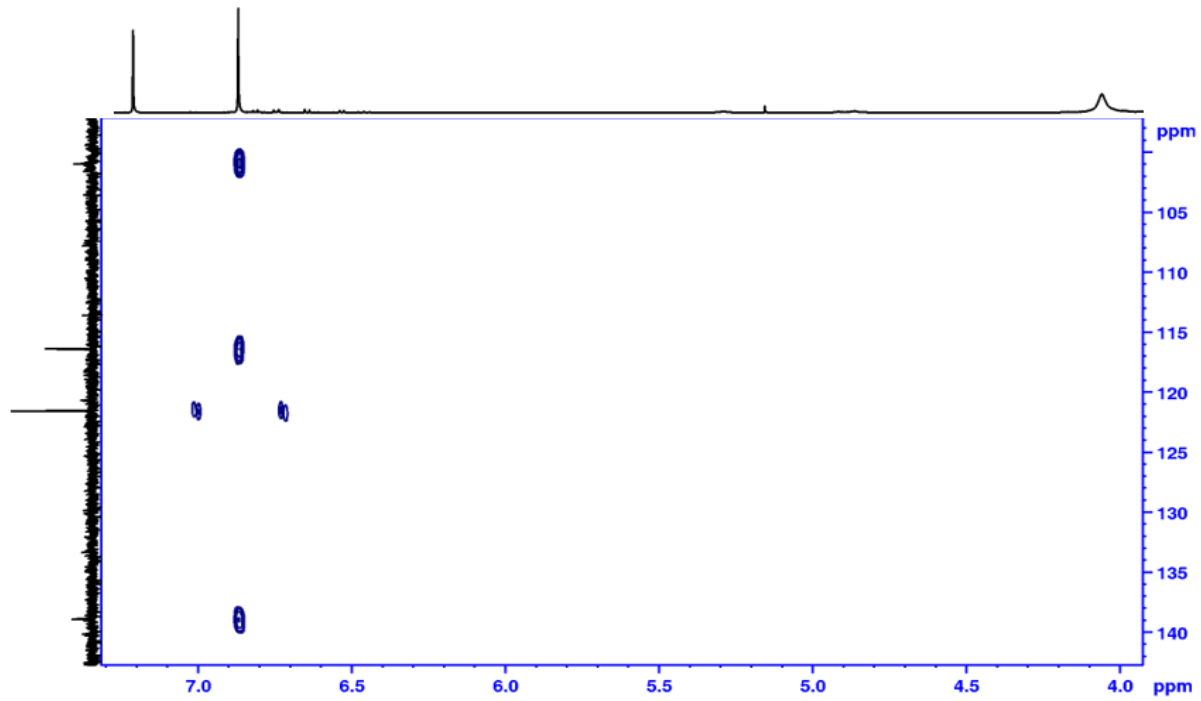

Figure 7.36. ^{1}H -^{13}C HMBC (600 MHz, $CDCl_3$) spectrum of compound **4b.**

7.1.13. Compound 4c

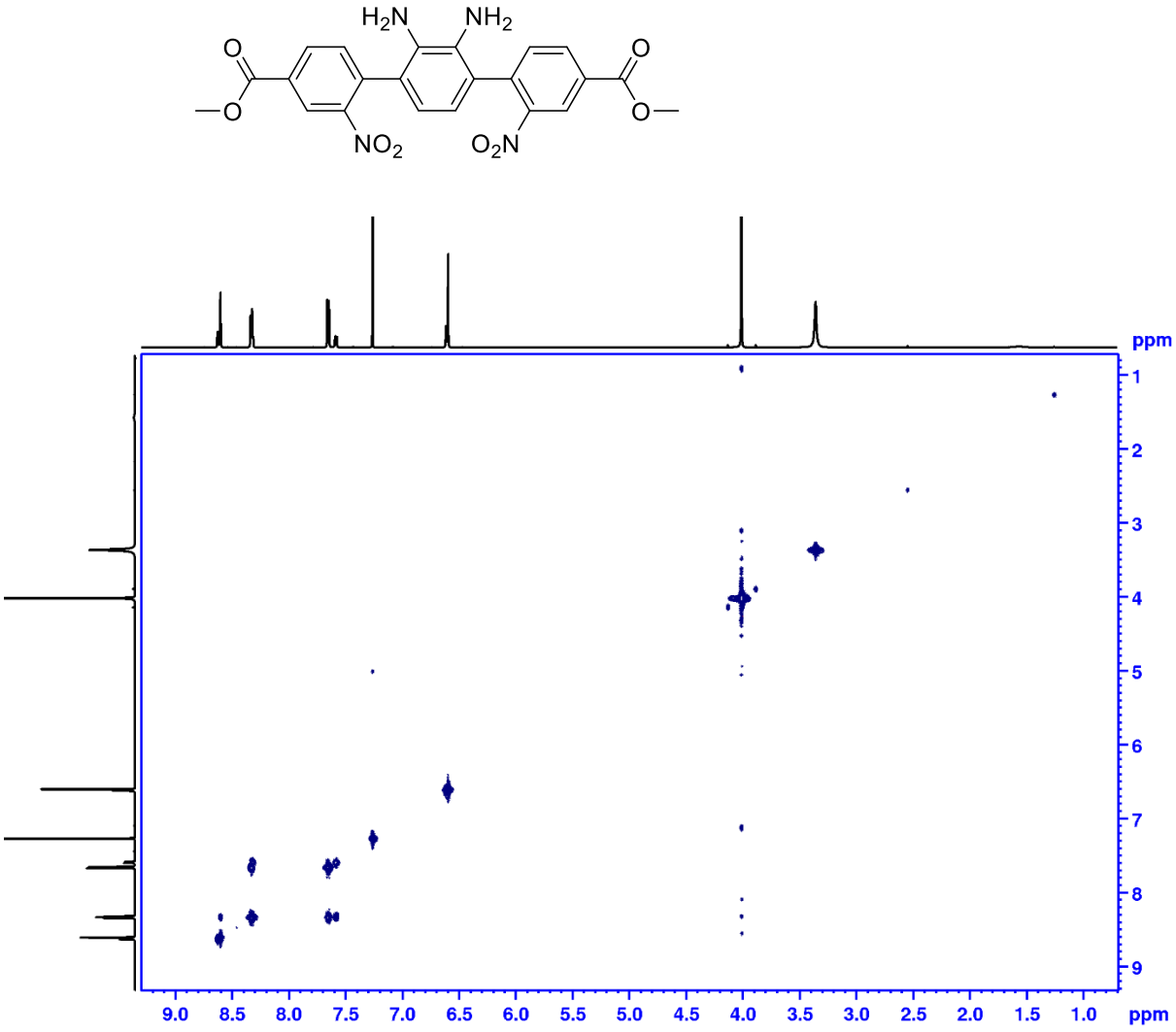

Figure 7.37. COSY (600 MHz, $CDCl_3$) spectrum of compound **4c.**

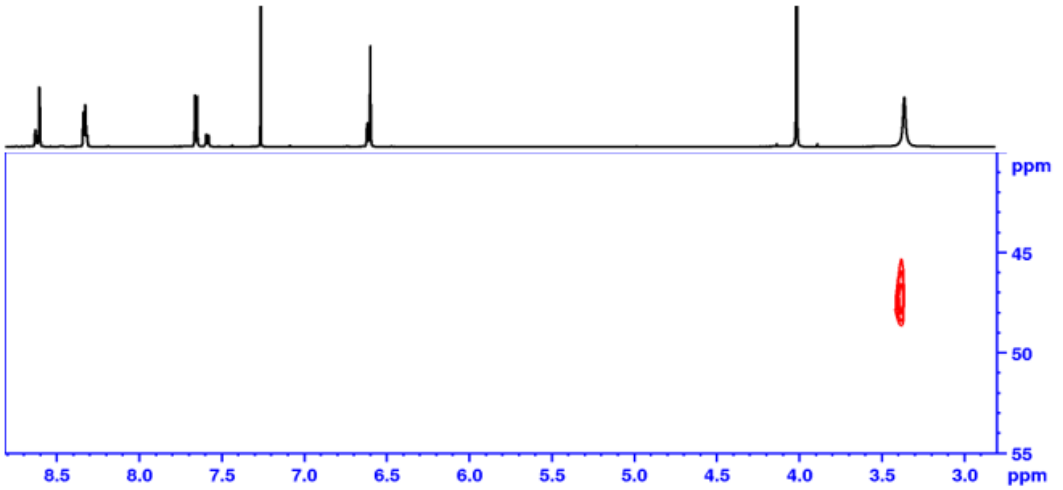

Figure 7.38. Unreferenced ^{1}H – ^{15}N HSQC (600 MHz, $CDCl_3$) spectrum of compound **4c**

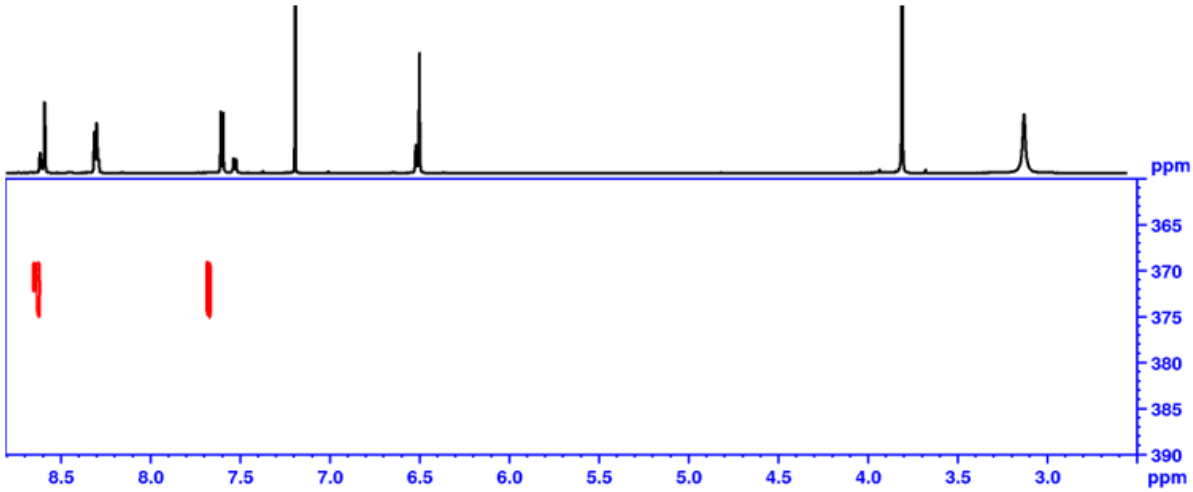

Figure 7.39. Unreferenced ^{1}H – ^{15}N HMBC (600 MHz, Pyr-d_5) spectrum of compound **4c**

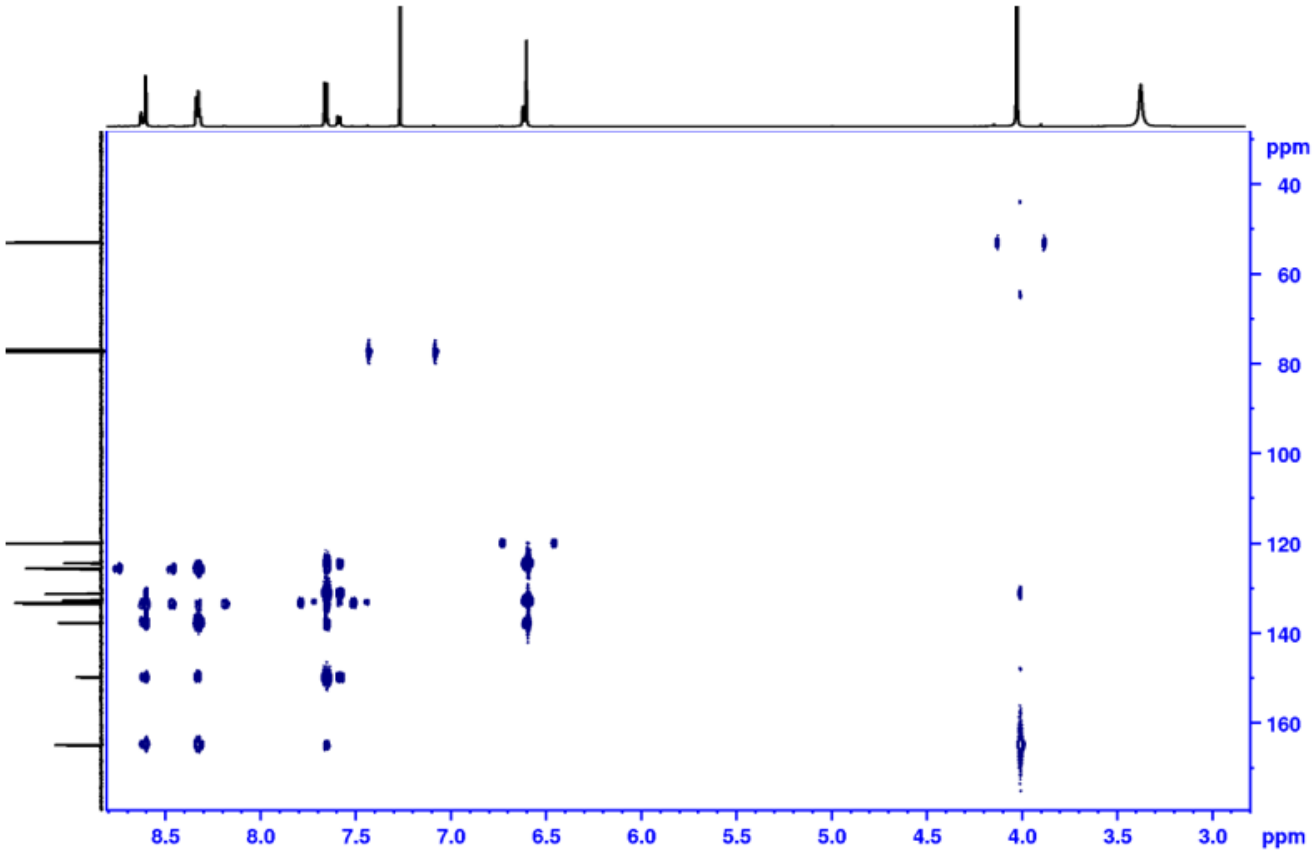

Figure 7.40. ^{1}H – ^{13}C HMBC (600 MHz, $CDCl_3$) spectrum of compound **4c**

7.1.14. Ligand L1

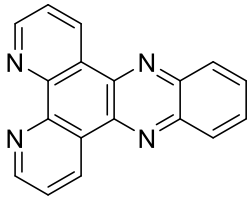

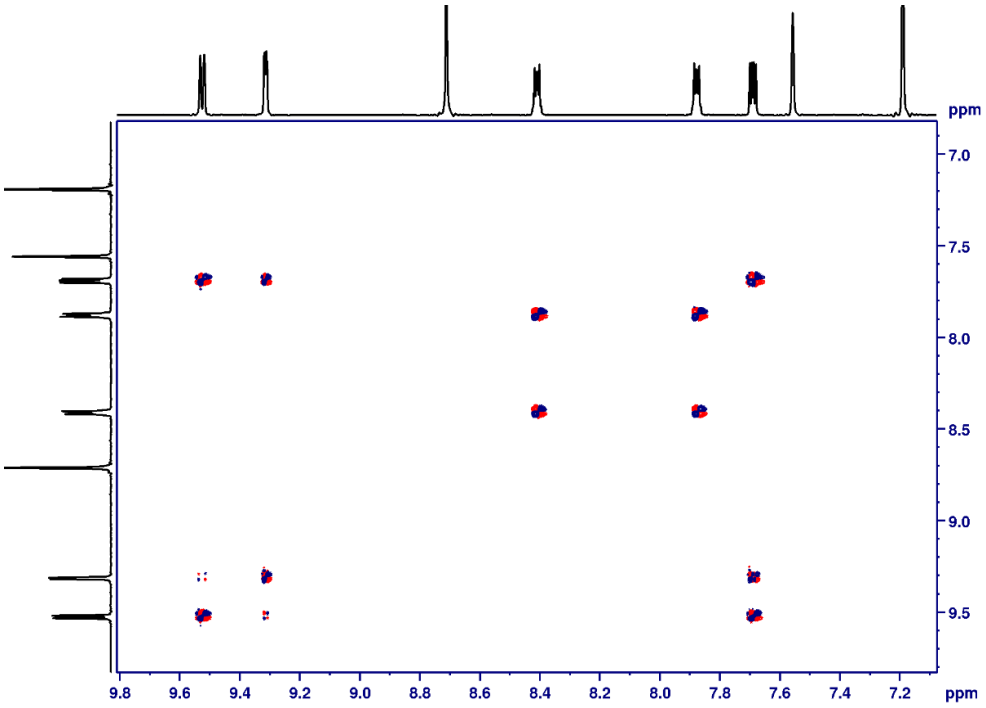

Figure 7.41. DQF–COSY (600 MHz, Pyr-d_5) spectrum of Ligand **L1.**

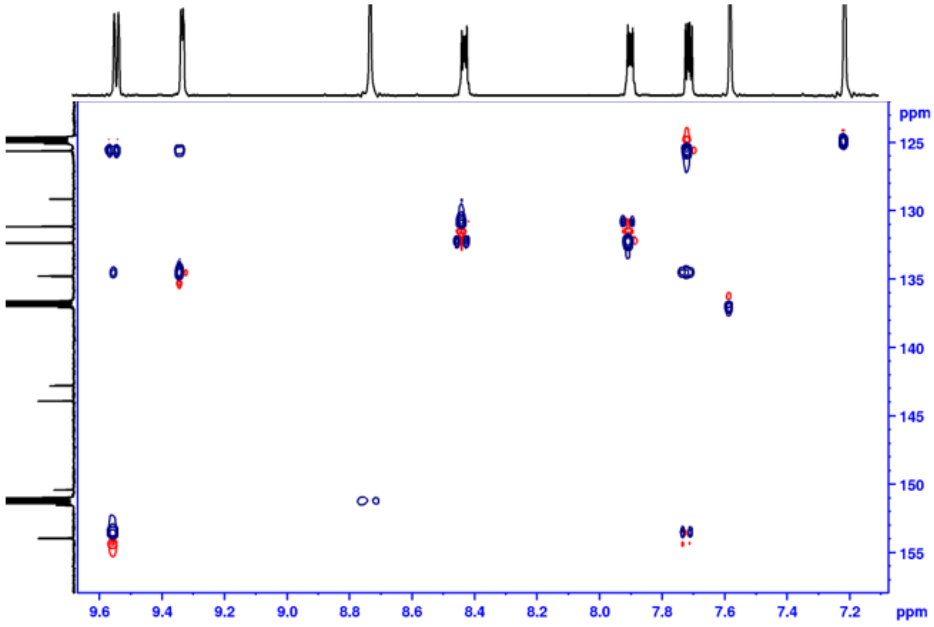

Figure 7.42. Aromatic region of ^{1}H – ^{13}C HSQC (600 MHz, Pyr-d_5) spectrum of Ligand **L1.**

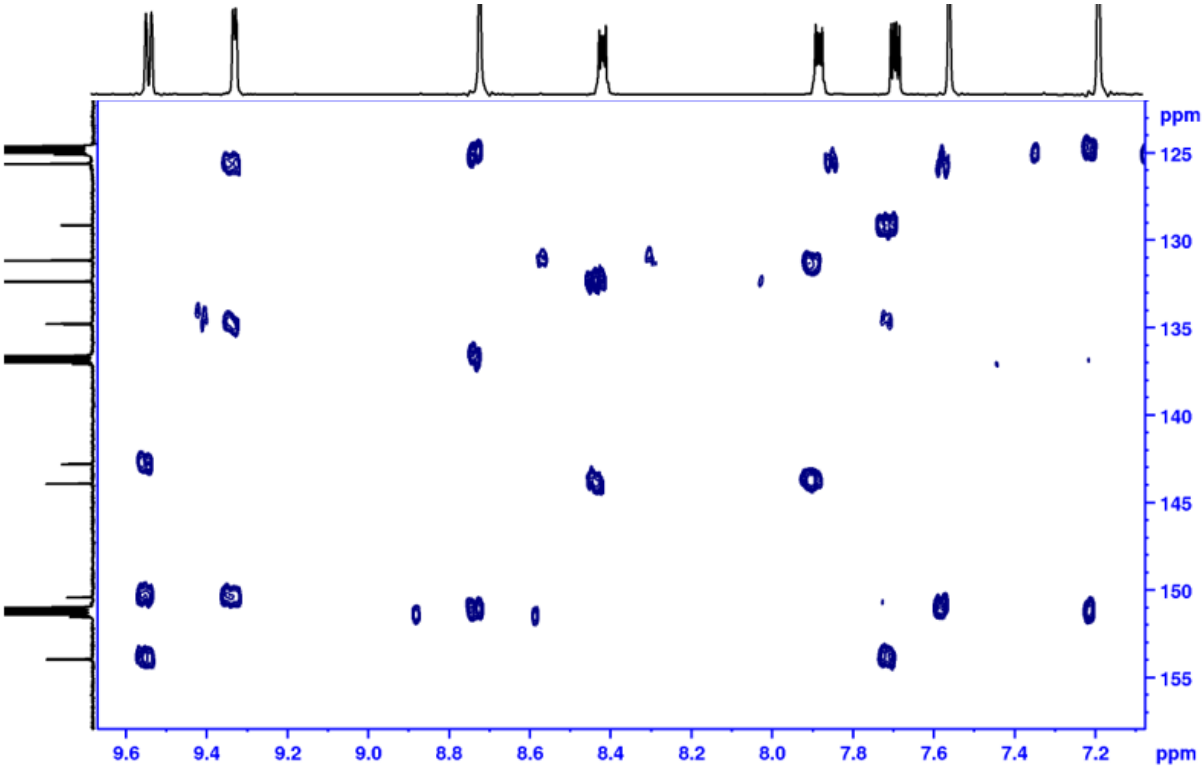

Figure 7.43. Aromatic region of ^{1}H – ^{13}C HMBC (600 MHz, Pyr-d_5) spectrum of Ligand **L1.**

7.1.15. Ligand L2

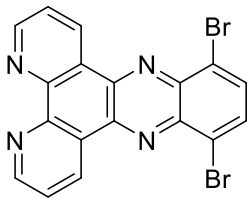

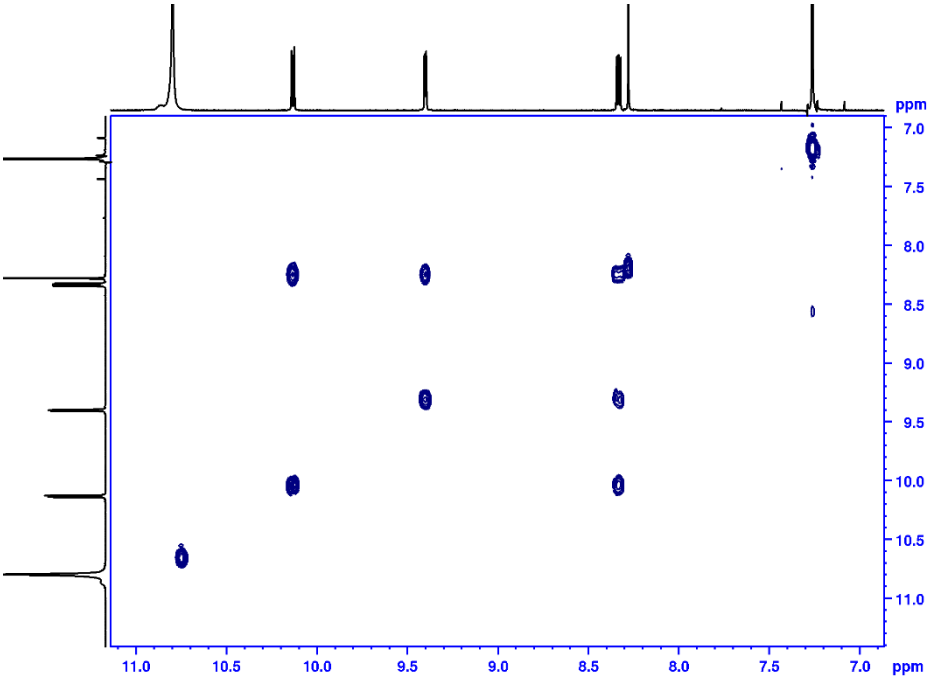

Figure 7.44. COSY (600 MHz, $CDCl_3$ + TFA-*d*) spectrum of Ligand **L2.**

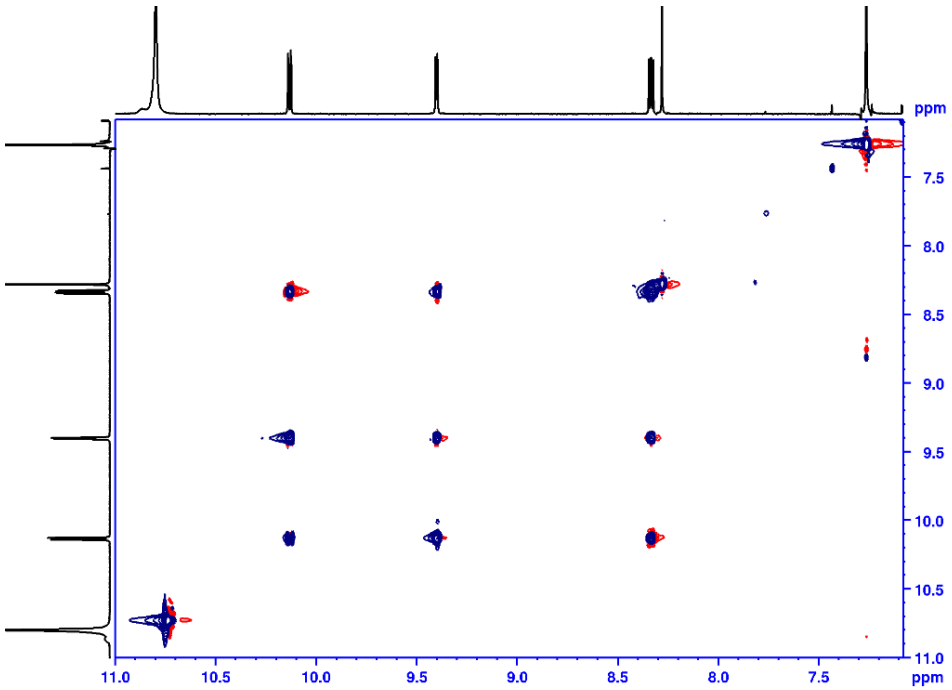

Figure 7.45. TOCSY (600 MHz, $CDCl_3$ + TFA-*d*) spectrum of Ligand **L2.**

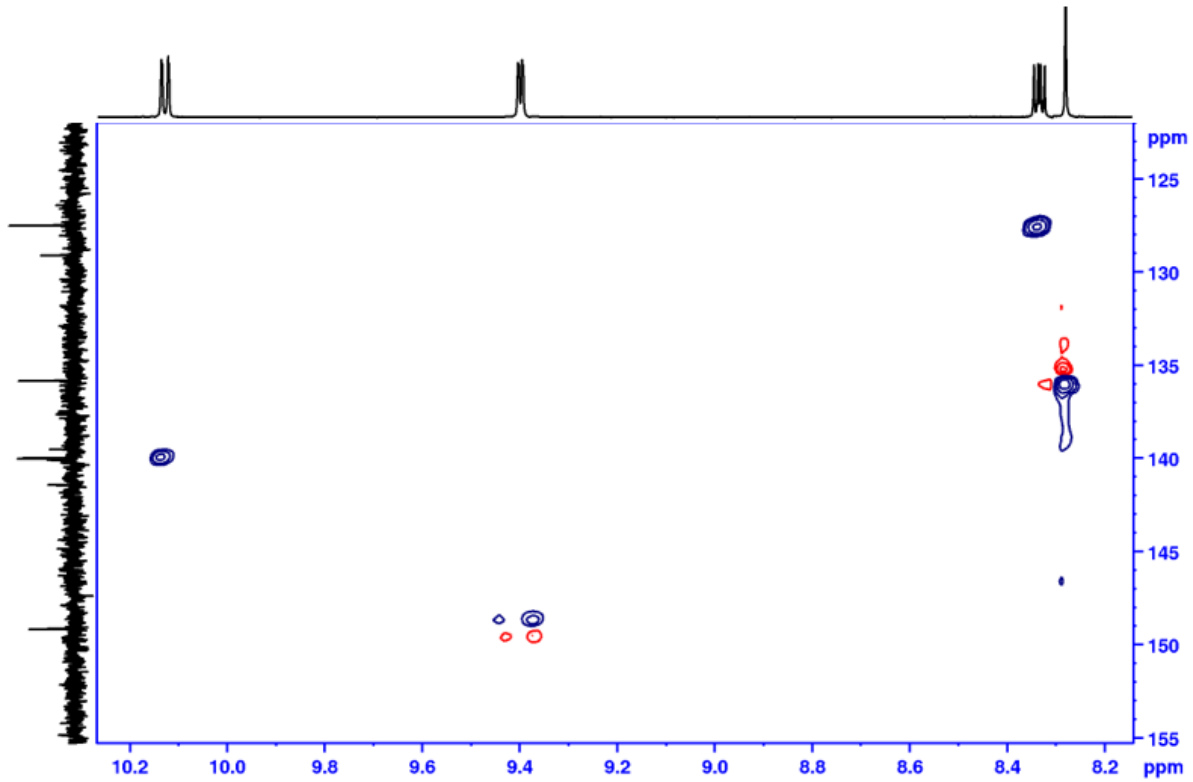

Figure 7.46. $^{1}H–^{13}C$ HSQC (600 MHz, $CDCl_3$ + TFA-*d*) spectrum of Ligand **L3.**

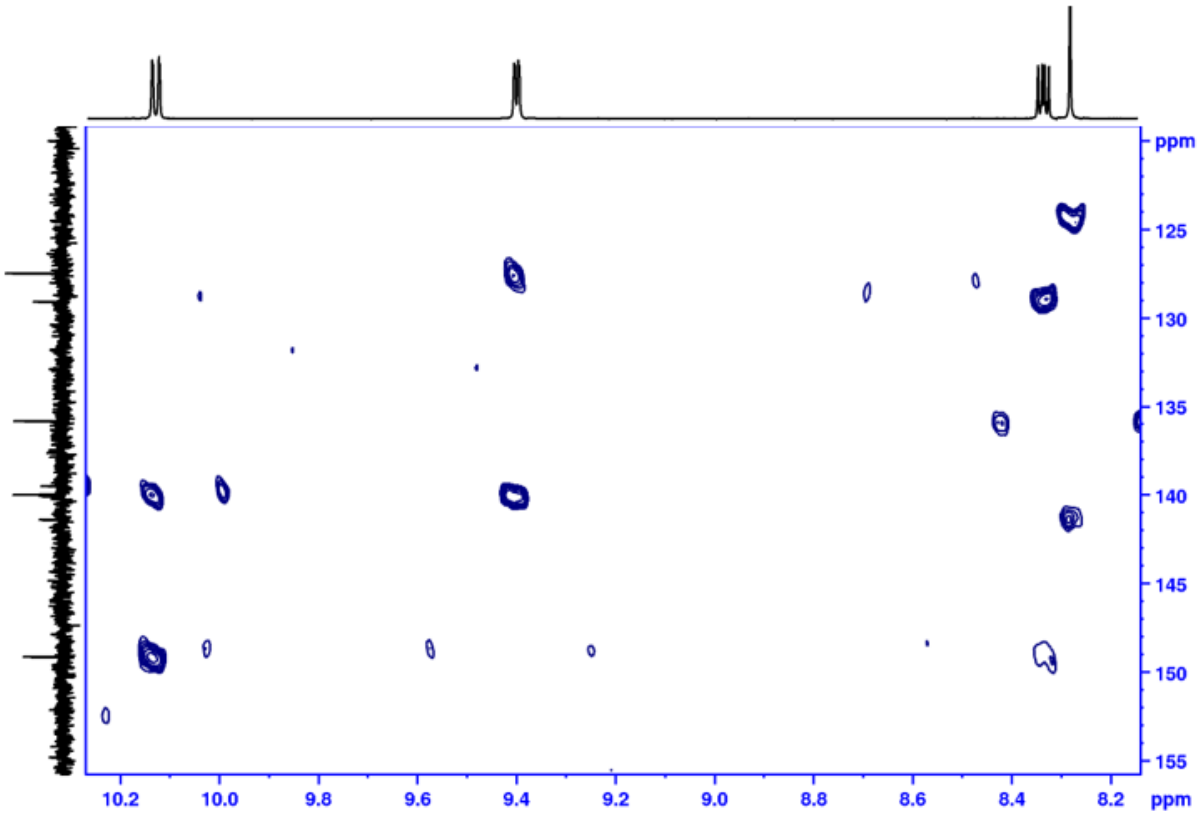

Figure 7.47. $^{1}H–^{13}C$ HMBC (600 MHz, $CDCl_3$ + TFA-*d*) spectrum of Ligand **L3.**

7.1.16. Ligand L3

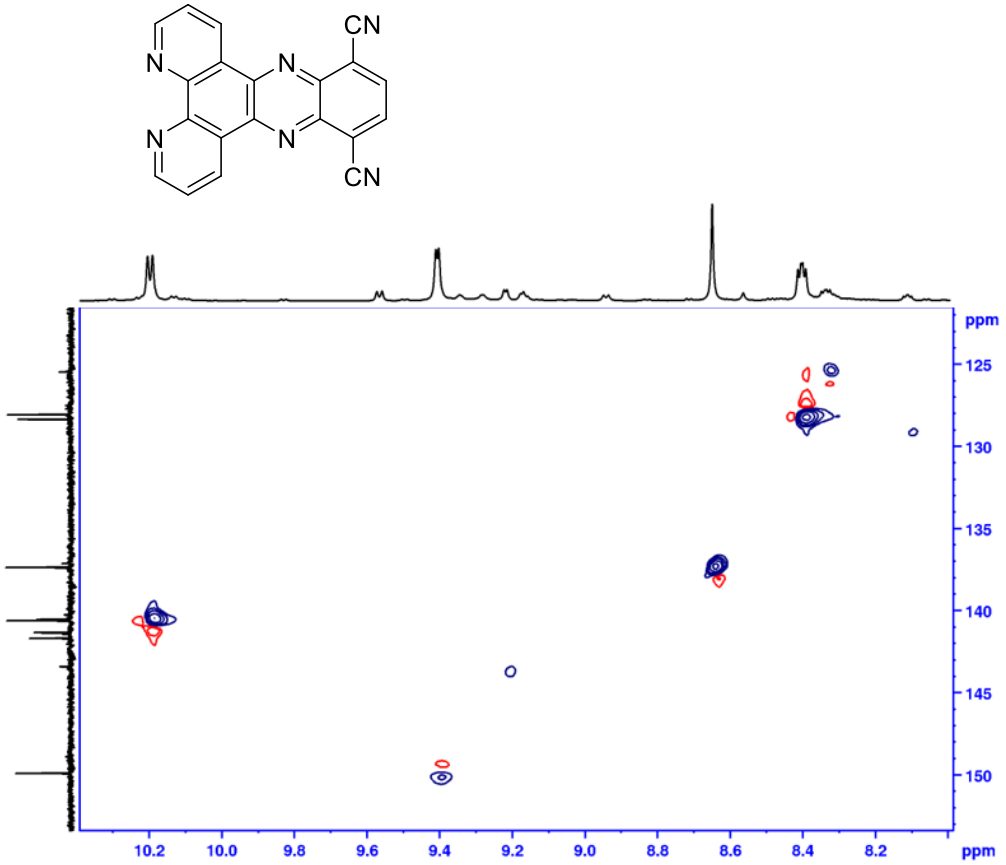

Figure 7.48. $^{1}H–^{13}C$ HSQC (600 MHz, $CDCl_3$ + TFA-*d*) spectrum of Ligand **L3.**

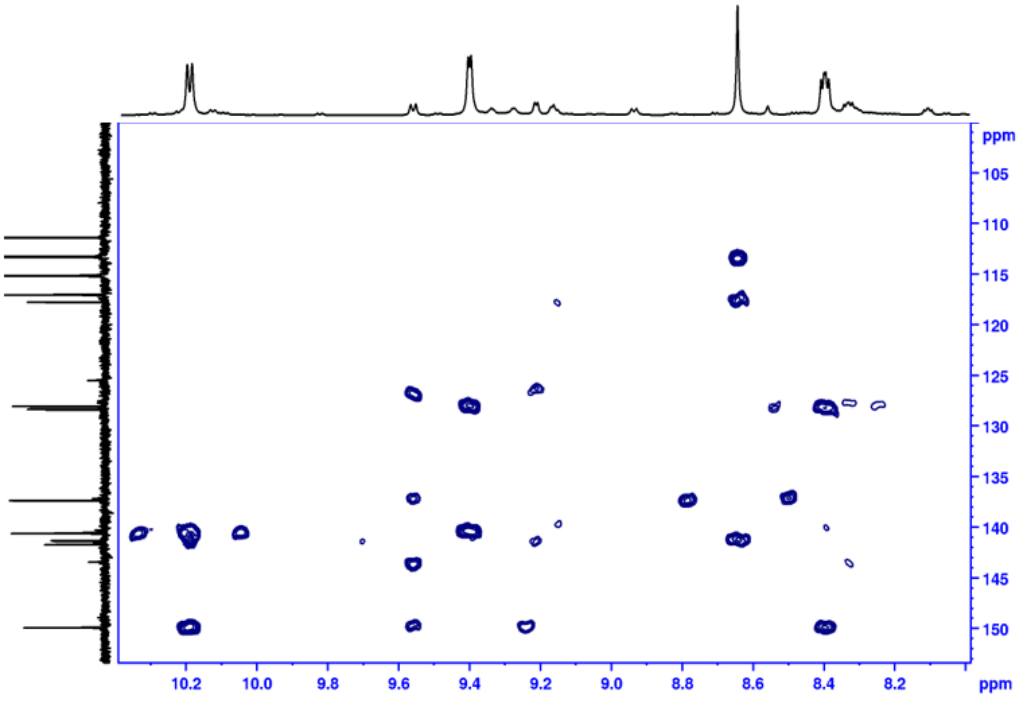

Figure 7.49. $^{1}H–^{13}C$ HMBC (600 MHz, $CDCl_3$ + TFA-*d*) spectrum of Ligand **L3.**

7.1.17. Ligand L4

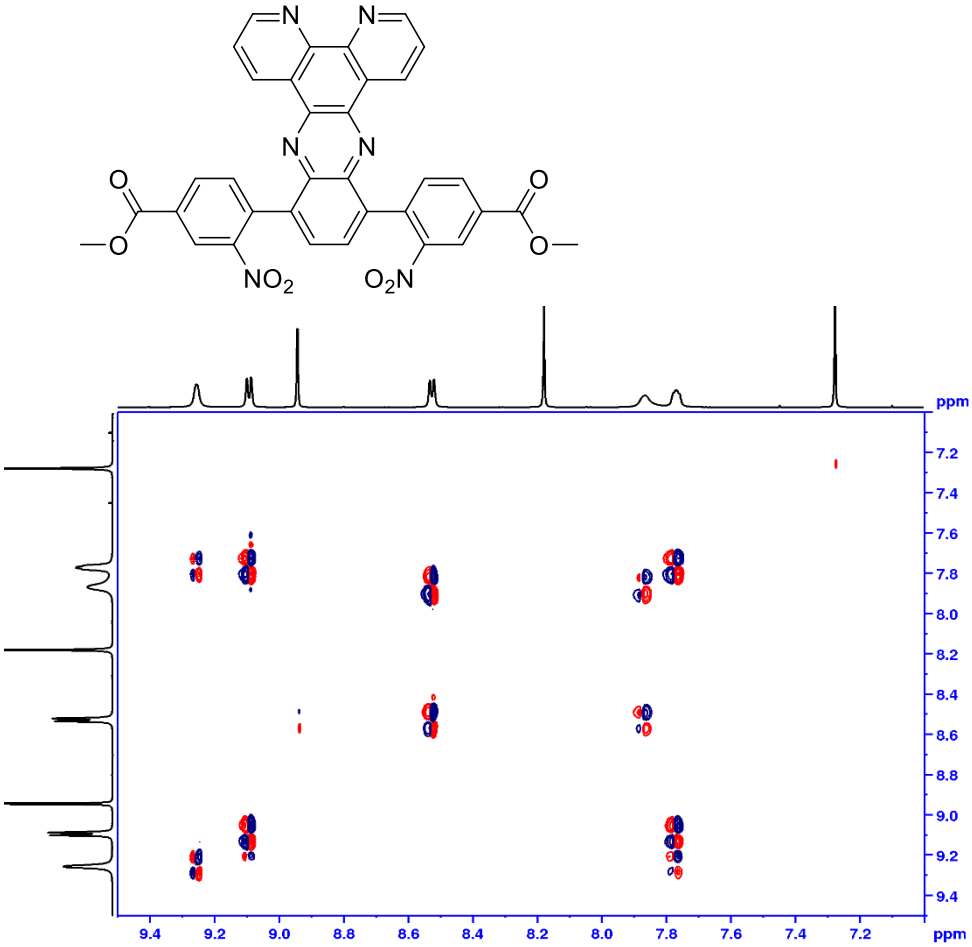

Figure 7.50. DQF–COSY (600 MHz, $CDCl_3$) spectrum of Ligand **L4.**

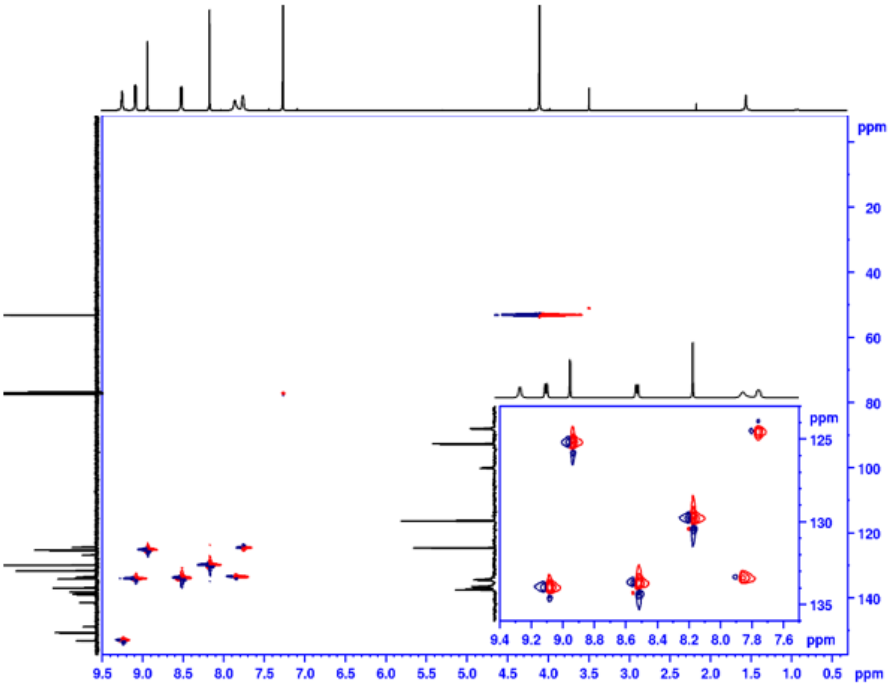

Figure 7.51. ^{1}H – ^{13}C HSQC (600 MHz, $CDCl_3$) spectrum of Ligand **L4.**

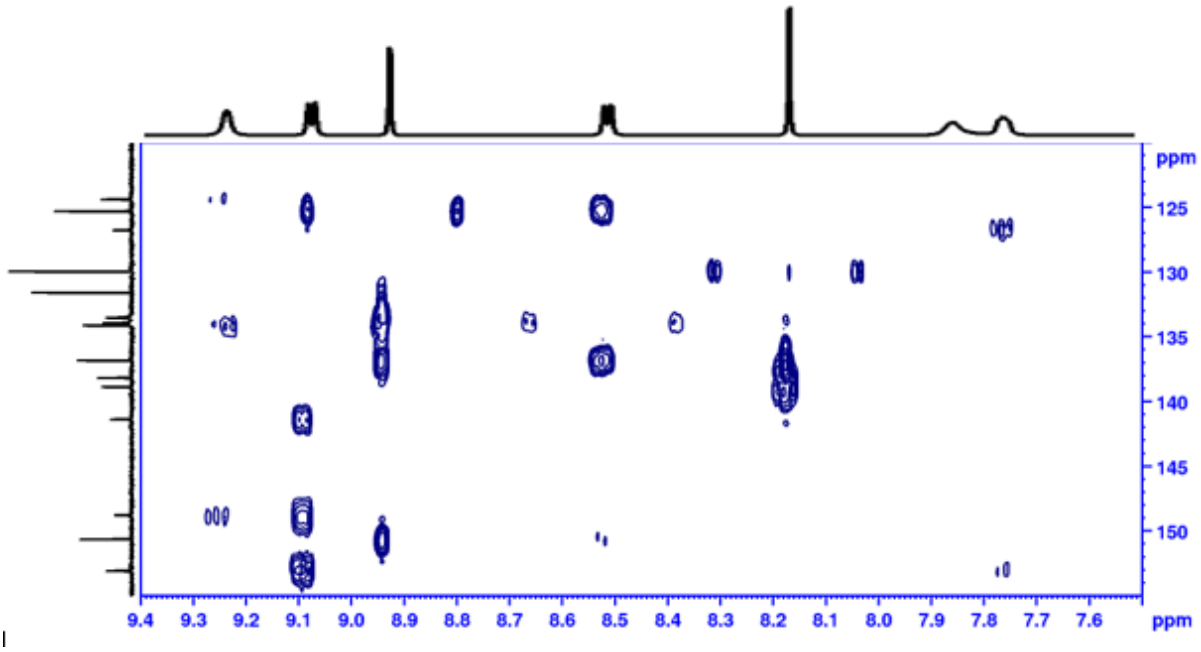

Figure 7.52. Aromatic region of ^{1}H – ^{13}C HMBC (600 MHz, $CDCl_3$) spectrum of Ligand **L4.**

7.1.18. Ligand L5 (Not reported in experimental section)

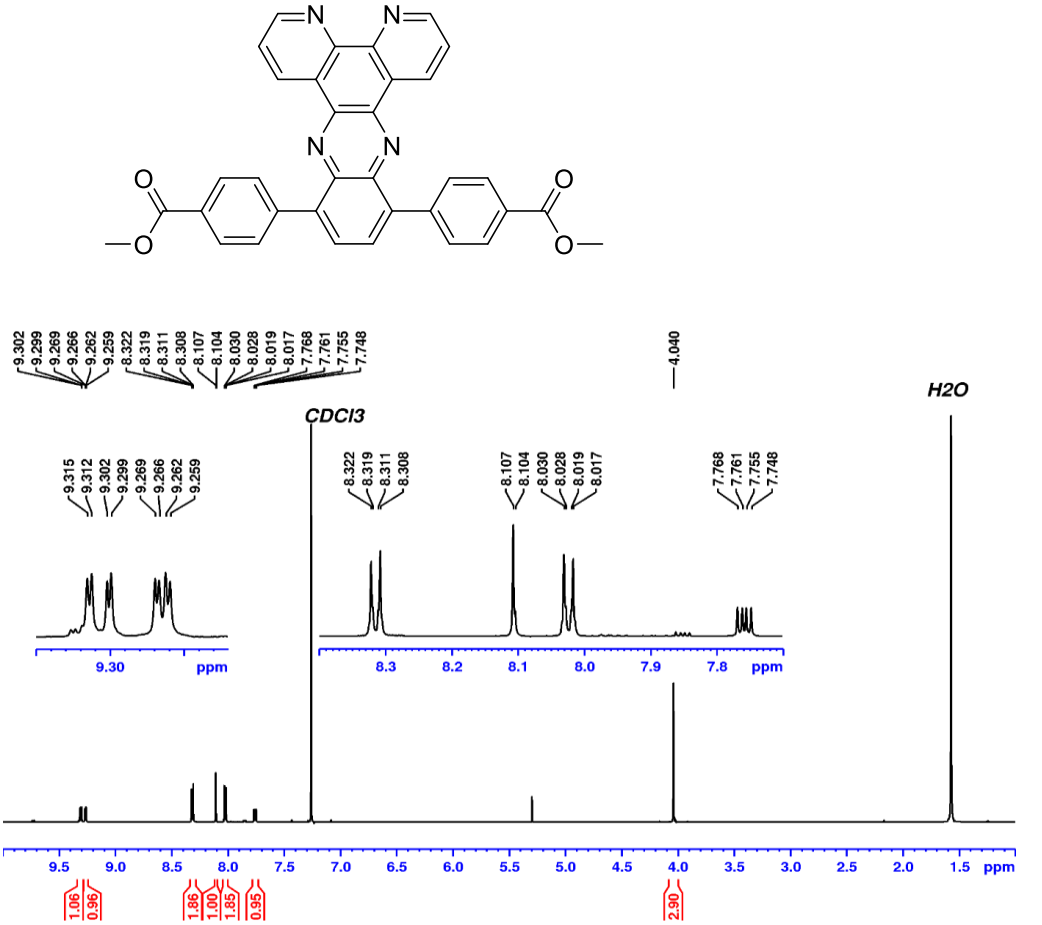

Figure 7.53. ^{1}H NMR (600 MHz, $CDCl_3$) spectrum of Ligand **L5.**

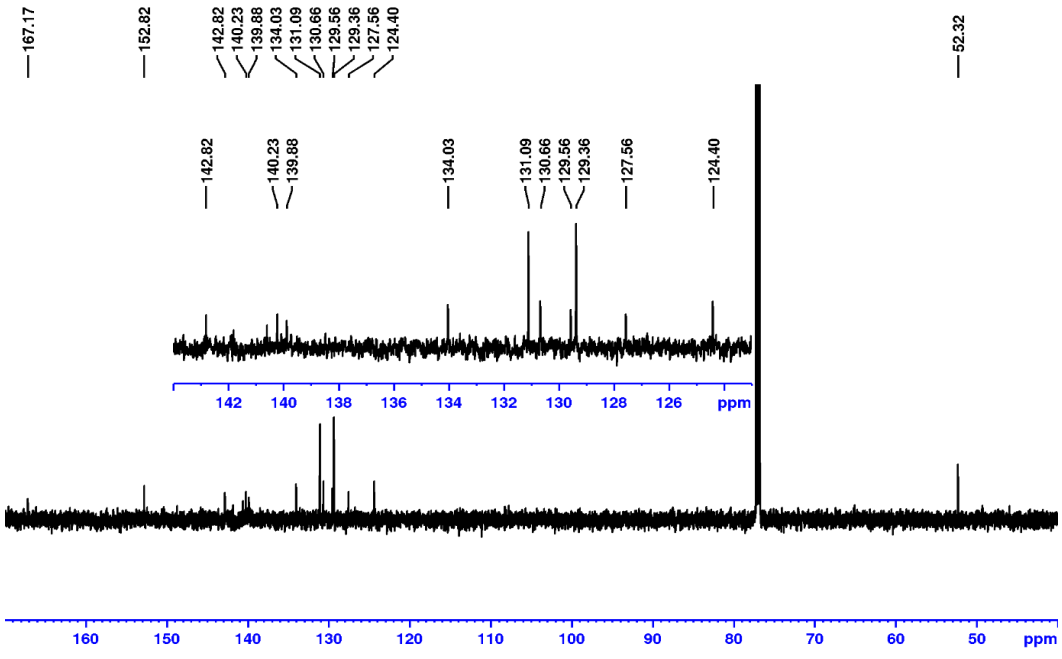

Figure 7.54. ^{13}C NMR (600 MHz, $CDCl_3$) spectrum of Ligand **L5.**

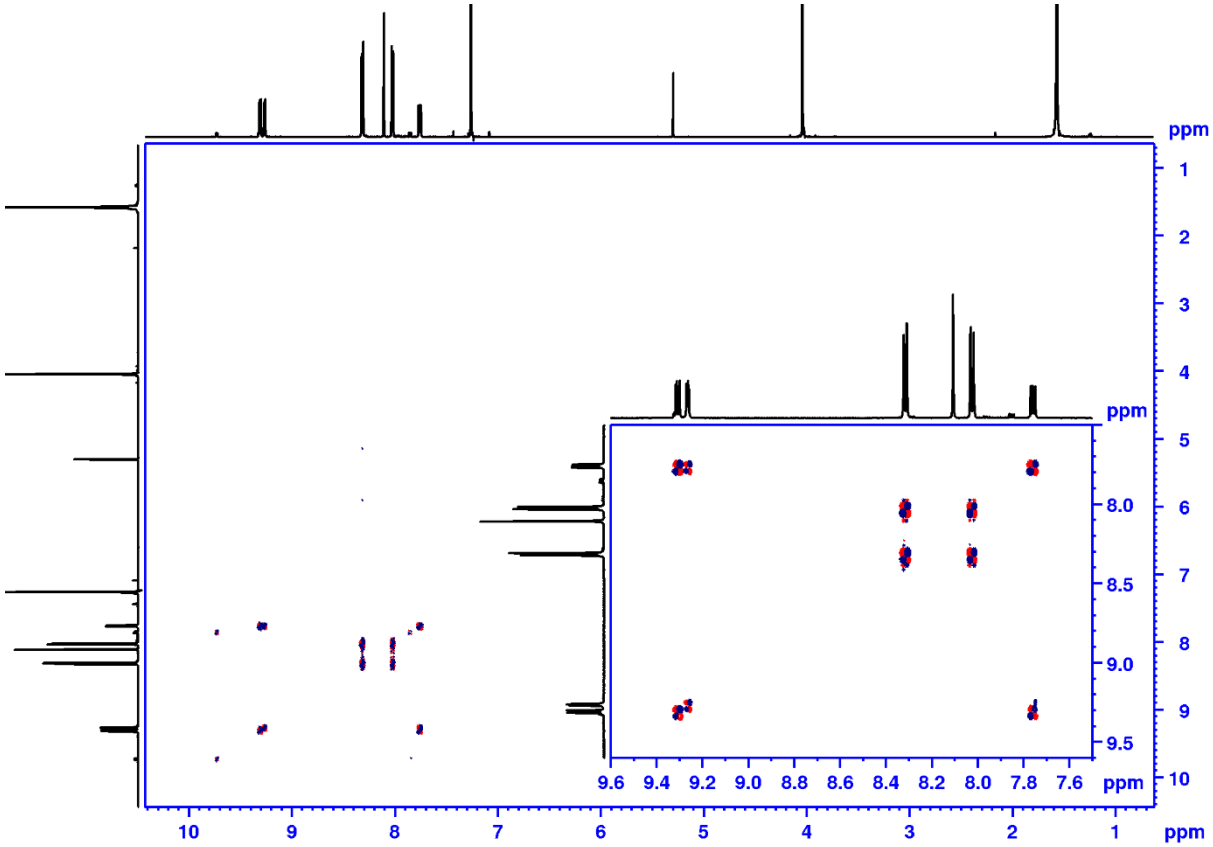

Figure 7.55. DQF–COSY (600 MHz, $CDCl_3$) spectrum of Ligand **L5.**

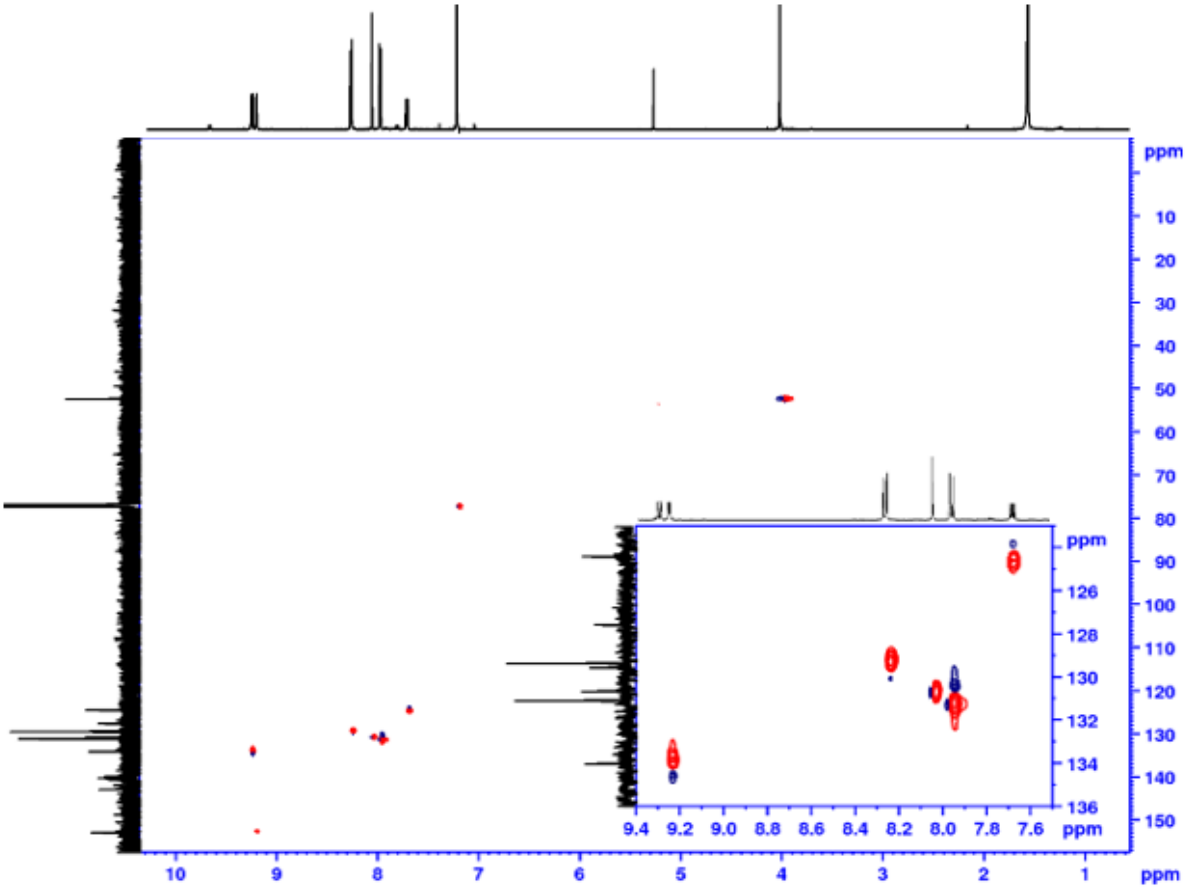

Figure 7.56. ^{1}H – ^{13}C HSQC (600 MHz, $CDCl_3$) spectrum of Ligand **L5**

7.1.19. Complex C1

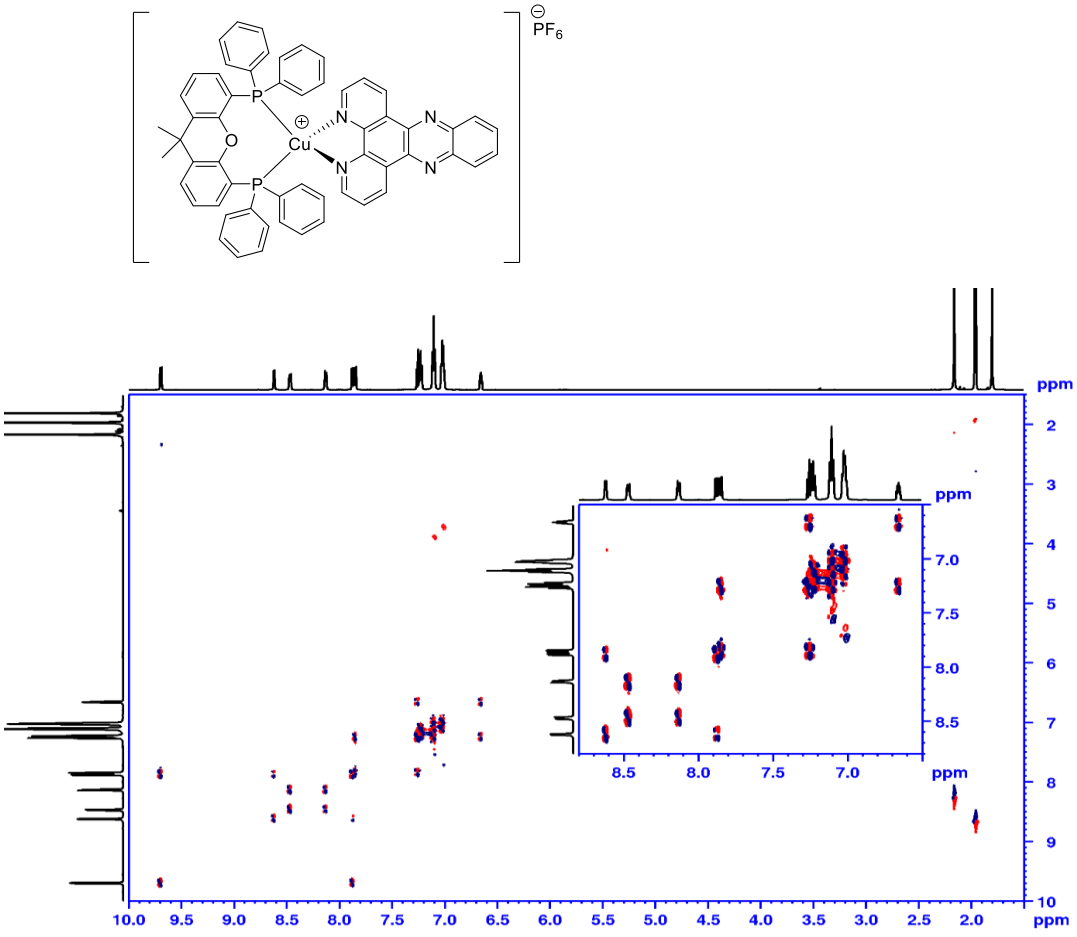

Figure 7.57. DQF–COSY (600 MHz, CD_3CN) spectrum of Complex **C1.**

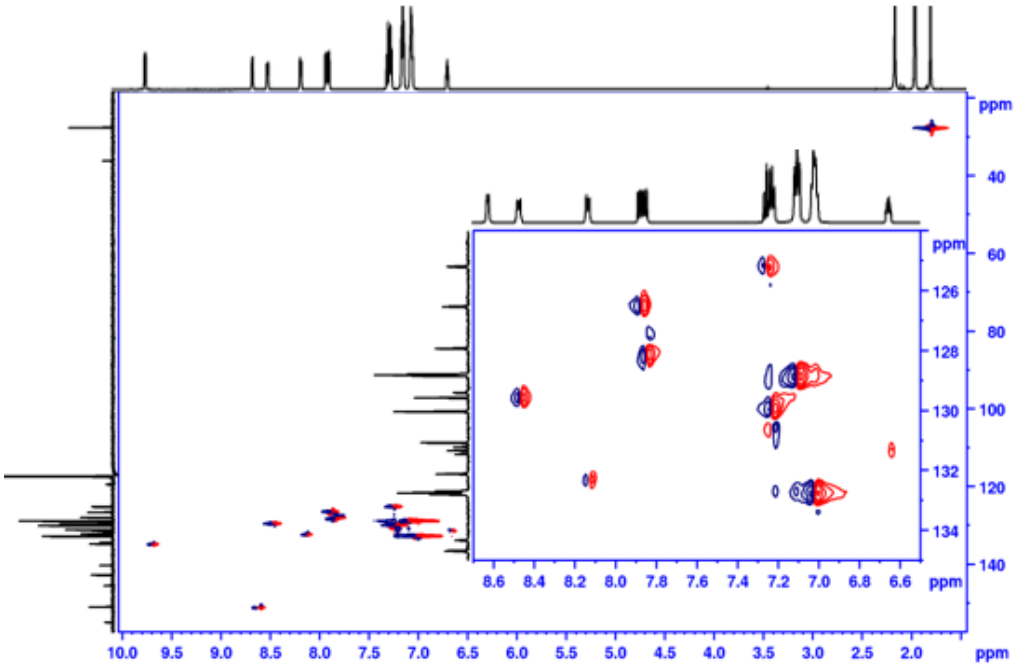

Figure 7.58. ^{1}H – ^{13}C HSQC (600 MHz, CD_3CN) spectrum of Complex **C1.**

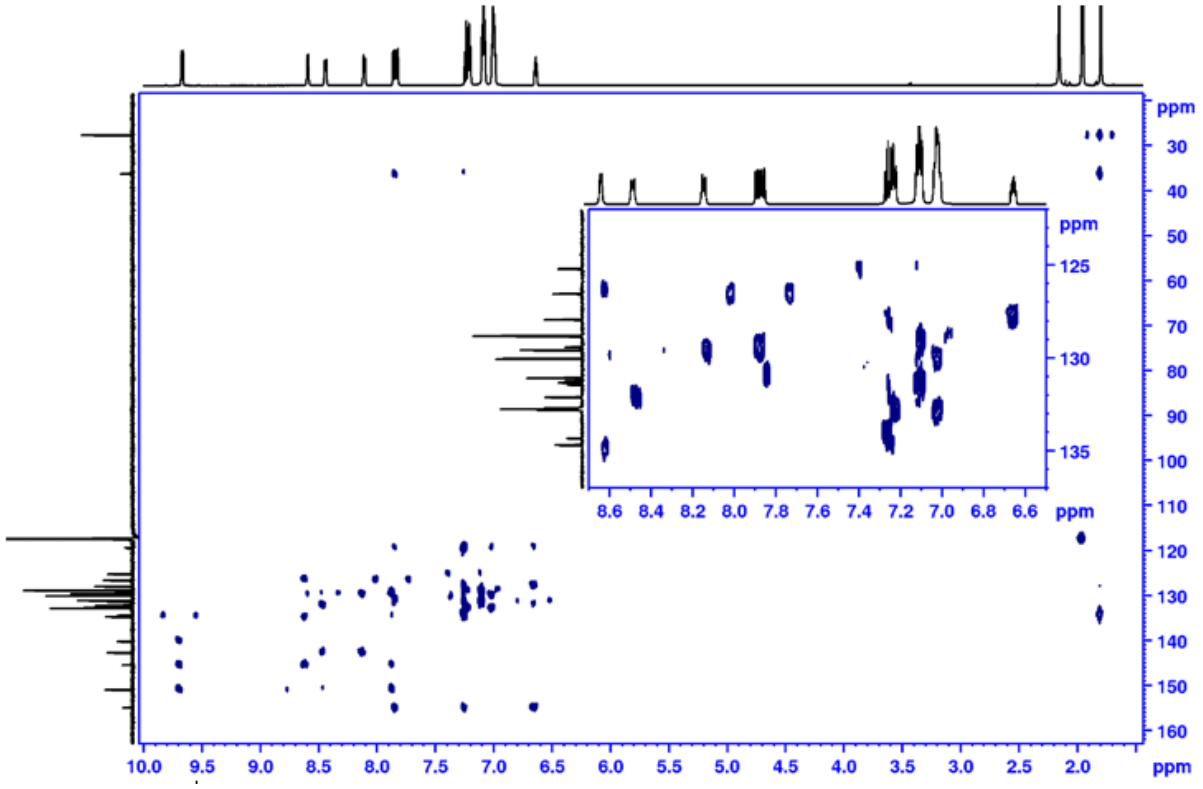

Figure 7.59. ^{1}H – ^{13}C HMBC (600 MHz, CD_3CN) spectrum of Complex **C1.**

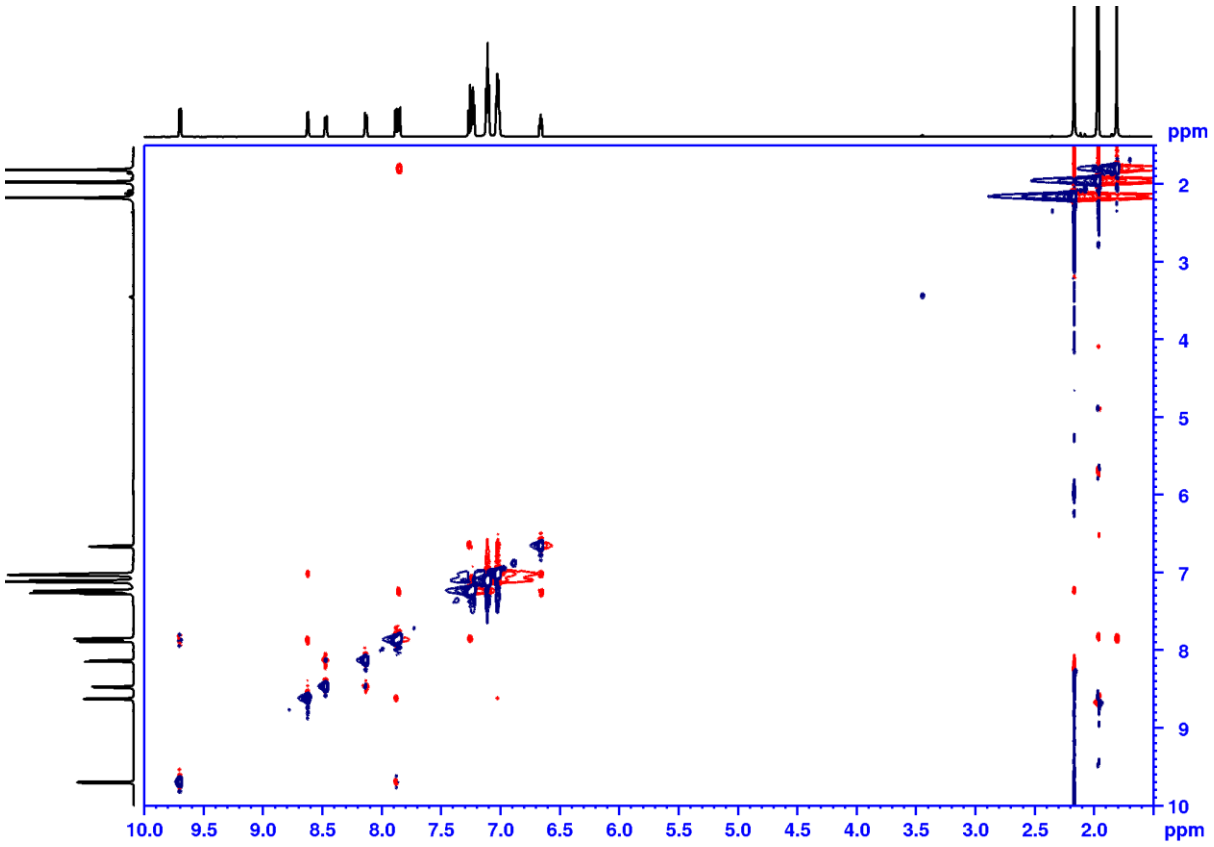

Figure 7.60. NOESY (600 MHz, CD_3CN) spectrum of Complex **C1.**

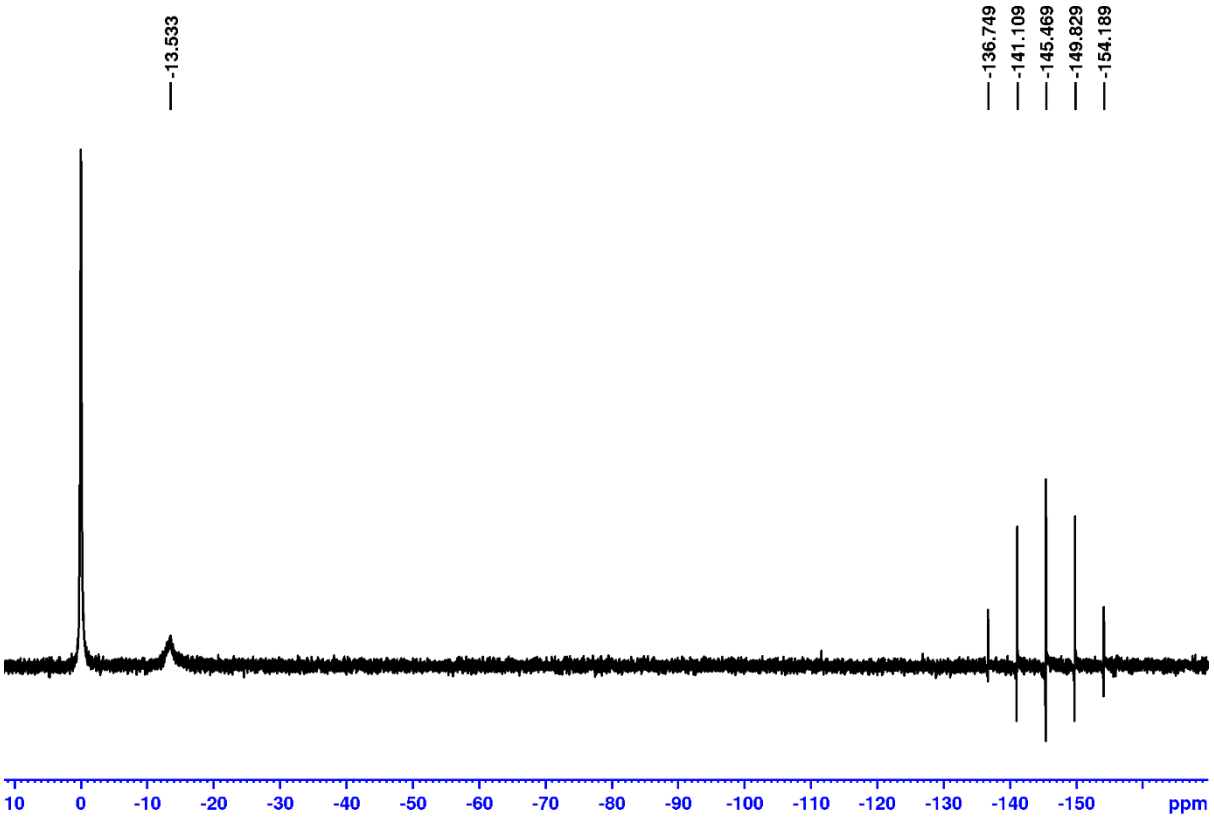

Figure 7.61. ^{31}P NMR (400 MHz, 85% H_3PO_4) spectrum of Complex **C1.**

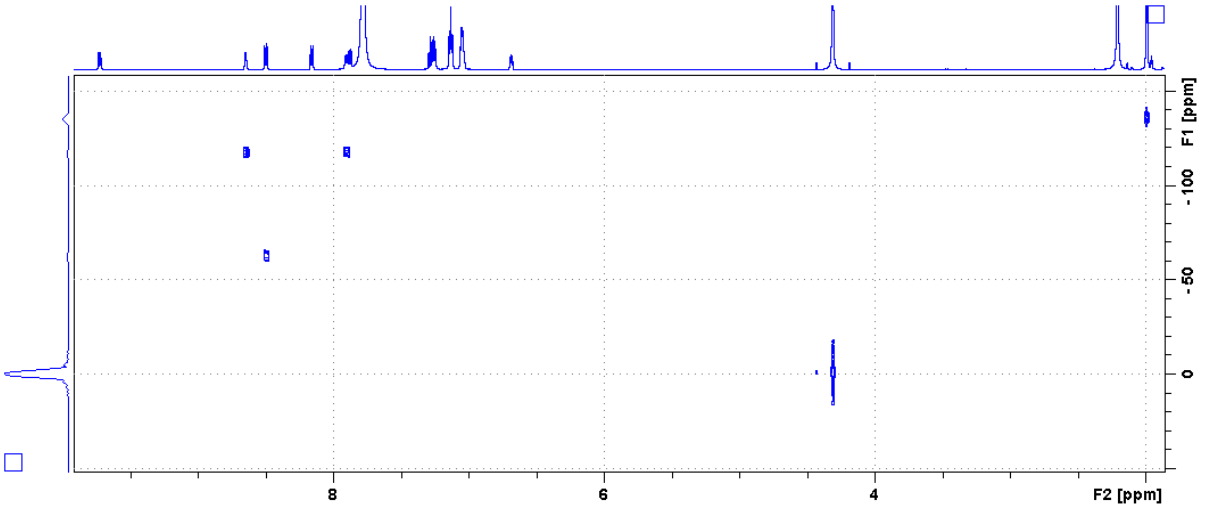

Figure 7.62. ^{15}N HMBC (600 MHz, CD_3NO_2) spectrum of Complex **C1.**

7.1.20. Complex C2

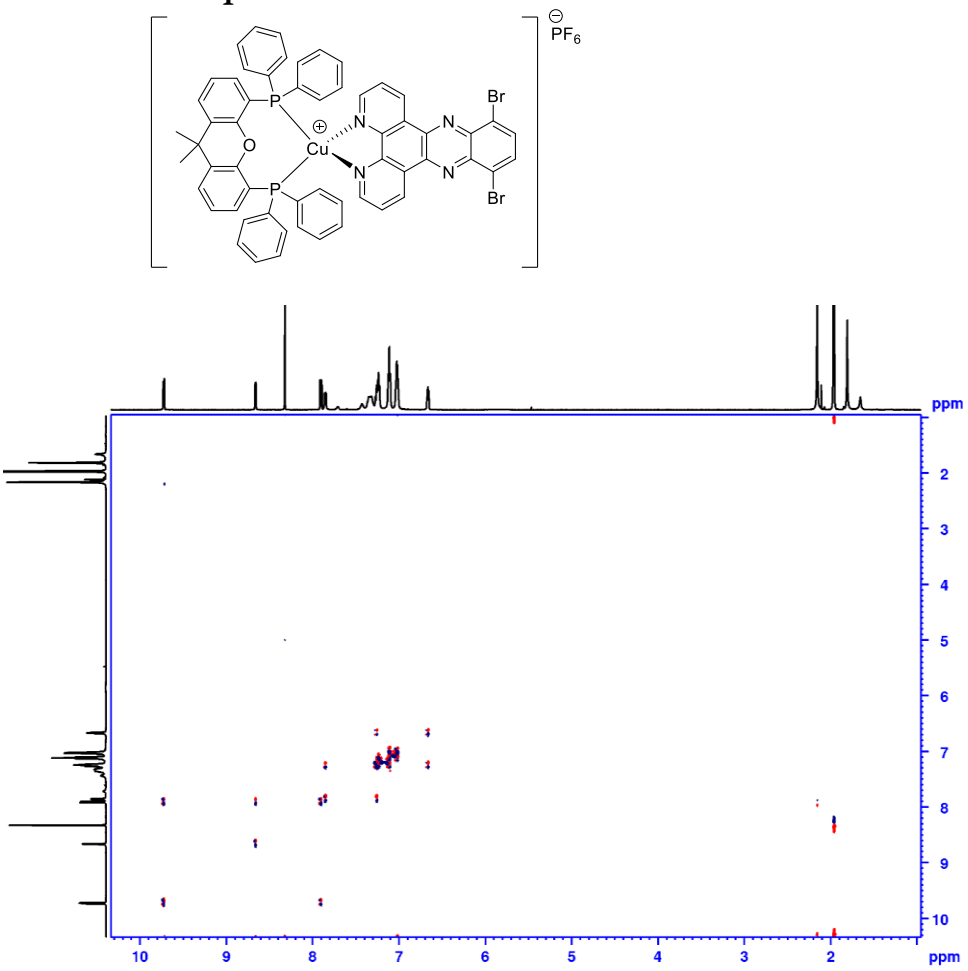

Figure 7.63. COSY-DQF (600 MHz, CD_3CN) spectrum of Complex **C2.**

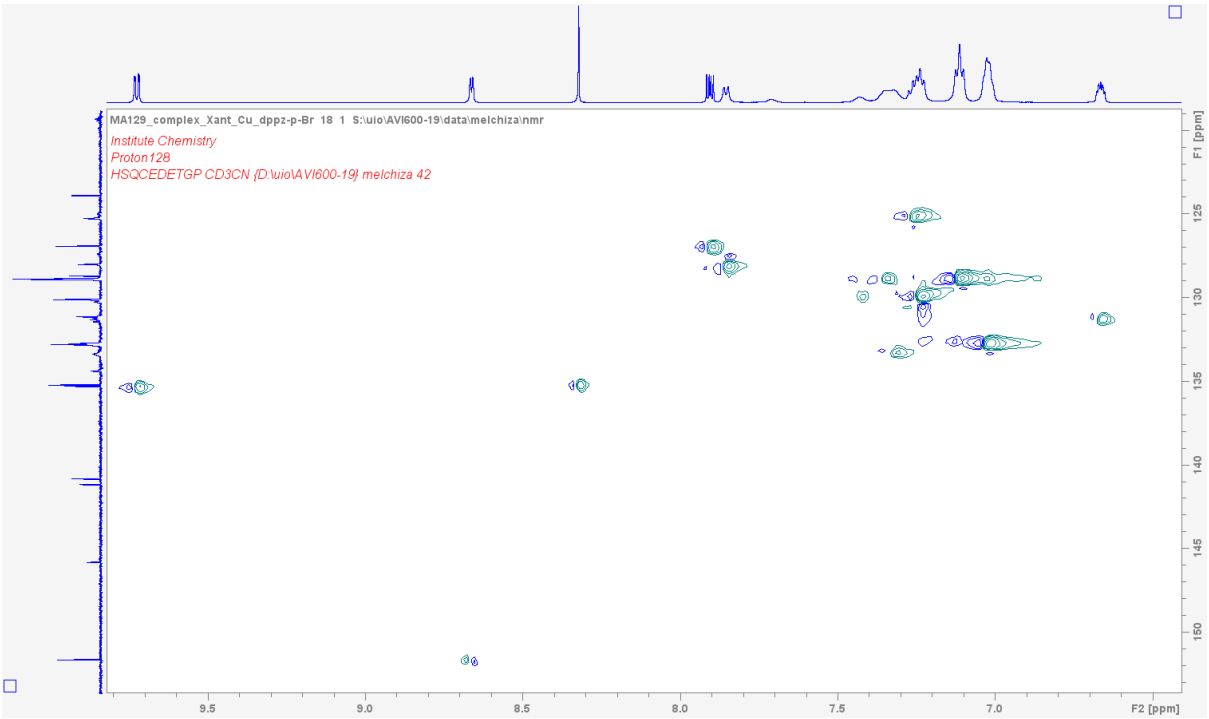

Figure 7.64. ^{1}H – ^{13}C HSQC (600 MHz, CD_3CN) spectrum of Complex **C2.**

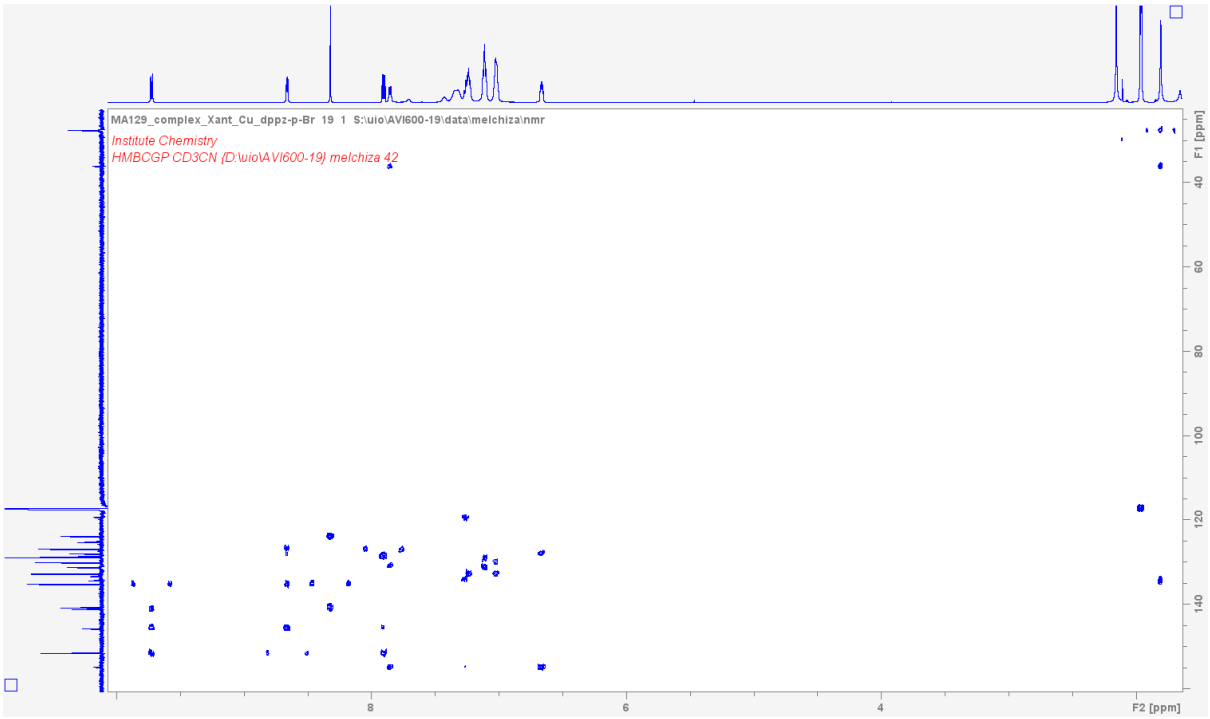

Figure 7.65. ^{1}H – ^{13}C HMBC (600 MHz, CD_3CN) spectrum of Complex **C2.**

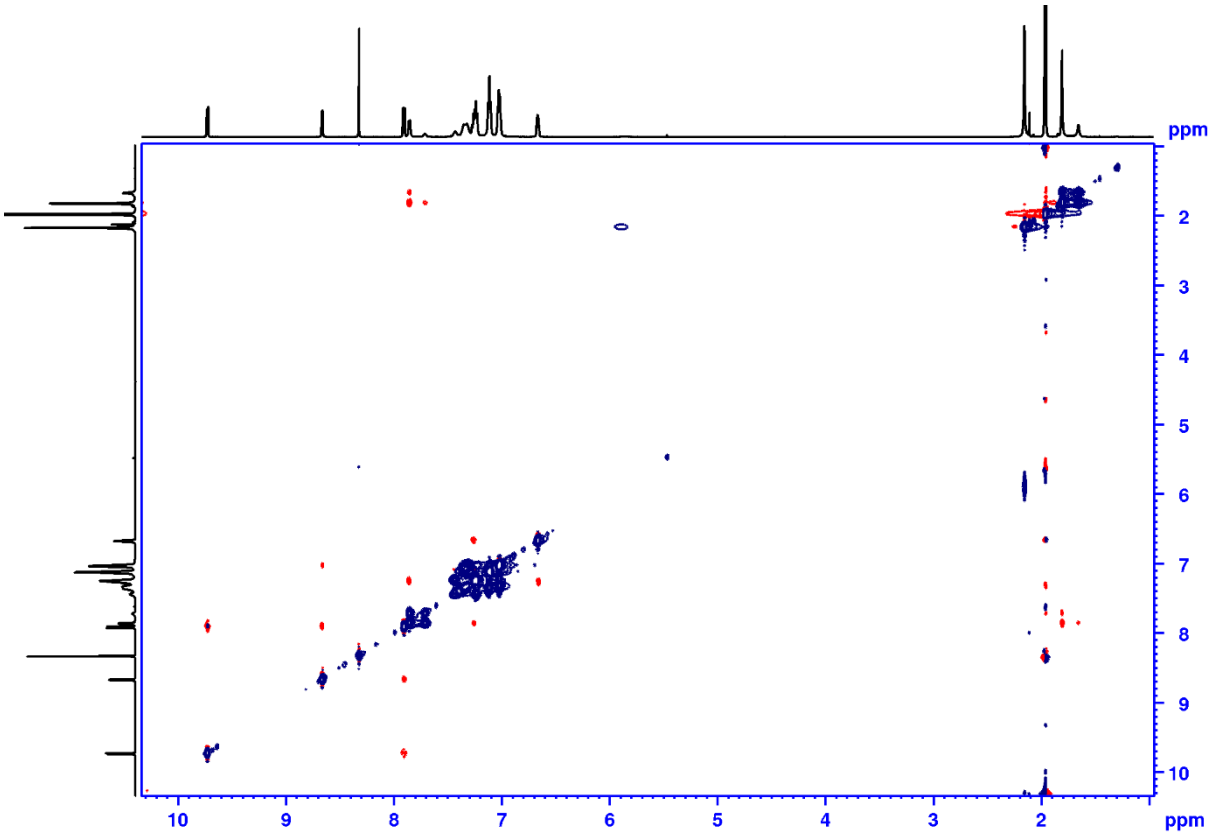

Figure 7.66. NOESY (600 MHz, CD_3CN) spectrum of Complex **C2.**

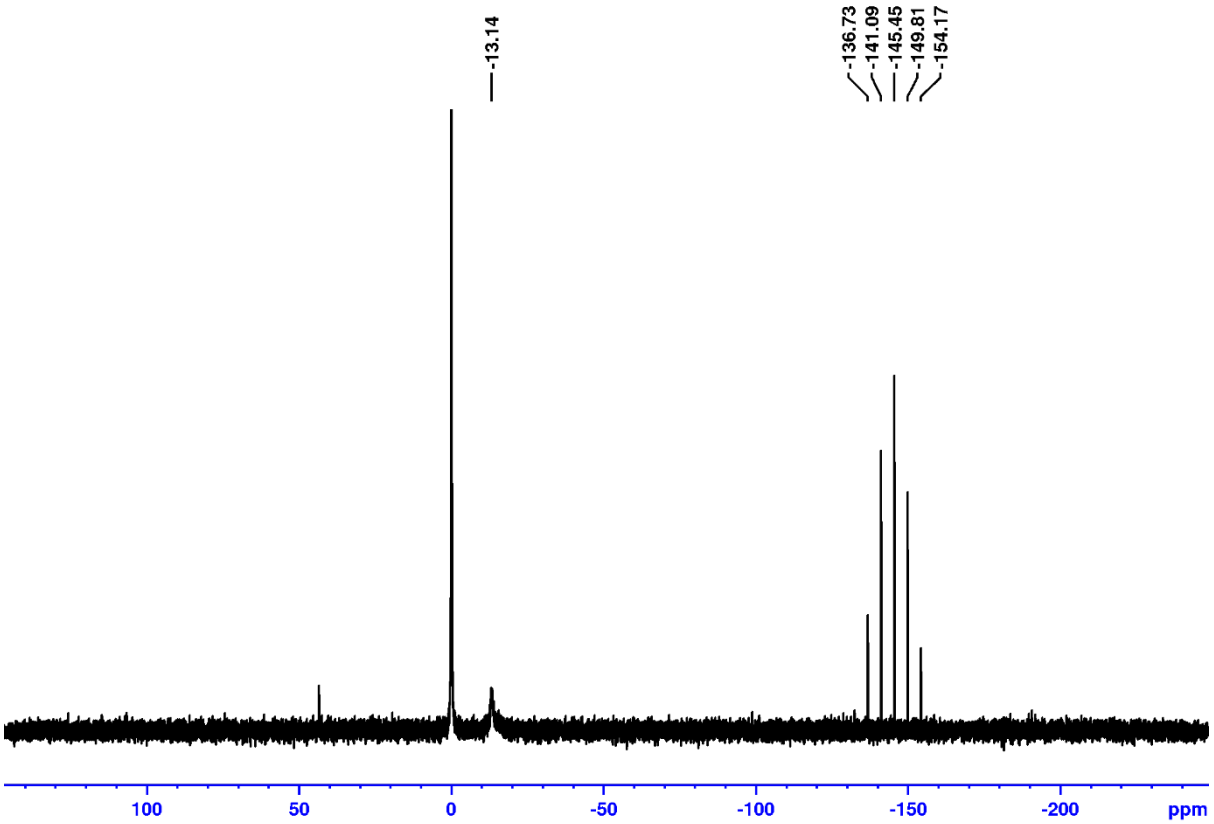

Figure 7.67. ^{31}P NMR (400 MHz, 85% H_3PO_4) spectrum of Complex **C2.**

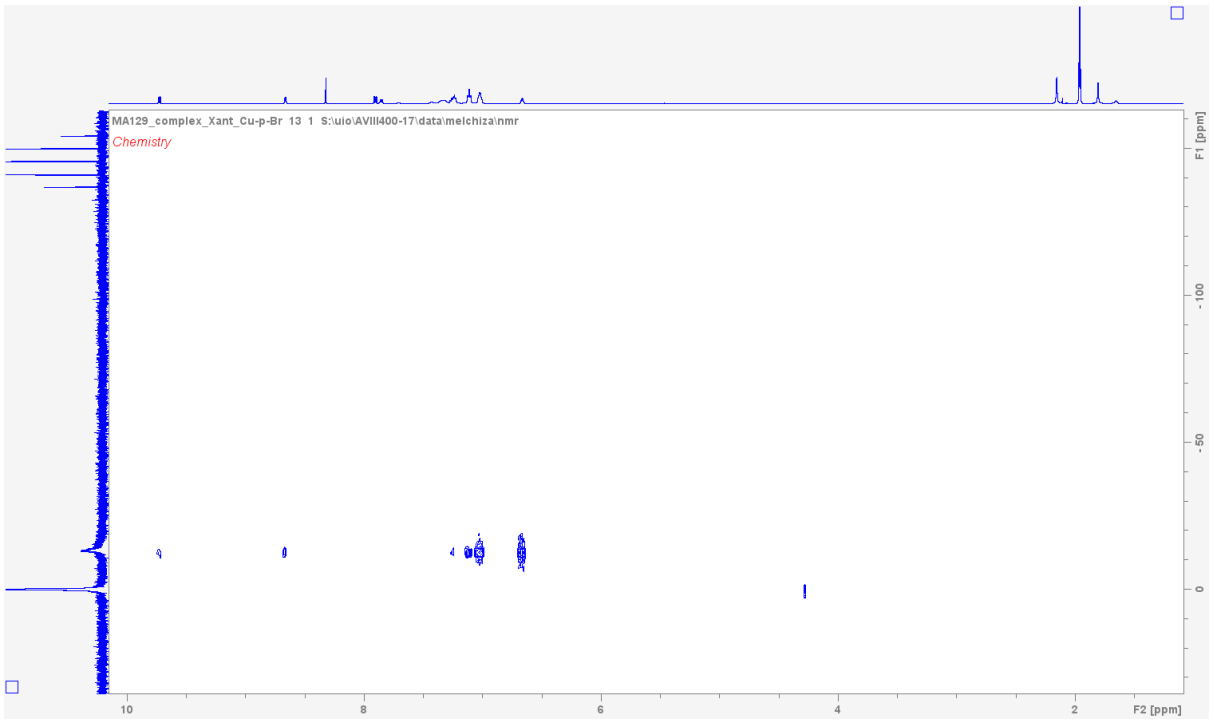

Figure 7.68. ^{31}P HMBC (400 MHz, 85% H_3PO_4) spectrum of complex **C2.**

7.1.21. Complex C3

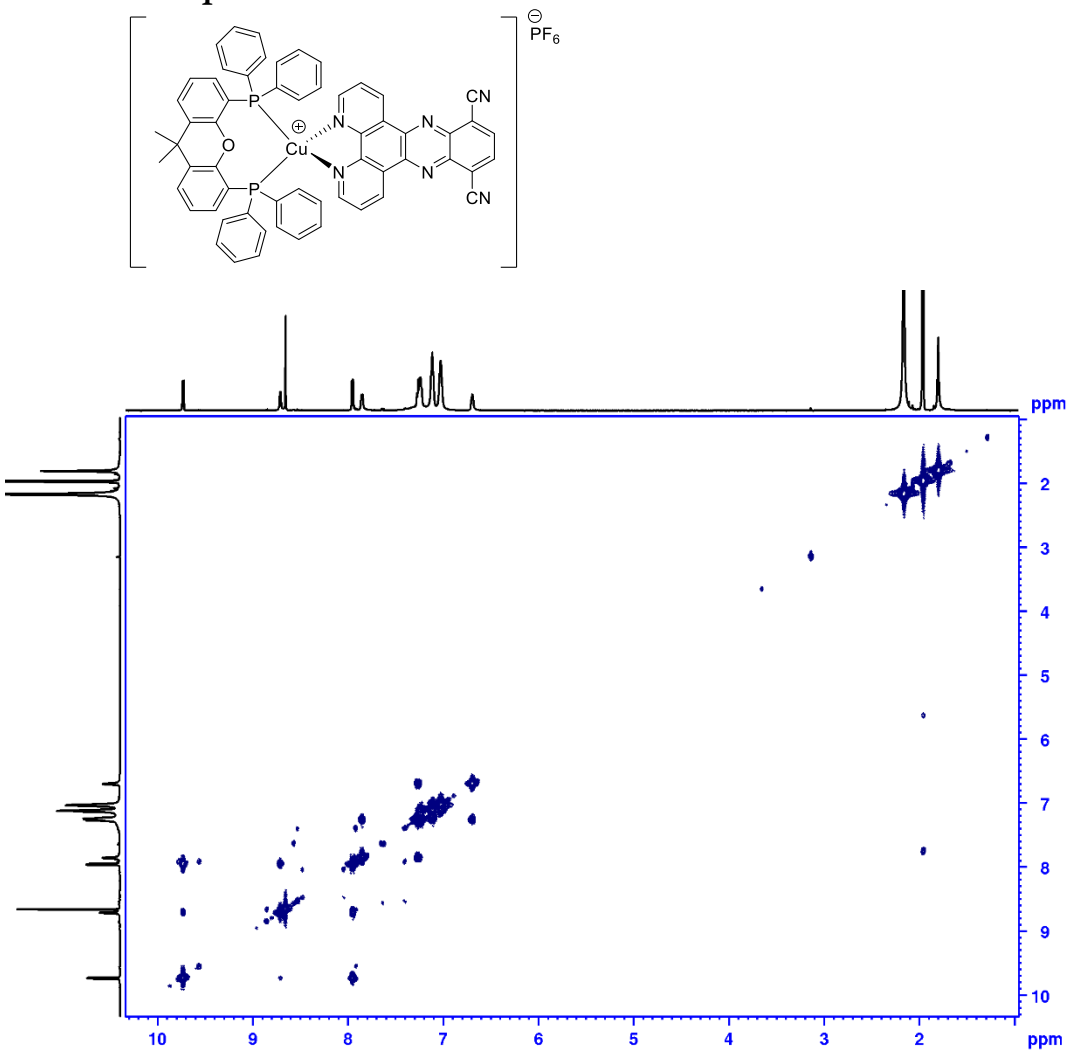

Figure 7.69. COSY (600 MHz, CD_3CN) spectrum of complex **C3.**

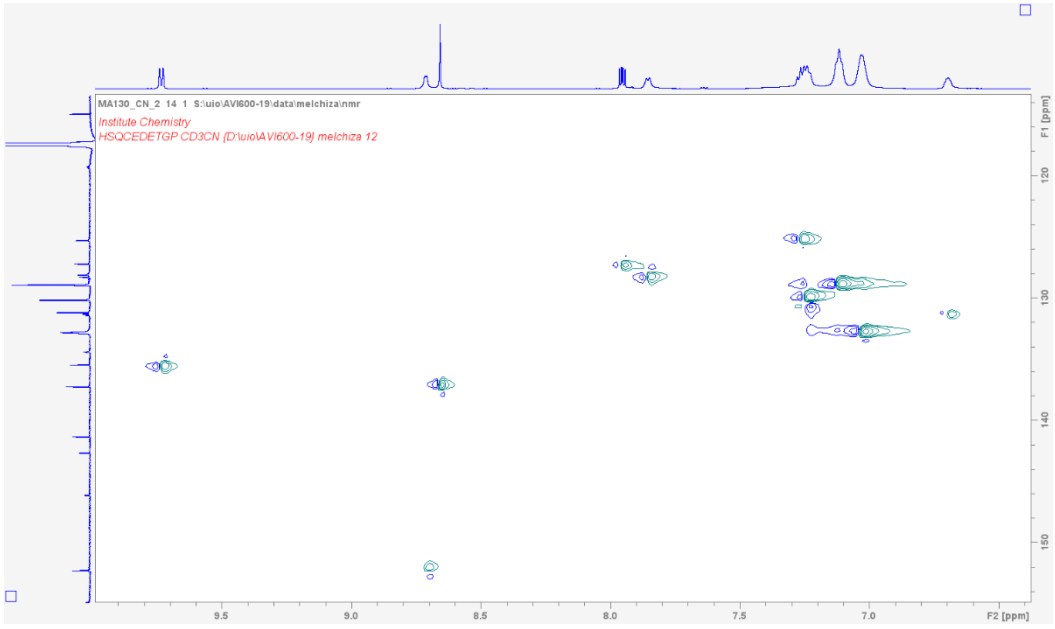

Figure 7.70. HSQC (600 MHz, CD_3CN) spectrum of complex **C3.**

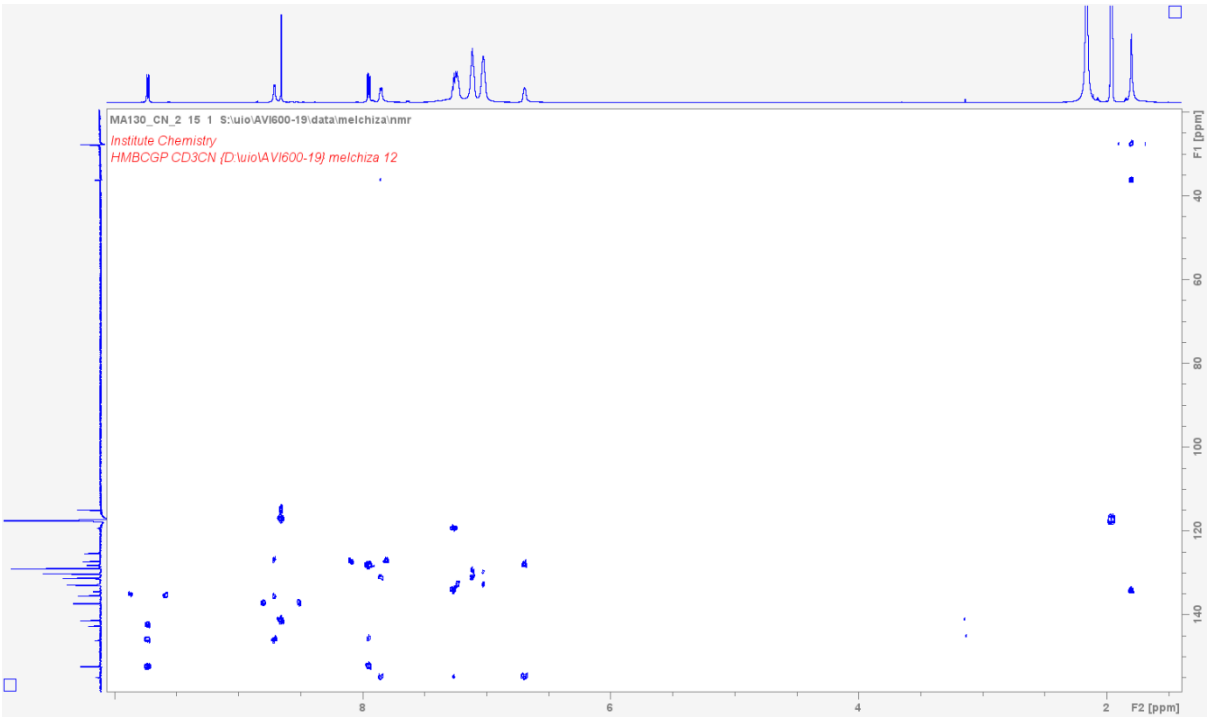

Figure 7.71. HMBC (600 MHz, CD_3CN) spectrum of complex **C3.**

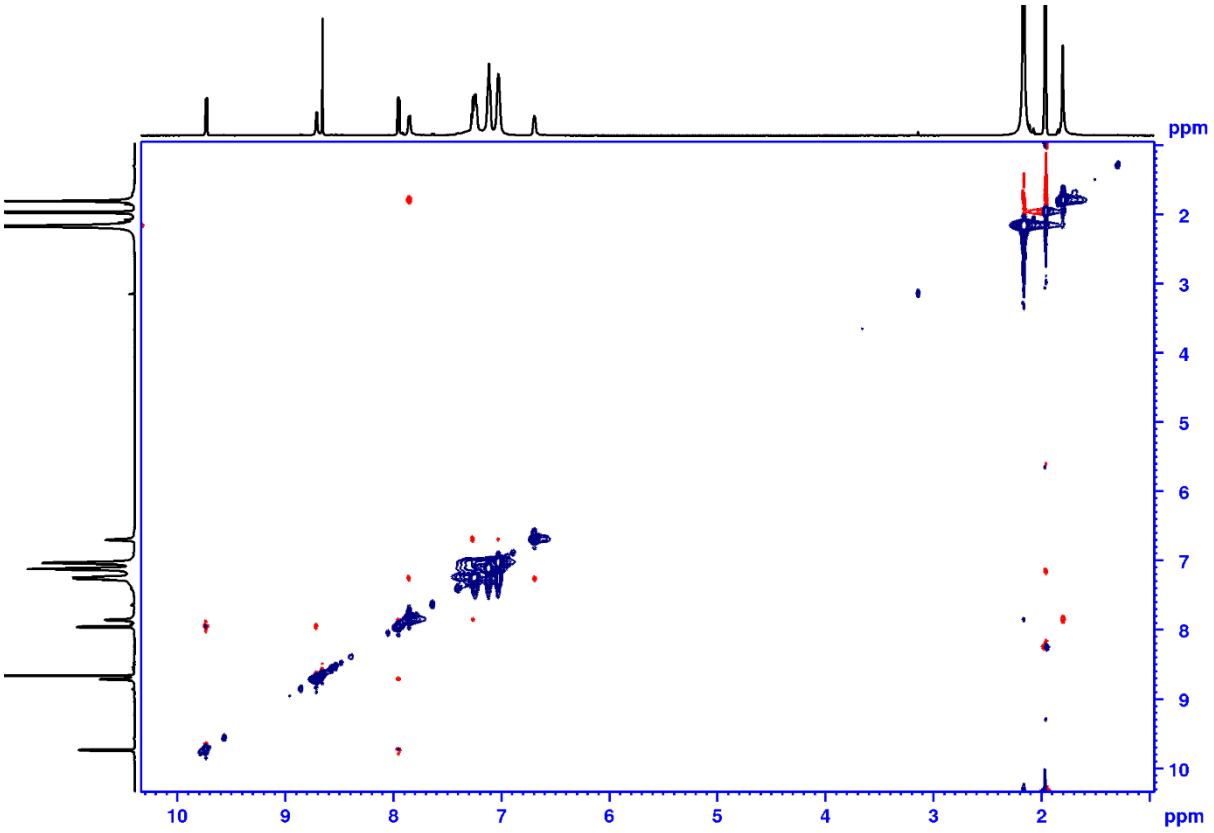

Figure 7.72. NOESY (600 MHz, CD_3CN) spectrum of complex **C3.**

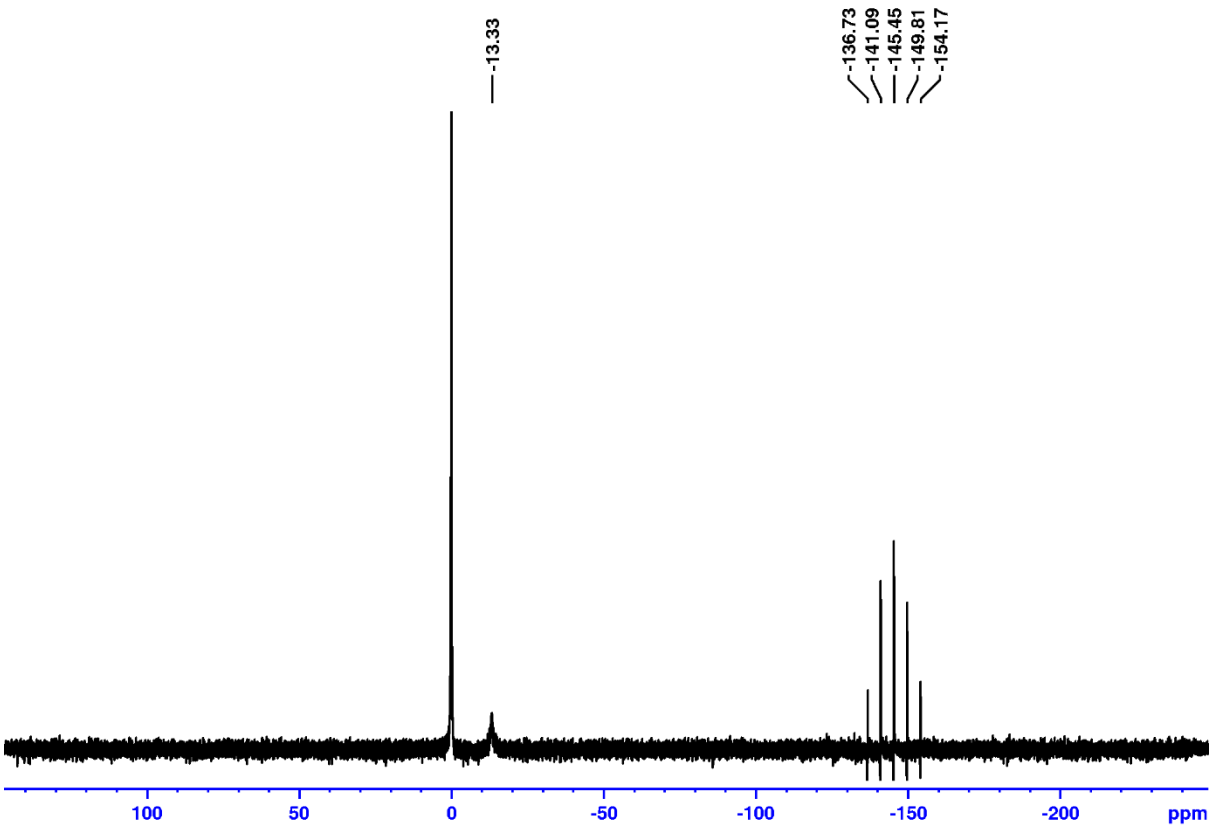

Figure 7.73. ^{31}P NMR (400 MHz, 85% H_3PO_4) spectrum of Complex **C3.**

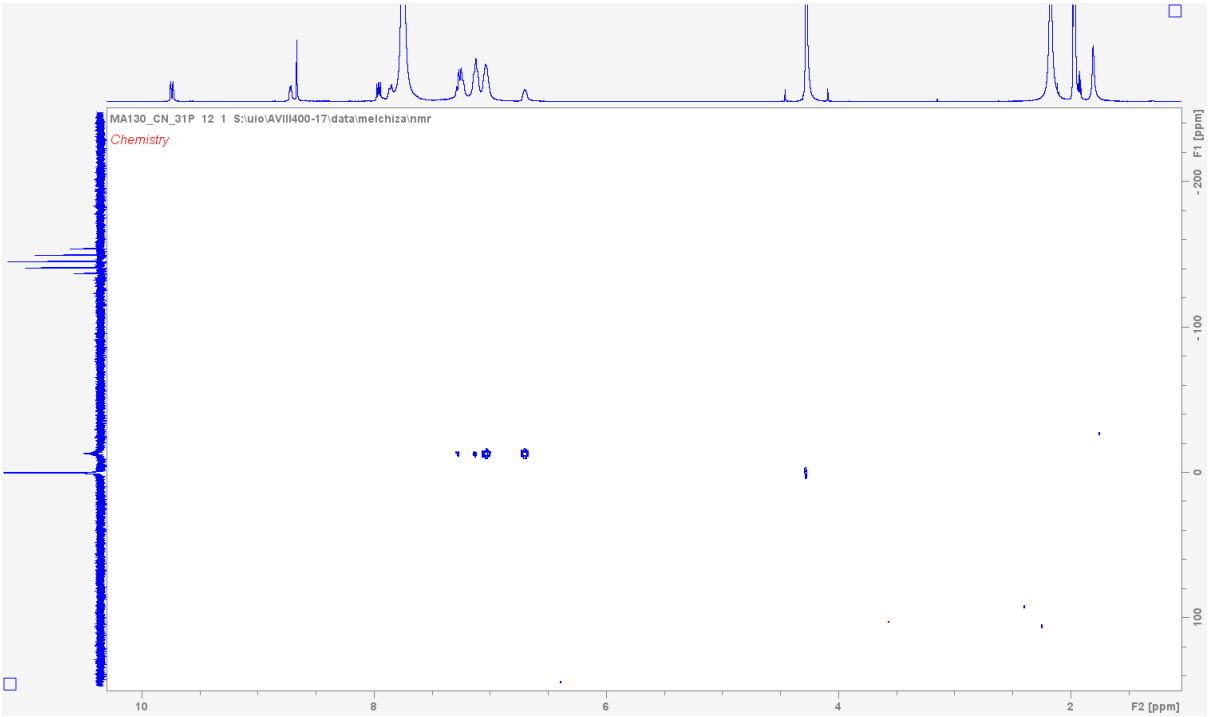

Figure 7.74. ^{31}P HMBC (400 MHz, 85% H_3PO_4) spectrum of Complex **C3.**

7.1.22. Complex C4

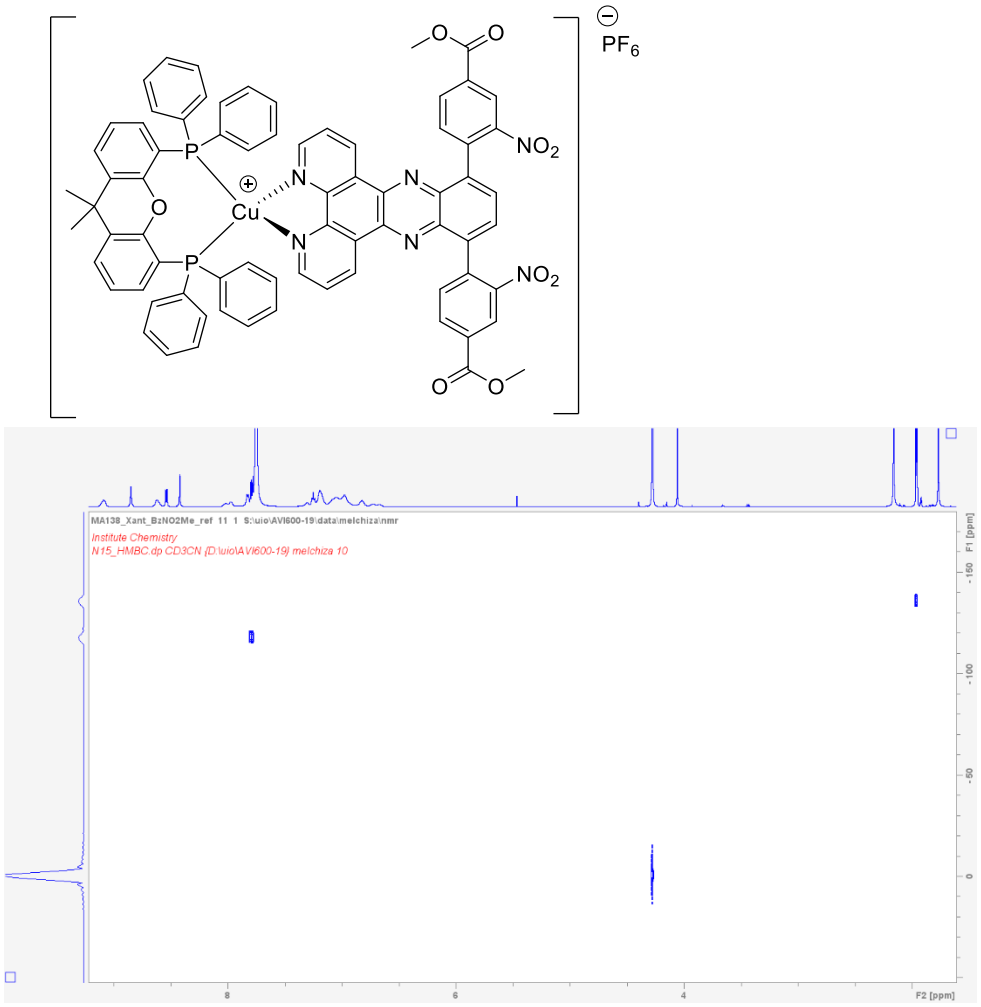

Figure 7.75. ^{1}H – ^{15}N HMBC (600 MHz, CD_3CN + CD_3NO_2) spectrum of Complex **C4.**

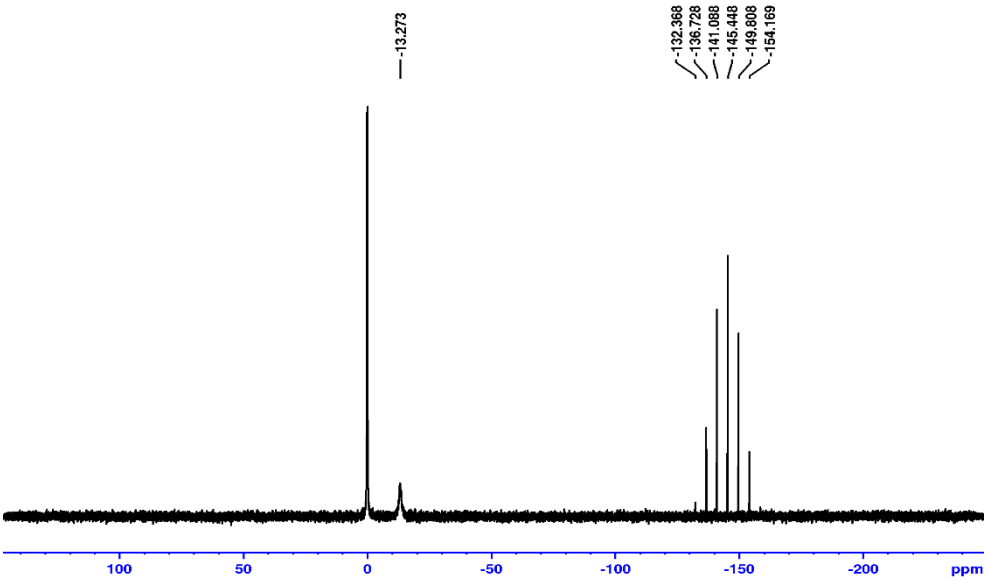

Figure 7.76. ^{31}P NMR (400 MHz, 85% H_3PO_4) spectrum of Complex **C4.**

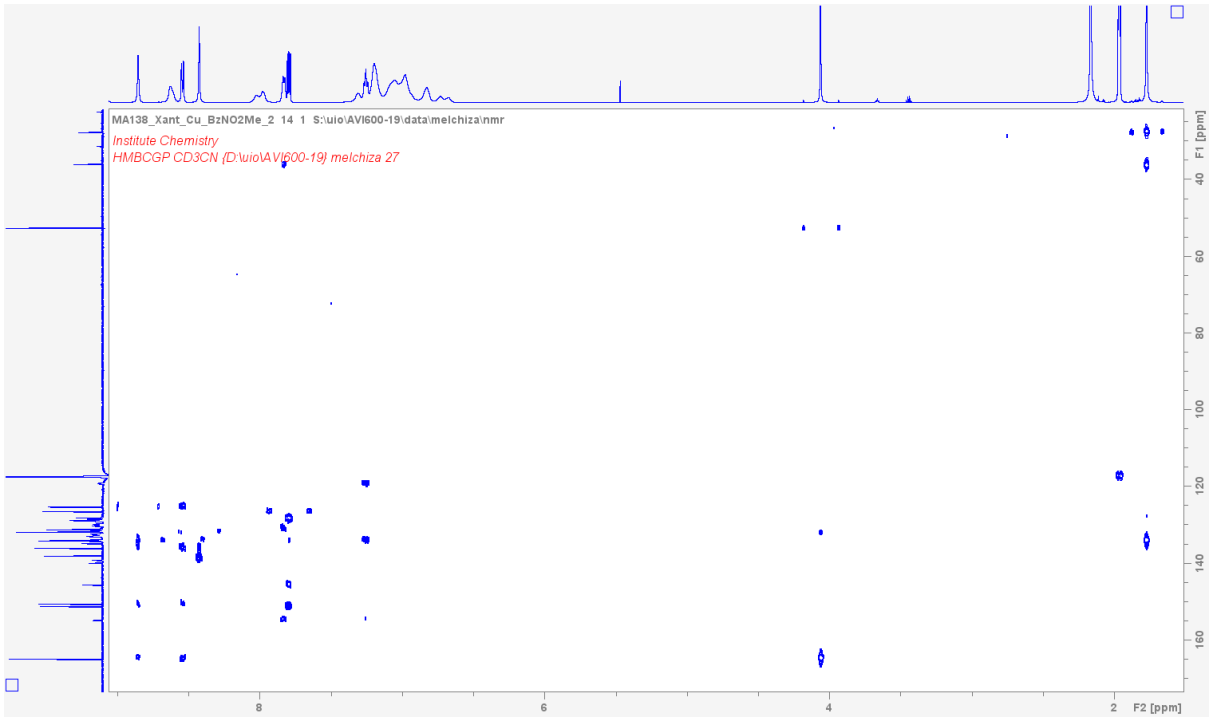

Figure 7.77. $^{1}H - ^{13}C$ HMBC (600 MHz, CD_3CN) spectrum of Complex **C4.**

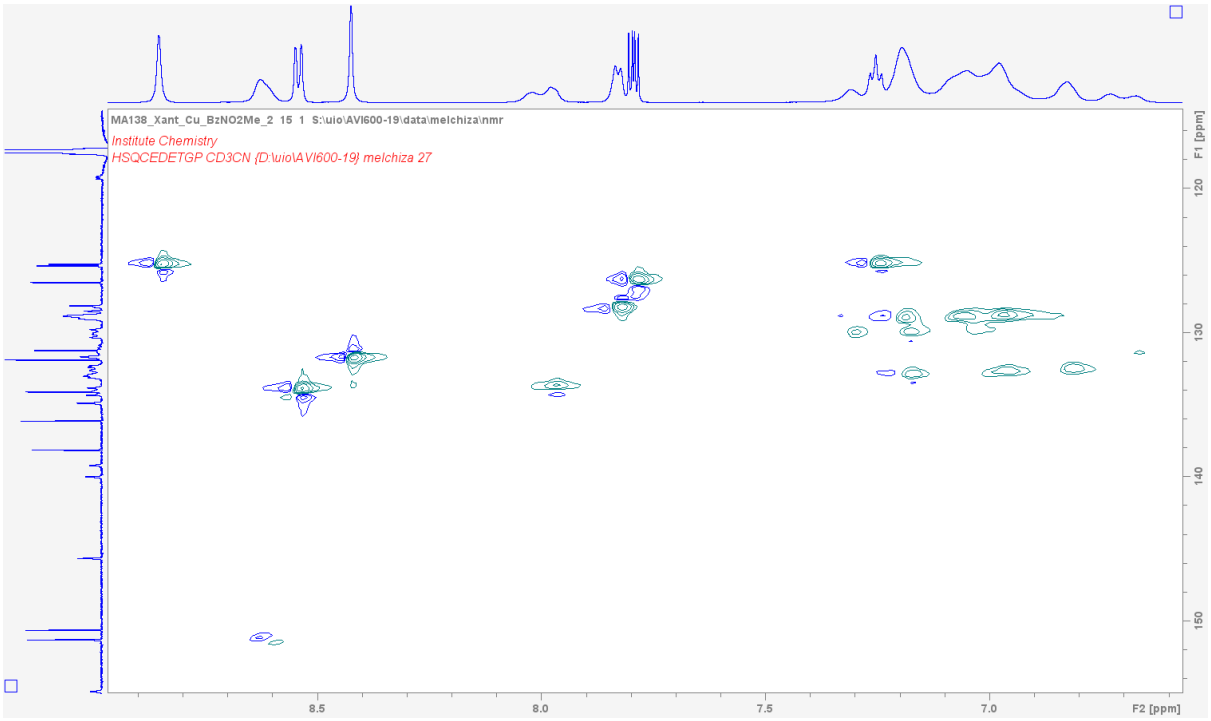

Figure 7.78. Aromatic region of $^{1}H - ^{13}C$ HSQC (600 MHz, CD_3CN) spectrum of Complex **C4.**

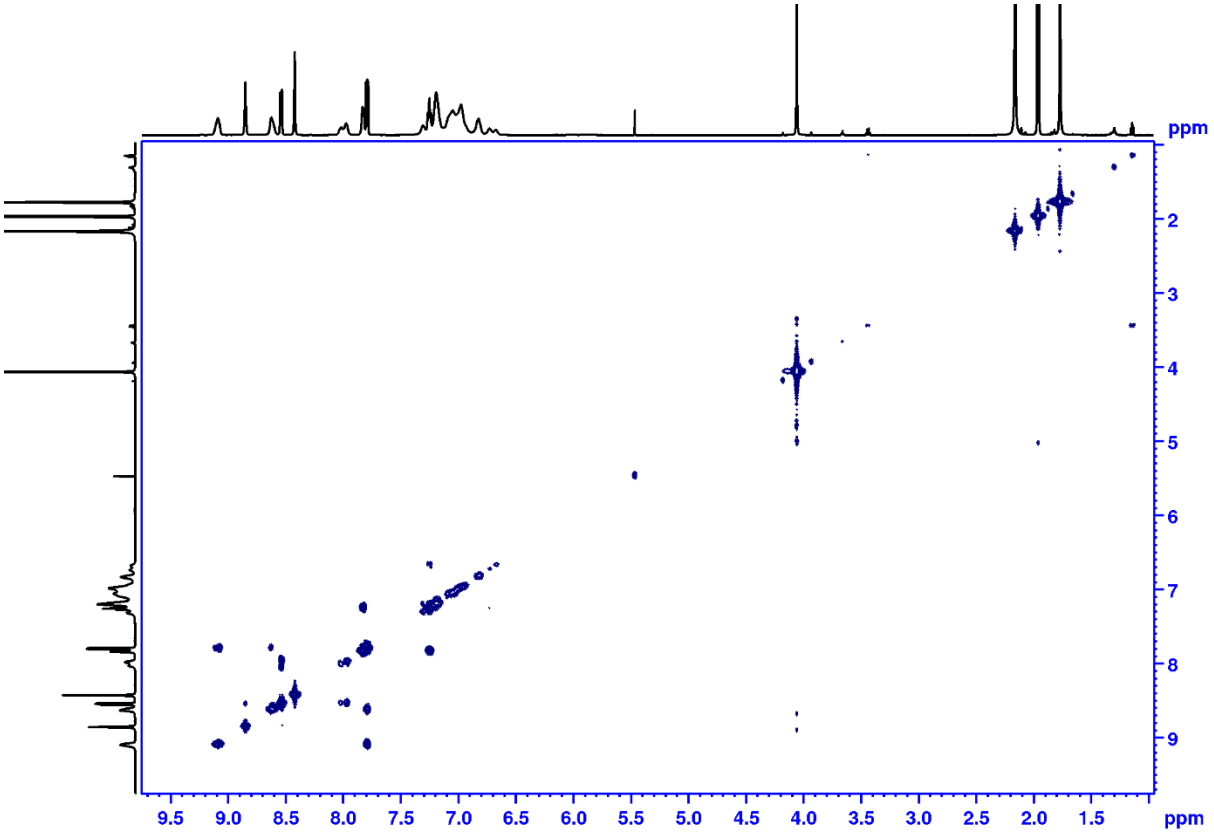

Figure 7.79. COSY (600 MHz, CD_3CN) spectrum of Complex **C4.**

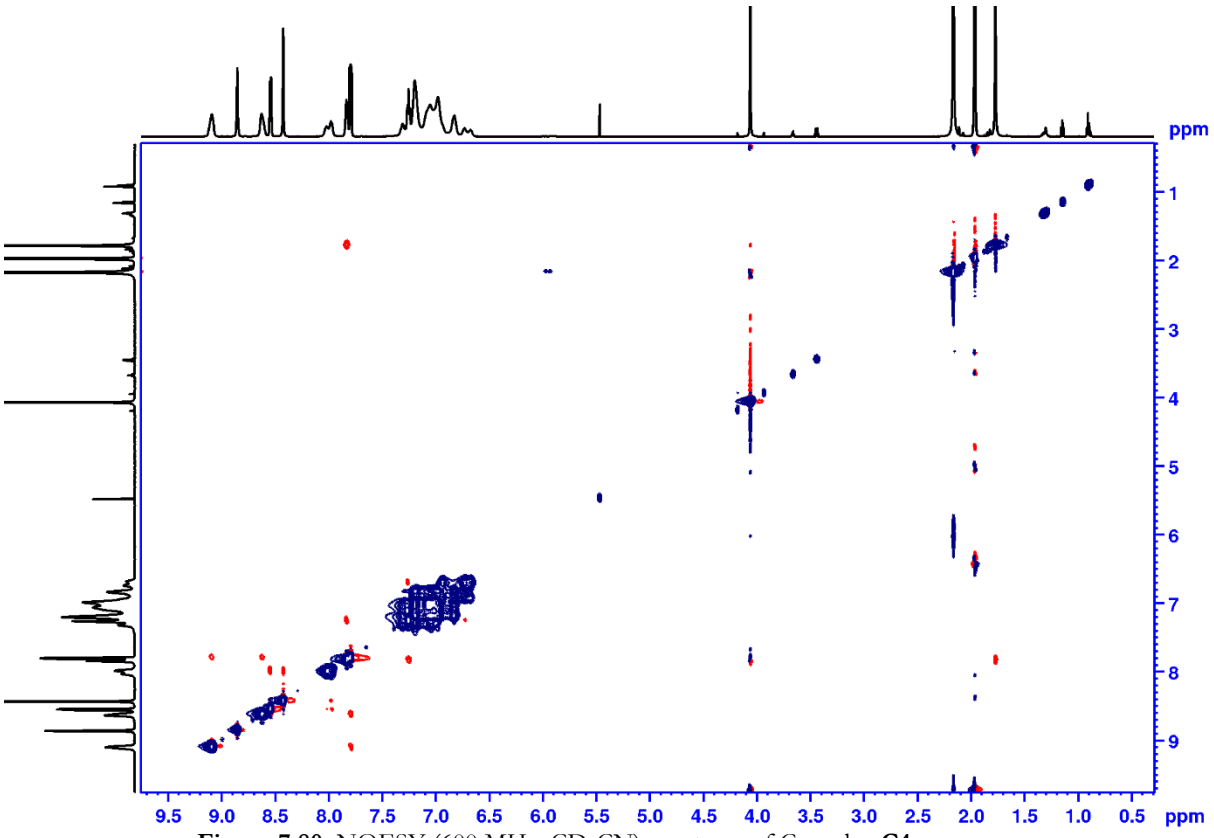

Figure 7.80. NOESY (600 MHz, CD_3CN) spectrum of Complex **C4.**

7.1.23. Complex C5

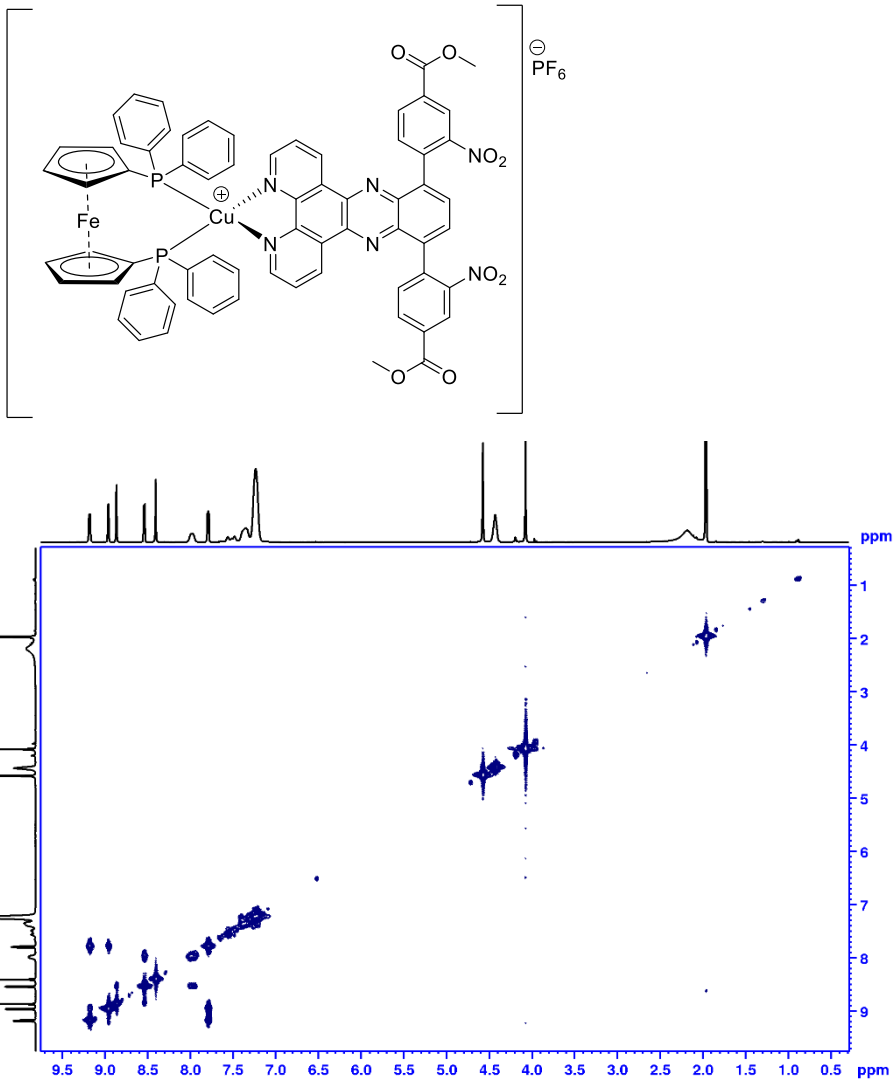

Figure 7.81. COSY (600 MHz, CD_3CN) spectrum of Complex **C5.**

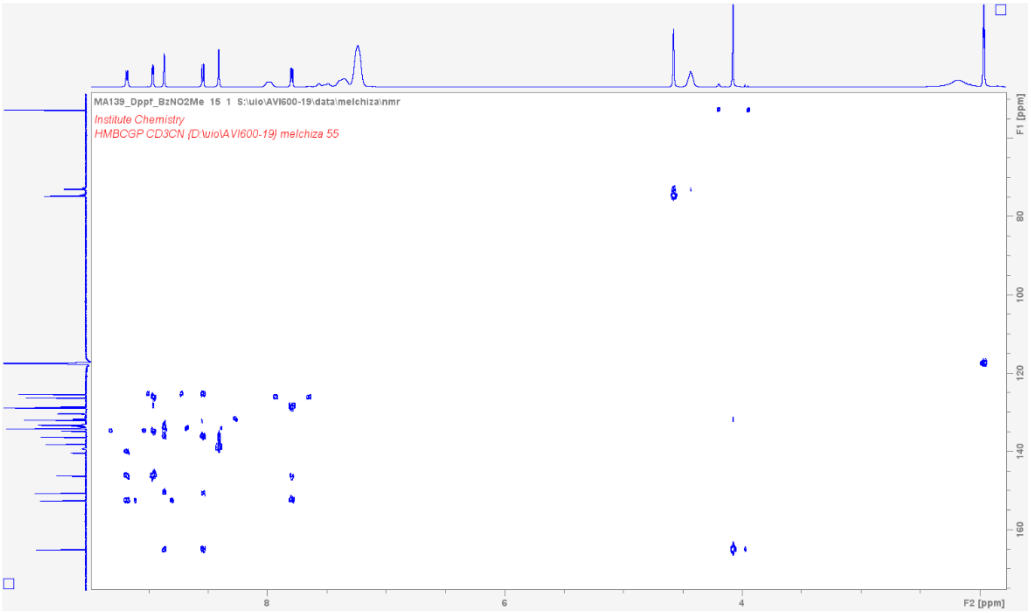

Figure 7.82. HMBC (600 MHz, CD_3CN) spectrum of Complex **C5.**

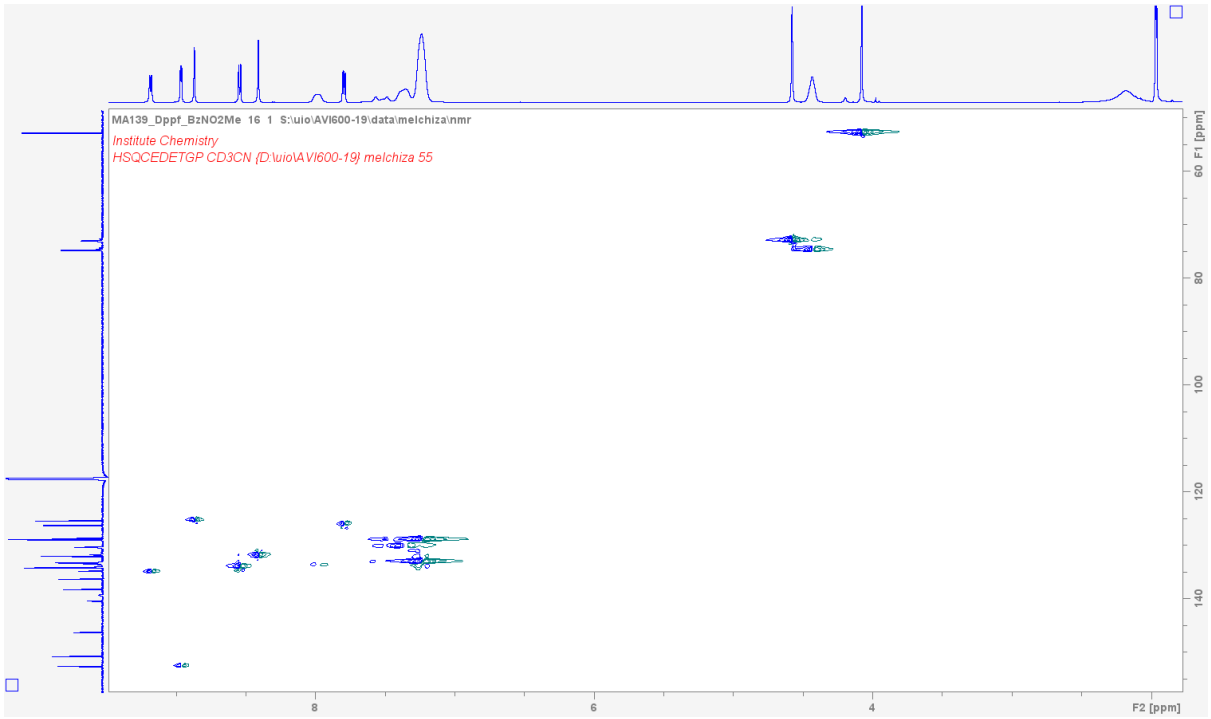

Figure 7.82. HSQC (600 MHz, CD_3CN) spectrum of Complex **C5.**

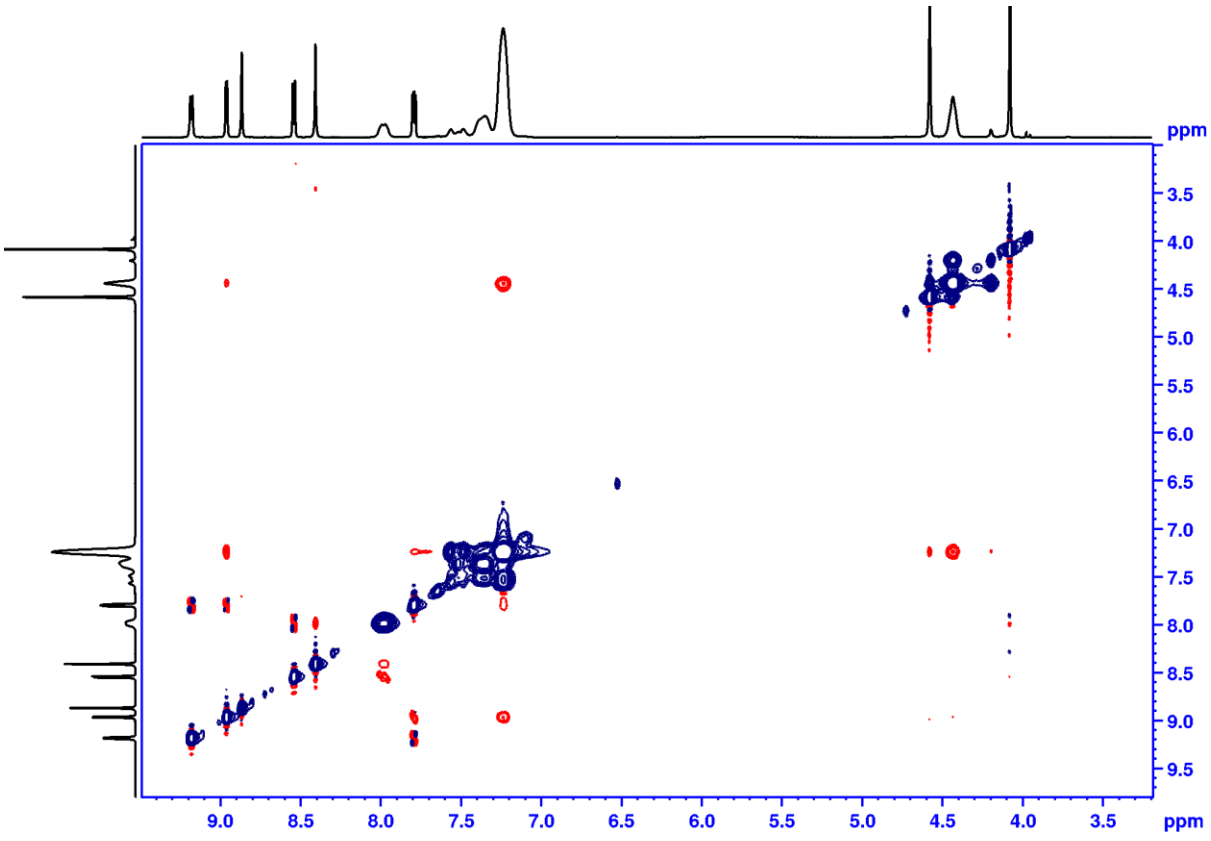

Figure 7.82. ROESY (600 MHz, CD_3CN) spectrum of Complex **C5.**

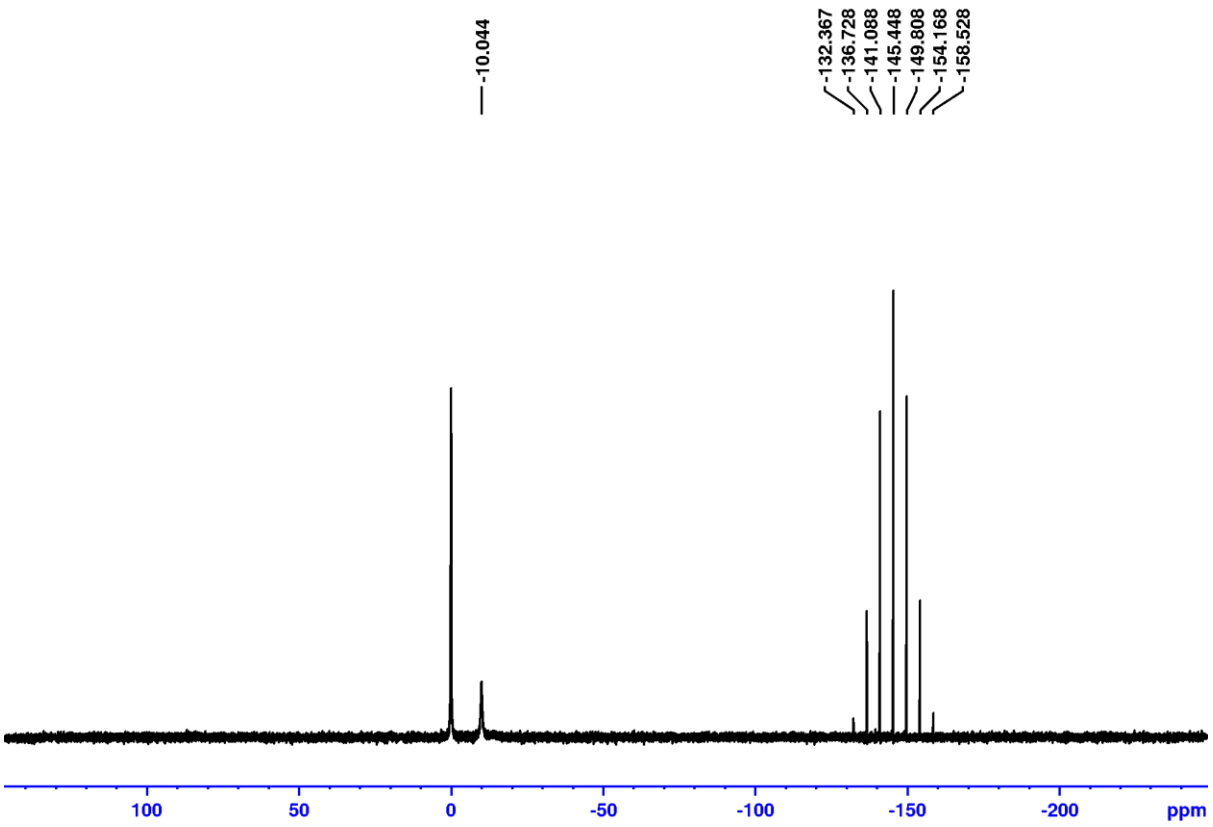

Figure 7.83. ^{31}P NMR (400 MHz, 85% H_3PO_4) spectrum of Complex **C5.**

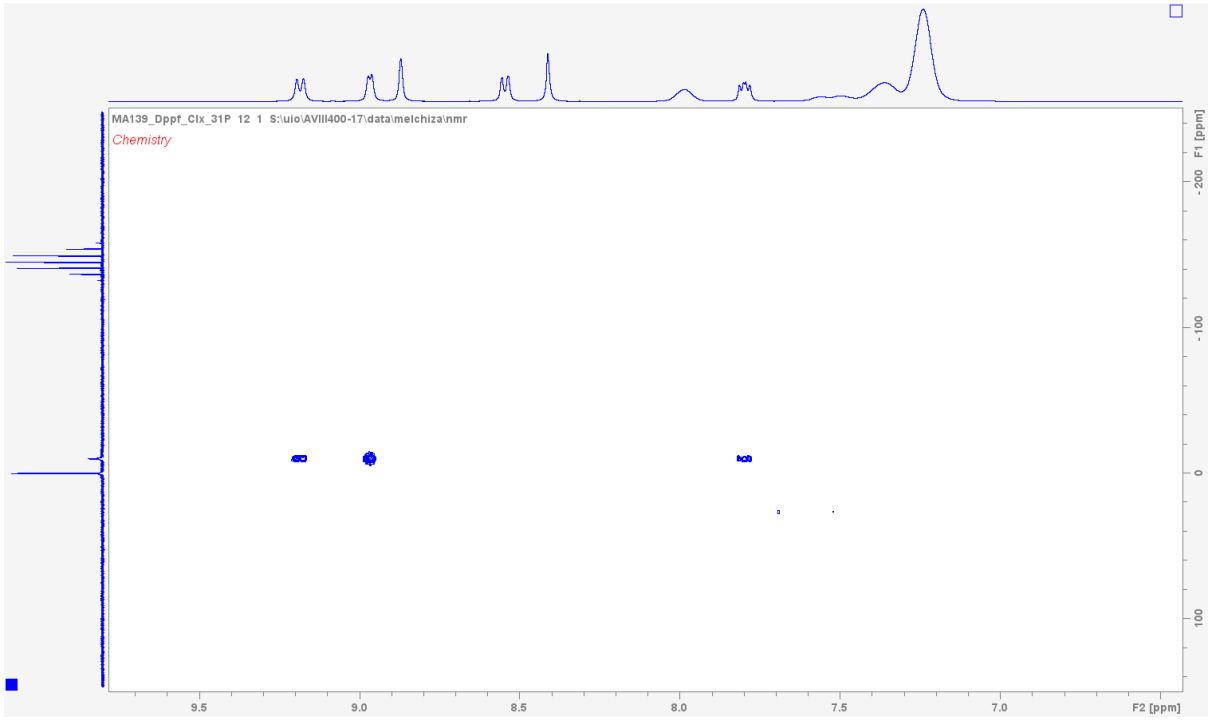

Figure 7.84. ^{31}P HMBC (400 MHz, 85% H_3PO_4) spectrum of Complex **C5.**

7.1.24. Complex C6

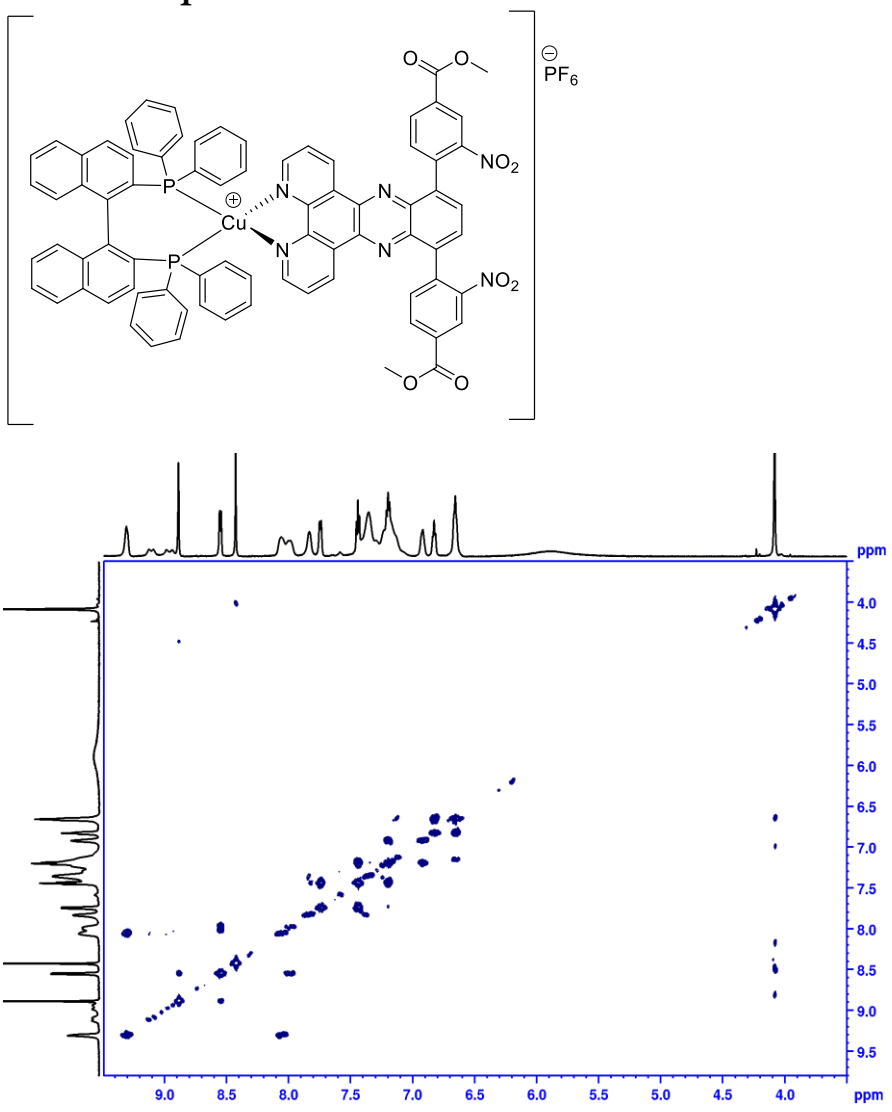

Figure 7.85. COSY (600 MHz, CD_3CN) spectrum of Complex **C6.**

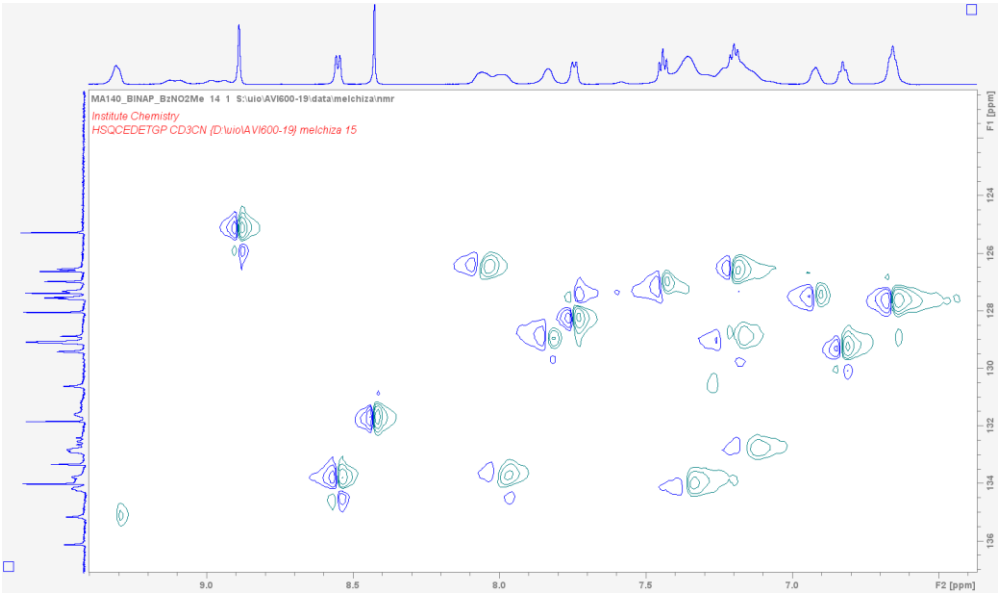

Figure 7.86. Aromatic region of HSQC (600 MHz, CD_3CN) spectrum of Complex **C6.**

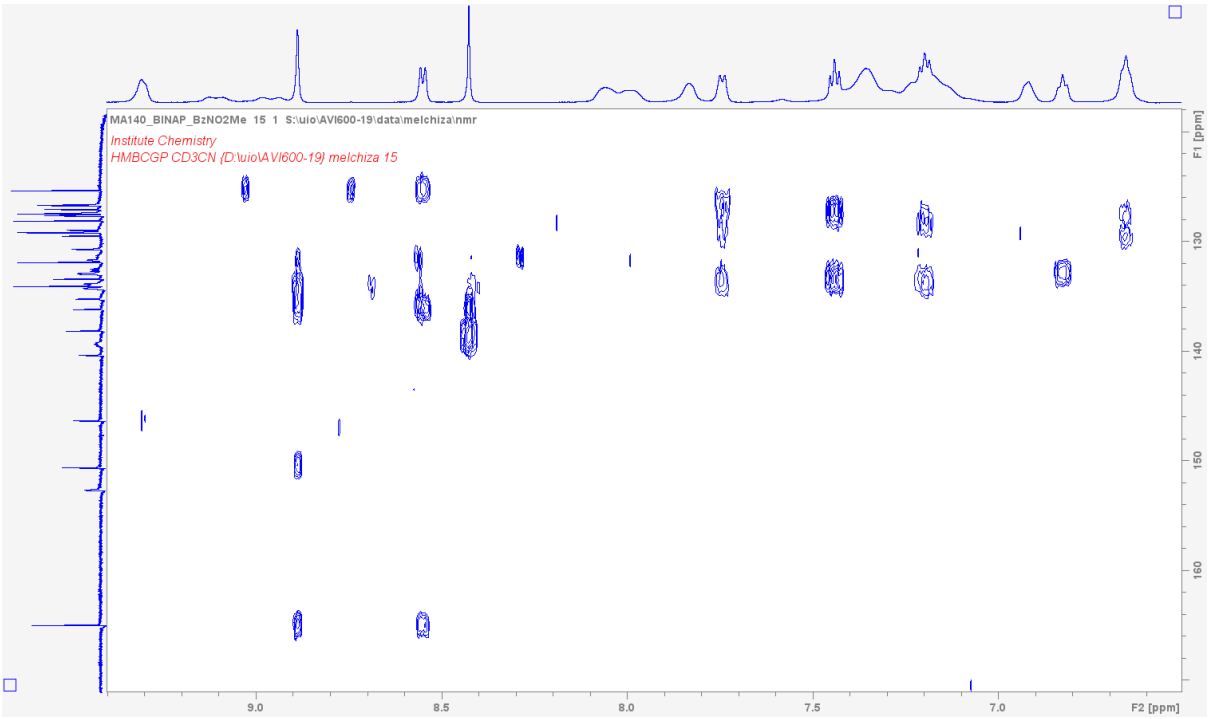

Figure 7.87. Aromatic region of HMBC (600 MHz, CD_3CN) spectrum of Complex **C6.**

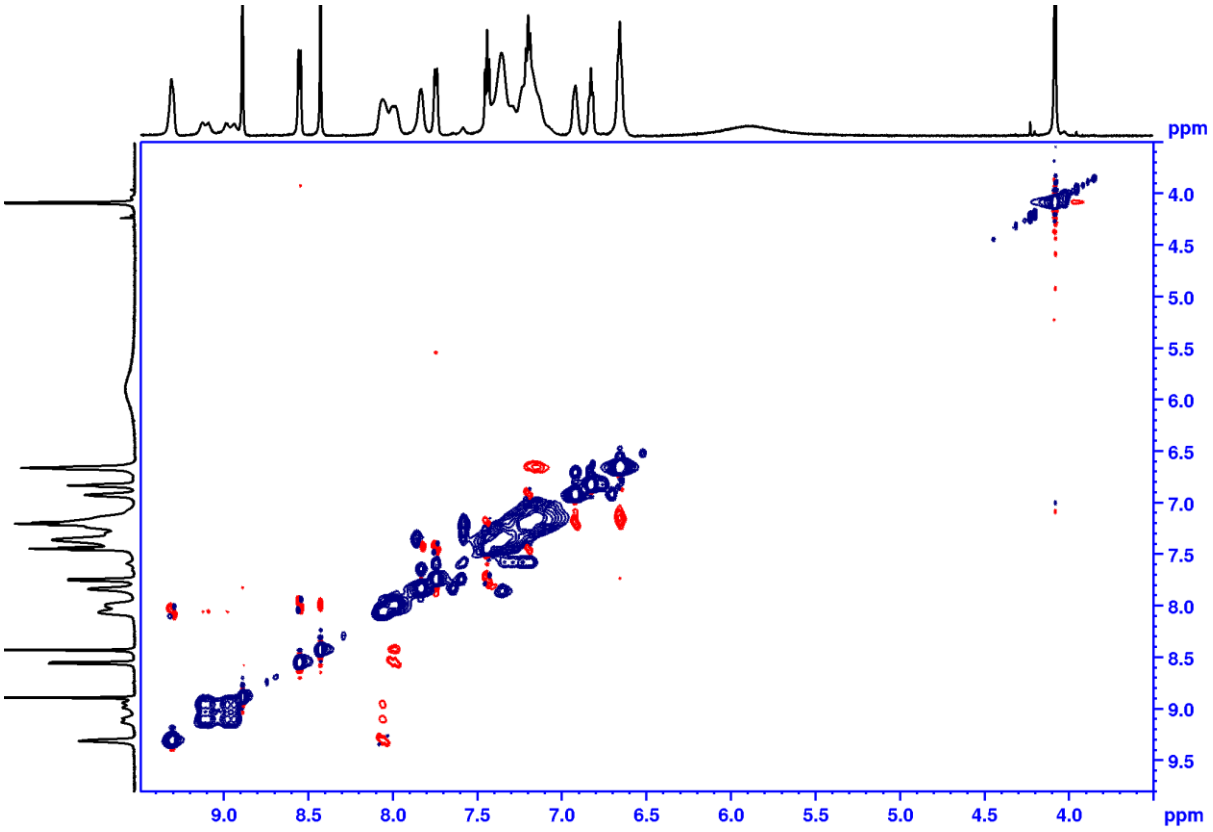

Figure 7.88. ROESY (600 MHz, CD_3CN) spectrum of Complex **C6.**

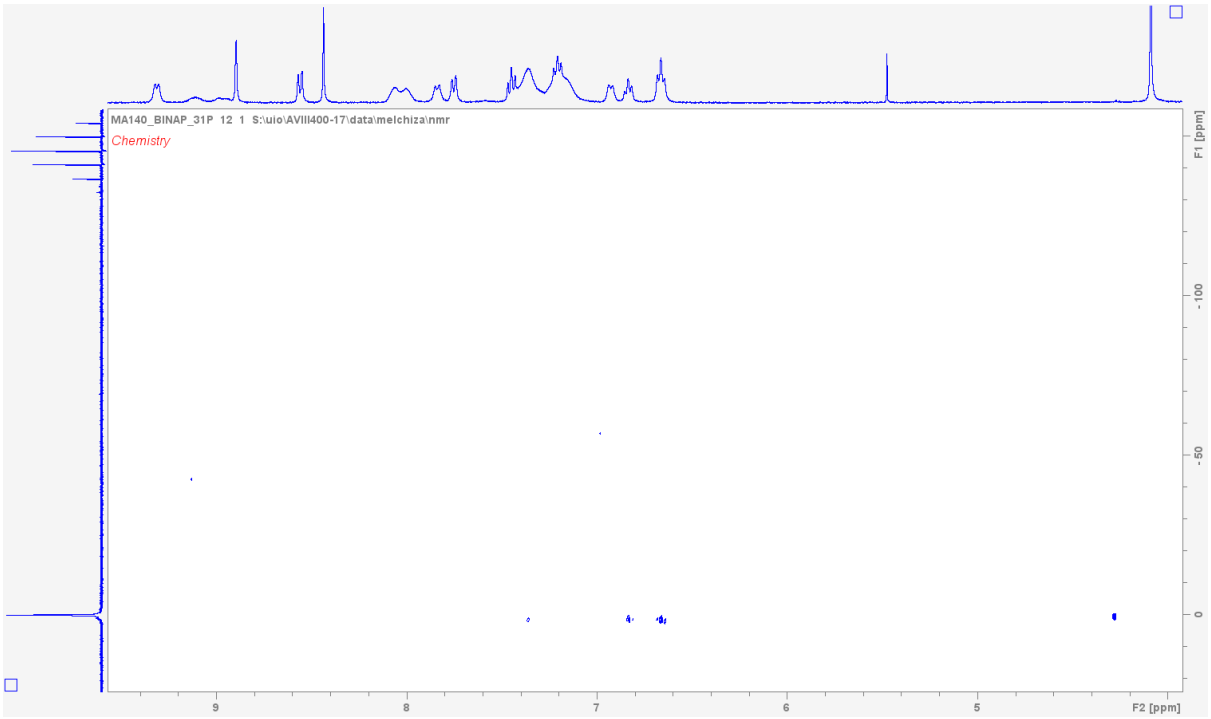

Figure 7.89. ^{31}P HMBC (400 MHz, 85% H_3PO_4) spectrum of Complex **C6.**

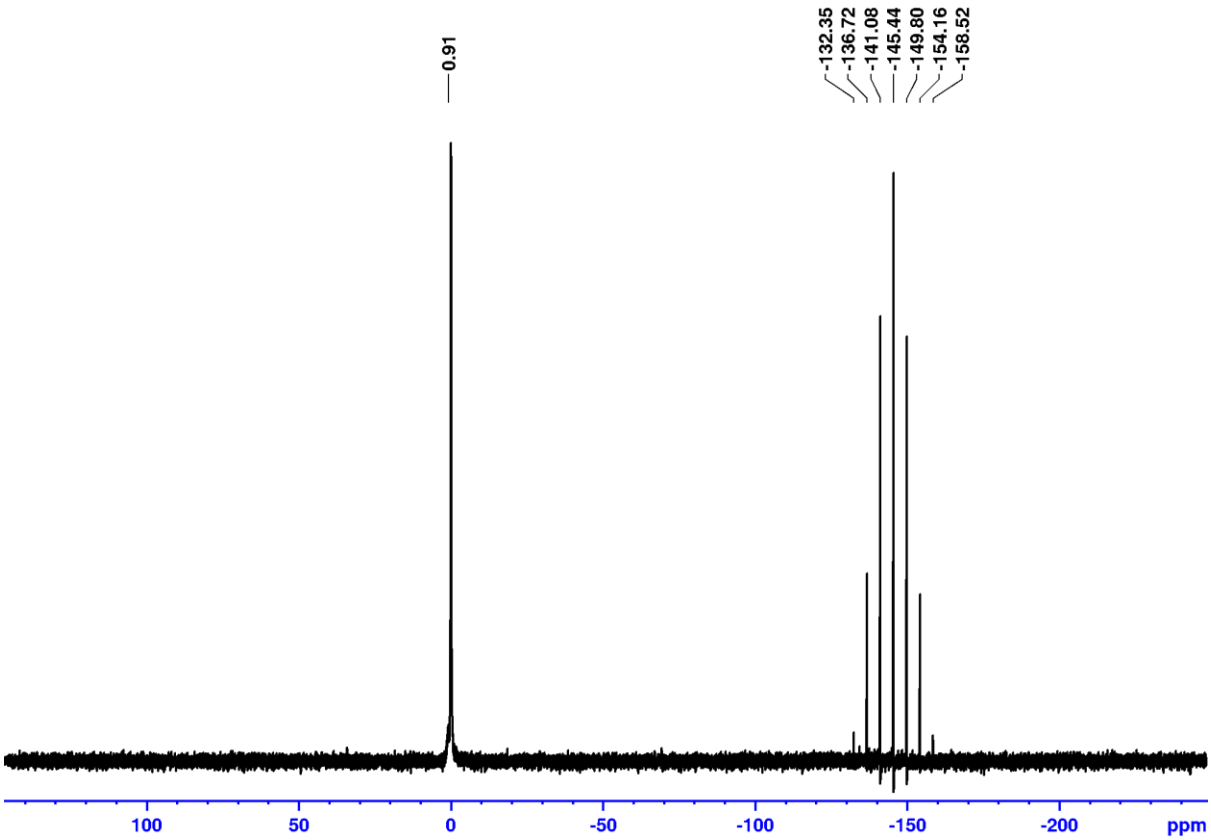

Figure 7.90. ^{31}P NMR (400 MHz, 85% H_3PO_4) spectrum of Complex **C6.**

7.2. Diffusion Ordered Spectroscopy (DOSY)

7.2.1. Complex C1

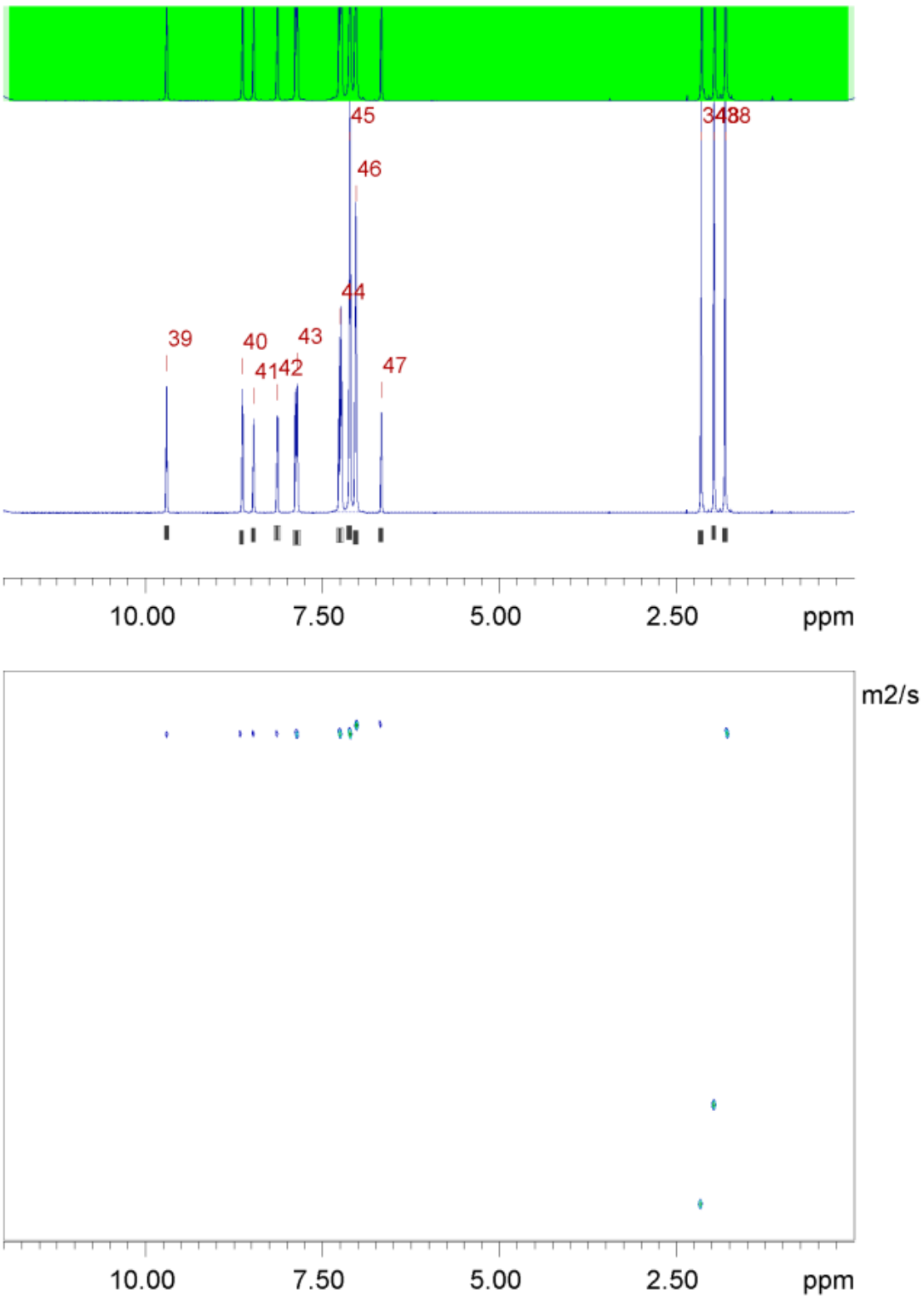

Figure 7.91. User-defined integration areas to calculate the DOSY (800 MHz, CD_3CN) of complex **C1.**

Table 7.1. DOSY parameters and peak list for complex **C1** generated by the Bruker Dynamics center.

Fitted function:	f (x) = Io * exp (-D * x^2 * gamma^2 * littleDelta^2 (bigDelta-littleDelta/3)* 10^4
used gamma:	26752 rad/(s*Gauss)
used little delta:	0.0014000 s
used big delta:	0.054900 s
used gradient strength:	variable
Random error estimation of data:	RMS per spectrum (or trace/plane)
Systematic error estimation of data:	worst case per peak scenario
Fit parameter Error estimation method:	from fit using calculated y uncertainties
Confidence level:	95%
Used peaks:	automatically picked peaks
Used integrals:	area integral
Used Gradient strength:	all values (including replicates) used

Peak name	F2 [ppm]	D [m2/s]	error
34	2.154	9.31e-09	2.789e-13
38	1.813	1.66e-09	3.763e-14
39	9.701	1.65e-09	1.095e-13
40	8.642	1.67e-09	9.678e-14
41	8.476	1.66e-09	1.035e-13
42	8.142	1.66e-09	1.206e-13
43	7.864	1.67e-09	6.196e-14
44	7.253	1.67e-09	4.120e-14
45	7.119	1.65e-09	2.634e-14
46	7.028	1.64e-09	2.628e-14
47	6.671	1.64e-09	1.046e-13
48	1.972	6.62e-09	1.475e-13

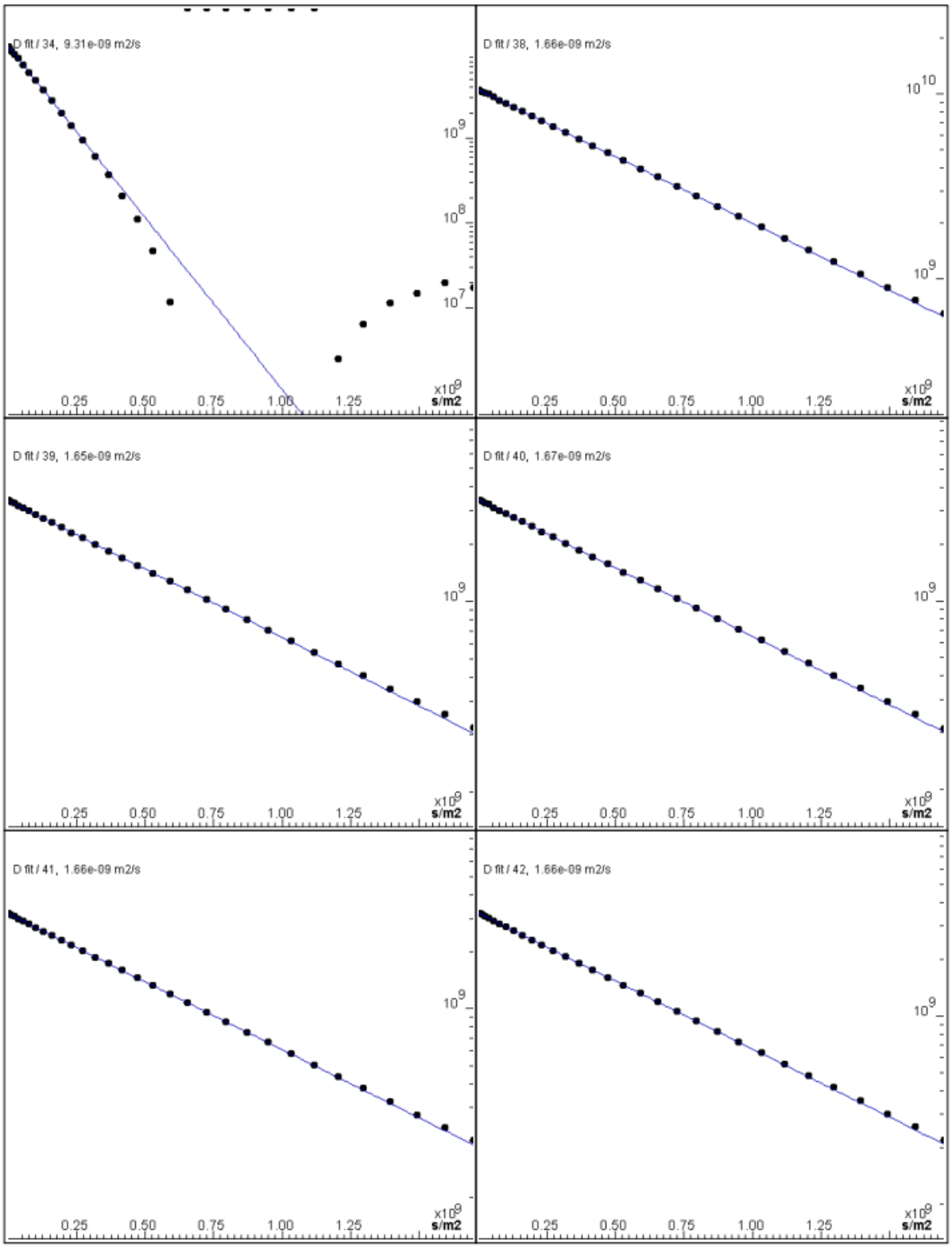
D fit / 34, 9.31e-09 m2/s
D fit / 38, 1.66e-09 m2/s
D fit / 39, 1.65e-09 m2/s
D fit / 40, 1.67e-09 m2/s
D fit / 41, 1.66e-09 m2/s
D fit / 42, 1.66e-09 m2/s
0.25
0.50
0.75
1.00
1.25
x10^9 s/m2

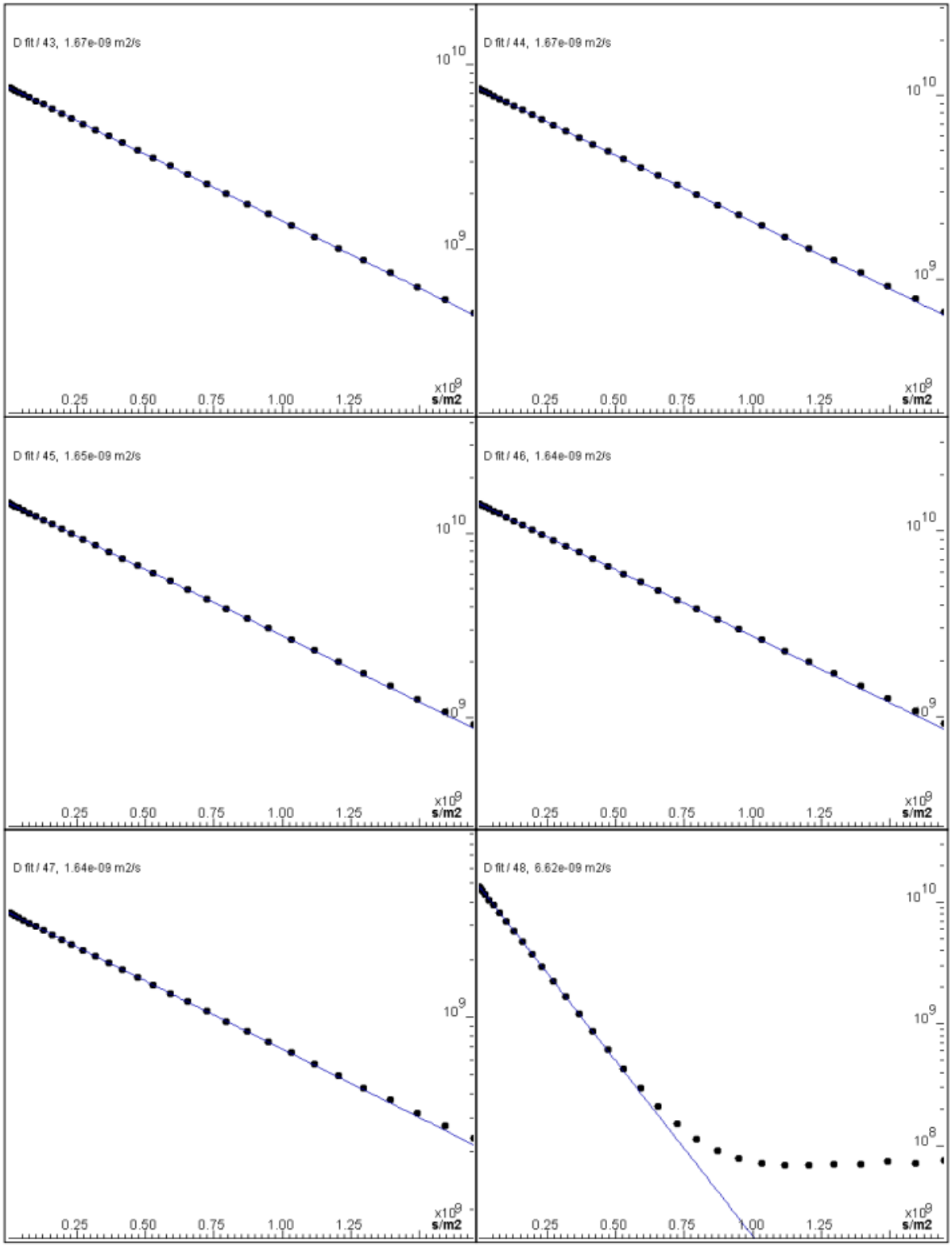

Figure 7.92. The integrals for selected integration areas at different gradient strength (dots) and their fits (lines) for complex **C1**.

7.2.2. Complex C2

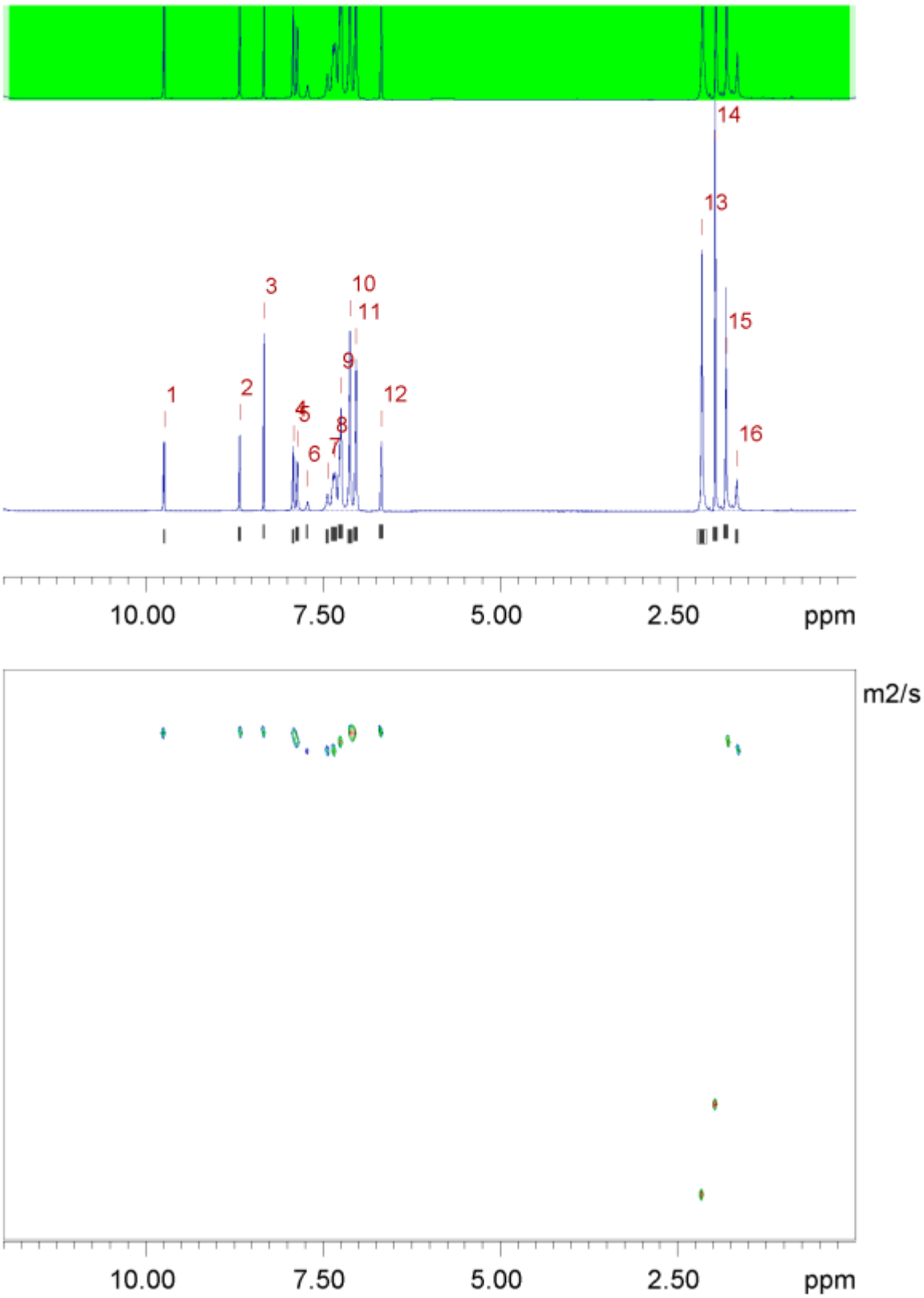

Figure 7.93. User-defined integration areas to calculate the DOSY (800 MHz, CD_3CN) of complex **C2.**

Table 7.2. DOSY parameters and peak list for complex **C2** generated by the Bruker Dynamics center.

Fitted function:	f (x) = Io * exp (-D * x^2 * gamma^2 * littleDelta^2 (bigDelta-littleDelta/3)* 10^4
used gamma:	26752 rad/(s*Gauss)
used little delta:	0.0014000 s
used big delta:	0.054900 s
used gradient strength:	variable
Random error estimation of data:	RMS per spectrum (or trace/plane)
Systematic error estimation of data:	worst case per peak scenario
Fit parameter Error estimation method:	from fit using arbitray y uncertainties
Confidence level:	95%
Used peaks:	automatically picked peaks
Used integrals:	area integral
Used Gradient strength:	all values (including replicates) used

Peak name	F2 [ppm]	D [m2/s]	error
1	9.739	1.75e-09	5.774e-12
2	8.672	1.76e-09	6.131e-12
3	8.333	1.76e-09	6.959e-12
4	7.918	1.77e-09	4.281e-12
5	7.862	1.80e-09	4.902e-12
6	7.718	1.87e-09	8.502e-12
7	7.439	1.87e-09	6.348e-12
8	7.341	1.87e-09	2.588e-12
9	7.249	1.81e-09	2.810e-12
10	7.119	1.80e-09	2.940e-12
11	7.035	1.79e-09	3.878e-12
12	6.676	1.79e-09	6.302e-12
13	2.154	9.37e-09	7.674e-11
14	1.968	6.77e-09	6.394e-11
15	1.816	1.83e-09	9.177e-12
16	1.666	1.92e-09	1.344e-11

7.2.3. Complex C3

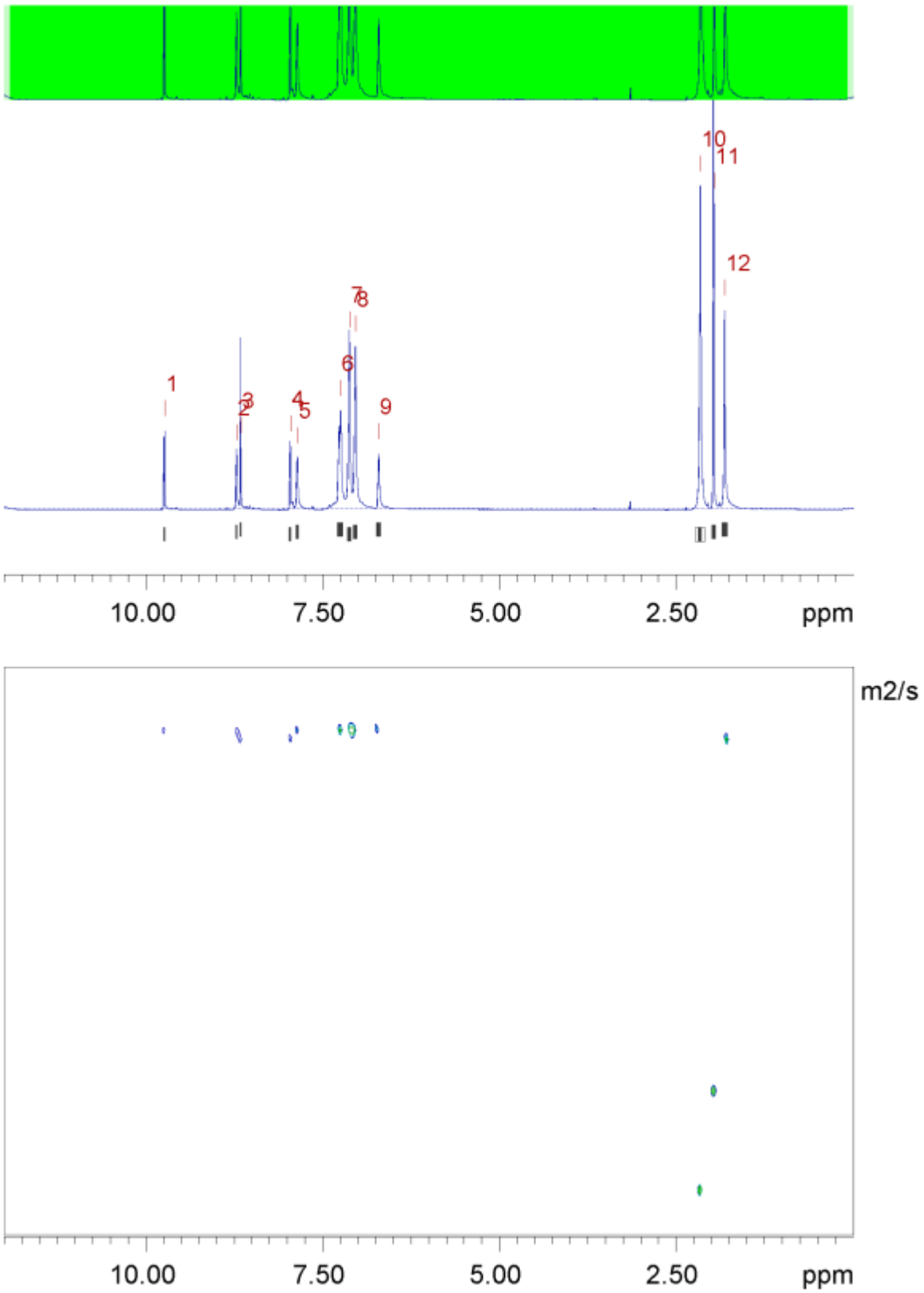

Figure 7.94. User-defined integration areas to calculate the DOSY (800 MHz, CD_3CN) of complex **C3.**

Table 7.3. DOSY parameters and peak list for complex **C3** generated by the Bruker Dynamics center.

Fitted function:	f (x) = Io * exp (-D * x^2 * gamma^2 * littleDelta^2 (bigDelta-littleDelta/3)* 10^4
used gamma:	26752 rad/(s*Gauss)
used little delta:	0.0014000 s
used big delta:	0.054900 s
used gradient strength:	variable
Random error estimation of data:	RMS per spectrum (or trace/plane)
Systematic error estimation of data:	worst case per peak scenario
Fit parameter Error estimation method:	from fit using arbitray y uncertainties
Confidence level:	95%
Used peaks:	automatically picked peaks
Used integrals:	area integral
Used Gradient strength:	all values (including replicates) used

Peak name	F2 [ppm]	D [m2/s]	error
1	9.739	2.04e-09	6.249e-12
2	8.718	2.04e-09	5.980e-12
3	8.660	2.05e-09	6.908e-12
4	7.958	2.06e-09	5.711e-12
5	7.858	2.05e-09	5.945e-12
6	7.246	2.05e-09	4.176e-12
7	7.122	2.05e-09	4.152e-12
8	7.037	2.03e-09	5.454e-12
9	6.706	2.01e-09	6.771e-12
10	2.157	9.79e-09	5.098e-11
11	1.963	7.05e-09	7.830e-11
12	1.811	2.08e-09	1.014e-11

7.2.4. Complex C4

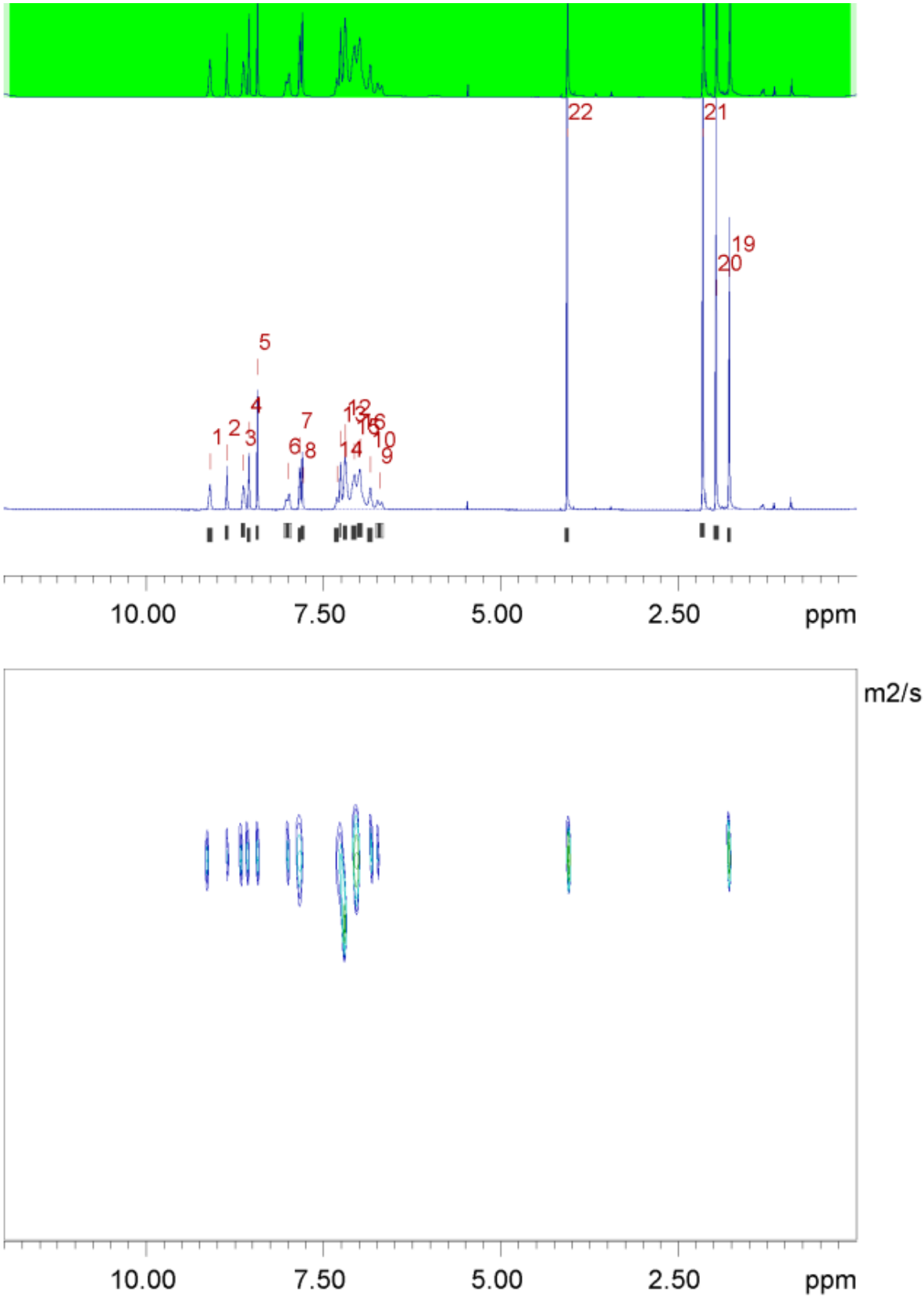

Figure 7.95. User-defined integration areas to calculate the DOSY (800 MHz, CD_3CN) of complex **C4.**

Table 7.4. DOSY parameters and peak list for complex **C4** generated by the Bruker Dynamics center.

Fitted function:	f (x) = Io * exp (-D * x^2 * gamma^2 * littleDelta^2 (bigDelta-littleDelta/3)* 10^4
used gamma:	26752 rad/(s*Gauss)
used little delta:	0.0015000 s
used big delta:	0.054900 s
used gradient strength:	variable
Random error estimation of data:	RMS per spectrum (or trace/plane)
Systematic error estimation of data:	worst case per peak scenario
Fit parameter Error estimation method:	from fit using calculated y uncertainties
Confidence level:	95%
Used peaks:	automatically picked peaks
Used integrals:	area integral
Used Gradient strength:	all values (including replicates) used

Peak name	F2 [ppm]	D [m2/s]	error
1	9.103	1.78e-09	1.679e-13
2	8.862	1.75e-09	1.754e-13
3	8.631	1.76e-09	1.514e-13
4	8.551	1.76e-09	1.288e-13
5	8.431	1.78e-09	1.199e-13
6	8.006	1.75e-09	1.992e-13
7	7.840	1.79e-09	1.087e-13
8	7.793	1.78e-09	1.133e-13
9	6.711	1.75e-09	2.747e-13
10	6.842	1.77e-09	1.500e-13
12	7.193	1.80e-09	5.566e-14
13	7.262	1.77e-09	9.385e-14
14	7.314	1.77e-09	2.751e-13
15	7.071	1.79e-09	6.748e-14
16	6.989	1.78e-09	6.328e-14
19	1.781	1.79e-09	4.169e-14
20	1.964	7.18e-09	1.843e-13
21	2.159	9.24e-09	2.035e-13
22	4.071	1.75e-09	4.067e-14

7.2.5. Complex C5

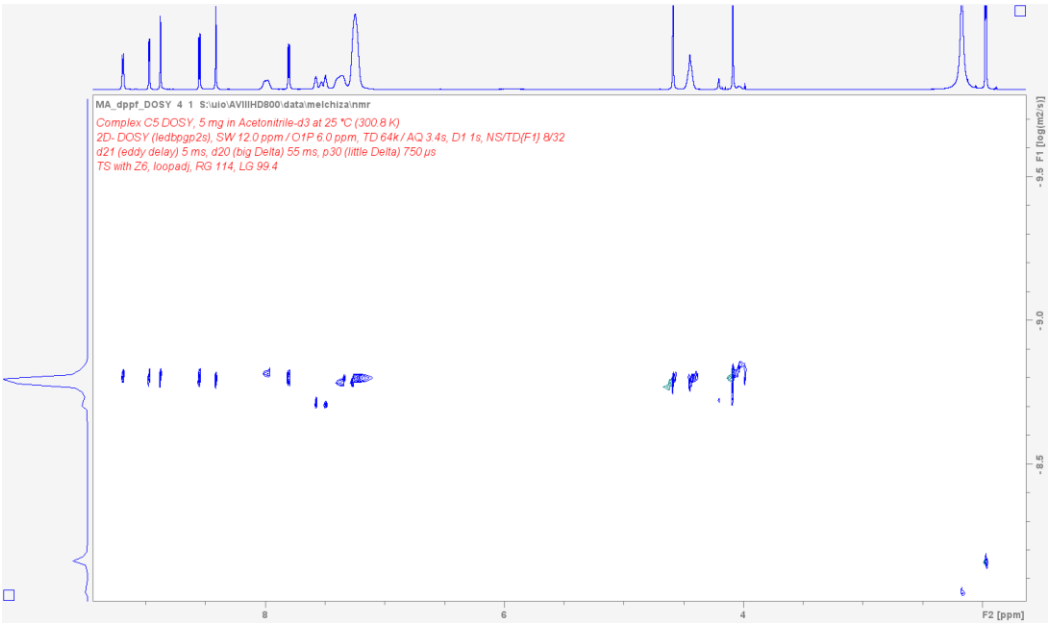

Figure 7.96. DOSY (800 MHz, CD_3CN) of complex **C5.**

Table 7.5. DOSY parameters and peak list for complex **C5** generated by the Bruker Dynamics center.

Fitted function:	f (x) = Io * exp (-D * x^2 * gamma^2 * littleDelta^2 (bigDelta-littleDelta/3)* 10^4
used gamma:	26752 rad/(s*Gauss)
used little delta:	0.0015000 s
used big delta:	0.054900 s
used gradient strength:	variable
Random error estimation of data:	RMS per spectrum (or trace/plane)
Systematic error estimation of data:	worst case per peak scenario
Fit parameter Error estimation method:	from fit using calculated y uncertainties
Confidence level:	95%
Used peaks:	automatically picked peaks
Used integrals:	area integral
Used Gradient strength:	all values (including replicates) used

Peak name	F2 [ppm]	D [m2/s]	error
1	9.190	1.61e-09	6.892e-14
2	8.969	1.62e-09	5.636e-14
3	8.875	1.61e-09	7.102e-14
4	8.549	1.61e-09	6.041e-14
5	8.411	1.61e-09	5.975e-14
6	7.991	1.58e-09	9.203e-14
7	7.797	1.60e-09	6.120e-14
8	7.576	1.93e-09	1.419e-13
9	7.523	1.94e-09	1.734e-13
10	7.490	1.90e-09	1.110e-13
11	7.362	1.65e-09	4.737e-14
12	7.244	1.65e-09	1.039e-14
13	4.584	1.64e-09	4.221e-14
14	4.442	1.67e-09	3.522e-14
15	4.083	1.61e-09	2.437e-14
16	2.168	9.36e-09	2.337e-13
17	1.963	6.97e-09	1.598e-13
18	4.202	1.91e-09	3.068e-13

7.2.6. Complex C6

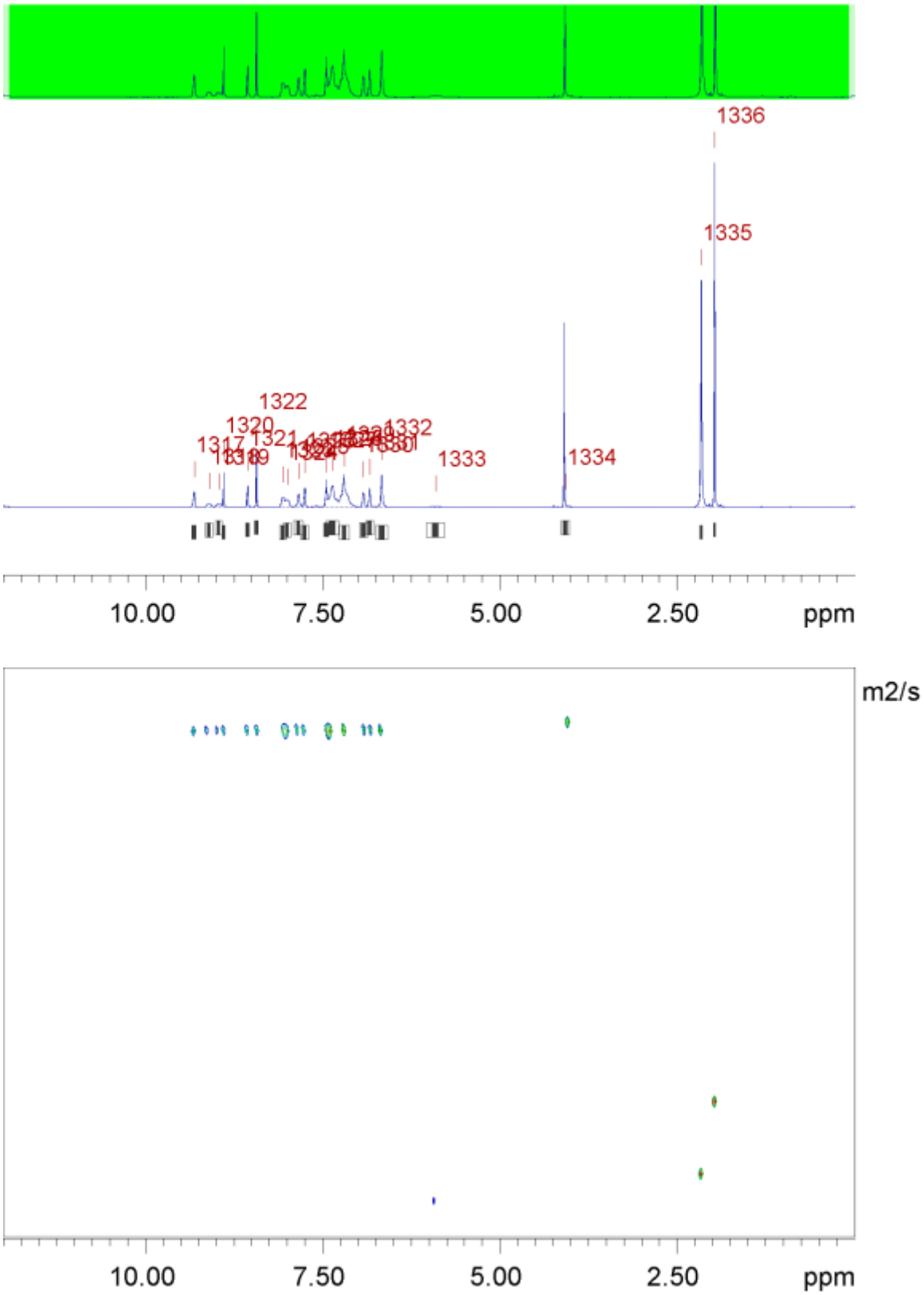

Figure 7.97. User-defined integration areas to calculate the DOSY (800 MHz, CD_3CN) of complex **C6.**

Table 7.6. DOSY parameters and peak list for complex **C6** generated by the Bruker Dynamics center.

Fitted function:	f (x) = Io * exp (-D * x^2 * gamma^2 * littleDelta^2 (bigDelta-littleDelta/3)* 10^4
used gamma:	26752 rad/(s*Gauss)
used little delta:	0.0015000 s
used big delta:	0.054900 s
used gradient strength:	variable
Random error estimation of data:	RMS per spectrum (or trace/plane)
Systematic error estimation of data:	worst case per peak scenario
Fit parameter Error estimation method:	from fit using arbitray y uncertainties
Confidence level:	95%
Used peaks:	automatically picked peaks
Used integrals:	area integral
Used Gradient strength:	all values (including replicates) used

Peak name	F2 [ppm]	D [m2/s]	error
1317	9.312	1.69e-09	4.127e-12
1318	9.104	1.70e-09	6.856e-12
1319	8.966	1.70e-09	7.448e-12
1320	8.897	1.68e-09	4.547e-12
1321	8.559	1.69e-09	3.345e-12
1322	8.432	1.69e-09	3.988e-12
1323	8.059	1.69e-09	4.589e-12
1324	8.001	1.68e-09	5.964e-12
1325	7.842	1.70e-09	6.471e-12
1326	7.753	1.70e-09	6.497e-12
1327	7.449	1.70e-09	4.238e-12
1328	7.364	1.70e-09	3.499e-12
1329	7.193	1.70e-09	3.508e-12
1330	6.924	1.69e-09	3.720e-12
1331	6.837	1.69e-09	4.459e-12
1332	6.667	1.69e-09	5.037e-12
1333	5.908	9.87e-09	2.805e-10
1334	4.072	1.67e-09	6.045e-12
1335	2.155	8.95e-09	4.371e-11
1336	1.969	6.92e-09	9.152e-12